Atul Avasthi 2K21PHDEE27 Thesis.pdf

Delhi Technological University

Document Details

Submission ID

trn:oid:::27535:114751885

Submission Date

Sep 28, 2025, 2:36 PM GMT+5:30

Download Date

Dec 6, 2025, 12:38 PM GMT+5:30

File Name

Atul Avasthi 2K21PHDEE27 Thesis.pdf

File Size

27.6 MB

238 Pages

50,779 Words

273,717 Characters

8% Overall Similarity

The combined total of all matches, including overlapping sources, for each database.

Filtered from the Report

▸ Bibliography

▸ Quoted Text

▸ Cited Text

▸ Small Matches (less than 10 words)

▸ Internet sources

▸ Crossref database

▸ Crossref posted content database

Exclusions

▸ 4 Excluded Sources

▸ 12 Excluded Matches

Match Groups

288 Not Cited or Quoted 8%
Matches with neither in-text citation nor quotation marks

0 Missing Quotations 0%
Matches that are still very similar to source material

0 Missing Citation 0%
Matches that have quotation marks, but no in-text citation

0 Cited and Quoted 0%
Matches with in-text citation present, but no quotation marks

Top Sources

0% 🌐 Internet sources

2% 📖 Publications

7% 👤 Submitted works (Student Papers)

Integrity Flags

1 Integrity Flag for Review

🚩 **Replaced Characters**
60 suspect characters on 32 pages
Letters are swapped with similar characters from another alphabet.

Our system's algorithms look deeply at a document for any inconsistencies that would set it apart from a normal submission. If we notice something strange, we flag it for you to review.

A Flag is not necessarily an indicator of a problem. However, we'd recommend you focus your attention there for further review.

Match Groups

🔴 **288** Not Cited or Quoted 8%
Matches with neither in-text citation nor quotation marks

💬 **0** Missing Quotations 0%
Matches that are still very similar to source material

📑 **0** Missing Citation 0%
Matches that have quotation marks, but no in-text citation

🔷 **0** Cited and Quoted 0%
Matches with in-text citation present, but no quotation marks

Top Sources

0% 🌐 Internet sources

2% 📖 Publications

7% 👤 Submitted works (Student Papers)

Top Sources

The sources with the highest number of matches within the submission. Overlapping sources will not be displayed.

1	**Submitted works**	
Anna University on 2024-09-05		**<1%**

2	**Submitted works**	
Indian Institute of Technology, Madras on 2015-04-06		**<1%**

3	**Submitted works**	
Uttar Pradesh Technical University on 2025-09-28		**<1%**

4	**Publication**	
Anco S. Blazev. "Solar Technologies for the 21st Century", Routledge, 2021		**<1%**

5	**Submitted works**	
IIT Delhi on 2014-03-17		**<1%**

6	**Submitted works**	
Waterford Institute of Technology on 2025-09-03		**<1%**

7	**Submitted works**	
Oklahoma State University on 2024-04-19		**<1%**

8	**Submitted works**	
Delhi Technological University on 2017-09-14		**<1%**

9	**Submitted works**	
Anna University on 2024-11-27		**<1%**

10	**Submitted works**	
Thapar University, Patiala on 2017-07-10		**<1%**

11 Submitted works

IIT Delhi on 2024-01-31   <1%

12 Submitted works

Sheffield Hallam University on 2024-09-12   <1%

13 Publication

Ton Duc Thang University   <1%

14 Submitted works

University of Glamorgan on 2025-09-19   <1%

15 Submitted works

Koc University on 2017-09-01   <1%

16 Submitted works

Government Engineering College, Thrissur on 2025-07-04   <1%

17 Submitted works

Jawaharlal Nehru Technological University on 2025-05-30   <1%

18 Submitted works

University of Nottingham on 2018-05-18   <1%

19 Submitted works

IIT Delhi on 2015-02-11   <1%

20 Submitted works

Jawaharlal Nehru Technological University on 2025-07-30   <1%

21 Submitted works

Universiti Teknologi MARA on 2018-09-27   <1%

22 Submitted works

Kingston University on 2025-09-20   <1%

23 Submitted works

University of Hertfordshire on 2025-05-05   <1%

24 Submitted works

Anna University on 2024-06-19   <1%

25   Submitted works

Independent College Dublin on 2022-06-18   <1%

26   Submitted works

City University of Hong Kong on 2025-04-06   <1%

27   Submitted works

KEDGE Business Schools on 2024-04-08   <1%

28   Submitted works

Feng Chia University on 2017-09-09   <1%

29   Submitted works

Napier University on 2024-08-21   <1%

30   Submitted works

University of Cape Town on 2012-12-23   <1%

31   Submitted works

Eastern Mediterranean University on 2014-10-24   <1%

32   Submitted works

Eiffel Corporation on 2022-05-24   <1%

33   Submitted works

Indian Institute of Technology, Madras on 2014-07-25   <1%

34   Publication

Ashwani Kumar, Sivasakthivel Thangavel, Gaurav Dwivedi. "Green Hydrogen Prod...   <1%

35   Submitted works

Cape Peninsula University of Technology on 2025-04-23   <1%

36   Submitted works

Dublin City University on 2025-08-03   <1%

37   Submitted works

Liverpool John Moores University on 2023-09-15   <1%

38   Submitted works

University of Southampton on 2025-02-24   <1%

39	Submitted works

University of Southern Queensland on 2025-08-26 <1%

40	Submitted works

De Montfort University on 2023-05-16 <1%

41	Submitted works

Liverpool John Moores University on 2025-04-17 <1%

42	Submitted works

The University of Manchester on 2014-09-05 <1%

43	Publication

Ahad Ghaemi, Zohreh Khoshraftar, Fereshteh Pouresmaeil. "CO Adsorbents - Adv... <1%

44	Publication

Seal, Will, Rohde, Carsten, Garrison, Ray. "EBOOK: Management Accounting, 6e", ... <1%

45	Submitted works

University of Edinburgh on 2016-04-19 <1%

46	Submitted works

University of Leeds on 2025-05-13 <1%

47	Submitted works

University of Melbourne on 2024-09-13 <1%

48	Submitted works

Free University of Bolzano on 2023-09-06 <1%

49	Submitted works

University of Nottingham on 2024-09-03 <1%

50	Submitted works

University of Queensland on 2018-03-22 <1%

51	Submitted works

iGroup on 2014-06-19 <1%

52	Submitted works

Blackboard Production (elp.northumbria.ac.uk) on 2025-05-19 <1%

53	Submitted works

Indian Institute of Technology (ISM), Dhanbad on 2025-08-28   <1%

54	Publication

Page, Megan T.. "Modeling Improvements to Vertical Bifacial Solar Arrays", Rutge...   <1%

55	Submitted works

The University of Fiji on 2021-07-06   <1%

56	Submitted works

Universiti Tenaga Nasional on 2024-10-10   <1%

57	Submitted works

Anna University on 2024-11-18   <1%

58	Submitted works

Anna University on 2025-01-09   <1%

59	Submitted works

Malta College of Arts,Science and Technology on 2023-06-06   <1%

60	Submitted works

Oxford Brookes University on 2015-05-05   <1%

61	Submitted works

University of Aberdeen on 2021-08-23   <1%

62	Submitted works

University of New South Wales on 2025-07-31   <1%

63	Submitted works

University of South Africa on 2025-07-21   <1%

64	Submitted works

University of Warwick on 2025-09-23   <1%

65	Submitted works

Edith Cowan University on 2024-05-13   <1%

66	Submitted works

Universitas Borneo Tarakan on 2025-03-15   <1%

67   Submitted works

University of Aberdeen on 2018-08-09   <1%

68   Submitted works

University of Basrah on 2020-03-03   <1%

69   Submitted works

Anna University on 2025-01-25   <1%

70   Submitted works

Delhi Technological University on 2017-05-04   <1%

71   Submitted works

Panjab University on 2014-02-18   <1%

72   Submitted works

University of Exeter on 2025-03-08   <1%

73   Publication

Jara Aguilera, Danilo Andres. "Synthetic Wind Data Series for the Chilean Wind Pa...   <1%

74   Submitted works

National University of Ireland, Galway on 2019-05-23   <1%

75   Publication

Dhiraj Magare, Prasiddh Trivedi, Kedar V. Khandeparkar. "Photovoltaic Modules - ...   <1%

76   Publication

Raza, Hamza Ahmad. "Application of Non-Contact Electrostatic Voltmeter for Sola...   <1%

77   Submitted works

APJ Abdul Kalam Technological University, Thiruvananthapuram on 2025-02-20   <1%

78   Publication

Arthur James Swart, Keshav Kumar, Bishwajeet Pandey, Sakshi Sharma. "Perovski...   <1%

79   Submitted works

IIT Delhi on 2018-03-08   <1%

80   Submitted works

Institute of Technology, Nirma University on 2015-06-25   <1%

81   Submitted works

RMIT University on 2020-09-03   <1%

---

82   Submitted works

The London College UCK on 2024-04-21   <1%

---

83   Submitted works

Universiti Tunku Abdul Rahman on 2013-01-12   <1%

---

84   Submitted works

University of Exeter on 2023-12-15   <1%

---

85   Submitted works

University of Huddersfield on 2017-04-28   <1%

---

86   Submitted works

University of Huddersfield on 2018-03-28   <1%

---

87   Submitted works

Waterford Institute of Technology on 2025-05-09   <1%

---

88   Submitted works

iGroup on 2014-06-16   <1%

---

89   Publication

Birudala Venkatesh Reddy, Y V Krishna Reddy, Md. Abdur Razzak, Surender Reddy...   <1%

---

90   Submitted works

Cranfield University on 2023-08-26   <1%

---

91   Submitted works

Higher Education Commission Pakistan on 2024-06-23   <1%

---

92   Submitted works

Kingston University on 2025-01-08   <1%

---

93   Submitted works

Monash University on 2024-05-26   <1%

---

94   Submitted works

RMIT University on 2017-11-06   <1%

---

95 Submitted works

RMIT University on 2020-11-01   <1%

96 Submitted works

SP Training on 2024-08-24   <1%

97 Publication

Satya Prakash Maurya, Akhilesh Kumar Yadav, Ramesh Singh. "Modeling and Sim...   <1%

98 Submitted works

Universiti Teknologi Petronas on 2025-07-28   <1%

99 Submitted works

Universiti Tenaga Nasional on 2025-01-27   <1%

100 Submitted works

University of Nottingham on 2014-09-05   <1%

101 Submitted works

northcap on 2024-10-06   <1%

102 Submitted works

universititeknologimara on 2025-02-16   <1%

103 Submitted works

Glasgow Caledonian University on 2017-05-03   <1%

104 Submitted works

Glasgow Caledonian University on 2023-05-18   <1%

105 Submitted works

Glyndwr University on 2025-05-16   <1%

106 Submitted works

Griffth University on 2019-10-18   <1%

107 Publication

Hazra, Jayanti. "Economic Analysis of Rooftop Solar Panels Montijo, Portugal", Uni...   <1%

108 Submitted works

IIT Delhi on 2012-08-27   <1%

109	Submitted works	
IIT Delhi on 2014-05-13		**<1%**

110	Submitted works	
IIT Delhi on 2014-07-30		**<1%**

111	Submitted works	
Indian Institute of Technology, Bombay on 2024-05-21		**<1%**

112	Submitted works	
KTH - The Royal Institute of Technology on 2013-02-14		**<1%**

113	Publication	
Khanal, Samip. "Engineering a Pathway to 100% Renewable Energy in Greater All...		**<1%**

114	Submitted works	
Liverpool John Moores University on 2024-09-10		**<1%**

115	Publication	
Moncef Krarti. "Energy Audit of Building Systems - An Engineering Approach", CR...		**<1%**

116	Submitted works	
RMIT University on 2023-07-21		**<1%**

117	Publication	
Sam Ghosh. "Startup Finance 2.0 - Value Creation, Tokenization, and the Next Era ...		**<1%**

118	Submitted works	
Universiti Malaysia Perlis on 2012-04-25		**<1%**

119	Submitted works	
University College London on 2024-09-11		**<1%**

120	Submitted works	
University of Canterbury on 2025-04-23		**<1%**

121	Submitted works	
University of Central Lancashire on 2025-03-12		**<1%**

122	Submitted works	
University of Glamorgan on 2023-09-11		**<1%**

123	Submitted works	
University of Glasgow on 2020-04-20		<1%

124	Submitted works	
University of Liverpool on 2019-11-04		<1%

125	Submitted works	
University of Nottingham on 2025-09-23		<1%

126	Submitted works	
University of Teesside on 2022-01-21		<1%

127	Submitted works	
Waterford Institute of Technology on 2025-05-11		<1%

128	Submitted works	
Addis Ababa University on 2024-10-11		<1%

129	Publication	
Al Zadjali, Muhannad Issa Ali. "Designing and Modeling of a Solar PV Park in Suha...		<1%

130	Submitted works	
Arab Academy for Science, Technology & Maritime Transport CAIRO on 2025-05-22		<1%

131	Submitted works	
Bahrain Polytechnic on 2023-12-31		<1%

132	Submitted works	
Indian Institute of Technology, Kanpur on 2024-06-26		<1%

133	Submitted works	
Kasetsart University on 2025-09-28		<1%

134	Submitted works	
Kingston University on 2024-09-09		<1%

135	Submitted works	
Maine Maritime Academy on 2025-07-21		<1%

136	Submitted works	
Monash University on 2021-01-13		<1%

137 Publication

Morten Helbæk, Ragnar Løvaas, Jon Mjølhus. "Financial Modelling and Asset Valu... <1%

138 Publication

Natarajan Balasubramanian Muthu Selvan, Venkatraman Thiyagarajan, Cheng Si... <1%

139 Submitted works

School of Business & Computer Science Limited on 2025-07-29 <1%

140 Submitted works

Singapore Institute of Technology on 2024-10-23 <1%

141 Submitted works

Universiti Pertahanan Nasional Malaysia on 2024-09-19 <1%

142 Submitted works

University of Central Lancashire on 2010-04-28 <1%

143 Submitted works

University of Edinburgh on 2025-04-28 <1%

144 Submitted works

University of Hull on 2024-09-11 <1%

145 Submitted works

University of Macau on 2025-05-05 <1%

146 Submitted works

University of Northumbria at Newcastle on 2024-05-09 <1%

147 Submitted works

Aligarh Muslim University, Aligarh on 2024-09-02 <1%

148 Submitted works

Anna University on 2024-06-18 <1%

149 Submitted works

Anna University on 2025-01-02 <1%

150 Submitted works

Anna University on 2025-02-08 <1%

151	Submitted works	
Arab Academy for Science, Technology & Maritime Transport CAIRO on 2021-08-30		**<1%**

152	Submitted works	
Associatie K.U.Leuven on 2025-08-13		**<1%**

153	Submitted works	
Bitlis Eren Ãniversitesi on 2017-08-11		**<1%**

154	Submitted works	
Brunel University on 2025-06-03		**<1%**

155	Submitted works	
Central Queensland University on 2023-09-06		**<1%**

156	Submitted works	
Central Queensland University on 2025-09-12		**<1%**

157	Submitted works	
Cranfield University on 2024-08-31		**<1%**

158	Submitted works	
Edith Cowan University on 2023-05-27		**<1%**

159	Submitted works	
European University of Lefke on 2014-12-25		**<1%**

160	Submitted works	
Florida International University on 2023-04-23		**<1%**

161	Submitted works	
Glasgow Caledonian University on 2025-04-23		**<1%**

162	Submitted works	
Heriot-Watt University on 2024-08-24		**<1%**

163	Submitted works	
IIT Delhi on 2013-07-14		**<1%**

164	Submitted works	
International Management Institute on 2020-09-29		**<1%**

165   Publication

Krishan Arora, Himanshu Sharma. "Innovations in Non-Conventional Energy Sour...   <1%

166   Publication

M. Premkumar, Pasumarthi Usha, Sujit Kumar, Manikanta Gopisetti. "Intelligent ...   <1%

167   Submitted works

Macquarie University on 2024-06-02   <1%

168   Submitted works

Malaviya National Institute of Technology on 2016-02-28   <1%

169   Submitted works

Masdar Institute of Science and Technology on 2014-05-26   <1%

170   Submitted works

National Institute of Technology, MIZORAM on 2024-07-24   <1%

171   Submitted works

Swinburne University of Technology on 2024-01-03   <1%

172   Submitted works

Teaching and Learning with Technology on 2024-09-16   <1%

173   Submitted works

Teaching and Learning with Technology on 2024-11-03   <1%

174   Submitted works

Universidade Estadual de Campinas on 2024-08-23   <1%

175   Submitted works

Universiti Tenaga Nasional on 2024-12-29   <1%

176   Submitted works

University of Aberdeen on 2021-08-16   <1%

177   Submitted works

University of Bradford on 2024-05-02   <1%

178   Submitted works

University of College Cork on 2025-04-02   <1%

179   Submitted works

University of East London on 2025-09-01   <1%

180   Submitted works

University of Energy and Natural Resources on 2021-10-06   <1%

181   Submitted works

University of Exeter on 2025-05-01   <1%

182   Submitted works

University of Exeter on 2025-08-20   <1%

183   Submitted works

University of Glasgow on 2025-08-15   <1%

184   Submitted works

University of Greenwich on 2020-04-24   <1%

185   Submitted works

University of Hull on 2025-09-10   <1%

186   Submitted works

University of Johannsburg on 2023-06-24   <1%

187   Submitted works

University of Johannsburg on 2023-08-27   <1%

188   Submitted works

University of New South Wales on 2012-10-15   <1%

189   Submitted works

University of New South Wales on 2019-11-27   <1%

190   Submitted works

University of Newcastle upon Tyne on 2010-08-31   <1%

191   Submitted works

University of Newcastle upon Tyne on 2013-08-21   <1%

192   Submitted works

University of Queensland on 2020-06-10   <1%

193	Submitted works

University of Sheffield on 2016-08-25   **<1%**

194	Submitted works

University of Sheffield on 2023-09-18   **<1%**

195	Submitted works

University of Stellenbosch, South Africa on 2024-11-14   **<1%**

196	Submitted works

University of Technology, Sydney on 2025-08-30   **<1%**

197	Submitted works

University of Teesside on 2023-05-08   **<1%**

198	Submitted works

University of Wales Swansea on 2018-10-01   **<1%**

199	Submitted works

University of Wales Swansea on 2019-09-11   **<1%**

200	Submitted works

Uttar Pradesh Technical University on 2025-09-02   **<1%**

201	Submitted works

Visayas State University on 2025-05-25   **<1%**

PERFORMANCE ANALYSIS OF GRID CONNECTED PV SYSTEM

A Thesis Submitted
In Partial Fulfillment of the Requirements
for the Degree of

DOCTOR OF PHILOSOPHY

by

ATUL AVASTHI

(Roll No. 2K21/PHDEE/27)

Under the Supervision of
Prof. Rachana Garg and Prof. Priya Mahajan
Department of Electrical Engineering
Delhi Technological University, Delhi - 110042

Department of Electrical Engineering

DELHI TECHNOLOGICAL UNIVERSITY

(Formerly Delhi College of Engineering)
Shahbad Daulatpur, Main Bawana Road, Delhi - 110042. INDIA

September, 2025

©DELHI TECHNOLOGICAL UNIVERISITY, DELHI-2025
ALL RIGHTS RESERVED

DELHI TECHNOLOGICAL UNIVERSITY
(Formerly Delhi College of Engineering)
Shahbad Daulatpur, Main Bawana Road, Delhi-42

CANDIDATE'S DECLARATION

I hereby certify that the work which is being presented in the thesis entitled **"PERFORMANCE ANALYSIS OF GRID CONNECTED PV SYSTEM"** in partial fulfillment of the requirements for the award of the Degree of Doctor of Philosophy and submitted in the **Department of Electrical Engineering** of the **Delhi Technological University, Delhi** is an authentic record of my own work carried out during the period from August 2021 to September 2025 under the supervision of Dr. Rachana Garg, Professor, Department of Electrical Engineering and Dr. Priya Mahajan, Professor, Department of Electrical Engineering, Delhi Technological University, Delhi.

The matter presented in this thesis has not been submitted by me for the award of any other degree of this or any other Institute.

(Atul Avasthi)

This is to certify that the candidate has incorporated all the corrections suggested by the examiners in the thesis and the statement made by the candidate is correct to the best of our knowledge.

Signature of Supervisors

Signature of External Examiner

DELHI TECHNOLOGICAL UNIVERSITY

(Formerly Delhi College of Engineering)
Shahbad Daulatpur, Main Bawana Road, Delhi-42

CERTIFICATE

Certify that **Atul Avasthi** (2K21/PHDEE/27) has carried out their work presented in this thesis entitled **"PERFORMANCE ANALYSIS OF GRID CONNECTED PV SYSTEM"** for the award of **Doctor of Philosophy** from Department of Electrical Engineering, Delhi Technological University, Delhi, under our supervision. The thesis embodies results of original work, and studies are carried out by the student himself and the content of the thesis do not form the basis for the award of any other degree to the candidate or to anybody else from this or any other University/Institute.

(Prof. Rachana Garg)   (Prof. Priya Mahajan)

Supervisor   Co-Supervisor

Date:

v

Abstract

This thesis presents an in-depth investigation into the design, control, and performance optimization of grid-connected and standalone solar photovoltaic (PV) systems, with a particular focus on floating solar PV (FSPV) technologies. As the global energy sector shifts towards clean and renewable sources, and with increasing land constraints in developing countries such as India, floating solar systems have emerged as a promising solution. This research addresses key technical, operational, and economic challenges associated with advanced PV system configurations, control methodologies, and deployment strategies.

This study presents a comprehensive design and performance analysis of both stand-alone and grid-connected solar PV systems. It includes the modeling of PV modules, DC-DC boost converters, and the implementation of advanced maximum power point tracking (MPPT) techniques such as perturb and observe (P&O), fuzzy logic control (FLC), and the bio-inspired flying squirrel search optimization (FSSO). For grid-connected operation, inverter control strategies based on synchronous reference frame theory (SRFT) and instantaneous reactive power theory (IRPT) are employed. Simulation results validate the superior tracking efficiency of the FSSO algorithm and demonstrate that SRFT-based control ensures improved harmonic mitigation, voltage stability, and power quality compliance under dynamic irradiance conditions.

A core focus of the thesis is the technical and economic assessment of floating solar PV systems. A comparative analysis is carried out between monofacial and bifacial PV modules installed on floating platforms. The results reveal that bifacial modules significantly outperform monofacial counterparts due to their ability to utilize reflected irradiance from the water surface. Enhanced energy yield, improved performance ratio (PR), and lower levelized cost of energy (LCOE) are observed, establishing bifacial FSPV as a superior choice for maximizing energy production.

The research further explores the role of solar tracking mechanisms such as fixed tilt, single-axis, and dual-axis, in optimizing the energy performance of

vi

floating PV installations. It is found that while dual-axis tracking achieves the highest energy gains, its application in floating systems must account for increased mechanical complexity and cost. Performance improvements are assessed under realistic operating conditions, considering water movement and structural stability.

Additionally, the thesis examines the effect of inverter loading ratio (ILR) on the performance and economic viability of FSPV systems. Multiple ILR configurations are analyzed to identify the optimal balance between energy generation, clipping losses, and cost efficiency. Seasonal solar resource variations are considered to propose site-specific ILR values that align with project financial objectives.

This research concludes by summarizing the significant contributions made in advancing MPPT and inverter control strategies, and in optimizing floating PV system design and operation. The findings offer practical guidelines for future PV installations and lay the groundwork for further research in areas such as long-term degradation modeling, hybrid PV-storage integration, and experimental validation of floating PV technologies under real-world conditions. The outcomes are expected to contribute meaningfully to the sustainable expansion of solar energy infrastructure, particularly in water-rich, land-scarce regions.

Acknowledgements

Writing this thesis has been an intellectually stimulating experience. I express my gratitude to God for the strength to pursue knowledge.

This thesis reflects my dedication to achieving an academic standard. I wish to acknowledge those who contributed to this endeavor.

I am particularly grateful to my supervisors, **Prof. Rachana Garg** and **Prof. Priya Mahajan** for their unwavering guidance and encouragement during my research. They inspired me to approach my research with zeal and resolve.

I am thankful to **Prof. Prateek Sharma** (Vice-Chancellor) and **Prof. Rinku Sharma** (Dean - Academic PG) for fostering a conducive research environment at Delhi Technological University. I extend my thanks to **Prof. Rachana Garg** for her visionary support as the Head of the Department and Chairperson of the DRC. I am indebted to **all the faculty members and staff** for their shared expertise that facilitated my research.

I would also like to acknowledge the Chandigarh Renewal Energy and Science & Technology Promotion Society (CREST) for providing information on the specifications of the equipment used in the plant and allowing the authors to visit the plant in Chapter 3. I appreciate everyone who supported me directly or indirectly throughout this work.

I thank **Dr. Abhishek Sharma** (Director, Bureau of Energy Efficiency), **Gaurav Yadav, Brijendra Senger, Dipak Prasad, Dr. Sudhanshu Mittal, Divyansh Shaily, Manvi Mishra, Priya** and **Shruti Prajapati** for their insightful discussions and technical assistance.

Ultimately, I am profoundly grateful to **my parents, wife,** and **daughter (Shree)** for their unwavering faith and support during my research journey.

Date: **Atul Avasthi**

Contents

x

xii

xiv

XV

List of Figures

xvi

xvii

xviii

List of Tables

xx

xxi

xxiii

List of Abbreviations

AC	Alternating Current
ACO	Ant Colony Optimization
AI-BSF	Aluminium Back Surface Field
AM	Air Mass
APF	Active Power Filter
As	Arsenic
BOS	Balance of System
CAPEX	Capital Expenditure
CFA	Central Financial Assistance
CDF	Cumulative Distribution Function
CE	Change in Error
CF	Capacity Factor
COP	Conference of Parties
CPSU	Central Public Sector Undertakings
CSP	Concentrated Solar Power
c-Si	Crystalline Silicon
D	Duty Cycle
DAT	Dual Axis Tracker
DC	Direct Current
DE	Differential Evolution
DNI	Direct Normal Irradiance
DPB	Discounted Payback

xxiv

E	Error
FL	Fuzzy Logic
FLC	Fuzzy Logic Controller
FSQ	Flying Squirrels
FSPV	Floating Solar Power Plant
FSSO	Flying Squirrel Search Optimization
FT	Fix Tilt
GA	Genetic Algorithm
Ga	Gallium
GHI	Global Horizontal Irradiance
GHG	Greenhouse Gas
GMPP	Global Maximum Power Point
GOI	Government of India
GW	Gigawatt
HDPE	High Density Polyethene
HSAT	Horizontal Single Axis Tracker
IAM	Incidence Angle Modifier
IC	Incremental Conductance
IGBT	Insulated Gate Bipolar Transistor
ILR	Inverter Loading Ratio
INC	Incremental Conductance
IRPT	Instantaneous Reactive Power Theory
IRR	Internal Rate of Return
ISTS	Inter-State Transmission Systems
LCOE	Levelized Cost of Energy
LDR	Light Dependent Resistor
LID	Light Induced Degradation
MAPE	Mean Absolute Percentage Error

MLE	Maximum Likelihood Estimation
MLF	Mismatch Loss Factor
MLPE	Module-Level Power Electronics
MNRE	Ministry of New and Renewable Energy
MPPT	Maximum Power Point Tracking
MW	Megawatt
MWh	Megawatt Hour
NB	Negative Big
NDC	Nationally Determined Contributions
NOS	Near Optimum Solution
NPV	Net Present Value
NS	Negative Small
NREL	National Renewable Energy Laboratory
OPEX	Operation and Maintenance Cost
OSP	Optimum Solution
P and O	Perturb and Observe
PB	Positive Big
PCC	Point of Common Coupling
PID	Potential Induced Degradation
PLL	Phase Locked Loop
PM-Kusum	PM Kisan Urja Suraksha Evam Utthan Mahabhiyan
PR	Performance Ratio
PS	Positive Small
PV	Photovoltaic
PWM	Pulse Width Modulation
RF	Renewable Energy
RES	Renewable Energy Sources
RMSE	Root Mean Square Error

xxvi

RS	Random Solution
SAM	System Advisor Model
SAT	Seasonal Axis Tracker
SLF	Soiling Loss Factor
SNAs	State Nodal Agencies
SRFT	Synchronous Reference Frame Theory
STC	Standard Test Condition
TLF	Temperature Loss Factor
VSC	Voltage Source Converter
VSI	Voltage Source Inverter
WOA	Whale Optimization Algorithm
ZR	Zero
kW	Kilowatt
kWh	Kilowatt Hour

List of Symbols

A	Area covered by PV module
A_i	Actual value
b	Empirical coefficient
C	Capacitor
C_D	Drag coefficient
C_L	Lift coefficient
C_i	Net cash flow in time i
C_t	Capital cost
$CE(k)$	Change in error
D	Diode / Duty cycle
D_{LID}	LID factor
D_r	Discount rate
ΔCF	Change in capacity factor (CF)
ΔCL	Change in clipping loss
ΔD	Duty cycle change
ΔI	Incremental investment cost
ΔI_L	Inductor current ripple
ΔPR	Change in performance ratio (PR)
ΔS	Annual saving net of future annual cost
ΔV	Ripple voltage
d_{at}	Location of squirrels at acorn tree
d_{ht}	Location of squirrels at hickory tree

xxviii

d_{max}	Maximum duty cycle
d_{min}	Minimum duty cycle
dnt	Location of squirrel at normal tree
DNI	Direct Normal Irradiance
$E(k)$	Error
E_A	Total DC energy from PV array
E_c	Clean PV module output power
E_{clip}	Clipping loss
E_{Grid}	Grid energy
E_L	Energy consumed by load
E_s	Soiled PV module output power
F_D	Drag force
F_L	Lift force
$FSPV_B$	Bifacial floating solar PV plant
$FSPV_M$	Monofacial floating solar PV plant
F_t	Fuel cost
FT	Fix Tilt
FSQ	Flying Squirrels
$FSSO$	Flying Squirrel Search Optimization
G_0	PV reference irradiance / Irradiance at normal incidence
G_{eff}	Effective irradiance after IAM correction
G_θ	Irradiance value at incidence angle θ
G_c	Gliding constant
G_d	Gliding distance
Ga	Gallium
GHG	Greenhouse Gas
GHI	Global Horizontal Irradiance
$GMPP$	Global Maximum Power Point

GW	Gigawatt
h	Overload factor
h_g	Height loss
H_T	Total in-plane irradiance
$HSAT$	Horizontal Single Axis Tracker
I_D	Diode current
I_0	Reverse saturation current
I_{La}, I_{Lb}, I_{Lc}	Load currents
I_{mp}	Current at maximum power point
I_{ph}	Photocurrent
I_{pv}	Output current of PV cell
I_{sa}, I_{sb}, I_{sc}	Three-phase grid currents
I_{sc}	Short-circuit current
I_{out}	Output current
i_d	Direct axis component
i_q	Quadrature axis component
IC	Incremental conductance
ILR	Inverter Loading Ratio
INC	Incremental conductance
IAM	Incidence Angle Modifier
$IGBT$	Insulated Gate Bipolar Transistor
K	Boltzmann's constant
K_m	Minimum number of iterations
k	Current iteration count / Step coefficient
kWh	Kilowatt Hour
L	Inductor
L_A	Array capture loss
L_f	Load interfacing inductor

xxx

L_{IAM}	IAM loss
L_{sys}	System loss
LID	Light Induced Degradation
M	Modulation index
$MAPE$	Mean Absolute Percentage Error
MLE	Maximum Likelihood Estimation
MLF	Mismatch Loss Factor
$MLPE$	Module-Level Power Electronics
$MNRE$	Ministry of New and Renewable Energy
$MPPT$	Maximum Power Point Tracking
MW	Megawatt
MWh	Megawatt Hour
m^2	Meter square
N	Number of years
N_p	Number of modules connected in parallel
N_s	Number of modules connected in series
NB	Negative Big
NOS	Near Optimum Solution
NS	Negative Small
NPV	Net Present Value
$NREL$	National Renewable Energy Laboratory
O_f	Operation and maintenance cost
$OPEX$	Operation and Maintenance Cost
OSP	Optimum Solution
P_{AC}	AC output power of plant
$P_{AC,rated}$	Rated AC output power of inverter
P_{max}	Maximum power
P_{MPP}	Power at maximum power point

P_c	Compensating real power
P_{DC}	DC output power of plant
$P_{DC,STC}$	DC output power of PV module under STC
P_g	Real power of the grid
P_I	Real power of the inverter
P_i	Rated power output of the i-th module in string / Predicted value
P_{loss}	Power loss in wiring
$P_{nt,o}$	Power consumption during night
P_{pv}	PV output power
$P_{S,op}$	Power consumption during operation
$P_{PV,rated}$	Rated output power of PV plant
P_{peak}	Peak power of PV system
PR	Performance Ratio
PS	Positive Small
PV	Photovoltaic
q	Charge of electron $(1.61 \times 10^{-19}\, C)$
p^*, q^*	Instantaneous active and reactive power
Q_c	Compensating reactive power
Q_g	Reactive power of the grid
Q_I	Reactive power of the inverter
RF	Renewable Energy
RES	Renewable Energy Sources
$RMSE$	Root Mean Square Error
RS	Random Solution
S	Surface area of body
S_c	Seasonal constant
S_{min}	Minimum seasonal constant
SF	Scaling factor

xxxii

T	Temperature in Kelvin
T_m	Module temperature
T_{ref}	Reference temperature
V	Velocity
V_{dc}	DC link voltage
$V_{dc,\text{ripple}}$	DC link voltage ripple
V_{in}	Input voltage
V_{LL}	RMS voltage of three-phase voltage
V_{mp}	Voltage at maximum power point
V_{oc}	Open-circuit voltage
V_{out}	Output voltage
V_{pv}	Output voltage of PV cell
V_{sa}, V_{sb}, V_{sc}	Three-phase grid voltages
VSI	Voltage Source Inverter
W/m^2	Watt per meter squared
Y_A	Array yield
Y_F	Final yield
Y_R	Reference yield
α, β	Two-axis stationary frame
η	Efficiency of the system
η_{LID}	Efficiency factor after degradation
$\eta_m(t)$	Module efficiency at time t
η_{m0}	Initial module efficiency
η_{mis}	Mismatch efficiency
η_{MV}	Medium voltage loss efficiency
η_{PV}	PV module efficiency
η_s	Soiling efficiency
η_T	Temperature efficiency correction factor

xxxiii

η_{sys}	System efficiency
γ_0	Temperature coefficient of power
λ	Lévy index

Chapter 1

INTRODUCTION

Energy plays a pivotal role in the socio-economic development of any nation, with a well-established correlation between electricity consumption and economic growth. As countries progress, their demand for reliable, secure, and sustainable energy sources intensifies. The conventional reliance on fossil fuels has led to multiple concerns such as rising fuel costs, finite reserves, and significant greenhouse gas emissions that contribute to environmental degradation and climate change.

In the context of developing nations like India, the challenge is twofold: to ensure energy security while simultaneously promoting environmental sustainability. A shortfall in energy availability can directly impede industrial growth, infrastructure development, and overall economic progress. Consequently, there is a growing emphasis on transitioning toward cleaner and renewable sources of energy that are not only environmentally benign but also socially acceptable and economically viable [1]. Most parts of India receive daily solar radiation ranging from 4 kWh/m^2 to 7 kWh/m^2 with sunny days, varying between 250 to 300 days annually [2]. India as per commitment in Conference of Parties 26 (COP), Glasgow, U.K has set an ambitious plan for achieving 50% of India's total installed capacity for electricity from non-fossil sources including solar generation by 2030. This commitment may not only augment power generation but also contribute largely to green energy production to help reduce climatic changes.

With the installation of 175 GW of generation capacity through renewable in the last nine years, the Indian power sector has experienced a significant transition from a power deficit to a power surplus nation [3]. India made a

commitment at the COP-21, Paris (France) to attain 40% of its installed electrical capacity from non-fossil energy sources by 2030 as part of its Nationally Determined Contributions (NDCs). The country has achieved this target in November 2021 i.e., 9 years ahead of schedule. India is currently heading toward meeting the updated targets from Glasgow's COP26, which states that by 2030, non-fossil fuel sources will account for 50% of installed capacity for power generation.

TABLE 1.1: Installed generation capacity details (Fuel-Wise) as of July 31, 2025

Fuel Type	Capacity (GW)	Share (%)
Nuclear	8.80	1.81
Large Hydro	49.62	10.24
Solar	119.02	24.55
Wind	52	10.73
Biomass Power/Cogeneration	8.17	1.68
Small Hydro Power	5.10	1.06
Total Non-Fossil Fuel	242.71	50.07

The Indian grid has now emerged as the world's largest integrated grid that can transmit power up to 1,12,250 MW through Inter-State Transmission Systems (ISTS). During February 2023 in rural areas, the average power availability per day has increased from 12 hours in 2015 to $22\frac{1}{2}$ hours while the average availability in cities is $23\frac{1}{2}$ hours. Around 24% of power is generated by the central sector, 25% is generated by the state sector and the rest 51% is generated by the private sector. The nation's overall generation, which includes power from renewable sources connected to the grid, increased from 1110.458 BU in 2014–15 to 1624.465 BU in 2022–2023 [4]. The details of installed generation capacity (Fuel-wise) as of 30.06.2025 is given in Table 1.1 [5]. There is a notable and accelerating shift towards non-fossil energy sources, which now account for 45.54% of the total capacity. Among these, solar power emerges as the leading contributor with 85.47 GW (19.15%), followed by hydro and wind power. The rapid expansion of solar capacity highlights the country's strategic focus on clean energy adoption. In this context, floating solar photovoltaic (FSPV) systems
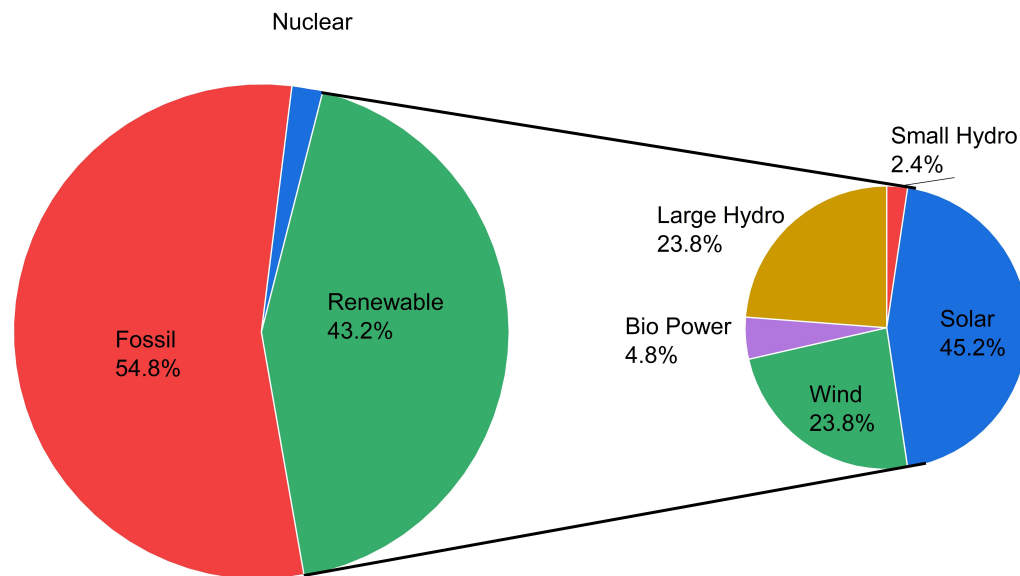
FIGURE 1.1: Share of various Sources of energy based on installed capacity

are gaining significant attention as an innovative solution to overcome land scarcity, reduce water evaporation, and enhance energy yield through improved thermal performance. The increasing share of solar energy in the national mix provides a strong foundation for the development and deployment of FSPV projects, particularly in regions with abundant water bodies and high solar potential. India stands 5th in solar PV deployment across the globe at the end of 2022 [6, 7]. The share of various sources of energy based on installed capacity is shown in Fig. 1.1.

1.1   Integration of Renewable Energy Sources

The integration of renewable energy sources (RES) into power systems has become a global imperative to combat climate change, reduce dependence on fossil fuels, and ensure long-term energy security. This integration can be
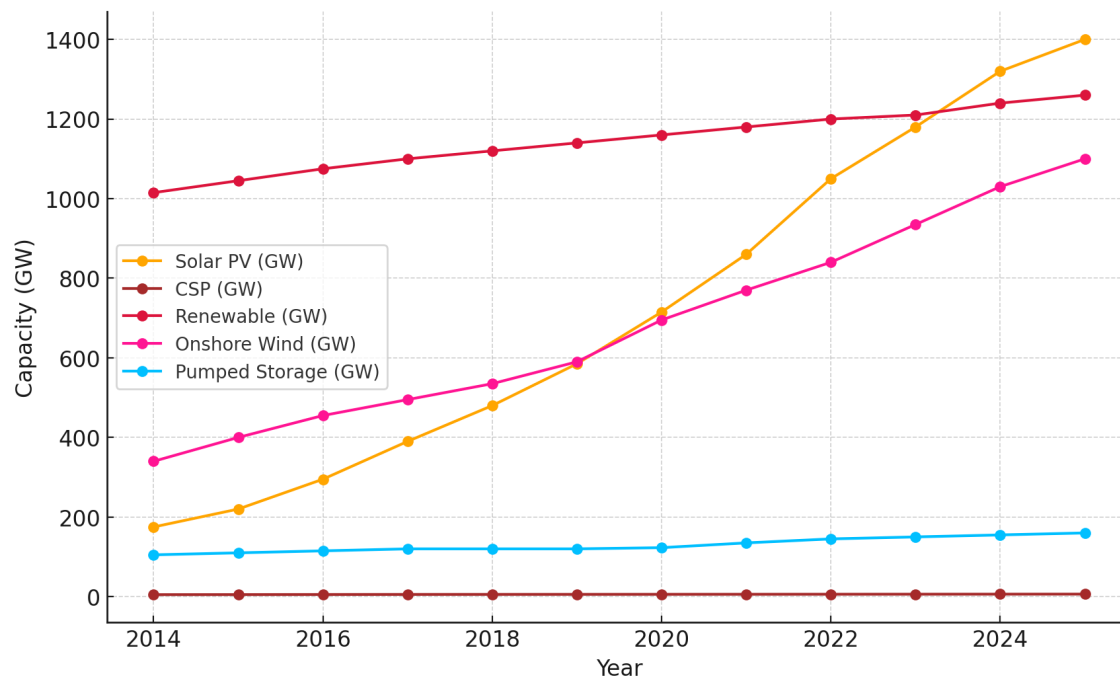
FIGURE 1.2: Renewable energy generation in global scenario
(IRENA 2023)

broadly classified into two perspectives: the worldwide scenario and the Indian
scenario.

1.1.1 Worldwide Scenario

Overall, renewable energy has experienced remarkable expansion over the past
decade, consistently surpassing annual growth projections. Fig. 1.2 illustrates the
global growth of renewable energy capacity from 2014 to July 2025, highlighting
significant trends in pumped storage, onshore wind energy, solar PV, concentrated
solar power (CSP) and hydropower.

Solar PV shows the most rapid and exponential increase, becoming a
dominant energy source by 2025. Onshore wind energy exhibits steady linear
growth, contributing significantly to the total capacity. In contrast, hydropower,
which was the leading renewable source in 2014, displays slower growth,
indicating possible saturation or limited new development. Pumped storage
capacity remains relatively stable, playing a supporting role in grid stability,
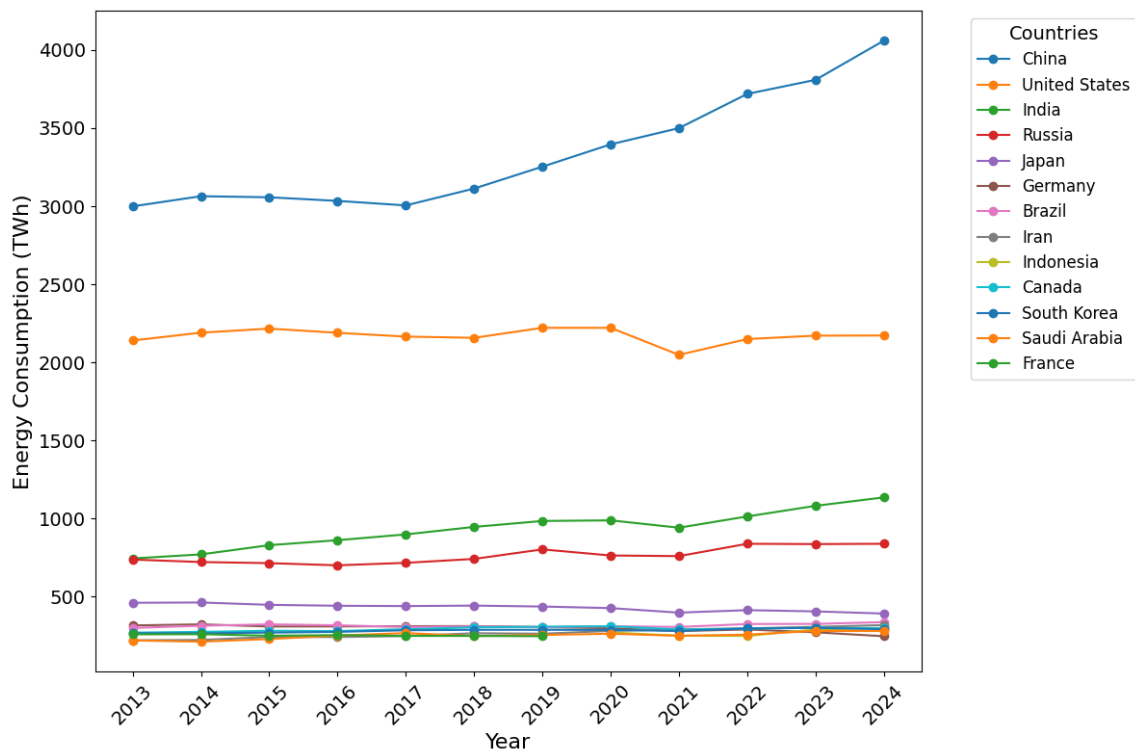
FIGURE 1.3: World energy consumption by country from Year 2014
to 2024

while CSP shows minimal growth due to higher costs and technological challenges. Overall, the data reflects a major shift towards solar and wind energy, driven by declining costs and technological advancements, with hydropower maintaining a steady but reduced share in the energy mix.

Fig. 1.3 illustrates the global energy consumption trends for major countries from 2013 to 2024. China leads the world in energy consumption, showing a consistent upward trend from around 3,000 TWh in 2013 to over 4,000 TWh by 2024, driven by rapid industrialization and urbanization. The United States follows with relatively stable consumption, fluctuating around 2,100–2,200 TWh throughout the period, reflecting improvements in energy efficiency and a transition toward renewables.

India demonstrates a significant surge in energy consumption, increasing from approximately 750 TWh in 2014 to nearly 1,300 TWh by 2024, highlighting the impact of population growth, industrial expansion, and rural electrification. Russia maintains a steady trend of around 700–750 TWh, while Japan
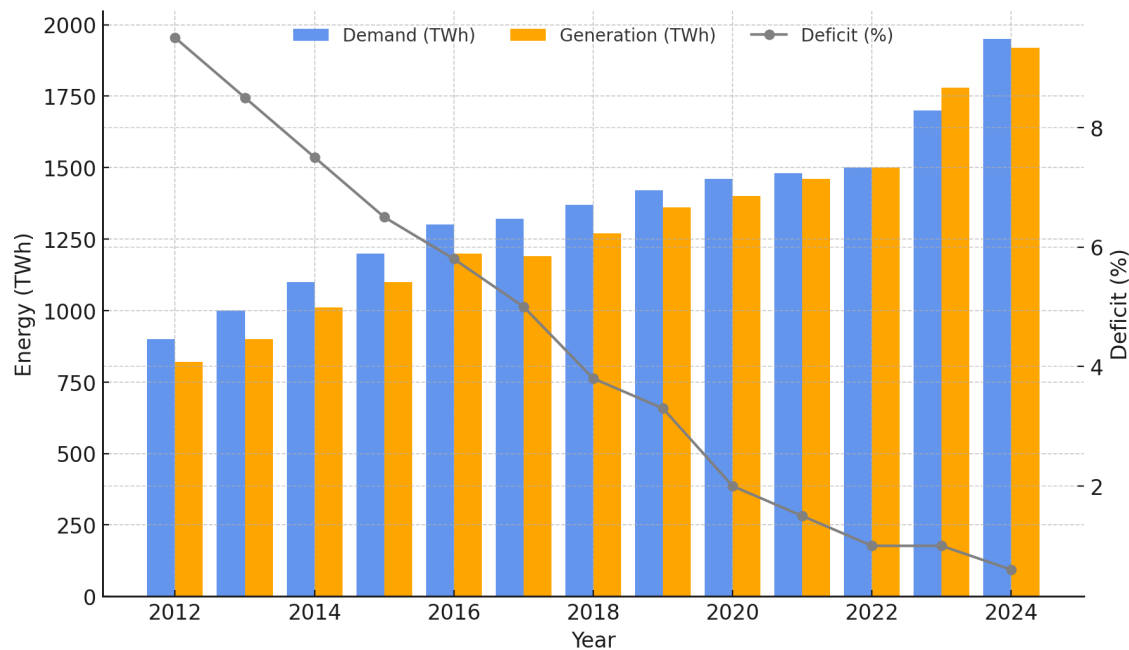
FIGURE 1.4: Energy generation and demand in Indian scenario

experiences a slight decline, dropping from 460 TWh in 2014 to around 544 TWh in 2024, owing to energy efficiency efforts and a post-Fukushima policy shift. Germany's energy consumption remains flat, around 310–320 TWh, as the country focuses on energy efficiency and renewable energy adoption under the Energiewende initiative. Brazil's consumption fluctuates slightly around 300 TWh, driven by hydropower reliance and economic variability. Saudi Arabia shows a gradual increase from about 228 TWh in 2014 to 403 TWh by 2024, aligned with industrial growth and population expansion. South Korea exhibits a modest rise, from 268 TWh in 2014 to 394 TWh in 2024, reflecting continued industrial and technological development.   France maintains a stable consumption trend around 250 TWh, primarily due to its reliance on nuclear power. Overall, the figure indicates that while developed nations like the United States, Japan, and Germany have stabilized or reduced their energy demands through efficiency and technological advancements, emerging economies, particularly India and Saudi Arabia, are driving global energy demand upward. This highlights the critical need for sustainable energy solutions, especially in rapidly growing economies.

1.1.2   Indian Scenario

Over the past decade, India's rapid GDP growth and economic development have led to a sharp rise in per capita energy consumption and overall energy demand. Between 2012 and 2024, both energy demand and generation increased significantly, as illustrated in Fig. 1.4. Energy demand grew from 900,000 GWh in 2012 to 1,948,956 GWh in 2024, reflecting an overall increase of approximately 116%, while energy generation rose from 800,000 GWh to 1,945,058 GWh, marking a growth of around 143% [5]. This consistent rise in demand can be attributed to rapid economic growth, industrialization, and increased per capita energy consumption. Meanwhile, the substantial improvement in generation capacity, driven by investments in thermal power plants, renewable energy sources, and grid modernization, played a key role in reducing the energy deficit. The energy deficit percentage decreased steadily from 9% in 2012 to 1.5% in 2018, eventually reaching near-zero levels by 2020, with minor fluctuations between 0.2% and 0.3% observed from 2022 to 2024 [8]. The near-elimination of the deficit demonstrates India's ability to match its growing energy needs through effective expansion and diversification of power generation. However, sustaining this balance in the future will require continued efforts in infrastructure development, renewable energy integration, and efficient grid management to meet rising energy demands while ensuring sustainability and reliability.

As of 2021, India reported an energy deficit of 0.5% and a peak demand deficit of 0.7%. To bridge the gap between demand and supply, the Government of India (GoI) has prioritized the expansion of renewable energy generation. Multiple policy initiatives have been introduced to promote the adoption and development of clean energy sources. Owing to its tropical geography, India holds vast renewable energy potential particularly in solar and wind positioning it favorably for a sustainable energy transition.

India has achieved a major milestone in this domain, with total installed renewable energy capacity exceeding 162.47 GW, including 97.86 GW from solar and 48.17 GW from wind power. This growth reflects the country's strong commitment to sustainable energy development and its strategic goal of reaching 500 GW of non-fossil fuel capacity by 2030. The rapid progress highlights India's proactive approach to clean energy deployment and its

Chapter 1. INTRODUCTION
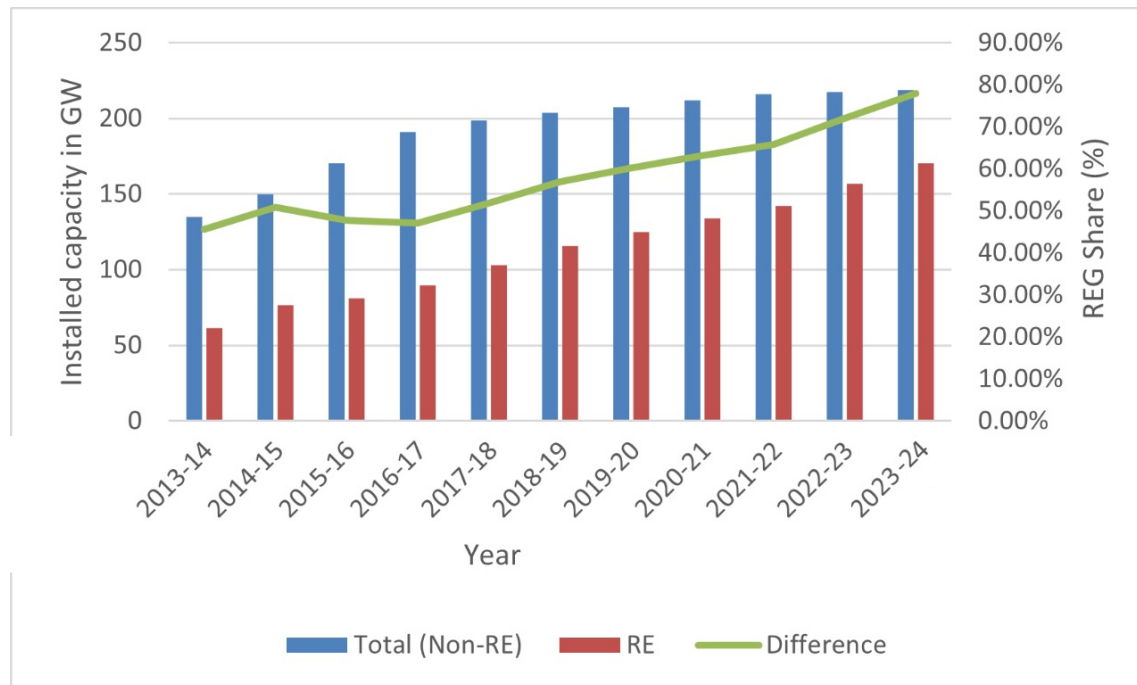
FIGURE 1.5: Year wise non-RES and RES installed capacity in India

contribution to global climate goals [9]. The current status of renewable energy generation (REG) in India's power sector is illustrated in Fig. 1.5.

The growth of installed electricity generation capacity in gigawatts (GW) in India from 2012-13 to 2022-23, with a breakdown between renewable energy (RE) and total installed capacity (including non-renewable sources). It also highlights the renewable energy generation (REG) share as a percentage of the total capacity, shown on a secondary axis. The data demonstrates a significant increase in RE capacity over the years, indicating a transition towards cleaner energy sources in the nation's energy mix.

The installed capacity of both RE and total power systems has consistently increased during the observed period. Renewable energy, represented by the red bars, shows a steeper growth trajectory compared to the non-renewable capacity. This rapid expansion is reflected in the upward trend of the REG share, represented by the green line, which approaches 70% in 2022-23. The steady increase in REG share underscores the growing importance of renewable energy in India's electricity generation sector.

The gap between total installed capacity and renewable capacity, indicative of

non-renewable energy, has remained stable for the initial years but shows signs of narrowing in recent years. This suggests that while non-renewable capacity is still being added, the rate of growth for renewables has significantly outpaced it. This trend reflects the combined effects of government policies, market shifts, and advancements in renewable energy technologies aimed at reducing dependence on fossil fuels.

1.2   Basic of Solar PV Cell

Photovoltaic is a combination of two words: "photo," meaning light, and "voltaic," meaning voltage. Photovoltaics (PV) refers to the generation of voltage when sunlight falls on a material. PV systems utilize semiconductor cells to convert solar energy into electrical energy [10]. The photovoltaic effect was initially discovered in 1839 by French scientist Edmond Becquerel during experiments with an electrolytic cell, where he observed an increase in current upon exposure to light [11]. Later, in 1877, Adams and Day developed the first selenium-based cell [12]. By 1914, selenium cells achieved a conversion efficiency of around 1%, but their widespread use was limited due to the presence of an energy barrier [13].

Over time, continuous improvements were made in solar cell technology. By 1958, silicon cells had reached an efficiency of 14%. Over the following two decades, research efforts focused on reducing the size and cost of solar cells. Due to their superior power-to-weight ratio, solar PV systems found extensive applications in space missions. However, in the early stages, the high cost of solar cells limited their broader adoption. The performance of solar cells has improved steadily as photovoltaic research advanced, leading to a significant reduction in costs. Currently, solar energy is harnessed and converted into electricity through photovoltaic panels composed of multiple solar cells made from semiconductor materials, primarily silicon. Silicon offers numerous benefits for energy production, including durability, reliability, noise-free operation, and fuel-free electricity generation.

1.2.1   Working Principle of PV Cell

The generation of electricity in solar cells is based on the photoelectric effect, where a photon i.e. a particle representing a quantum of light or electromagnetic radiation transfers its energy to an electron, elevating it to a higher energy state. The basic operating principle of a solar cell is to generate charge carriers (electron-hole pairs) when exposed to light, separate these carriers, and direct them through an external circuit, resulting in the generation of electrical energy.

When light strikes the solar cell, minority carriers are electrons in the p-type region and holes in the n-type region are produced within the semiconductor material. This leads to an increase in the concentration of minority carriers, causing their drift across the depletion region. Once the circuit is closed and connected to an external load, the movement of electrons results in direct current (DC) [14, 15]. Since most domestic electrical appliances operate on alternating current (AC), an inverter is required to convert the DC output into usable AC.

1.2.2   Types of Photovoltaic Cell

Photovoltaic (PV) technologies are generally classified into four generations: crystalline silicon (c-Si) technology, thin-film technology, organic and polymer solar cells, and dye-sensitized solar cells.   Emerging and experimental technologies, such as concentrated solar power (CSP), nanotubes, and quantum dots, are still in the early stages of development [16].   While various PV technologies are available in the market, c-Si-based PV modules are the most commonly used for large-scale PV systems due to their cost-effectiveness and high efficiency. Silicon-based PV cells can be categorized into three types.

Mono-Si Cell

Mono-Si photovoltaic (PV) modules have been in use for a long time due to their reliability and high efficiency. Each cell is made from a single, high-quality silicon crystal, which results in better performance but at a higher cost compared to polycrystalline and thin-film cells. The conversion efficiency of Mono-Si modules is typically reported to range from 15% to 20% in commercial

applications [17]. These modules also have a longer lifespan of 25–30 years, although they come at a significantly higher price [18].

Poly-Si Cell

Poly-Si, composed of multiple small silicon crystals, serves as the primary material for PV modules. Poly-Si cells are widely used in module manufacturing due to their lower cost, although they are less efficient than Mono-Si cells. They require a larger area for installation in exchange for lower power output. Poly-Si modules typically have a lifespan of 20 to 25 years. The conversion efficiency of poly-Si PV modules is reported to range from 13% to 16% in commercial applications [19].

GaAs Cell

GaAs solar cells are made from a composite semiconductor material consisting of gallium (Ga) and arsenic (As), structured similarly to silicon. Compared to silicon-based solar cells, GaAs cells offer higher efficiency and are lighter. However, they are considerably more expensive than both Mono-Si and Poly-Si solar cells. GaAs cells feature a multijunction structure due to the incorporation of aluminum, phosphorus, antimony, and indium alloys, which enhances their efficiency and reduces the temperature coefficient. This structure provides superior heat resistance, making GaAs cells ideal for Concentrated Solar Power (CSP) modules. The conversion efficiency of GaAs solar cells is reported to be around 29% [20, 21].

Perovskite Solar Cell

A perovskite solar cell is a type of solar cell that incorporates a perovskite-structured compound, typically a hybrid organic-inorganic material based on lead or tin halides, as the light-absorbing active layer. Perovskite materials, such as methylammonium lead halides, are inexpensive to produce and relatively easy to manufacture. These materials possess several intrinsic properties, including a broad absorption spectrum, rapid charge separation, long

electron and hole transport distances, and extended carrier separation lifetimes, making them highly promising candidates for solid-state solar cells [22].

1.3   Types of PV Systems

In general, PV systems can be classified into two main types based on their configuration and application:

1.3.1   Stand-Alone PV System

Stand alone PV systems, which function independently of the main power grid, provide a practical solution for improving energy access in rural areas where grid reliability remains a concern. To address the electricity and lighting requirements of local communities, institutions, and individuals in these regions, the Ministry of New and Renewable Energy (MNRE) offers Central Financial Assistance (CFA) under the Stand alone and Decentralized Solar PV Applications Program. This support facilitates the deployment of solar street lights, solar study lamps, and solar power packs. State Nodal Agencies (SNAs) are primarily responsible for executing this program at the local level.

Additionally, the PM-KUSUM Scheme is instrumental in promoting off-grid solar solutions by facilitating the installation of standalone solar pumps, solarizing existing agricultural pumps, and developing grid-connected solar power plants with capacities up to 2 MW. As of June 2024, India has achieved an installed capacity of 3.44 GW of off-grid solar power, contributing to the country's total solar capacity of 85.47 GW [23].

1.3.2   Grid-Connected PV System

Grid-connected solar photovoltaic (PV) systems rely on power conditioning units or inverters to transform the direct current (DC) electricity generated by solar panels into alternating current (AC) electricity, which is subsequently supplied to the power grid. This category encompasses various initiatives, including the development of solar parks and ultra-mega solar power projects, the rooftop solar program, the Central Public Sector Undertaking (CPSU)

Scheme Phase-II (government producer scheme), and the Prime Minister Kisan Urja Suraksha Evam Utthaan Mahaabhiyan (PM-KUSUM). As of June 2024, India had achieved a cumulative installed capacity of 82.03 GW of grid-connected solar power [23].

1.4   Configuration of Solar PV Plant

The configuration of a solar photovoltaic (PV) plant refers to the systematic integration of its primary components, including PV modules, power conditioning units (such as inverters), mounting structures, and balance-of-system (BOS) elements. The design and layout are determined based on site-specific factors such as available area, irradiance profile, and load demand. Configurations vary across rooftop, ground-mounted, and floating systems, each engineered to optimize energy yield, reliability, and cost-effectiveness under given environmental and operational conditions.

1.4.1   Terrestrial Solar PV Plant

Terrestrial solar photovoltaic (PV) plants are land-based systems that convert solar radiation into electricity using PV technology. They are broadly classified into rooftop and ground-mounted systems. Rooftop PV systems, installed on buildings, are typically small-scale and ideal for urban areas with limited space, offering benefits like reduced electricity costs and decentralized generation. These systems may be grid-connected, off-grid, or hybrid, though they can face challenges such as shading and structural constraints. Ground-mounted PV systems are installed on open land and are suited for utility-scale power generation. They offer optimized energy output and easier maintenance but require significant land and higher infrastructure costs. Together, these systems contribute significantly to reducing fossil fuel dependency and advancing renewable energy adoption.

1.4.2 Floating Solar PV plant

To address these limitations, floating solar photovoltaic (FSPV) systems have been introduced as a novel and increasingly viable solution. In FSPV installations, PV modules are mounted on buoyant structures that float on the surface of water bodies such as reservoirs, lakes, ponds, and canals. These systems offer several distinct advantages, including a reduced land footprint, mitigation of water evaporation, and improved module efficiency due to the cooling effect provided by the water surface. Despite certain challenges such as higher capital costs, increased structural complexity, and potential environmental concerns. Floating solar power plants present a promising complement to conventional ground-mounted systems, particularly in regions characterized by limited land availability and abundant inland water resources.

1.5 Motivation and Research objectives

Floating solar photovoltaic (FSPV) systems have gained considerable attention as a viable alternative to land-based PV installations, especially in regions with limited land availability. By deploying PV modules over water bodies, FSPV systems not only conserve land but also benefit from enhanced module efficiency due to the natural cooling effect of water. The integration of bifacial PV modules, which capture irradiance from both sides, further improves energy yield particularly over reflective water surfaces.

To enhance performance further, solar tracking technologies are being explored to maintain optimal module orientation throughout the day, thereby increasing solar energy capture. Additionally, optimizing the inverter loading ratio (ILR) is the ratio of PV array DC capacity to inverter AC capacity—plays a critical role in maximizing energy output while minimizing clipping losses and cost.

The decreasing cost of PV technologies, combined with advancements in bifacial modules, floating structures, tracking mechanisms, and ILR optimization, makes FSPV systems increasingly attractive. These developments form the core motivation for this research, which aims to evaluate and enhance the techno-economic performance of FSPV plants using bifacial modules, solar

tracking, and optimized ILR configurations. The present thesis has addressed the challenges by integrating them as specific research objectives:

1. Development of control algorithms for tracking of Maximum Power Point.

2. Design and development of inverter control algorithms for grid connected PV system.

3. Techno-economic analysis of a solar photovoltaic plant.

4. Performance enhancement of solar PV module considering various environmental parameters.

1.6   Problem Identification

To achieve the defined objectives, the following key problems have been identified:

1. Traditional MPPT techniques like P&O and FLC perform poorly under rapidly changing irradiance, leading to slow tracking and power losses in standalone PV systems. Similarly, conventional inverter control methods in grid-connected PV systems suffer from poor power quality and weak synchronization. Hence, there is a need for advanced MPPT algorithms and robust inverter control strategies for improved efficiency and stability.

2. The rapid growth of solar PV has increased land pressure, especially in densely populated and agricultural areas, making floating solar PV (FSPV) systems an attractive alternative to conserve land and reduce environmental impacts. While bifacial modules offer higher energy yield by capturing sunlight on both sides, their technical and economic performance on floating platforms compared to monofacial modules remains underexplored, with limited data on efficiency, energy output, and cost benefits, creating uncertainty for stakeholders.

3. Although solar tracking systems such as seasonal adjustable tilt (SAT), horizontal single-axis tracking (HSAT), and dual-axis tracking (DAT) have shown promise in ground-mounted applications, their effectiveness in

floating PV systems is not well documented. There is a need to evaluate their technical feasibility, energy gains, and economic impact in the context of FSPV systems.

4. The inverter loading ratio (ILR), or DC-to-AC ratio, significantly influences PV system performance. An undersized inverter may cause energy losses through clipping, while an oversized inverter increases system cost without proportional energy gains. For floating solar systems, determining the optimal ILR that balances energy output and economic performance is an open problem, especially when accounting for seasonal variations and site-specific conditions.

1.7   Structure of the Thesis

This chapter serves as a preliminary exposition of the thesis and conveys a detailed examination of the Indian power sector, including both ground-mounted and floating solar power technologies, in addition to the essential motivations for the research and the specified research goals.

The literature review concerning monofacial and bifacial photovoltaic solar modules, the design and components of floating solar power plants, as well as the technical and economic parameters associated with floating solar power facilities, along with the mitigation of carbon dioxide emissions, has been elaborated upon in Chapter 2. Furthermore, Chapter 2 delineates the recognized research deficiencies and proposes strategies to address the identified research deficiencies.

Chapter 3 analyzes and enhances the efficiency of photovoltaic systems via sophisticated control methodologies and empirical evaluations. Furthermore, this chapter presents the development and implementation of an inverter control algorithm for a grid-connected photovoltaic (PV) system.

Chapter 4 evaluates the feasibility of bifacial floating solar power plants versus monofacial ones.   It performs an economic analysis to compare cost-effectiveness and financial viability. Furthermore, it assesses environmental benefits, focusing on carbon emission reductions, to ascertain the sustainability of bifacial solar power plants.

Chapter 5 delves into the various solar photovoltaic tracking technologies employed in floating solar photovoltaic plants, in addition to examining the losses associated with such floating solar power installations. Furthermore, it encompasses a comprehensive analysis of the probability distribution pertinent to this floating solar power plant.

Chapter 6 seeks to enhance energy output in floating solar PV systems through the evaluation of inverter loading ratios (ILRs) on energy production, effectiveness, and economic sustainability. Additionally, it investigates seasonal performance variations and their design ramifications. The assessment of the levelized cost of energy (LCOE) and financial viability offers crucial insights for engineers and policymakers to improve PV system efficacy and economic benefits.

A detailed conclusion along with the scope of future work and references is presented in Chapter 7.

1.8 Concluding Remarks

This chapter presents a detailed overview of the research carried out in this dissertation. It highlights the motivation and objectives that shaped the study, clearly specifies the research issues addressed, and provides a chapter-wise summary of the work accomplished.

19

Chapter 2

LITERATURE SURVEY

2.1   Introduction

Chapter 1 outlines the objectives, motivation, and identification of the research problems. To develop a comprehensive understanding of these problems, an extensive literature review has been conducted in the relevant areas associated with this research work. This chapter presents the brief review on the maximum power point tracking (MPPT) control algorithms, inverter control algorithms, monofacial and bifacial floating solar PV plants, tracking technologies in floating solar PV plants, and inverter loading ratio (ILR) and its impact on floating solar PV systems. In the following sections, each topic is briefly discussed and reviewed without aiming for exhaustiveness. The references cited in this chapter are representative rather than comprehensive.

2.2   Maximum Power Point Tracking (MPPT) Control Algorithms

Solar PV is a clean and sustainable energy source, but its power output fluctuates with weather and sunlight variations. To reduce these losses and improve efficiency, Maximum Power Point Tracking (MPPT) techniques are essential.

2.2.1   Conventational and Intelligent MPPT Algorithms

The control and analysis of solar photovoltaic (PV) systems using Perturb and Observe (P&O) and fuzzy logic controller (FLC) based maximum power point

Chapter 2. LITERATURE SURVEY

tracking (MPPT) algorithms have been extensively studied to enhance the efficiency and reliability of solar energy systems. The P&O algorithm is widely favored for its simplicity and ease of implementation, but it suffers from limitations such as steady-state oscillations and slow convergence under rapidly changing irradiance conditions [24] . To address these issues, hybrid approaches combining P&O with fuzzy logic have been developed, offering improved performance by leveraging the strengths of both methods. Fuzzy logic controllers provide enhanced stability and robustness, particularly under variable environmental conditions, by adapting to changes in irradiance and load, thus reducing oscillations and improving tracking accuracy [25], [26] and [27]. Studies have shown that hybrid P&O-FLC algorithms can significantly reduce voltage and current ripples compared to traditional methods, achieving faster stabilization and better performance under sudden weather changes [28] [29]. Moreover, these hybrid systems have demonstrated superior tracking speed and accuracy, effectively minimizing power losses and enhancing the overall efficiency of PV systems [30] [31]. The integration of fuzzy logic into P&O algorithms allows for adaptive step size adjustments, which further optimizes the tracking process by reducing steady-state errors and improving dynamic response. Simulation and experimental results consistently indicate that fuzzy logic-based MPPT controllers outperform traditional P&O methods, making them a promising solution for real-time applications in PV systems [26] [29]. Overall, the combination of P&O and fuzzy logic in MPPT algorithms represents a significant advancement in the control of solar PV systems, offering a balanced approach that enhances both performance and computational efficiency [32] [27].

2.2.2   Bio inspired MPPT Algorithms

The Flying Squirrel Search Optimization (FSSO) algorithm, inspired by the gliding and foraging behavior of flying squirrels, has emerged as a promising metaheuristic approach for Maximum Power Point Tracking (MPPT) in photovoltaic (PV) systems, offering rapid convergence and high tracking efficiency under varying irradiance and temperature conditions [33–35]. By categorizing candidate solutions into hickory, acorn, and ordinary trees, and updating their positions using stochastic and deterministic rules, FSSO

effectively avoids local optima and achieves superior steady-state accuracy compared to traditional methods such as Perturb and Observe (P&O) and Incremental Conductance (INC) [36]. Several studies have demonstrated that integrating FSSO with hybrid approaches, including Differential Evolution (DE) [37] and Particle Swarm Optimization-trained neural networks [38], enhances its adaptability and response time, particularly under partial shading conditions. Experimental and simulation-based results show that coupling FSSO with power electronic converters such as SEPIC and Boost converters minimizes voltage/current ripple and yields MPPT efficiencies exceeding 99.9% [39]. Furthermore, FSSO has been successfully applied in standalone and grid-connected PV systems, hybrid PV–thermoelectric generator configurations, and real-time embedded control platforms, consistently outperforming other bio-inspired algorithms such as Genetic Algorithm (GA), Ant Colony Optimization (ACO), and Whale Optimization Algorithm (WOA) in terms of convergence speed, stability, and robustness [33, 40, 41]. These advancements establish FSSO as a highly effective MPPT solution with strong potential for deployment in diverse environmental and operational conditions.

2.3   Inverter Control Algorithms

Reliable control of Voltage Source Converters (VSCs) is essential for stable and compliant grid integration of solar photovoltaic (SPV) systems in microgrids. Among the various control strategies, the *Synchronous Reference Frame Theory* (SRFT) is adopted as the primary method in this study due to its proven capability in accurately extracting the fundamental component [42], enabling independent regulation of active and reactive power [43], and ensuring robust performance under a wide range of grid operating conditions [44]. In order to provide a fair assessment of the proposed approach, the Instantaneous Reactive Power Theory (IRPT) is also implemented as a benchmark control strategy. While IRPT offers advantages in terms of straightforward real-time power decomposition [45], SRFT demonstrates superior stability [46] and dynamic performance [47], making it the preferred choice for this work.

The IRPT, also known as the *pq* theory, was introduced by Akagi *et al.* and has been extensively applied for harmonic mitigation [48], reactive power compensation [49], and fault ride-through control in PV inverters [50]. It operates in the time domain by directly decomposing three-phase instantaneous power into active and reactive components [51]. Although IRPT is effective for fast compensation [52], its performance can deteriorate in weak grid conditions [53], during frequency deviations [54], or under unbalanced voltages due to its sensitivity to phase-locked loop (PLL) inaccuracies [55]. For this reason, in the present work, IRPT is employed solely as a comparative benchmark to evaluate the improvements achieved with SRFT.

In contrast, SRFT transforms three-phase voltages and currents into a synchronously rotating $dq0$ reference frame aligned with the grid voltage vector [42]. This decoupling facilitates precise control, where the direct-axis (d) component regulates active power [47] and the quadrature-axis (q) component regulates reactive power [46]. SRFT inherently suppresses harmonics [43] and enhances system stability, particularly during fluctuating irradiance [44], unbalanced loading [46], and voltage sag conditions [43]. Furthermore, recent advancements such as adaptive PLL integration [44], model predictive control [47], and sliding mode current regulation [46] have improved SRFT's transient response and compliance with IEEE 519 harmonic standards. In this study, the SRFT-based control is implemented with an adaptive PLL and optimized PI regulators to achieve fast dynamic response, low total harmonic distortion, enhanced reactive power support, and stable operation during low-voltage ride-through events. Comparative results against IRPT clearly demonstrate SRFT's superior capability in terms of power quality, stability, and adherence to modern grid codes.

2.4 Floating Solar Power Plant

Floating solar photovoltaic systems have evolved to offer higher energy yields and efficiency, with improvements in design, instrumentation, and technology. Key advancements include tracking systems, bi-facial panels, and AI integration, addressing challenges like safety and standardization for sustainable energy

production [56]. The development of floating photovoltaic (FPV) systems has gained attention due to their advantages.   The paper summarizes typical installed FPV systems, innovative designs, and hybrid applications, highlighting critical structural considerations and future challenges like survivability and environmental impact [57]. Floating PV systems, or floato-voltaics, have evolved through technological advancements like dual-glass PV modules and specialized anchoring systems, enhancing performance and durability. They address land scarcity and integrate effectively with hydropower infrastructure, making them a cost-effective energy solution [58]. The paper discusses the rapid growth of floating photovoltaic (FPV) systems as a clean energy source, driven by land scarcity and carbon reduction needs. It highlights advancements in PV module structures, site suitability factors, and integration with other technologies for enhanced efficiency[59]. The paper reviews the evolution of floating photovoltaic (FPV) systems, highlighting advancements in technology, efficiency improvements due to water cooling, and the integration of FPV into energy strategies, particularly emphasizing their potential in energy-deficient regions like Africa [60]. The paper discusses the emergence of floating photovoltaic (FPV) systems as a renewable energy technology, highlighting their advantages over land-based solar arrays, such as increased land-use efficiency and reduced water evaporation, while addressing challenges and opportunities for integration with energy storage systems [61].

Floating Photovoltaic (FPV) systems save land by utilizing water surfaces, alleviating land scarcity. Additionally, they benefit from water's cooling effects, leading to improved power generation efficiency, with experimental results showing up to a 10% increase in power output[62]. Floating photovoltaics (FPV) save land area and can provide improved cooling effects compared to ground-mounted PV systems. However, the cooling advantage varies by FPV technology, and it may not always surpass that of open rack ground-mounted systems [63]. Ground-mounted photovoltaic systems offer advantages such as land savings through optimized design and placement, and a cooling effect in shaded areas, reducing soil temperature by up to 7 °C, which can enhance local microclimate conditions in arid regions [64]. Floating Photovoltaic (FPV) systems save land by utilizing water surfaces and benefit from enhanced cooling, leading to higher operating efficiencies compared to ground-mounted PV (GPV)

systems.   Additionally, FPV reduces water evaporation, providing further economic advantages [65]. Floating photovoltaic systems offer advantages such as reduced land investment, decreased water evaporation, and suppression of algae growth. Additionally, they utilize water bodies as heat sinks, lowering working temperatures and enhancing efficiency, resulting in a 17.84% increase in electrical performance[66].

2.4.1   Monofacial Floating Solar PV Plant

Floating solar photovoltaic (FPV) systems using monofacial modules have shown improved energy yield compared to ground-mounted systems due to passive cooling from water surfaces, which lowers module temperature by 5–10°C [67] [68]. These thermal advantages enhance performance, particularly in hot climates [69] [70]. Optimal tilt angles (10°–20°) improve irradiance capture while maintaining structural stability [71]. Studies using PVSyst and SAM [72] [73] report capacity factors of 15–20%, with reduced soiling losses over water [74], though biofouling and shading remain concerns [75]. Economically, FPV systems reduce land costs and water evaporation [76] [77] [78] with competitive LCOE [79].   However, research gaps exist in long-term degradation, optimal inverter loading ratios, and real-time performance under dynamic water conditions [80] [81] [82].

2.4.2   Bifacial Floating Solar PV Plant

Bifacial technology absorbs radiation on both sides, yielding up to 30% more energy than monofacial modules under optimal conditions. Bifacial cells also provide higher current density and power, especially in low light, enhancing overall efficiency compared to monofacial cells[83]. The paper focuses on the comparative performance of monofacial and bifacial photovoltaic technologies, highlighting that bifacial modules exhibit higher sensitivity to configuration parameters and can achieve significantly increased back-side radiation, emphasizing the importance of optical control for enhanced efficiency[84]. Bifacial technology captures sunlight on both sides of the panel, enhancing energy production compared to monofacial systems, which only utilize one side.

This results in higher performance ratios and reduced Levelized Cost of Energy (LCOE) for bifacial installations[85]. The paper focuses on bifacial photovoltaic technology, highlighting its 30.54%–34.93% higher performance compared to monofacial panels in India. Bifacial technology captures sunlight on both sides, enhancing efficiency, while monofacial panels only utilize sunlight on one side [86]. The paper focuses on bifacial solar cells, which can outperform monofacial devices under adverse conditions. Bifacial cells utilize a transparent back-buffer layer, enhancing carrier lifetimes and achieving higher efficiencies, with reported values of 7.6% and 12.5% for back and front illumination, respectively [87].

The albedo effect significantly enhances bifacial module performance in floating solar power plants, resulting in a 12.4% higher annual energy production compared to monofacial modules. This increase is attributed to the reflection of sunlight from the water surface [88]. The study indicates that bifacial gain decreases nonlinearly at high albedo due to partial shading from rear-side support structures. Increasing the distance between the beam and the module can significantly reduce this loss, enhancing overall energy generation in floating solar plants [89]. The paper indicates that albedo absorption in the proposed bifacial perovskite/silicon tandem solar cell enhances short-circuit current, resulting in a bifacial gain of 10%–30% for albedo levels between 15% and 45%, significantly improving efficiency in solar applications [90].

2.5   Performance Analysis of Solar PV Plant

Performance analysis of a solar PV plant helps evaluate its energy output, efficiency, and reliability under real operating conditions. Such analysis is essential for identifying losses, improving design, and ensuring sustainable power generation.

2.5.1   Technical Analysis

The performance parameters of the floating solar power plant include array yield, performance ratio (88.95%), capacity factor (15.04%), efficiency, and energy density, with significant influences from ambient temperature and weak correlation with irradiance [91]. The floating solar photovoltaic (FSPV) system

achieved a performance ratio (PR) of 86.7% and demonstrated 9.84% higher efficiency compared to land-based PV modules. It is projected to generate 26,465.7 MWh of energy annually while conserving water and reducing CO_2 emissions [92]. The floating photovoltaic (FPV) system achieved an average electrical efficiency of 23.40% and a performance ratio of 0.87. In partially shaded conditions, the performance was 18.90% efficiency and a ratio of 0.79, demonstrating effective energy production [93] [94]. Performance parameters of floating solar power plants include reduced thermal drift losses, energy gains from cooling and tracking mechanisms, and the ability to utilize unexploited water areas. Efficiency improvements range from 8-20% depending on panel design and reflector use [95].

2.5.2   Economical Analysis

The economic analysis of monofacial versus bifacial floating solar power plants reveals distinct advantages and challenges for each technology. The paper conducts a comprehensive economic feasibility analysis of floating photovoltaic systems, comparing monofacial and bifacial technologies. It emphasizes the need for cost reduction and highlights the potential for enhanced efficiency and reliability in diverse marine environments, particularly for energy-deficient regions [60]. The paper focuses on optimizing bifacial solar power plants, revealing that established design guidelines often do not minimize levelised cost of electricity (LCOE). Bifacial configurations can yield up to 23% lower LCOE compared to conventional setups, enhancing economic viability [96]. The paper highlights that economic factors influencing bifacial PV systems include surface area, light reflection fraction, and geographical location. Bifacial floating PV systems offer advantages over monofacial systems, particularly in dual land use scenarios, enhancing overall efficiency and output [97].

2.6   Tracking Technologies in Floating PV Plant

Floating solar PV plants are an emerging solution to meet rising energy demands while utilizing water surfaces efficiently. Integrating tracking technologies further

boosts energy generation by aligning panels with the sun's movement throughout the day.

2.6.1   Fix Tilt FPV Plant

Tracking technology in floating solar power plants boosts energy efficiency and output by aligning PV modules with the Sun's movement. A fixed tilt PV module in a floating solar power plant typically has a 35-degree slope, maximizing yearly energy production. This configuration benefits from cooling effects and can reduce thermal drift losses, enhancing overall efficiency compared to land-based systems [95]. For floating solar PV, a tilt angle less than 45° is optimal for performance, while angles greater than 55° result in higher temperatures compared to conventional systems. A height of 1500 mm with 0° tilt provides maximum cooling [98]. The paper focuses on a single-axis solar tracker design using a sun sensor system, which can be adapted for floating solar power plants to enhance efficiency by tracking sunlight, potentially increasing energy generation compared to fixed-structure systems [99].

2.6.2   Single Axis based FPV Plant

A single-axis tracking mechanism in floating photovoltaic systems increases annual energy generation by 11% compared to fixed systems, enhancing energy density and efficiency, ultimately contributing to higher power output and better utilization of solar resources in reservoirs[100]. The paper discusses a single axis solar tracker model optimized for energy collection, which can be applicable in floating solar power plants. It emphasizes reduced mechanical wear and energy consumption while achieving high energy collection efficiency with fewer panel displacements[101]. The paper focuses on a uniaxial solar-tracking strategy for sloping terrains, not specifically addressing horizontal axis solar trackers in floating solar power plants. It emphasizes optimizing tilt angles to enhance solar irradiance and reduce shading effects in fixed installations[102]. The paper discusses single-axis tracking mechanisms for floating photovoltaic systems, which enhance solar output by optimizing panel orientation. This technology

Chapter 2. LITERATURE SURVEY

can increase annual energy generation by 11%, improving efficiency compared to fixed mounting systems in floating solar power plants [103].

2.6.3   Dual Axis based FPV Plant

The integration of dual-axis solar trackers in floating solar power plants can significantly enhance energy efficiency by optimizing the capture of solar irradiance throughout the day. Dual-axis solar tracking systems, which adjust both the azimuth and altitude angles of solar panels, have been shown to increase energy production by 24.6% to 33.23% compared to fixed systems [104], [105]. These systems utilize various control strategies, such as light-dependent resistors (LDRs) and time-based GPS, to maintain optimal alignment with the sun, even under diffused sunlight conditions [104] and [106]. The use of closed-loop feedback systems and advanced control mechanisms, such as the Wheatstone bridge circuit and feedback control theory, further enhances the precision and reliability of these trackers [107], [106] and [108]. Additionally, the implementation of novel designs, such as parallel mechanisms and improved self-test architectures, reduces mechanical complexity and increases the reliability of the systems by addressing potential faults[109] and [110]. In floating solar power plants, where space and orientation can be more flexible, dual-axis trackers can be particularly beneficial, as they allow for maximum solar energy capture without the constraints of land-based installations. Moreover, the concurrent design methodologies and optimization strategies discussed in the literature ensure that these systems maintain a balance between energy consumption and tracking accuracy, further enhancing their applicability in floating solar installations [111]. Overall, the deployment of dual-axis solar trackers in floating solar power plants represents a promising approach to maximizing energy yield and improving the overall efficiency of photovoltaic systems.

Floating solar power plants, while offering innovative solutions to land scarcity and providing environmental benefits, face several challenges that lead to energy losses. One significant source of loss is the motion induced by ocean waves, which causes continuous changes in the tilt angle of solar panels, leading to sub-optimal sunlight intake and reduced energy efficiency. Experimental

studies have shown that wave-induced rotational movements can result in a power loss of up to 12.7% under certain conditions, highlighting the importance of implementing wave attenuation technologies to minimize these effects [112] [113]. Additionally, structural failures due to adverse weather conditions, such as high winds and heavy rains, can lead to mechanical deformations and partial sinking of the platforms, further impacting energy production. For instance, a case study in Brazil reported significant structural damage during a storm, necessitating repairs and the introduction of more robust anchoring systems to withstand such conditions [114]. Despite these challenges, floating solar power plants offer advantages over land-based systems, such as reduced water evaporation and algae growth, which can improve water quality and system efficiency [115] and [116]. Moreover, floating systems benefit from passive cooling effects, which enhance energy generation efficiency by maintaining lower temperatures beneath the panels[115] and [116]. The feasibility of floating solar plants has been demonstrated in various locations, such as India and Bangladesh, where they contribute to significant energy production and environmental benefits, including water conservation and CO_2 emission reductions [117] and [118]. However, to maximize their potential, it is crucial to address the mechanical and environmental challenges that lead to energy losses, ensuring the reliability and sustainability of floating solar power plants [119] and [120].

2.7   Inverter Loading Ratio in FSPV Plant

Determining the optimal inverter loading ratio (ILR) for floating solar power plants involves balancing several factors, including energy efficiency, cost, and environmental conditions. The ILR, which is the ratio of the photovoltaic (PV) array capacity to the inverter capacity, significantly impacts the energy output and financial performance of solar power systems. High ILRs can lead to increased inverter clipping losses, where excess energy is not converted due to inverter capacity limits, thus potentially leading to an overestimation of energy output in performance models [121]. Studies suggest that the optimal ILR varies depending on local climate conditions, with a typical ratio being around 1.2,

although this can be adjusted based on specific irradiance and temperature profiles to maximize power absorption and minimize costs [122]. For instance, in regions with lower solar potential, higher ILRs, such as 1.51 to 1.66, may be more beneficial, although they can result in clipping losses up to 14% of total annual energy production [123]. Financial analyses indicate that an ILR of 1.2 to 1.3 can optimize the net present value (NPV) and internal rate of return (IRR) for utility-scale PV plants, especially when incentives for renewable energy are considered. Moreover, the integration of smart inverters, which can manage voltage and reactive power, allows for a more flexible approach to ILR, potentially increasing energy injection and profitability in residential systems [124]. The optimization of ILR should also consider the time-of-use electricity pricing and climate conditions to maximize lifetime profits, as demonstrated in a study for a 10 kW system in London, Ontario, where an ILR of 2 was found to be optimal [125]. Overall, the choice of ILR should be tailored to the specific conditions of the installation site, taking into account both technical and economic factors to achieve the best performance and financial outcomes for floating solar power plants.

2.8   Identified Research Gaps

Despite substantial progress in research on solar PV plants and floating solar photovoltaic (PV) plants in perticular critical challenges remain unresolved. Drawing from the comprehensive literature review conducted, the following research gaps have been identified:

1. Current MPPT control algorithms exhibit potential for improvement in accurately and rapidly tracking the global maximum power point under variable solar irradiances.

2. While floating solar PV systems have been widely studied, research on bifacial configurations remains limited. Given their potential for enhanced energy yield, further investigation into bifacial floating PV systems is warranted.

3. Despite its proven benefits in ground mounted PV plant, tracking technology has seen limited application and analysis in floating solar power plants. Comprehensive studies evaluating its technical a feasibility in floating configurations are lacking.

4. Existing studies on inverter loading ratio (ILR) primarily target ground-mounted PV systems, neglecting floating solar PV's distinct thermal and irradiance conditions. Limited research addresses ILR's impact on FPV system performance, clipping losses, and LCOE using validated simulation models. This research fills this gap by systematically analyzing ILR effects on floating PV performance and economics.

2.9   Concluding Remarks

In this chapter, a comprehensive literature review on floating solar photovoltaic (FPV) systems and related technological domains has been presented. Key contributions by researchers in both the technical and economic aspects of FPV systems have been discussed. An overview of various tracking technologies applicable to floating PV installations has been provided. The impact of inverter loading ratio on system performance parameters has also been reviewed. Additionally, existing research on MPPT algorithms and inverter control strategies for grid-connected PV systems has been analyzed. Based on the critical review of existing literature, prominent research gaps in the domain of grid-tied floating solar PV systems have been identified.

33

Chapter 3

DESIGN AND ANALYSIS OF SOLAR PV SYSTEMS

3.1   Introduction

Solar photovoltaic (PV) systems have emerged as a vital component of modern energy infrastructure, offering clean and renewable energy solutions for both remote and grid-connected applications. As the demand for reliable and efficient solar energy systems continues to grow, it becomes essential to explore not only their design but also their dynamic performance under real-world conditions.

This chapter provides a comprehensive framework for the design, modelling, and performance evaluation of both stand-alone and grid-connected PV systems. It begins with the theoretical design of PV modules, power converters, and maximum power point tracking (MPPT) techniques, including conventional Perturb and Observe (P&O), fuzzy logic, and bio-inspired optimization algorithms. The design and configuration of grid-connected PV systems are also discussed in detail, with particular emphasis on the boost converter, inverter, and DC-link dynamics.

To ensure efficient integration with the utility grid, advanced inverter control strategies such as Synchronous Reference Frame Theory (SRFT) and Instantaneous Reactive Power Theory (IRPT) are implemented. Finally, the chapter concludes with a comparative analysis of the control strategies under varying irradiance levels, highlighting their impact on system stability and power quality.

3.2   Design and Modelling of Stand-Alone Solar PV System

Stand-alone solar PV systems operate independently from the grid and are widely used in remote areas. The design process involves selecting an appropriate PV array, designing power conversion stages, and implementing MPPT techniques to enhance energy extraction.

3.2.1   Design of PV Cell

The electrical behavior of a photovoltaic (PV) cell is commonly represented by an equivalent circuit model, as illustrated in Fig. 3.1. This model comprises a current source that simulates the photocurrent generated by incident sunlight, connected in parallel with a diode that captures the nonlinear characteristics of the PV cell. To account for internal losses, a series resistance (R_{se}) is included to represent contact and bulk resistances, while a shunt resistance (R_{sh}) models leakage currents across the p-n junction.
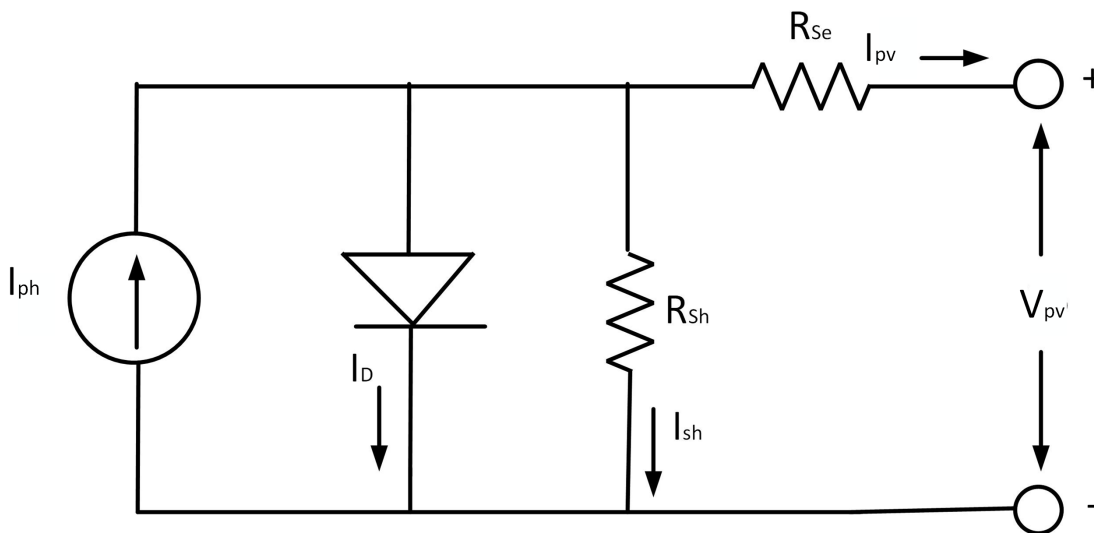
FIGURE 3.1: Equivalent circuit of PV cell

The mathematical expression for the output current (I_{pv}) of a PV cell, derived from the equivalent circuit, is given by equation (3.1):

$$I_{pv} = I_{ph} - I_D - I_{sh} \tag{3.1}$$

where I_{ph} is the photocurrent, which is proportional to the incident solar irradiance. I_D represents the diode current, given by the Shockley diode equation (3.2):

$$I_D = I_0 \left(e^{\frac{q(V_{pv} + I_{pv}R_{se})}{nkT}} - 1 \right) \tag{3.2}$$

where I_{sh} is the shunt leakage current through R_{sh}, expressed in equation (3.3).

$$I_{sh} = \frac{V_{pv} + I_{pv}R_{se}}{R_{sh}} \tag{3.3}$$

where T: Temperature in Kelvin; q: Charge of an electron ($1.61 \times 10^{-19}C$); k: Boltzmann's constant ($1.39 \times 10^{-23}J/K$); η: Ideality factor of the diode; I_0: Reverse saturation current of the diode; V_{pv}: Output voltage of the PV cell; I_{pv}: Output current of the PV cell

Since the shunt resistance (R_{sh}) is typically very high, the current (I_{sh}) flowing through it is negligible and has minimal impact on the overall I–V characteristics of the PV module. Therefore, the output current equation of the single-diode model can be simplified in equation (3.4):

$$I_{pv} = I_{ph} - I_0 \left(e^{\frac{q(V_{pv} + I_{pv}R_{se})}{nkT}} - 1 \right) \tag{3.4}$$

The total power output of the PV array, based on the series-parallel configuration of modules, can be calculated using equaton (3.5):

$$P_{array} = P_{max} \times (N_s \times N_p) \tag{3.5}$$

where $N_s = 6$ is the number of modules connected in series, $N_p = 6$ is the number of modules connected in parallel, and $P_{max} = 305.226$ W is the rated power output of a single module in equation (3.6).

$$P_{array} = 305.226 \times (6 \times 6) = 10.98 \text{ kW} \tag{3.6}$$

36   *Chapter 3.   DESIGN AND ANALYSIS OF SOLAR PV SYSTEMS*

In this study, the SunPower SPR-305NE photovoltaic (PV) module is selected for simulation and performance analysis due to its high efficiency and reliability under varying environmental conditions. This monocrystalline silicon module is known for its superior energy yield and stable electrical characteristics, making it a suitable choice for both terrestrial and floating PV applications. The module operates under standard test conditions (STC), which include an irradiance of 1000 W/m^2, cell temperature of 25°C, and air mass (AM) of 1.5. The detailed electrical and physical specifications of the SPR-305NE module are listed in Table 3.1, and these parameters serve as input for the simulation and modeling processes carried out in this work.

TABLE 3.1:   Electrical parameters of SunPower SPR-305NE PV module

Parameter	Value
Maximum Power (P_{max})	305.226 W
Open Circuit Voltage (V_{oc})	64.2 V
Short Circuit Current (I_{sc})	5.96 A
Voltage at Maximum Power Point (V_{mp})	54.7 V
Current at Maximum Power Point (I_{mp})	5.96 A
Reference Temperature (T_{ref})	25°C
Number of Series-Connected Modules	6
Number of Parallel-Connected Modules	6

3.2.2   Design of Boost Converter

A boost converter is a DC-DC power electronic converter used in stand-alone solar PV systems to step up the voltage from the photovoltaic (PV) module to a higher required level. It ensures efficient energy transfer from the PV array to the load or battery storage. It operates based on the principle of energy storage in an inductor and release to the load via a controlled switching mechanism in Fig. 3.2. The key components of a boost converter include:

In a DC-DC boost converter, the Inductor (L) stores energy when the switch is ON, the Switching Device (MOSFET/IGBT) controls the energy transfer, the Diode (D) prevents reverse current flow, the Capacitor (C) smoothens the output
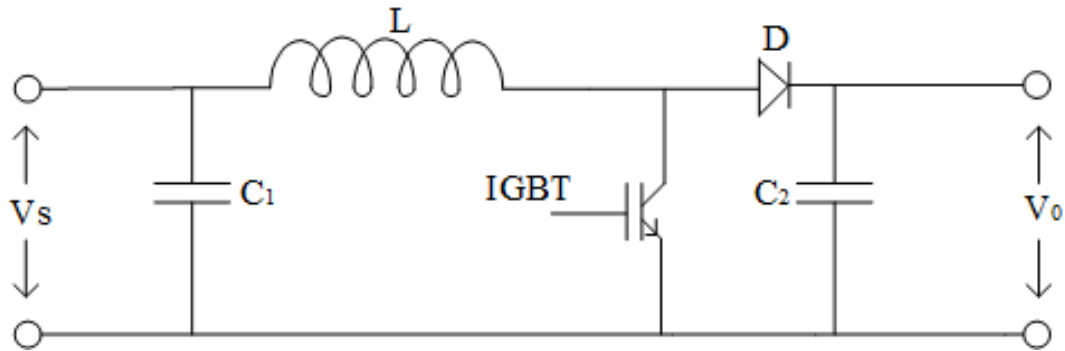
FIGURE 3.2: Equivalent circuit of DC-DC boost converter

voltage, and the Load (R) represents the connected load such as a battery or DC appliances. The boost converter output voltage is given in equation (3.7).

$$V_o = \frac{V_s}{1 - d} \tag{3.7}$$

where V_s = Input voltage (PV module voltage); V_o = Output voltage (desired boosted voltage); d = Duty cycle ($0 < d < 1$)

Inductor Selection:

The minimum inductor value is given in equation (3.8).

$$L = \frac{(1 - d)V_s}{f_s \Delta I_L} \tag{3.8}$$

where, f_s are the switching frequency (Hz) and ΔI_L are the inductor current ripple (A)

Capacitor Selection:

The output capacitor value is determined as in equation (3.9).

$$C_2 = \frac{I_{out}}{f_s \Delta V} \tag{3.9}$$

where, I_{out} are the output current (A) and ΔV are the ripple voltage (V).

Diode Selection:

The selected diode should withstand the peak current and reverse voltage in equation (3.10).

$$V_D \geq V_{\text{o}}, \quad I_D \geq I_{\text{out}} \tag{3.10}$$

where V_D is the voltage acrcoss diode and I_D is the current through diode

Switching Device:

The MOSFET or IGBT must handle the peak voltage and current:

$$V_{\text{DS}} \geq V_{\text{o}}, \quad I_{\text{DS}} \geq I_{\text{in}} \tag{3.11}$$

where V_{DS} is the voltage acrcoss switch, I_{DS} is maximum current rating of the device and I_{in} is is the input current (or the peak current that flows through the switch).

A boost converter is a crucial component in a stand-alone solar PV system, allowing for efficient power conversion and voltage regulation. Proper selection of components ensures reliable operation and improved system efficiency.

3.2.3   Maximum Power Point Tracking (MPPT)

MPPT is crucial in PV applications due to variable output voltage influenced by environmental factors. Maximum power trackers optimize the power output from PV arrays, enhancing system efficiency. To achieve maximum power, an MPPT technique must be employed that dynamically regulates power extraction. MPPT controllers are engineered to persistently track the maximum power point. Effective MPPT controllers are essential for adjusting operating points through modulation of the boost converter's duty cycle. The MPPT controllers used in this present works are as:

3.2.3.1 Perturb and Observe Algorithm:

P&O Technique is a common technique for tracking maximum power from a PV system. By this technique, minor perturbation of voltage is introduced causing

variation of power of PV module and compared with previous output power. If the present output power is greater than the previous power than PV voltage moved in positive direction and vice-versa. One of the major drawbacks of the Perturb and Observe Technique technique is that it causes oscillations around the maximum

The working of P&O algorithm operates by periodically perturbing the PV array's operating voltage and observing the resulting change in power. Based on the power variation, the algorithm decides whether to increase or decrease the voltage. The flow chart of this technique is presented in Fig. 3.3
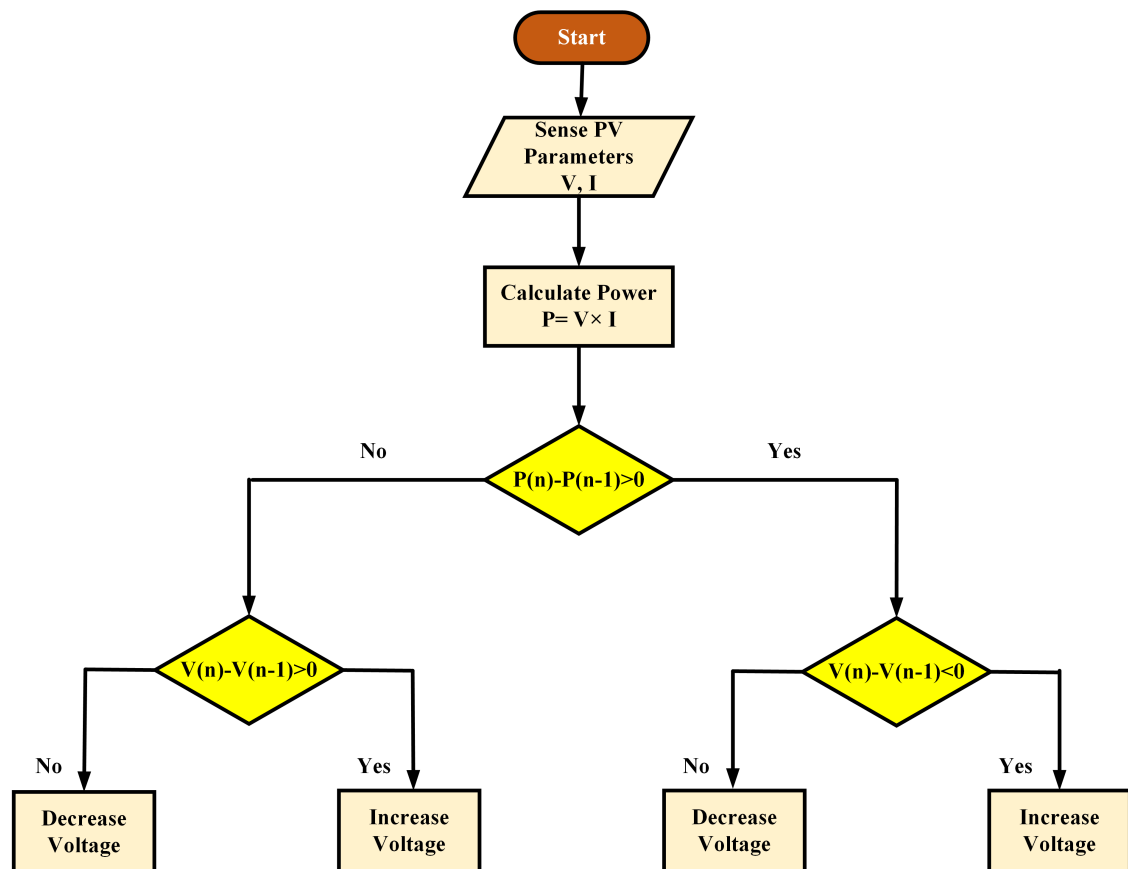
FIGURE 3.3: Flow chart of perturb and observe technique

The mathematical formulation of instantaneous power output of a PV module is given by:

$$P = V \times I \tag{3.12}$$

where P, V and I are the output power, voltage, and current of the PV module (W). To track the maximum power point (MPP), the derivative of power with respect to voltage is analyzed:

$$\frac{dP}{dV} = \frac{d(VI)}{dV} \tag{3.13}$$

Applying the product rule:

$$\frac{dP}{dV} = I + V\frac{dI}{dV} \tag{3.14}$$

At the maximum power point (MPP):

$$\frac{dP}{dV} = 0 \Rightarrow I + V\frac{dI}{dV} = 0 \tag{3.15}$$

Rearranging:

$$\frac{dI}{dV} = -\frac{I}{V} \tag{3.16}$$

The P&O algorithm perturbs the voltage V and observes the corresponding change in power P. The decision-making process follows:

- If $dP/dV > 0$, increase V to move towards MPP.

- If $dP/dV < 0$, decrease V to move towards MPP.

Mathematically, the voltage update rule is:

$$V(k+1) = \begin{cases} V(k) + \Delta V, & \text{if } \frac{dP}{dV} > 0 \\ V(k) - \Delta V, & \text{if } \frac{dP}{dV} < 0 \end{cases} \tag{3.17}$$

where $V(k)$ = Present operating voltage; $V(k+1)$ = Updated voltage; ΔV = Voltage perturbation step size

3.2.3.2 Fuzzy Logic Controller Algorithm:

A Fuzzy Logic Controller (FLC) for Maximum Power Point Tracking (MPPT) in a standalone solar PV system can significantly enhance performance under

varying irradiance and temperature conditions. It offers a more flexible and intelligent alternative to conventional MPPT algorithms like Perturb & Observe (P&O) and Incremental Conductance (IC) by handling nonlinearities effectively. Fig. 3.4 shows the block diagram for fuzzy logic controller. The FLC process consists of three steps: fuzzification, rule base lookup table, and defuzzification.
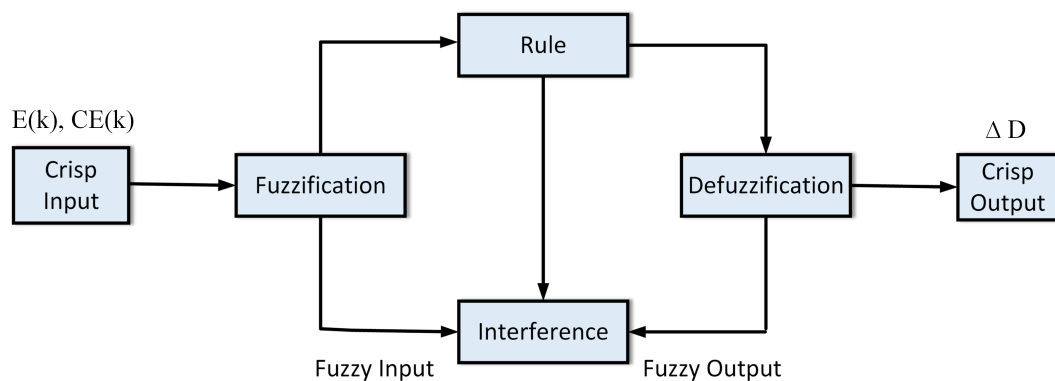
FIGURE 3.4: Block diagram of FLC controller MPPT

Fuzzification is the first stage of the FLC. It converts the actual value into fuzzy values combined with the membership function. It takes error (E) and change in error (CE) with stored membership function.

Rule base look up table is second state of fuzzy logic defines logical relation between the input values and output values. The logic of rule base inference is based on the IFTHEN. This fuzzy inference process is done by Mamdani's method.

Defuzzification is third stage of fuzzy logic which converts fuzzy values into crisp output. It is also the inverse of the fuzzification process. This process converts all fuzzy output values to their respective output membership function. The center of gravity method, also called centroid defuzzification is commonly used.

The inputs for the proposed Fuzzy Logic (FL) controller are Error (E) and change in Error (CE). The output from the FL controller is the change in duty

cycle (δD). The input variables are defined as follows:

$$E(K) = \frac{P(K) - P(K-1)}{V(K) - V(K-1)} \tag{3.18}$$

$$CE(K) = E(K) - E(K-1) \tag{3.19}$$

Table 3.2 shows a rule base used in the fuzzy logic controller. Each variable is characterized using five linguistic fuzzy levels: NB (Negative Big), NS (Negative Small), ZE (Zero), PS (Positive Small), and PB (Positive Big). These membership functions form the basis for the fuzzy inference mechanism employed in the controller design.

TABLE 3.2: Fuzzy rule base table for E and CE

$E \downarrow$ $CE \rightarrow$	NB	NS	ZE	PS	PB
NB	PB	PS	NB	NS	NS
NS	PS	PS	NB	NS	NS
ZE	NS	NS	NS	PB	PB
PS	NS	PB	PS	NB	PB
PB	NB	NB	PB	PS	PB

3.2.3.3 Bio Inspired based Flying Squirrel Search Optimization Algorithm

Conventional MPPT algorithms such as Perturb and Observe (P&O) often exhibit limitations under rapidly varying irradiance and partial shading conditions, including slow convergence, steady-state oscillations, and the tendency to track local maxima instead of the global maximum power point (GMPP). To overcome these challenges, bio-inspired optimization techniques have gained attention due to their adaptive nature, robustness, and superior global search capabilities, making them well-suited for dynamic and non-linear PV environments.

Flying squirrel search optimization technique (FSSO) is to mimic the search food technique of flying squirrel (FS). The potential solution vector are assign as the position of an FS whereas fitness of FSs are assign as quality of food source.

Based on their fitness value, The positions of FSs are divided into three categories: optimum solution (OS) (hickory nut tree), near optimum solution (NOS) (acorn nut tree), and random solution (RS) (normal tree).During the autumn season, squirrel gliding from one tree to another tree for finding the food to meet daily needs (acorn tree nuts) in forest. After achieving daily needs, they starts foraging for hickory tree nuts that will help them in winter season. Storage of hickory tree nuts (optimum solution) will help them in retaining their energy needs in winter season and decrease the food foraging journey. At the end of winter season, FSs are active again. This proposed MPPT algorithm uses the cooperation of FSs, and positions updated without the predator's presence.

In this algorithm, some suppositions are considered for the FSSO technique in MPPT that is PV power output Ppv take as objective, i.e., food source and Position of FSs is taken as the boost converter's duty cycle (d). To implement FSSO algorithm, the following steps are considered.

Starting

In this stage, N number of flying squirrels are located at several trees, which are different values of the duty cycle of the boost converter in equation (3.20):

$$d_i = d_{\min} + \frac{(i-1)(d_{\max} - d_{\min})}{N}, \quad i = 1, 2, \ldots, N \tag{3.20}$$

where i is the iteration count. $d_{\max}$ and $d_{\min}$ are the maximum and minimum values for the boost converter's duty cycle, which are taken as 10% and 90% of the acceptable duty cycle for the boost converter. The range of the duty cycle d_i is from 0 to 0.5.

Robustness Assessment

In the assessment process, the DC-DC boost converter is systematically regulated with every duty cycle (i.e., location of individual FSs). For an individual duty cycle d, the instant PV power output $P_{PV}(d)$ is taken as the quality of the food source. This step continues throughout the entire range of the duty cycle. The objective function (f) for MPPT is characterized using equation (3.21).

$$f(d) = \max(P_{\text{PV}}(d)) \tag{3.21}$$

Revelation and Grading

The hickory tree will have a duty cycle related to maximum power output. The next most essential location for FS is on acorn trees. The remaining FSs are taken into account on the normal tree.

Location Update

After checking the periodical supervising condition, the duty cycle is updated. If the duty cycle is revised using equation (3.22).

$$S_c^k < S_{\min} \tag{3.22}$$

where S_c^k is seasonal constant at current iteration count and $S_{\min}$ is minimum seasonal value.

Seasonal Supervising Condition

Food search behavior is significantly affected by seasonal changes. Squirrels are more energetic in autumn compared to winter. Periodical supervising conditions prevent the algorithm from being trapped in local minima. For a single-dimensional space, the seasonal constant (S_c) and its minimum seasonal value ($S_{\min}$) are calculated using (3.23) and (3.24).

$$S_c^k = \left| d_{\text{at}}^k - d_{\text{ht}} \right| \tag{3.23}$$

$$S_{\min} = \frac{10e^{-6}}{365^{k/(k_m/2.5)}} \tag{3.24}$$

where d_{ht} and d_{at} denote the locations of squirrels at a hickory tree and an acorn tree, respectively; k represents the current iteration count, and k_m is the maximum number of allowed iterations. The positions of flying squirrels (FSs) on normal trees (i.e., the duty cycle of NTFSs) are relocated using the Lévy distribution to enhance the search space as in equation (3.25).

$$d_{\text{nt}}^{(k+1)} = d_{\text{nt}}^k + l \tag{3.25}$$

where d_{nt} denotes the location of squirrels at a normal tree, and l represents the step length.

$$l \approx k \left(\frac{u}{|g|^{(1/\epsilon)}} \right) (d_{\text{ht}} - d_{\text{nt}}) \tag{3.26}$$

where the Lévy index ϵ and step coefficient k are chosen as 1.5 and 1.25, respectively. The variables u and g follow a normal distribution:

$$u = N(0, \sigma_u^2), \quad g = N(0, \sigma_g^2) \tag{3.27}$$

If Γ denotes the gamma function, then the variables σ_u and σ_g are defined as:

$$\sigma_u = \left(\frac{\Gamma(1 + \epsilon) \sin\left(\frac{\pi \epsilon}{2}\right)}{\Gamma\left(\frac{1+\epsilon}{2}\right) \epsilon^{(2-\epsilon)/2}} \right)^{1/\epsilon}, \quad \sigma_g = 1 \tag{3.28}$$

where

$$\Gamma(n) = (n - 1)! \tag{3.29}$$

Routine Revision

Flying squirrels (FSs) are initially located at the hickory tree. Some FSs move toward the acorn tree from the hickory tree, while others transition from normal trees to the acorn tree. Meanwhile, some FSs shift from normal trees to the hickory tree. The corresponding duty cycles are updated using the following equations (3.30),(3.31),(3.32) and (3.33).

$$d_{\text{at}}^{(k+1)} = d_{\text{at}}^k + g_d G_c (d_{\text{ht}}^k - d_{\text{at}}^k) \tag{3.30}$$

$$d_{\text{nt}}^{(k+1)} = d_{\text{nt}}^k + g_d G_c (d_{\text{ht}}^k - d_{\text{nt}}^k) \tag{3.31}$$

$$d_{\text{nt}}^{(k+1)} = d_{\text{nt}}^k + g_d G_c (d_{\text{at}}^k - d_{\text{nt}}^k) \tag{3.32}$$

Chapter 3. DESIGN AND ANALYSIS OF SOLAR PV SYSTEMS

where G_c and G_d represent the gliding constant and gliding distance, respectively. The estimated value of G_c is chosen as 1.90. The gliding distance is given by:

$$g_d = \frac{h_g}{s_f \tan \theta} \tag{3.33}$$

$$\tan \theta = \frac{F_D}{F_L} \tag{3.34}$$

where h_g is the height loss, taken as 8 m. The gliding distance g_d is divided by an appropriate numerical value. The scaling factor s_f is selected as 18 to keep g_d within the range of 0.5 to 1.11. The scaling factor assists in maintaining the desired balance between the exploration and exploitation phases. F_L is the lift force, whereas F_D is the drag force, defined in equation (3.35) and, (3.36).

$$F_D = \frac{1}{2} \rho V^2 S C_D \tag{3.35}$$

$$F_L = \frac{1}{2} \rho V^2 S C_L \tag{3.36}$$

where ρ is the density of air, taken as 1.204 kg/m^3; V is the velocity of FSs, taken as 5.25 m/s; S is the surface area of the body, taken as 154 cm^2; C_D is the drag coefficient, taken as 0.6, and C_L is the lift coefficient, which varies in the range $[0.675, 1.5]$.

Convergence Measurement

The optimization process is completed when the maximum number of iterations is reached. The output is the duty cycle at which the boost converter operates while tracking the maximum power.

Re-initialization

The MPPT algorithm depends on time variation, as changes in weather conditions affect the performance of flying squirrels (FSs). The location of FSs, i.e., the duty cycle, will be reinitialized to search for a new optimum maximum power. In this

FIGURE 3.5: Schematic diagram of grid connected PV system

process, the duty cycle is reinitialized after detecting a change in solar insolation through the following constraint equation (3.37).

$$\frac{P_{\text{PV}}^{(k+1)} - P_{\text{PV}}^{k}}{P_{\text{PV}}^{(k+1)}} \geq \Delta P(\%) \tag{3.37}$$

3.3 Design of Grid Connected PV System

This section presents the modeling and design of a grid-tied solar PV system. Fig. 3.5 illustrates the schematic diagram of a double-stage grid-tied PV system, comprising a 3.2 kW PV array connected to a three-phase grid at 415 V, 50 Hz. The system comprises two-stage power conversion: first, the variable DC output from the PV array is boosted to a fixed DC voltage of the required magnitude using a boost converter. This is followed by a grid-connected PV inverter, which converts the DC voltage into an AC voltage of the appropriate magnitude and frequency to supply the AC load. Simulation studies are carried out using MATLAB Simulink.

3.3.1   PV Array

The PV array is modeled in MATLAB/Simulink using the inbuilt PV module block, configured based on the required ratings and specifications. For this study, Sun modules are employed, each delivering a maximum power of 329 W. The open-circuit voltage V_{oc} and short-circuit current I_{sc} are 46.65 V and 9.35 A, respectively. The voltage and current at the maximum power point are 37.58 V and 8.78 A. A 3.2 kW PV array is formed by configuring two strings, each comprising five PV modules connected in series.

3.3.2   Design of Boost Converter

In the proposed system, the inductor and capacitor values are determined as 5 mH and 2.2 μF, respectively, using equations (3.8) and (3.9). The converter's reference duty cycle is obtained through the MPPT algorithm, while a switching frequency of 10 kHz is applied to generate the gating signal for the IGBT switch in the boost converter.

3.3.3   DC Link Voltage

The DC link voltage V_{DC} must be greater than twice the peak value of the line-to-line supply voltage to ensure effective inverter operation. For a three-phase system, it is determined using the equation (3.38):

$$V_{dc} = \frac{2\sqrt{2} \cdot V_{LL}}{\sqrt{3} \cdot m} \tag{3.38}$$

where, V_{LL} is the RMS value of three-phase AC side voltage, which is 415V, m is the modulation index and is taken as 0.96.

3.3.4   DC Link Capacitor

The DC-link capacitor must be sufficiently large to accommodate system dynamics, as its size depends on the instantaneous energy required by the VSI during transient conditions. The DC-link voltage should remain stable despite

fluctuations in load and power generation. The value of the DC-link capacitor can be calculated using equation (3.39):

$$C_{dc} = \frac{I_M}{2\omega V_{dc,ripple}}$$ (3.39)

where I_M is the PV array current at maximum power, ω is the grid angular frequency, and $V_{dc,\text{ripple}}$ is the allowable ripple in the DC link voltage, taken as 2% of V_{dc}. For the proposed system, the calculated value of the DC link capacitance C_{dc} is 3.2 μF, while a capacitor of 5 μF is selected to ensure adequate performance.

3.3.5 Interfacing Inductors

Interfacing inductors L_f are installed on the AC side of the PV inverter to connect the inverter to the grid. These inductors help minimize the ripple in the inverter's output current. The design of the interfacing inductors is based on equation (3.40)

$$L_f = \frac{\sqrt{3}\, m\, V_{dc}}{12\, h\, f_s\, \Delta i}$$ (3.40)

where Δi is the current ripple, taken as 10% of the inverter current, f_s is the switching frequency, taken as 10 kHz in the present work, and h is the overload factor, taken as 1.2. The calculated value of the interfacing inductor L_f is '7.5 mH for the proposed system.

3.3.6 Design of Inverter
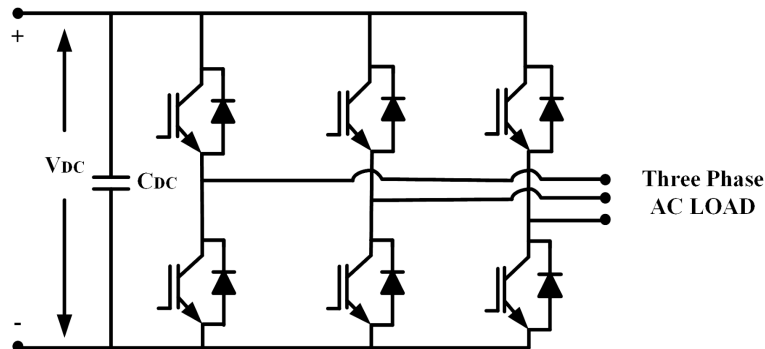
FIGURE 3.6: Equivalent circuit of three phase voltage source inverter

Chapter 3. DESIGN AND ANALYSIS OF SOLAR PV SYSTEMS

The output of the DC-DC converter is transformed into AC voltage using a three-phase inverter. A two-level, three-phase Voltage Source Inverter (VSI) with six IGBT switches, as illustrated in Fig. 3.6, is employed for this purpose. Each IGBT switch must be capable of blocking the full DC link voltage; therefore, the voltage rating of the switches should be selected accordingly. The current rating of each switch is determined by the total current flowing through it, which includes both the PV array current and the harmonic compensating current.

3.3.7   Inverter Control Algorithms

Various control algorithms are available for generating reference currents for the Voltage Source Inverter (VSI). Synchronous reference frame theory (SRFT) algorithm and Instantaneous Reactive Power Theory (IRPT) is used for the control of VSI.

3.3.7.1 Synchronous Reference Frame Theory (SRFT) algorithm
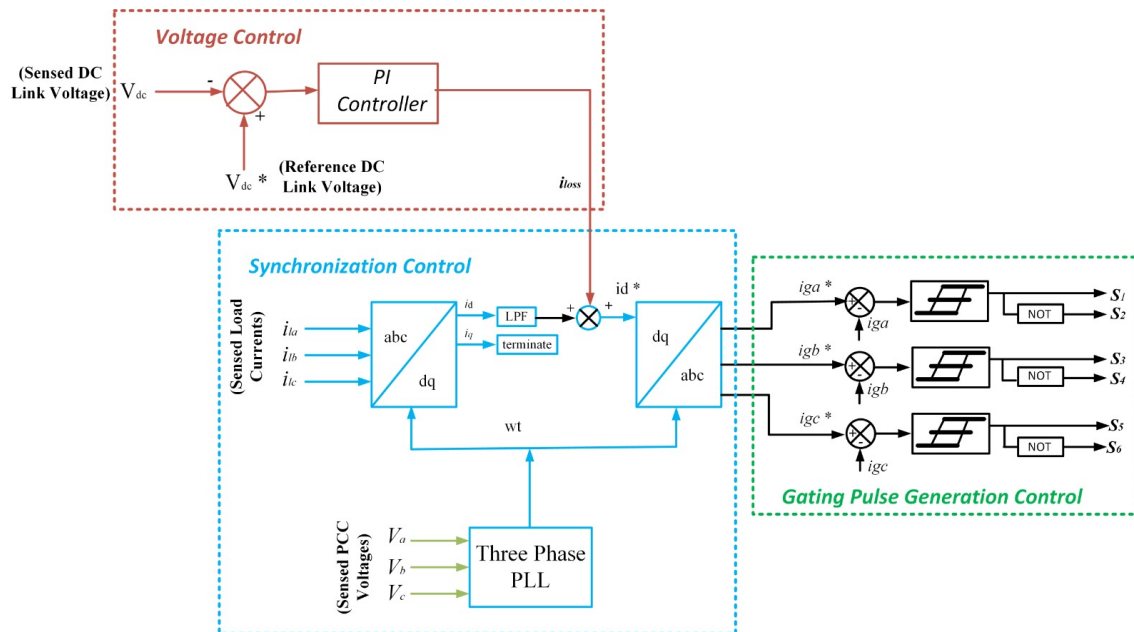
FIGURE 3.7: Block diagram of SRFT algorithm for inverter control

Synchronous Reference Frame Theory (SRFT) is one of the most widely adopted techniques for controlling three-phase grid-connected power electronic

converters, including inverters used in photovoltaic (PV) systems, active power filters (APFs), and other power quality enhancement devices as in Fig. 3.7. SRFT enables effective decoupled control of active and reactive power by transforming the three-phase system variables from the stationary *abc* frame to a synchronously rotating *dq*0 reference frame aligned with the grid voltage vector. This transformation simplifies the control structure by converting sinusoidal signals into DC quantities, thereby allowing the use of conventional PI controllers for current regulation and improving the dynamic response of the system under varying grid and load conditions.

In a three-phase balanced system, the fundamental components of voltages and currents are sinusoidal and oscillate at the grid frequency. The SRFT transforms these quantities into a synchronously rotating *dq* reference frame using a Phase-Locked Loop (PLL) to track the grid phase angle. In this frame, the fundamental frequency components become direct current (DC) quantities, which significantly simplifies their control using conventional PI controllers. This approach enables independent and precise regulation of active and reactive power exchange between the inverter and the grid. The implementation of the SRFT involves the following steps:

Measurement of System Quantities: Initially, the instantaneous three-phase voltages and currents at the point of common coupling (PCC) are measured:

$$\mathbf{v}_{abc} = \begin{bmatrix} v_a \\ v_b \\ v_c \end{bmatrix}, \quad \mathbf{i}_{abc} = \begin{bmatrix} i_a \\ i_b \\ i_c \end{bmatrix} \tag{3.41}$$

where v_a, v_b, v_c are the instantaneous phase voltages of the three-phase system, measured at the point of common coupling (PCC). i_a, i_b, i_c are the instantaneous phase currents of the three-phase system, also measured at the PCC.

Clark's Transformation: The measured phase variables are first transformed into a two-axis stationary orthogonal reference frame $(\alpha\beta)$ using the Clark's transformation:

Chapter 3. DESIGN AND ANALYSIS OF SOLAR PV SYSTEMS

$$
\begin{bmatrix} x_\alpha \\ x_\beta \end{bmatrix} = \frac{2}{3} \begin{bmatrix} 1 & -\frac{1}{2} & -\frac{1}{2} \\ 0 & \frac{\sqrt{3}}{2} & -\frac{\sqrt{3}}{2} \end{bmatrix} \begin{bmatrix} x_a \\ x_b \\ x_c \end{bmatrix} \tag{3.42}
$$

where x_a, x_b, x_c are the original three-phase signals (voltage or current), and x_α, x_β are the transformed two-phase signals in a stationary orthogonal system. This transformation is applied to both voltage and current signals.

Park Transformation: Subsequently, the stationary $\alpha\beta$ components are converted into the synchronously rotating dq reference frame by employing the Park transformation:

$$
\begin{bmatrix} x_d \\ x_q \end{bmatrix} = \begin{bmatrix} \cos\theta & \sin\theta \\ -\sin\theta & \cos\theta \end{bmatrix} \begin{bmatrix} x_\alpha \\ x_\beta \end{bmatrix} \tag{3.43}
$$

where θ denotes the instantaneous grid voltage angle estimated by the PLL; x_d are the direct-axis (d-axis) component and x_q are quadrature-axis (q-axis) component. .

Current Control Strategy: In the dq reference frame, the direct-axis component (i_d) primarily determines the active power exchanged with the grid, while the quadrature-axis component (i_q) governs the reactive power.   Accordingly, reference currents (i_d^*, i_q^*) are generated based on the desired active and reactive power set-points.   Typically, the active power reference is derived from the output of a maximum power point tracking (MPPT) algorithm in PV systems, whereas the reactive power reference is often set to zero to maintain unity power factor. The current tracking errors are defined as:

$$
e_d = i_d^* - i_d, \quad e_q = i_q^* - i_q \tag{3.44}
$$

These errors are processed by independent PI controllers to generate the voltage commands in the dq frame:

$$
v_d^* = PI(e_d), \quad v_q^* = PI(e_q) \tag{3.45}
$$

where v_d^*, v_q^* are reference/control voltages in the dq frame generated by the PI controllers.

Inverse Transformations: The computed dq reference voltages are then transformed back to the stationary $\alpha\beta$ frame and subsequently to the three-phase abc frame using the inverse Park and Clarke transformations, respectively:

$$
\begin{bmatrix} v_\alpha^* \\ v_\beta^* \end{bmatrix} = \begin{bmatrix} \cos\theta & -\sin\theta \\ \sin\theta & \cos\theta \end{bmatrix} \begin{bmatrix} v_d^* \\ v_q^* \end{bmatrix}, \tag{3.46}
$$

$$
\begin{bmatrix} v_a^* \\ v_b^* \\ v_c^* \end{bmatrix} = \begin{bmatrix} 1 & 0 \\ -\frac{1}{2} & \frac{\sqrt{3}}{2} \\ -\frac{1}{2} & -\frac{\sqrt{3}}{2} \end{bmatrix} \begin{bmatrix} v_\alpha^* \\ v_\beta^* \end{bmatrix} \tag{3.47}
$$

where v_α^*, v_β^* voltages in the stationary $\alpha\beta$ frame. v_a^*, v_b^*, v_c^* actual three-phase voltage references to be applied at the inverter output.

Pulse Width Modulation: Finally, the three-phase reference voltages are employed to generate the gating signals for the inverter switches using a pulse width modulation (PWM) technique, typically sinusoidal PWM or space vector PWM, to ensure precise voltage synthesis.

3.3.7.2 Instantaneous Reactive Power Theory (IRPT) Algorithm

The Instantaneous Reactive Power Theory (IRPT), also known as the pq Theory, is a fundamental approach for the real-time analysis and control of power flow in three-phase power systems, particularly in active power filtering and power quality enhancement applications. First proposed by Akagi et al., this theory enables the decomposition of instantaneous power into its active and reactive components directly in the time domain without requiring frequency-domain transformations.

In a three-phase system, instantaneous voltages and currents are generally unbalanced and non-sinusoidal due to nonlinear loads. The IRPT transforms the three-phase quantities into an orthogonal $\alpha\beta$ stationary reference frame using the Clarke transformation. This transformation allows for the instantaneous

Chapter 3. DESIGN AND ANALYSIS OF SOLAR PV SYSTEMS
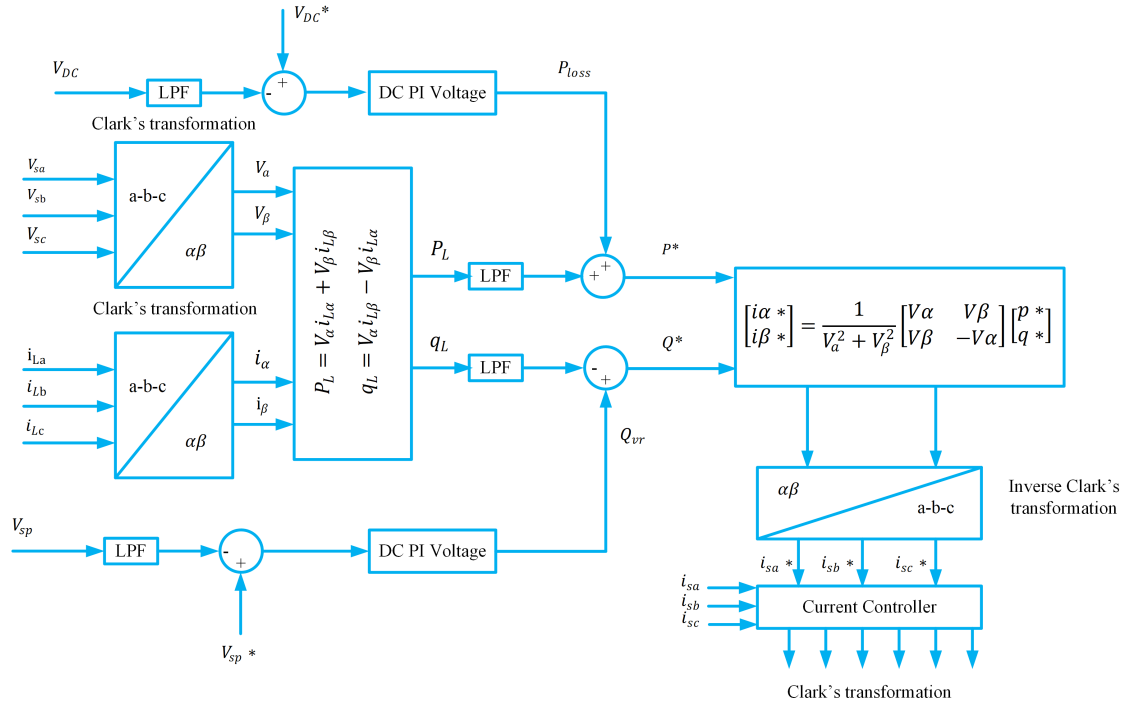
FIGURE 3.8: Block diagram of IRPT algorithm for inverter control

computation of real and reactive power components, which can be used to design control strategies for power compensation as in Fig. 3.8. The implementation of the IRPT consists of the following steps:

The instantaneous three-phase voltages and currents at the point of common coupling (PCC) are measured:

$$\mathbf{v}_{abc} = \begin{bmatrix} v_a \\ v_b \\ v_c \end{bmatrix}, \quad \mathbf{i}_{abc} = \begin{bmatrix} i_a \\ i_b \\ i_c \end{bmatrix} \tag{3.48}$$

Clarke Transformation: The measured phase variables are transformed to the two-axis stationary reference frame $(\alpha\beta)$ using the Clarke transformation:

$$\begin{bmatrix} x_\alpha \\ x_\beta \end{bmatrix} = \sqrt{\frac{2}{3}} \begin{bmatrix} 1 & -\frac{1}{2} & -\frac{1}{2} \\ 0 & \frac{\sqrt{3}}{2} & -\frac{\sqrt{3}}{2} \end{bmatrix} \begin{bmatrix} x_a \\ x_b \\ x_c \end{bmatrix} \tag{3.49}$$

where x_α is the α-axis component, aligned with an arbitrary reference in the stationary frame. x_β is the β-axis component, perpendicular to the α-axis (90° phase difference).

Instantaneous Power Calculation: In the $\alpha\beta$ frame, the instantaneous active (p) and reactive (q) power are defined as:

$$\begin{bmatrix} p \\ q \end{bmatrix} = \begin{bmatrix} v_\alpha & v_\beta \\ v_\beta & -v_\alpha \end{bmatrix} \begin{bmatrix} i_\alpha \\ i_\beta \end{bmatrix} \tag{3.50}$$

where v_α, v_β are the voltages in the stationary $\alpha\beta$ frame. i_α, i_β are the currents in the stationary $\alpha\beta$ frame. p is the instantaneous active power. q is the instantaneous reactive power.

Reference Compensation Currents: For power compensation, the desired reference currents are computed by eliminating the unwanted components (e.g., reactive power and harmonic power) from the total instantaneous power. The desired instantaneous powers (p^*, q^*) are defined according to the compensation objective (e.g., to achieve unity power factor and harmonic-free source current). The reference currents in the $\alpha\beta$ frame are then calculated in equation (3.51).

$$\begin{bmatrix} i_\alpha^* \\ i_\beta^* \end{bmatrix} = \frac{1}{v_\alpha^2 + v_\beta^2} \begin{bmatrix} v_\alpha & v_\beta \\ v_\beta & -v_\alpha \end{bmatrix} \begin{bmatrix} p^* \\ q^* \end{bmatrix} \tag{3.51}$$

where i_α^*, i_β^* are the reference currents in the stationary $\alpha\beta$ frame; v_α, v_β are the voltages in the stationary $\alpha\beta$ frame; p^*, q^* are the reference active and reactive powers.

Inverse Clarke Transformation: Finally, the reference currents in the $\alpha\beta$ frame are transformed back to the original three-phase system using the inverse Clarke transformation using equation (3.52).

$$\begin{bmatrix} i_a^* \\ i_b^* \\ i_c^* \end{bmatrix} = \sqrt{\frac{2}{3}} \begin{bmatrix} 1 & 0 \\ -\frac{1}{2} & \frac{\sqrt{3}}{2} \\ -\frac{1}{2} & -\frac{\sqrt{3}}{2} \end{bmatrix} \begin{bmatrix} i_\alpha^* \\ i_\beta^* \end{bmatrix} \tag{3.52}$$

where i_α^*, i_β^* are the reference currents in the stationary $\alpha\beta$ frame; i_a^*, i_b^*, i_c^* are the reference three-phase currents to be applied at the inverter output.

These reference currents are then used to generate the gating signals for the active filter or inverter using an appropriate current control method, such as hysteresis or PWM current control.

3.4   Results and Discussions

In this study, FSSO-based MPPT is implemented for both standalone and grid-connected PV systems, while IRPT and SRFT algorithms are applied for inverter control in the grid-connected PV system. The performance results of P&O, FLC, and FSSO MPPT controllers obtained through MATLAB simulations are presented, along with the outcomes of SRFT and IRPT-based inverter control strategies for the grid-connected PV system.

3.4.1   Performance analysis of standalone PV system with FSSO MPPT controller under variable solar irradiances

The simulation was implemented in MATLAB 2017 and executed on a system equipped with an Intel Core i3 processor and 16 GB of RAM. Fig. 3.9 presented the dynamic performance of the proposed Flying Squirrel Search Optimization (FSSO) based Maximum Power Point Tracking (MPPT) algorithm under varying solar irradiance levels. The simulation was carried out for irradiance levels of 1000 W/m^2, 600 W/m^2, and 400 W/m^2, which represent a wide range of real-world operating conditions. The corresponding output power response of the photovoltaic (PV) system was monitored over time to assess the tracking capability of the algorithm.

The results clearly demonstrate that the FSSO-based MPPT controller achieves effective and reliable tracking of the maximum power point across all irradiance conditions.   The controller exhibits fast convergence, minimal steady-state oscillations, and negligible overshoot, indicating its high tracking precision and dynamic responsiveness. As expected, the output power decreases proportionally with the reduction in solar irradiance, confirming the consistency of the algorithm's operation with the fundamental characteristics of PV systems.

3.4. Results and Discussions

57
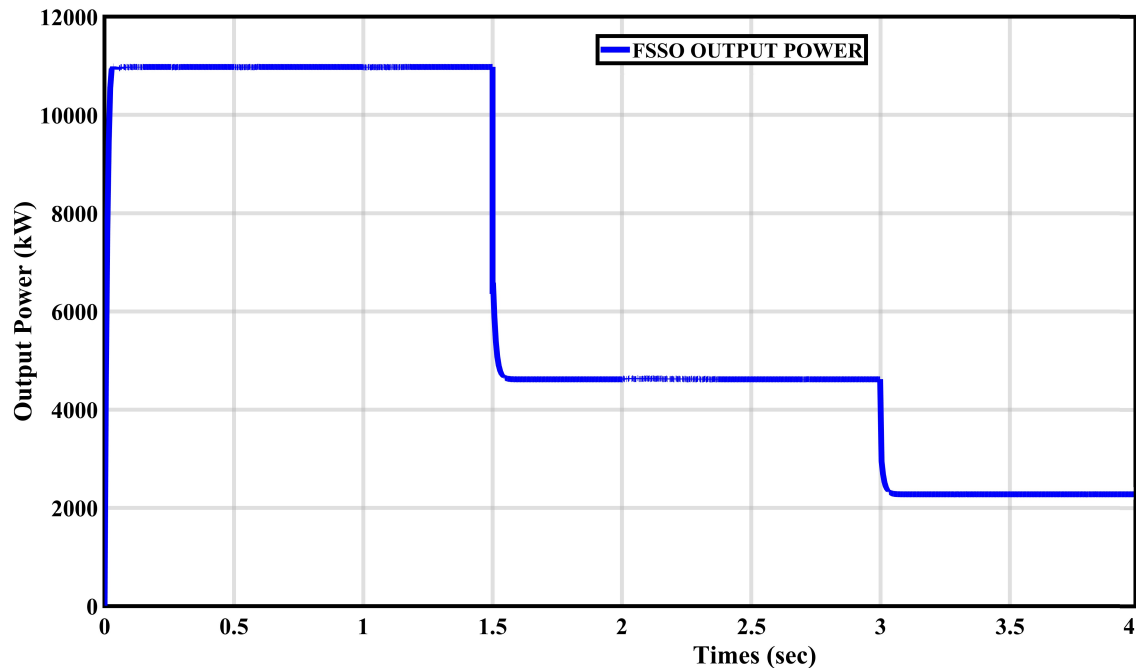
FIGURE 3.9: Simulation results of FSSO controller under different irradiations

Notably, the transitions between irradiance levels are handled smoothly by the controller, without any instability or performance degradation. This highlights the robustness and adaptability of the FSSO algorithm in dynamically changing environmental conditions.

3.4.1.1 Comparison of FSSO MPPT Controller with Conventional MPPT Techniques

To evaluate the tracking performance of the proposed flying squirrel search optimization (FSSO)-based MPPT technique, a comparative simulation study was conducted alongside fuzzy logic controller (FLC) and conventional perturb and observe (P&O) algorithms. The PV system was subjected to step changes in solar irradiance levels at 1000 W/m^2, 600 W/m^2, and 400 W/m^2, and the corresponding output power responses were observed.

Fig. 3.10 shows that the FSSO-based MPPT algorithm consistently achieves rapid convergence to the maximum power point (MPP) with minimal steady-state oscillations across all irradiance levels. In contrast, the FLC offers

Chapter 3. DESIGN AND ANALYSIS OF SOLAR PV SYSTEMS
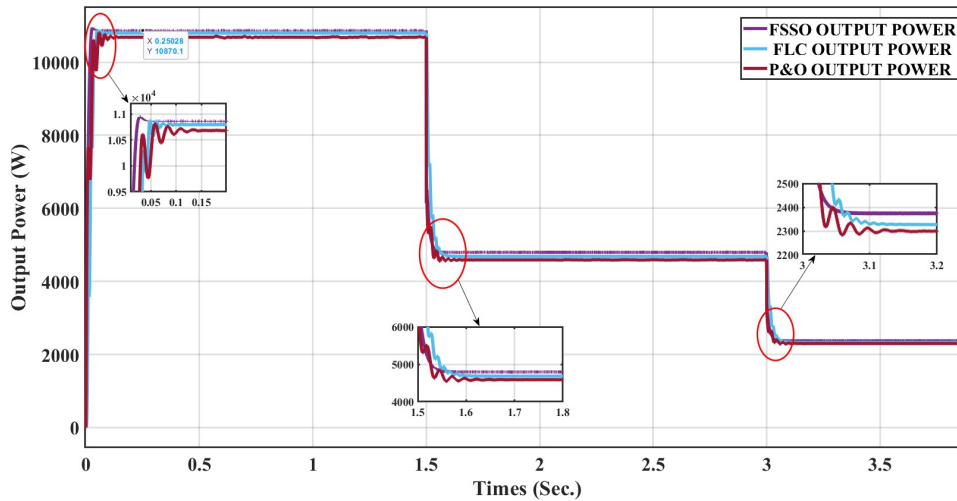
FIGURE 3.10: Comparison of PV output power using FSSO, FLC,
and P&O algorithms under different irradiance levels.

moderate performance—better than P&O but inferior to FSSO in tracking speed
and accuracy, particularly under low irradiance. The conventional P&O method
exhibits noticeable delay, deviation from the true MPP, and increased transient
oscillations. At high irradiance (1000 W/m^2), all three algorithms achieved
near-MPP operation; however, at 400 W/m^2, the superiority of FSSO became
evident. FSSO maintained stable and precise power tracking, while P&O
suffered significant performance degradation and FLC exhibited intermediate
behavior. These results confirm that the proposed FSSO algorithm is both
effective and computationally efficient, making it suitable for real-time
embedded implementation.

The performance metrics such as overshoot, undershoot, and settling time are
quantitatively evaluated and summarized in Table 3.3. Among the three
algorithms, the FSSO-based MPPT controller exhibits the shortest settling time
and minimal transient error.

The efficiency of the MPPT tracking is calculated using the equation (3.53).

$$\%\eta = \frac{P_{\text{tracked}}}{V_{\text{MPP}} \times I_{\text{MPP}}} \times 100 \qquad (3.53)$$

where P_{tracked} denotes the power tracked by the PV system, with V_{MPP} and
I_{MPP} representing the voltage and current at the maximum power point.

3.4. Results and Discussions 59

TABLE 3.3: Comparison analysis between P&O, FLC, and FSSO MPPT controller

Irradiance (W/m^2)	Overshoot (%)			Undershoot (%)			Settling Time (sec.)		
	P&O	FLC	FSSO	P&O	FLC	FSSO	P&O	FLC	FSSO
1000	1.21	0.74	0.73	9.42	2.23	0	0.15	0.12	0.05
600	5.61	5.57	0	0.94	0	0	0.12	0.08	0.06
400	15.89	9.45	0	0.87	0	0	0.13	0.11	0.06

Table 3.4 summarizes the maximum power extracted and tracking efficiency of the proposed FFSO technique against conventional methods. At 1000 W/m^2, the FFSO extracts 10.86 kW, compared to 10.80 kW by FLC and 10.69 kW by P&O.

TABLE 3.4: Output power and efficiency of different MPPT techniques

Irradiance (W/m^2)	P&O		FLC		FSSO	
	P_{MPP} (kW)	η (%)	P_{MPP} (kW)	η (%)	P_{MPP} (kW)	η (%)
1000	10.69	97.27	10.80	99.44	10.86	99.99
600	4.60	95.25	4.68	97.07	4.80	99.56
400	2.40	96.19	2.33	97.24	2.37	99.24

3.4.2 Performance Analysis of Grid Connected PV System with FSSO MPPT Controller

This section presents a detailed performance evaluation of a grid-connected solar photovoltaic (PV) system incorporating control strategies for both maximum power extraction and efficient grid interfacing.

To regulate the voltage source inverter (VSI) and ensure power quality during grid integration, two control strategies are Instantaneous Reactive Power Theory (IRPT) and Synchronous Reference Frame Theory (SRFT) are employed. These schemes generate precise current references for active and reactive power management while mitigating grid-injected harmonics. Key parameters,

including grid power, load power, current quality, and dynamic stability, are evaluated to assess the performance of the FSSO-based MPPT controller with these inverter controls. Both IRPT and SRFT are analyzed under solar irradiances of 1000 W/m², 600 W/m², and 400 W/m² to provide a comparative evaluation.
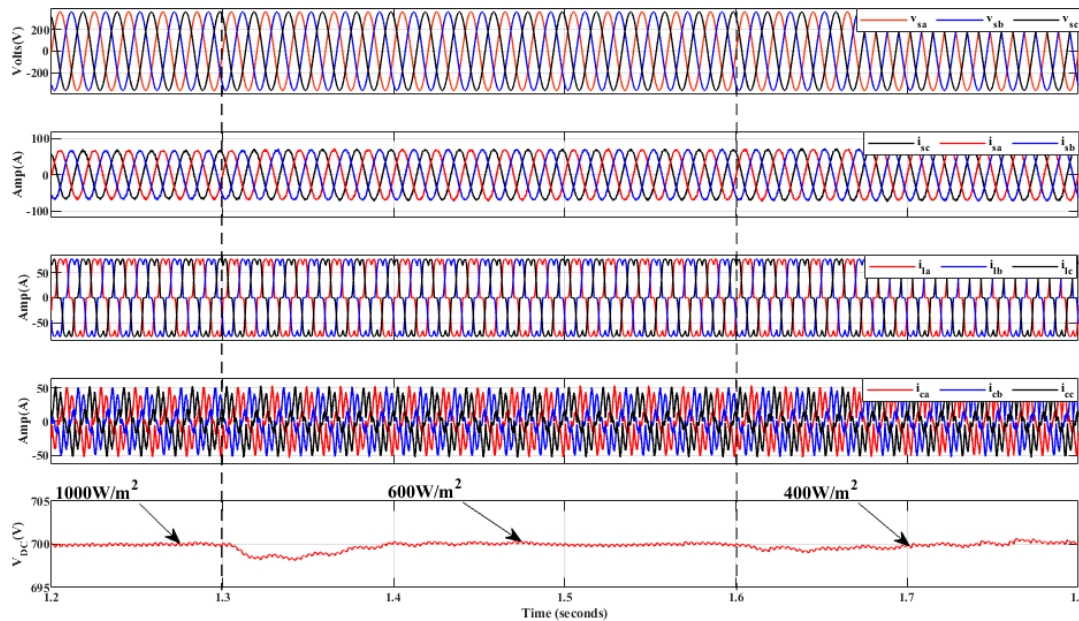
FIGURE 3.11: Analysis of grid voltage, grid current, load current, compensating current, and DC-link voltage using IRPT-based inverter control.

3.4.2.1 Analysis of IRPT based Inverter Control Algorithm for Grid Connected PV System under Constant Load Demand

Instantaneous Reactive Power Theory (IRPT) control is also analyzed under the same varying solar irradiance conditions of 1000 W/m², 600 W/m², and 400 W/m² to provide a comparative perspective. Fig. 3.11 shows that the IRPT controller maintains the three-phase source voltages in a balanced and sinusoidal form, with source current amplitudes adjusting appropriately to match the available PV power.

The load currents remain constant due to load connected to syetm. The compensating currents dynamically adapt to inject the necessary harmonic and reactive components, ensuring that the grid currents stay close to sinusoidal.

Fig. 3.12 illustrates the behaviour of active and reactive power components, supply voltage and current, and PV power generation for the grid-connected PV system controlled using the Instantaneous Reactive Power Theory (IRPT) under varying irradiance levels of 1000 W/m^2, 600 W/m^2, and 400 W/m^2.
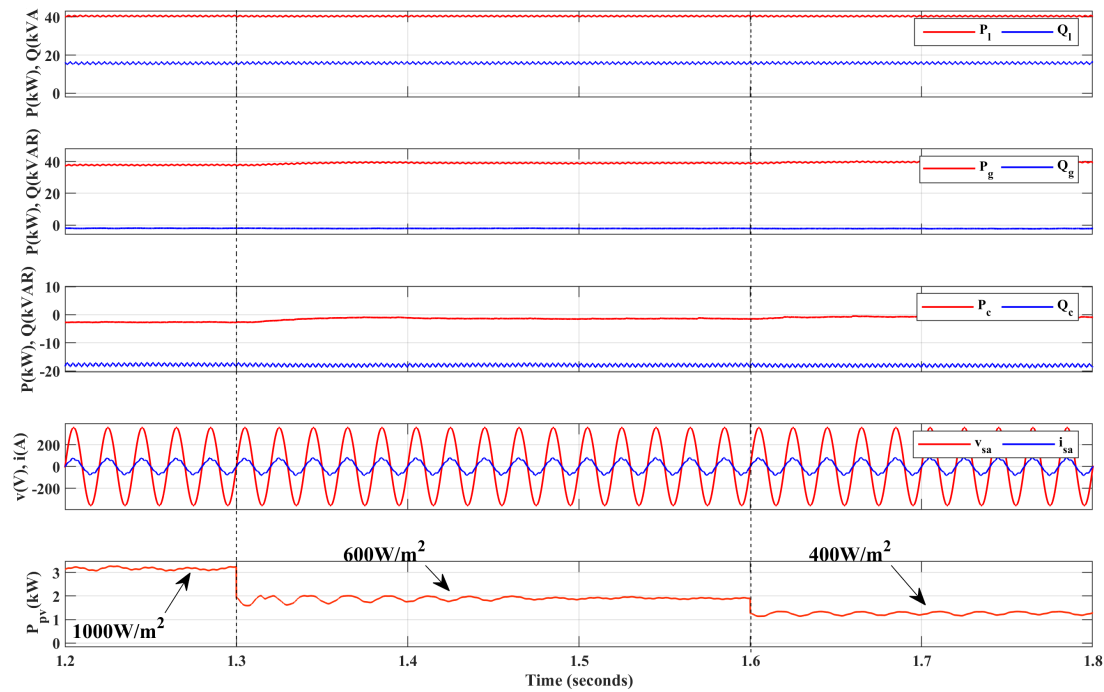
FIGURE 3.12: Grid active power (P_g), load power (P_l), compensating power (P_c), and PV power (P_{PV}) under varying irradiance for IRPT-controlled PV system.

The active power supplied by the grid (P_g) remains nearly constant to meet the load demand, compensating for the reduction in PV generation as irradiance decreases. The grid's reactive power (Q_g) also stays within acceptable limits, indicating that the IRPT controller provides necessary reactive power support. The load active (P_l) and reactive (Q_l) power are stable around 40 kW and 2 kVAr, respectively, confirming constant load conditions. The inverter's compensating power (P_c and Q_c) dynamically adjusts to manage the reactive and harmonic currents. However, slight fluctuations can be seen compared to the SRFT control, especially at lower irradiance levels. The supply phase voltage and current waveforms confirm that the current remains sinusoidal and mostly in phase with the voltage, demonstrating acceptable power factor correction. The PV array

power output (P_{PV}) clearly decreases from about 3 kW at 1000 W/m^2 to around 1.2 kW at 400 W/m^2, as expected.

In summary, IRPT provides reliable active and reactive power balancing and maintains acceptable power quality under varying irradiance, but exhibits slightly higher ripple and less precise voltage and harmonic control compared to SRFT. Thus, SRFT is preferred for applications demanding stringent power quality. The harmonic spectrum shows a fundamental at 50 Hz with a THD of 4.75%. Fig.3.13 show the total harmonic distortion (THD) of grid current for the nonlinear load which is under IEEE standard.
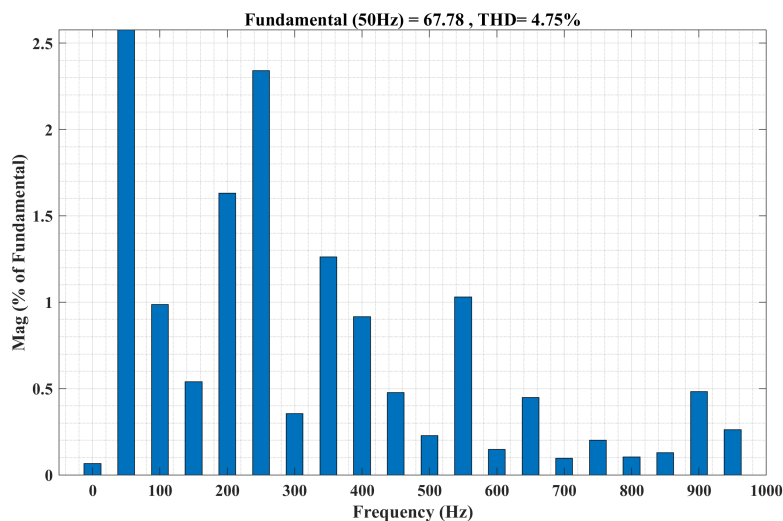
FIGURE 3.13: THD of grid current for nonlinear load using IRPT control

3.4.2.2 Analysis of IRPT based Inverter Control Algorithm for Grid Connected PV System under Varying Load Demand

The performance of the instantaneous reactive power theory (IRPT) based inverter control algorithm is evaluated for a grid-connected photovoltaic (PV) system under dynamic load conditions. Two cases are analyzed: a sudden load decrease at $t = 1.0$ s and a load increase at $t = 2.0$ s. The corresponding grid voltage and current, load and compensating current and dc link voltage are illustrated in Fig. 3.14.
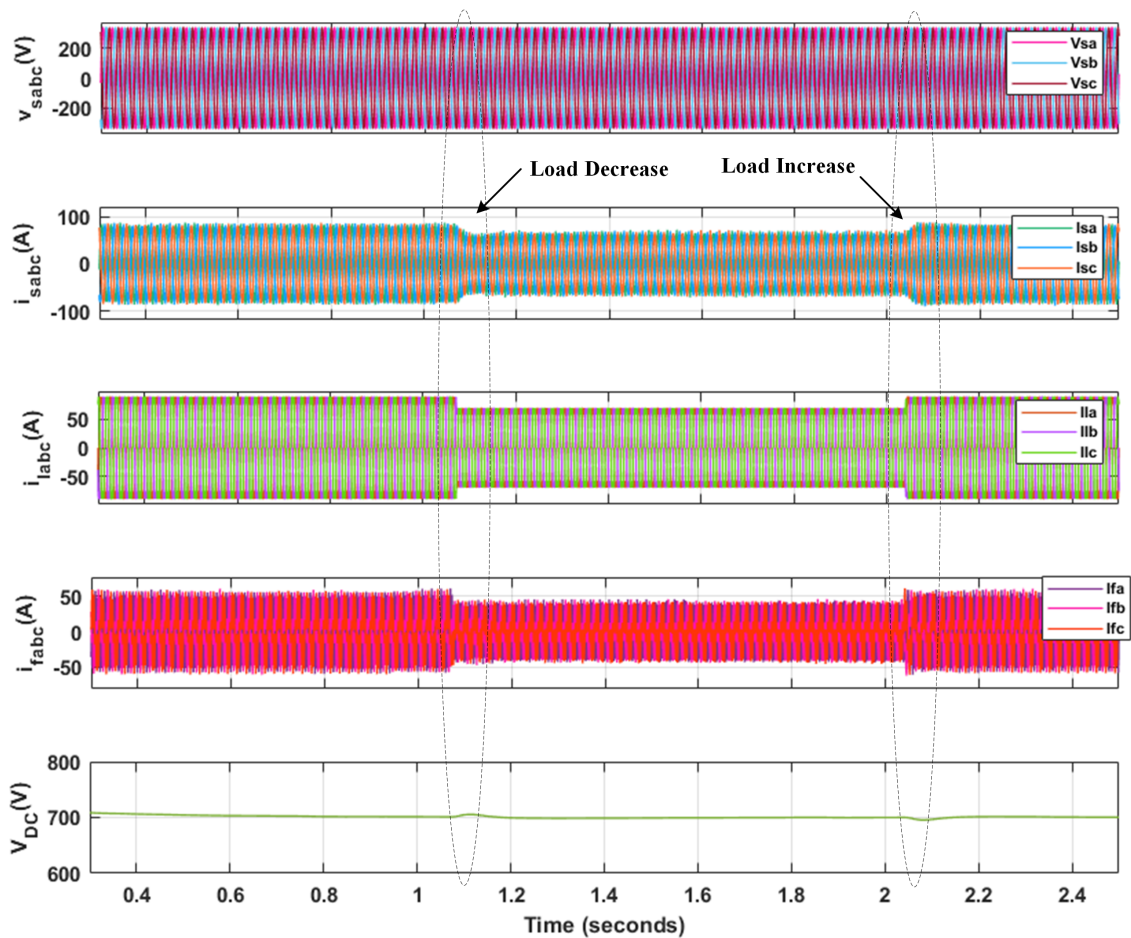
FIGURE 3.14: Voltage and current waveforms of the IRPT-based inverter control algorithm under varying load conditions.

Fig. 3.14 shows the three-phase grid voltages (V_{sa}, V_{sb}, V_{sc}) along with the associated grid currents (i_{sa}, i_{sb}, i_{sc}), load currents (i_{la}, i_{lb}, i_{lc}), and filter currents (i_{fa}, i_{fb}, i_{fc}). During the load change events, the IRPT controller ensures that the grid currents remain nearly sinusoidal and balanced, despite sudden transients in the load. This indicates effective harmonic and reactive power compensation by the inverter. The DC-link voltage (V_{dc}) remains stable around 700 V, with only minor fluctuations during load disturbances, validating the robustness of the control strategy.

The power flow response, presented in Fig. 3.15, further confirms the controller's effectiveness. The real and reactive power supplied by the grid (P_g, Q_g), the inverter (P_I, Q_I), and the compensator (P_c, Q_c) are tracked. At

Chapter 3. DESIGN AND ANALYSIS OF SOLAR PV SYSTEMS

$t = 1.0\,\text{s}$, when the load decreases, the inverter instantaneously adjusts its output by reducing the real power injection. Conversely, at $t = 2.0\,\text{s}$, when the load demand increases, the inverter supplies the required additional real power while maintaining reactive power support. The PV power output (P_{PV}) remains nearly constant at around $3\,\text{kW}$, confirming that the IRPT controller effectively manages power sharing between the PV source, grid, and local load.
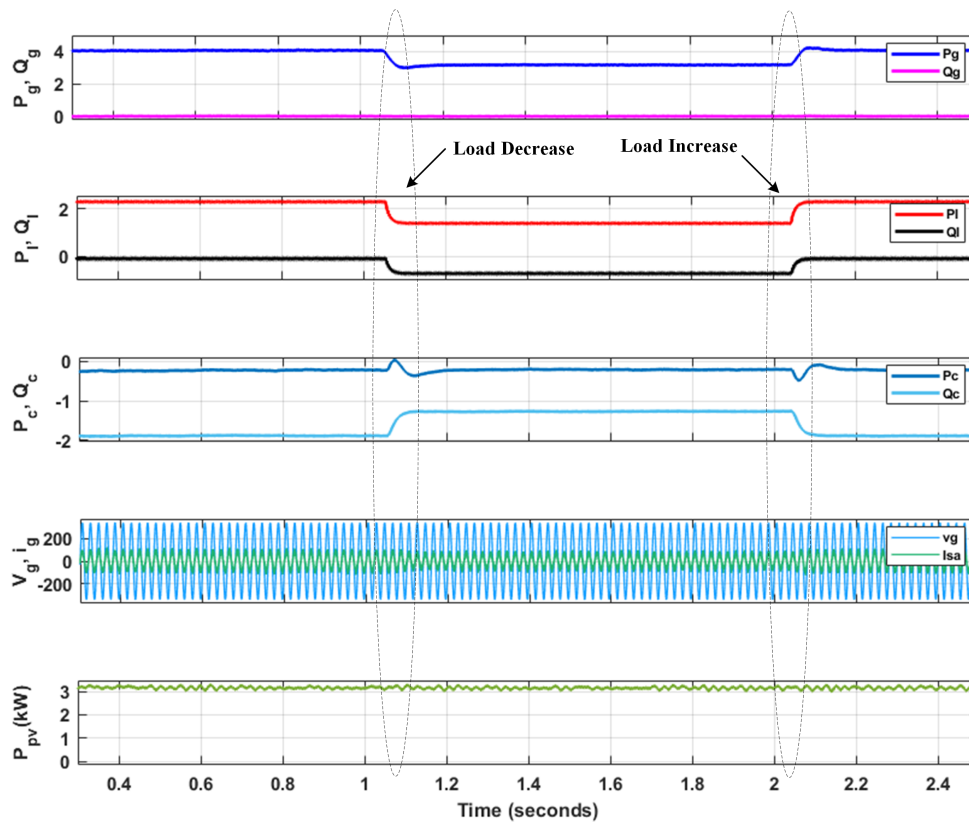
FIGURE 3.15:   Power flow response of the IRPT-based inverter control algorithm under varying load conditions.

3.4.2.3 Analysis of SRFT based Inverter Control Algorithm for Grid Connected PV System Under Constant Load Demand

The dynamic behavior of the grid-connected photovoltaic (PV) system controlled by the Synchronous Reference Frame Theory (SRFT) is demonstrated for varying levels of solar irradiance, specifically $1000\,\text{W/m}^2$, $600\,\text{W/m}^2$, and $400\,\text{W/m}^2$. The waveform plots indicate that the three-phase source voltages (v_{sa}, v_{sb}, and v_{sc})

remain balanced and purely sinusoidal with peak amplitudes close to ± 325 V, corresponding to an RMS voltage of about 230 V per phase. This confirms that the connection to the utility grid maintains stable voltage levels, and the inverter operation does not introduce any voltage distortion under different irradiance conditions as in Fig. 3.16.
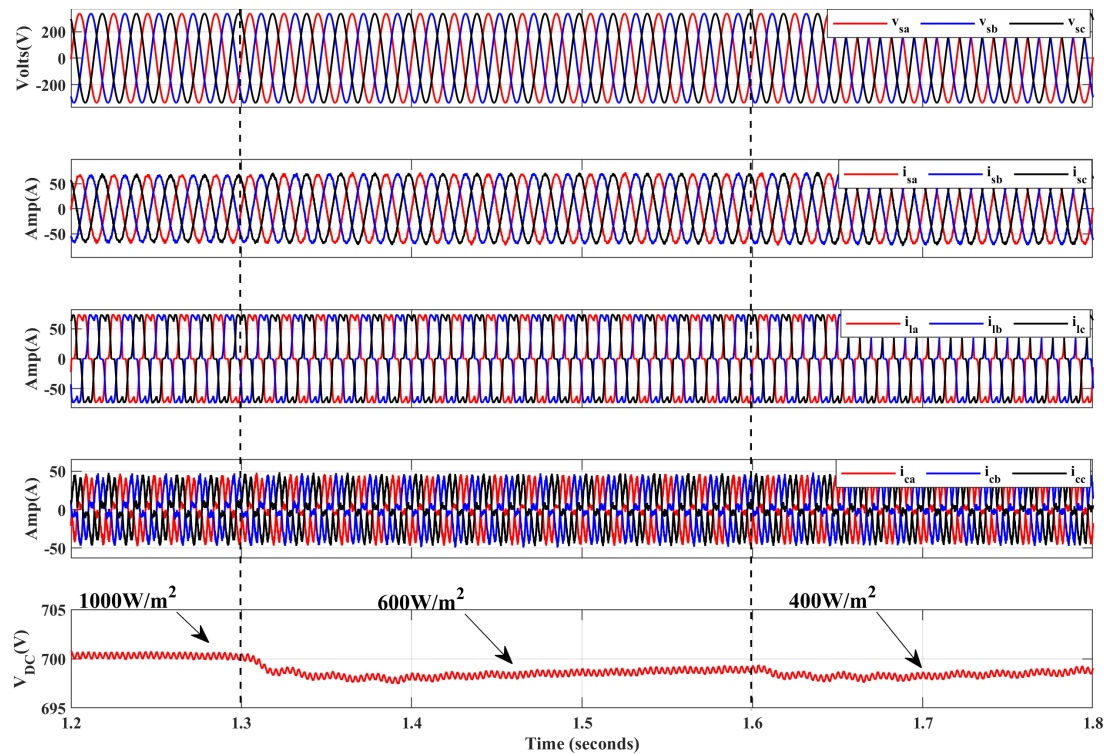
FIGURE 3.16: Analysis of grid voltage, grid current, load current, compensating current, and DC-link voltage using SRFT-based inverter control.

The three-phase source currents (i_{sa}, i_{sb}, and i_{sc}) exhibit an amplitude that changes proportionally with the available solar power. When the irradiance is 1000 W/m^2, the source current peaks at approximately ± 50 A. As the solar irradiance drops to 600 W/m^2, the source current magnitude reduces to around ± 35 A, and further decreases to approximately ± 25 A at 400 W/m^2. This demonstrates that the PV array generates less active power under reduced sunlight, and the controller responds accordingly by reducing the current drawn from the source while maintaining the sinusoidal shape and synchronization with the grid voltages. This behavior verifies the SRFT controller's capability to

Chapter 3. DESIGN AND ANALYSIS OF SOLAR PV SYSTEMS
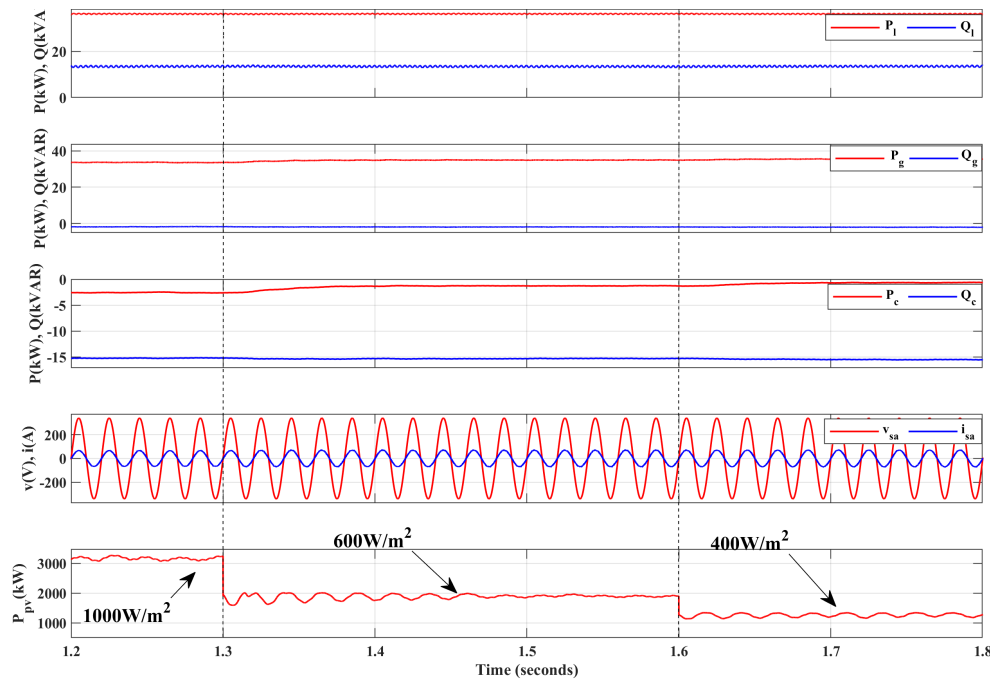
FIGURE 3.17: Waveforms of grid power (P_g), load power (P_l), compensating power (P_c), and PV power (P_{PV}) under varying irradiance with SRFT control.

ensure high power quality and unity power factor operation even during fluctuating power generation.

The load currents (i_{la}, i_{lb}, i_{lc}) remain nearly constant at ± 50 A, confirming steady load demand independent of PV variations. As PV power decreases, the grid compensates for the deficit without distortion in grid current waveforms.

The compensating currents (i_{ca}, i_{cb}, i_{cc}) adapt dynamically to ensure sinusoidal source currents and proper power sharing. At 1000 W/m^2, their peaks are ± 20 A, increasing to ± 35 A and ± 45 A at 600 W/m^2 and 400 W/m^2, respectively, thereby injecting the required harmonic and reactive components.

The DC-link voltage (V_{DC}) remains well-regulated, varying only from 703 V (1000 W/m^2) to 698 V (400 W/m^2), demonstrating the robustness of the controller and MPPT algorithm.

Overall, the SRFT-based control strategy ensures high-quality grid currents, stable DC-link voltage, and reliable PV grid power sharing under fluctuating irradiance, confirming its suitability for practical grid-connected PV applications.

Fig. 3.17 shows the performance of the SRFT-controlled grid-connected PV

system under irradiance levels of 1000, 600, and 400 W/m². Grid power (P_g, Q_g) remains stable as it compensates for reduced PV output, while load power stays constant at 40 kW and 2 kVAr. The inverter compensator injects about –5 kW and –15 kVAr, with active power decreasing as irradiance drops, but reactive compensation remaining steady.

The supply voltage stays sinusoidal (±325 V) and the current remains in phase, with amplitude reducing alongside PV power, indicating good power factor and harmonic control. PV generation drops from 3 kW to 1.2 kW as irradiance decreases. Overall, the SRFT controller ensures stable, high-quality power flow under varying solar conditions.

The harmonic spectrum shows a fundamental at 50 Hz with a THD of 4.03%. Higher-order harmonics are very low, confirming that the SRFT control keeps grid current nearly sinusoidal and within IEEE 519-2014 limits as in Fig. 3.18.
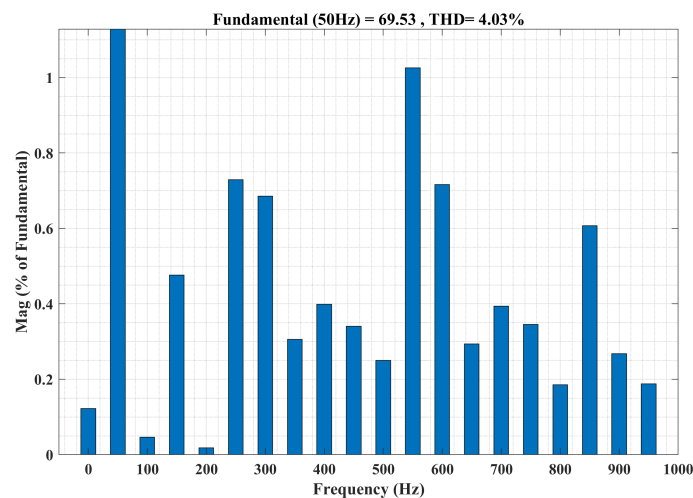
FIGURE 3.18: THD of grid current for non linear load using SRFT control

3.4.2.4 Analysis of SRFT based Inverter Control Algorithm for Grid Connected PV System under Varying Load Demand

The synchronous reference frame theory (SRFT) based inverter control algorithm is implemented and analyzed for a grid-connected photovoltaic (PV) system under varying load conditions. Two disturbance scenarios are considered: a sudden load decrease at $t = 1.0\,\text{s}$ and a load increase at $t = 2.0\,\text{s}$. The grid

Chapter 3. DESIGN AND ANALYSIS OF SOLAR PV SYSTEMS

voltage and current, load and compensating currents and dc link voltage are shown in Fig. 3.19.
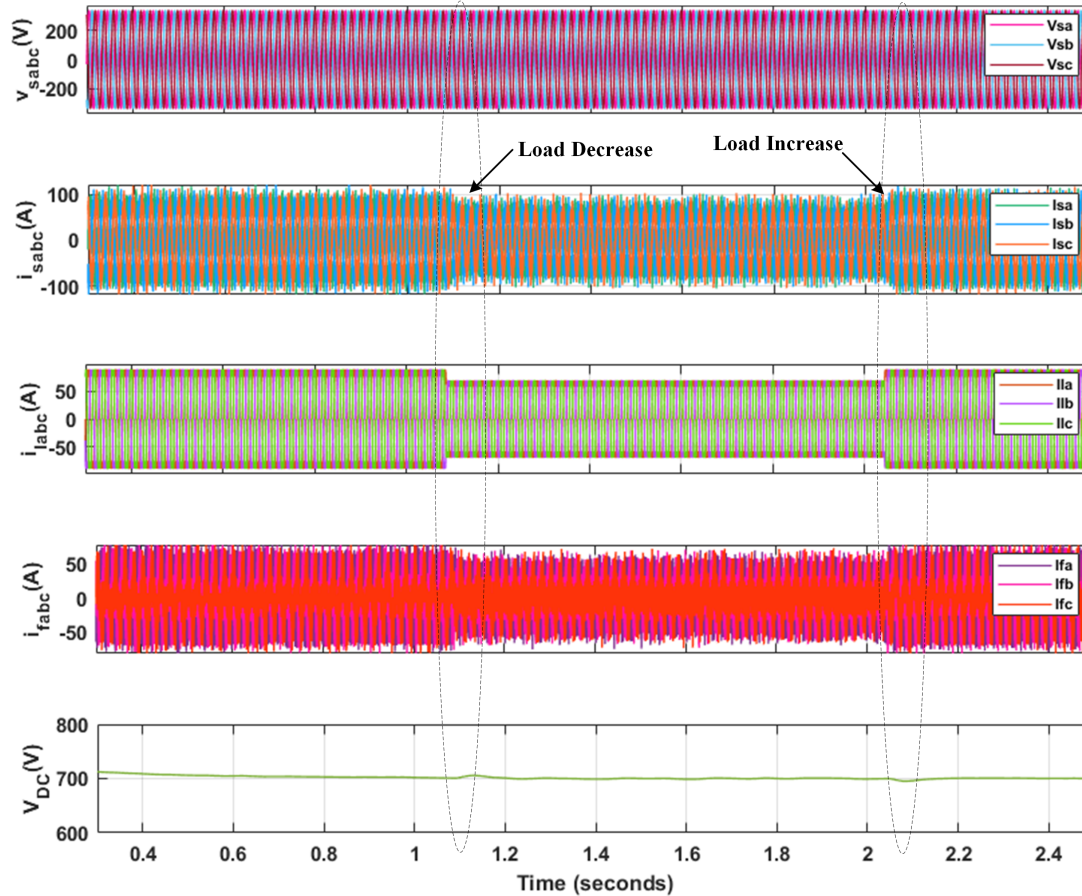
FIGURE 3.19: Voltage and current waveforms of the SRFT-based inverter control algorithm under varying load conditions.

Fig. 3.19 illustrates the three-phase grid voltages (V_{sa}, V_{sb}, V_{sc}) along with grid currents (i_{sa}, i_{sb}, i_{sc}), load currents (i_{la}, i_{lb}, i_{lc}), and filter currents (i_{fa}, i_{fb}, i_{fc}). It can be observed that the SRFT controller maintains nearly sinusoidal and balanced grid currents, even during load transients. The load decrease at $t = 1.0$ s results in a corresponding drop in current amplitude, while the increase at $t = 2.0$ s produces a proportional rise in current. The filter currents compensate effectively for harmonics and reactive components, ensuring the quality of grid currents. Moreover, the DC-link voltage (V_{dc}) is regulated around 700 V with only slight fluctuations during disturbances, confirming the stability of the SRFT algorithm.
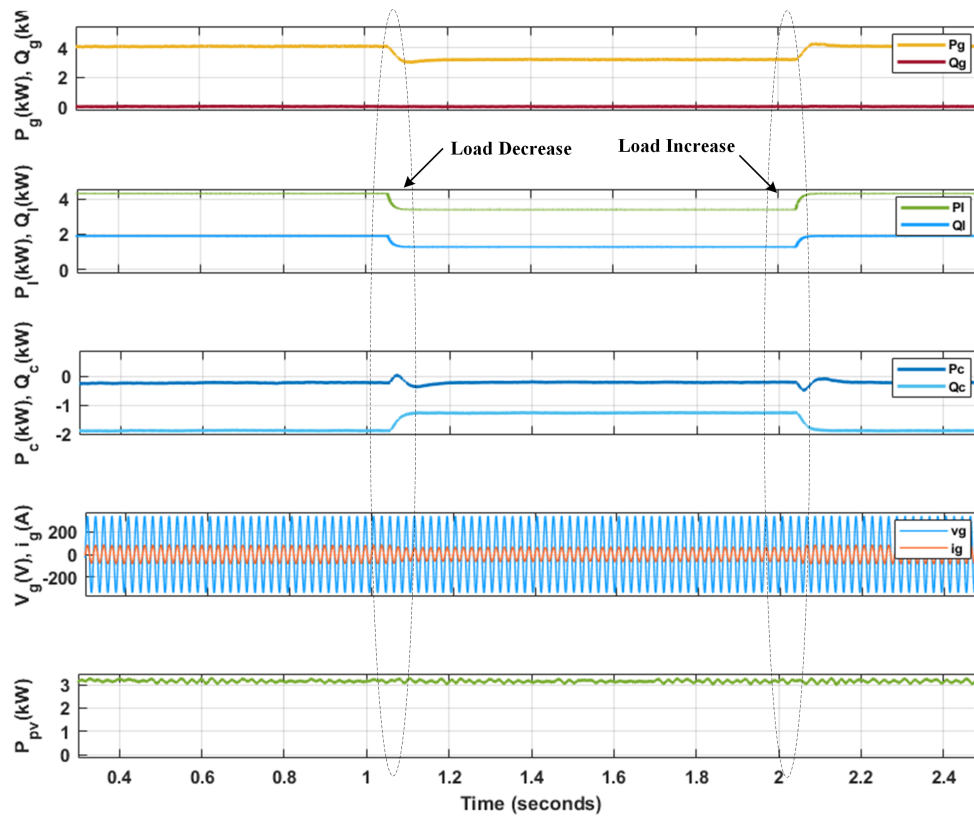
FIGURE 3.20: Power flow response of the SRFT-based inverter control algorithm under varying load conditions.

The power flow response in Fig. 3.20 shows the real and reactive power of the grid (P_g, Q_g), inverter (P_I, Q_I), and compensator (P_c, Q_c). During load reduction, both real and reactive power demand decrease, and the inverter lowers its contribution accordingly. When the load increases at $t = 2.0\,\text{s}$, the inverter quickly supplies additional real power to support the grid. The PV output (P_{PV}) remains nearly constant at about 3 kW, confirming that the SRFT controller efficiently utilizes PV power while maintaining power balance among grid and load.

3.4.2.3 Comparative Analysis of IRPT and SRFT Control Agorithms for Grid Connected PV System with FSSO MPPT Control

To evaluate the effectiveness of the implemented control strategies, a comparative analysis is carried out between the Instantaneous Reactive Power

70   *Chapter 3. DESIGN AND ANALYSIS OF SOLAR PV SYSTEMS*

Theory (IRPT) and Synchronous Reference Frame Theory (SRFT) controllers for the grid-connected PV system. Table 3.5 summarizes the key performance metrics, highlighting their behavior under varying irradiance conditions in terms of power quality, voltage stability, harmonic distortion, and overall control complexity.

TABLE 3.5: Comparison of SRFT and IRPT control strategies for grid-connected PV system with FSSO MPPT Control

Parameter	IRPT Control	SRFT Control
Grid Voltage	Balanced, sinusoidal	Balanced, sinusoidal
Source Current	Slightly more ripple	Highly sinusoidal, minimal ripple
Reactive Power	Less robust under varying irradiance	more accurate
DC-Link Voltage	Minor fluctuations	Very stable
THD	4.75%	4.03%
Power Control	Good, minor fluctuations	Smooth, minimal oscillations
Complexity	Simpler, uses $\alpha\beta$ frame	Requires PLL and dq transformation
Power Quality	Acceptable	Superior

3.5   Concluding Remarks

In this chapter, the design and simulation of stand-alone and grid-connected solar PV systems have been systematically carried out. The performance of conventional and intelligent MPPT techniques was compared, showing that the bio-inspired FSSO method achieved faster tracking and higher efficiency under varying irradiance levels. For grid-connected operation with FSSO MPPT Control, both SRFT and IRPT control strategies ensured acceptable power quality and stable inverter performance. However, the comparative analysis revealed that the SRFT control with FSSO MPPT provided superior harmonic

3.5. Concluding Remarks   71

suppression, more stable DC link voltage, and better overall power quality than the IRPT approach.

73

Chapter 4

TECHNO-ECONOMIC ANALYSIS OF SOLAR PV PLANT

4.1   Introduction

The previous chapter presented the design and simulation of stand-alone and grid-connected PV systems, comparing MPPT methods (P&O, FLC, and FSSO), where FSSO showed the best performance. For grid integration, SRFT and IRPT inverter controls were analyzed, with SRFT proving superior in terms of power quality, lower THD, and stable DC-link voltage.

In continuation, this chapter presents a comprehensive techno-economic analysis of grid-connected photovoltaic (PV) systems, focusing on both rooftop and floating configurations. It evaluates the performance of a 1.34 kW rooftop PV plant at Delhi Technological University and a 2 MW floating solar PV (FSPV) plant in Chandigarh. Using simulation tools, a detailed comparative study is conducted between monofacial and bifacial modules in floating installations, analyzing parameters such as energy generation, performance ratio (PR), efficiency, levelized cost of energy (LCOE), payback period, and CO_2 emission reductions. Unlike previous studies that often focus solely on monofacial systems or technical performance, this work adopts an integrated approach such as combining technical, economic, and environmental assessments to address existing research gaps and highlight the enhanced feasibility and benefits of bifacial floating PV technology for large-scale sustainable deployment.

4.2   Types of Solar Photovoltaic (PV) Plants based on Location

Solar photovoltaic (PV) systems are categorized based on their site of installation and structural configuration into two primary types: terrestrial solar PV plants and floating solar PV plants as in Fig. 4.1. Each type has specific technical, spatial, and economic considerations that influence its deployment and performance in different geographic and environmental settings [126, 127].
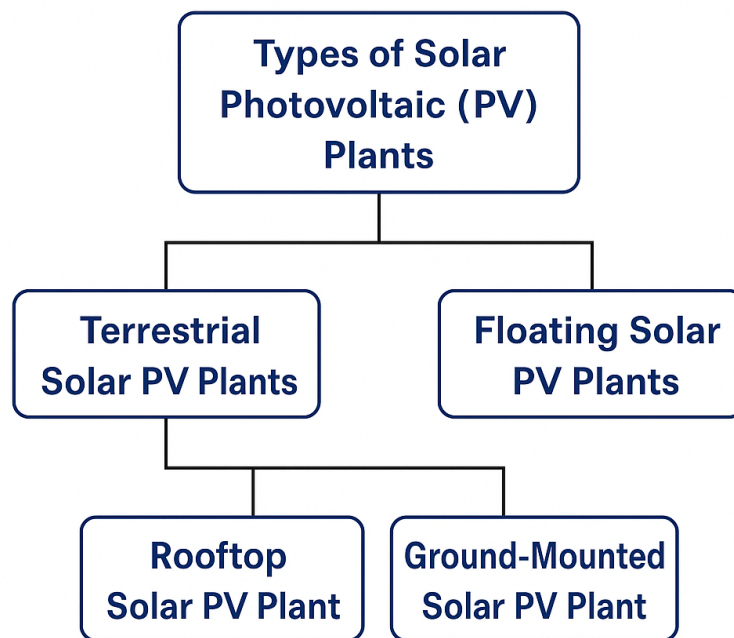
FIGURE 4.1: Classification of Solar Photovoltaic (PV) Plants

4.2.1   Terrestrial Solar PV Plants

Terrestrial PV systems are installed on land and can be further classified into the following two subcategories:

- **Rooftop Solar PV Plants:** These systems are mounted on the rooftops of residential, commercial, or institutional buildings. They are typically used for small- to medium-scale decentralized power generation, particularly in

urban and semi-urban areas. Rooftop systems are connected either to the grid or operate as standalone systems, depending on the application.

- **Ground-Mounted Solar PV Plants:** These installations are deployed on open plots of land, often optimized for utility-scale power generation. Ground-mounted systems require dedicated land, usually in rural or industrial areas, and involve higher capital investment due to site development and mounting infrastructure.

In the present study, only the rooftop solar PV plant configuration is considered for detailed analysis. This focus is driven by the growing relevance of rooftop systems in decentralized energy planning, particularly in urban environments where land availability is limited. Rooftop PV systems also support net metering policies and contribute significantly to national solar energy targets under missions such as the Jawaharlal Nehru National Solar Mission (JNNSM) [128].

4.2.2   Floating Solar PV Plants

Floating solar PV plants, also known as floating photovoltaic (FPV) systems, involve the installation of PV modules on floating platforms placed over water bodies such as reservoirs, lakes, ponds, or irrigation canals. This innovative approach leverages otherwise unused water surfaces for clean energy generation. Floating solar PV plants offer several advantages over terrestrial systems:

- **Efficient Land Use:** By utilizing water surfaces, FPV systems reduce the demand for scarce land resources, which is particularly valuable in densely populated regions or areas with limited available land.

- **Enhanced Performance:** The presence of water beneath the PV modules provides a natural cooling effect, reducing the operating temperature of the modules and improving their efficiency and lifespan.

- **Reduction of Water Evaporation:** FPV systems can help reduce water evaporation from reservoirs, contributing to better water resource management.

- **Synergy with Hydropower:** Floating solar installations on hydropower reservoirs can complement existing infrastructure, enabling hybrid energy generation and grid stability.

Despite these advantages, floating solar PV plants pose unique challenges, including the need for robust anchoring systems, potential impacts on aquatic ecosystems, and additional considerations for corrosion and maintenance in humid environments.

4.3   Key Components of Terrestrial and Floating Solar Power Plant

Both terrestrial and floating solar power plants have similar basic components needed to convert sunlight into electricity. However, each type has some unique parts and design requirements based on where and how it is installed. The main components are described below.

4.3.1   Photovoltaic Modules

PV modules are the primary components responsible for converting solar energy into direct current (DC) electricity through the photovoltaic effect. These modules are composed of multiple solar cells connected in series and/or parallel configurations to achieve the desired output power.

In this study, two different systems are considered: a rooftop PV plant and a floating solar PV (FSPV) plant. Both systems employ monocrystalline silicon technology but differ in the module types and configurations, as described below.

4.3.1.1 Rooftop Solar PV Plant Module

The rooftop PV system utilizes monocrystalline silicon PV modules, known for their higher efficiency and compact design. The selected module complies with international standards IEC 61730 and IEC 61215 [129]. The technical specifications of the module (ENVIRO PVM6-335) are provided in Table 1 in Appendix.

4.3.1.2 Floating Solar PV (FSPV) Plant Modules

Solar PV modules is one the root element of the FSPV plant. The PV modules can be classified as: Monofacial PV modules is capture sunlight only from the front side. They are simple and cost effective whereas bifacial PV modules are capture sunlight from both front and rear sides, taking advantage of reflected light from water, resulting in higher energy generation. The FSPV system incorporates both monofacial and bifacial PV modules, allowing a comparative evaluation of their performance under similar environmental conditions. Bifacial modules, equipped with a transparent backsheet or glass-on-glass construction, can capture reflected sunlight from the rear side in addition to direct irradiation on the front surface. This enhances their energy yield, particularly over reflective surfaces such as water.
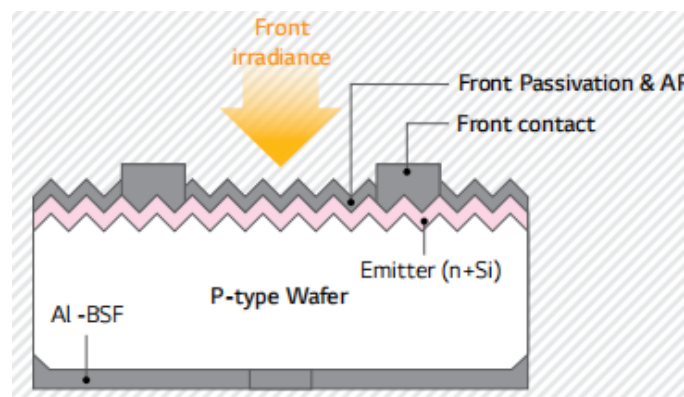
FIGURE 4.2: Construction structure of a monofacial PV module (FSPV plant).

Fig. 4.2 illustrate the basic structures of monofacial silicon solar cells, respectively. The monofacial solar cell is constructed using a p-type wafer with an n^+ emitter layer and a rear Al-BSF (Back Surface Field). It is designed to absorb light only from the front surface, and it includes a front surface passivation layer and an antireflection coating to enhance efficiency. In contrast, the bifacial solar cell, depicted in Fig. 4.3, uses an n-type wafer with p^+ emitter and n^+ BSF regions, and includes passivation layers on both the front and rear surfaces. This architecture enables it to absorb light from both sides, increasing the overall energy yield. These structural distinctions significantly impact the light absorption capability and energy conversion efficiency of the solar cells.
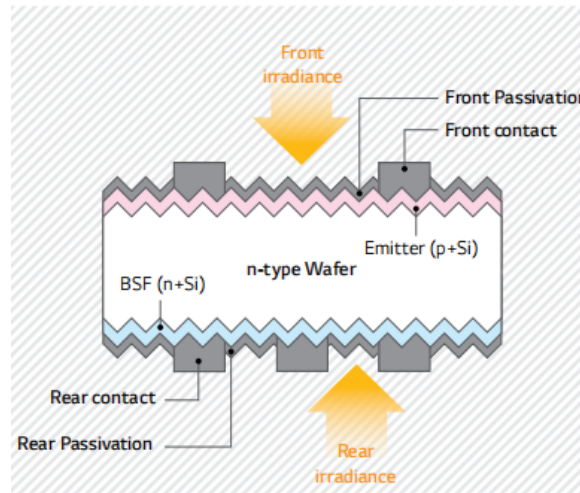
FIGURE 4.3: Construction structure of a bifacial PV module (FSPV plant).

The specifications of the monofacial and bifacial PV modules used in the study are shown in Table 2 in Appendix. Both modules have the same peak power of 540 Watt. However, the bifacial module has a higher open-circuit voltage and conversion efficiency. The bifacial module also features a bifacial factor of 70%, which allows it to harvest additional energy from the rear side. This characteristic enhances its energy yield, especially under high albedo or reflective surface conditions.

4.3.2   Solar PV Inverter

Photovoltaic (PV) inverters convert variable DC output from solar panels into AC for grid integration or local consumption. They ensure efficient energy conversion, maintain grid compliance, and support system stability. Modern inverters incorporate Maximum Power Point Tracking (MPPT) to maximize energy extraction, along with advanced grid features such as synchronization, fault detection, and power quality control. The technical specifications of inverters used in the rooftop and floating solar PV (FSPV) plants are summarized in Table 3 and 4, respectively in Appendix.

FIGURE 4.4: Mounting structures for terrestrial Plants

4.3.3   Mounting Structures

Mounting structures provide mechanical support and ensure stable, efficient operation of solar PV systems. Their design varies based on the installation type viz. terrestrial (ground-mounted or rooftop) or floating.

4.3.2.1 Terrestrial Plants

For ground-mounted systems, metal frames or trackers hold the PV modules at the right tilt and direction. Rooftop systems use racks fixed securely to building roofs, as in Fig. 4.4.

4.3.2.2 Floating Plants

Floaters, also called pontoons, are one of the main components of FSPV. It is a rugged structure that holds solar panels and other components during the entire project time.   Floaters are usually made of fiber-reinforced plastic (FRP), high-density polyethylene (HDPE), medium-density polyethylene (MDPE), polystyrene foam, hydroelastic floating membranes, or ferro-cements to provide sufficient buoyancy and stability to the entire system [100]. Different types of floaters are utilized for different FPV installations, based on factors such as geographical location, material availability, transportation options, construction

FIGURE 4.5: Floater structure made from high-density polyethylene (HDPE).

plans, and other relevant considerations. Fig. 4.5 is a floater which is made of HDPE material and was used at the study site.

4.3.4   Anchoring and Mooring System for FPV Plant

As floating solar PV modules and other equipment are placed in water bodies, they are susceptible to fluctuations in water levels that may arise from factors such as the monsoon, wind speed, or changes in the amount of water. To mitigate these challenges, FSPV plants are anchored and moored to prevent fluctuations in water levels. The optimal method for mooring an FPV depends on its location, soil quality, and water level. Among these factors, the anchor tension type is the most widely used method in FPV technology [130].

4.4   Performance Parameters of Solar PV plant

4.4.1   Technical Parameters

For assessing the effectiveness and economic viability of solar power plants, technical performance is crucial, encompassing factors such as energy production, yields, performance ratio, capacity factor, module and system efficiency, and array and inverter losses [131]. In this study, several parameters were employed to evaluate the performance of the grid-connected PV system.

4.4.1.1 Array Yield (Y_A)

The yield of a PV array is a measurement of the energy output in relation to the rated power output. It is commonly stated as a percentage of the array's daily, monthly, or yearly DC energy output to its rated power output, as specifed in equation (4.1). Numerous variables, including the weather, shade, orientation, and tilt of the array, might have an impact on this yield [132].

$$Y_A = \frac{E_A}{P_{\text{PV, rated}}} \tag{4.1}$$

where $P_{\text{PV, rated}}$ denotes the PV system's rated output power in kWp, and E_A is the total DC energy production from the PV arrays in kWh.

4.4.1.2 Final Yield (Y_F)

The final yield of a PV system can be obtained by dividing the total AC energy output over a specifc amount of time (daily, monthly, or annually) by the rated power output of the PV array, as stated in equation (4.2) [133].

$$Y_F = \frac{E_G}{P_{\text{PV, rated}}} \tag{4.2}$$

where E_G is the total AC energy output from the inverter in kWh, and $P_{\text{PV, rated}}$ is the rated output power of the PV system in kWp.

4.4.1.3 Reference Yield (Y_R)

The reference yield is calculated by dividing the total in-plane irradiance (H_t) by the PV reference irradiance (G_0). The maximum energy that can be produced under perfect circumstances is represented by this measurement, as described in equation (4.3). Y_R serves as an indicator of the solar radiation resources available to the PV system and is influenced by factors such as location, PV array orientation, as well as month-to-month and year-to-year variability [133].

$$Y_F = \frac{H_t}{G_0} \tag{4.3}$$

where, H_t is the total horizontal irradiance on the array plane (W/m^2) and G_0 is the global irradiance at the STC (W/m^2).

4.4.1.4 Performance Ratio (PR)

The performance ratio (PR) indicates the relationship between final yield (Y_F) and reference yield (Y_R), as stated in equation (4.4).

$$PR = \frac{Y_F}{Y_R} \tag{4.4}$$

The PR of a PV plant falls within the range of 60% to 90% due to the variability of the operating environment and system characteristics. A high PR indicates efficient functioning, as it signifies a significant proportion of incident solar energy being converted into usable electricity. Conversely, a low PR suggests significant losses or inefficiencies within the system [134].

4.4.1.5 Capacity Utilization Factor (CUF)

CUF is defined as the deviation between a plant's actual output and its theoretical maximum out-put, as given in equation (4.5) [135].

$$\text{CUF} = \frac{\text{Actual annual output in MWh}}{365 \times 24 \times \text{Installed capacity of plant (MW)}} \tag{4.5}$$

4.4.1.6 PV Array Efficiency (η_{PV})

Solar PV module efficiency is defined as its ability to convert solar energy into electrical energy, as given in equation (4.6) [133]:

$$\eta_{\text{PV}} = \frac{E_A}{A \times H_T} \times 100 \tag{4.6}$$

where E_A is the DC energy produced at the PV array (kWh), A is the total area covered by the PV module (m^2), and H_T is the net daily solar radiation falling on the PV module (kWh/m^2/day).

4.4.1.7 String Inverter Efficiency (η_{inv})

String inverter efficiency is the ratio of output AC energy (E_G) to input DC energy (E_A). E_G represents the energy produced at the grid side, while E_A is the energy produced at the PV array. This efficiency is given by equation (4.7) [136]:

$$\eta_{\text{inv}} = \frac{E_G}{E_A} \times 100 \tag{4.7}$$

4.4.1.8 System Efficiency (η_{sys})

System efficiency is the ratio of energy produced at the grid to the net daily solar radiation falling on the surface area of solar modules, as defined by equation (4.8) [133]:

$$\eta_{\text{sys}} = \frac{E_G}{A \times H_T} \times 100 \tag{4.8}$$

4.4.1.9 Array Capture Losses (L_A)

The losses incurred in array capture, denoted as L_A, signify the operational inefficiencies of the array, indicating its inability to fully harness the available irradiance. These losses are calculated as the variance between the reference yield and the array yield, as given in equation (4.9) [133]:

$$L_A = Y_R - Y_A \tag{4.9}$$

Array losses are typically related to PV module losses, such as soiling losses and incidence angle modifier (IAM) losses. IAM losses occur when the array surface is not perfectly perpendicular to the sun's rays, leading to energy losses due to reflection from the surface materials. Weather conditions at the site can further influence these losses.

4.4.1.10 System Losses (L_s)

System losses occur when DC energy is converted into AC energy. These losses are primarily attributed to the inverter and other system components, as defined in equation (4.10) [133]:

Chapter 4. TECHNO-ECONOMIC ANALYSIS OF SOLAR PV PLANT

$$L_s = Y_A - Y_F \tag{4.10}$$

System losses are significantly influenced by the efficiency of the system components, particularly the inverter.

4.4.2 Economic Parameters

Solar power plants are becoming increasingly popular as a source of renewable energy, and their economic analysis is an important consideration for invest in this technology. The total cost of the project, including installation, running costs, and maintenance, must be estimated accurately to calculate the LCOE and revenue generation potential [135]. The following are some key factors that are typically considered when conducting an economic analysis of a solar power plant.

4.4.2.1 Net Present Value (NPV)

The net present value (NPV) of a project's cash inflows and outflows during its lifetime is given by equation (4.11). A positive NPV indicates that the project is financially viable and can generate a return on investment over its lifetime. If the NPV is positive, the investment is economically acceptable; if it is negative, it is not [135].

$$\text{NPV} = \sum_{i=0}^{N} \frac{C_i}{(1 + D_r)^i} \tag{4.11}$$

where C_i is the net cash flow in time period i, D_r is the discount rate, and N is the total number of years in the PV system's lifetime.

4.4.2.2 Internal Rate of Return (IRR)

The internal rate of return (IRR) is the discount rate that makes the net present value (NPV) of the project's cash inflows equal to the net present value of its cash outflows, as shown in equation (4.12). In other words, it is the rate of return at which the project's NPV becomes zero. A higher IRR indicates a more profitable investment or project [135].

$$0 = \sum_{i=0}^{N} \frac{C_i}{(1 + D_r)^i} \tag{4.12}$$

4.4.2.3 Payback Period (PBP)

The payback period (PBP) is the duration required for a project to generate sufficient revenue to offset the initial capital expenditure. The payback period of a solar power facility is influenced by various factors, such as the plant's size and capacity, the expenses associated with equipment and installation, and the quantity of electricity produced and sold. Typically, the payback period for a solar power plant is between five and ten years. It is given by equation (4.13):

$$\text{PBP} = \frac{\text{Investment in project}}{\text{Annual savings}} \tag{4.13}$$

4.4.2.4 Levelized Cost of Energy (LCOE)

The levelized cost of energy (LCOE) is computed by dividing a power plant's lifetime electricity production by the total cost of constructing and maintaining that plant. The LCOE accounts for all costs associated with building and operating the power plant, including the initial capital cost, ongoing maintenance and operating costs, and the cost of fuel or other resources. It is given by equation (4.14):

$$\text{LCOE} = \frac{\text{Investment in project}}{\text{Generation of energy over lifetime}} \tag{4.14}$$

4.4.3 Environmental Impact and CO$_2$ Mitigation Potential of Solar PV Systems

A common misconception persists that solar photovoltaic (PV) systems are entirely emission-free. While this holds true during the electricity generation phase, it overlooks emissions generated across the full life cycle of the PV system. These include emissions associated with raw material extraction, module manufacturing, transportation, installation, routine maintenance, and eventual decommissioning [137, 138]. Consequently, any comprehensive

environmental assessment of solar PV technologies must account for these life-cycle emissions to accurately estimate their overall environmental impact.

To evaluate the environmental benefits of solar PV deployment, particularly in terms of carbon dioxide (CO_2) mitigation, a set of standard equations is employed. Equation (4.15) estimates the total CO_2 emissions resulting from the PV system itself, based on its life-cycle emission factor and annual energy generation. Equation (4.16) quantifies the potential CO_2 reductions achieved by offsetting grid electricity, while Equation (4.17) provides the net annual mitigation by subtracting the system's own emissions from the avoided grid emissions.

This analysis focuses solely on emissions from PV modules; emissions from other system components such as mounting structures, inverters, or floatation devices (in the case of floating solar PV systems) are not included.

$$\text{Annual } CO_2 \text{ emissions from PV plant} = E_A \times LC_e \tag{4.15}$$

$$\text{Annual } CO_2 \text{ reduction by PV plant} = E_A \times EF_G \tag{4.16}$$

$$\text{Net } CO_2 \text{ mitigation} = CO_2 \text{ reduction} - CO_2 \text{ emissions} \tag{4.17}$$

where E_A is the annual energy generation (kWh/year); LC_e is the life-cycle ; CO_2 emission factor of the PV module (kg CO_2/kWh); EF_G is the grid emission factor (kg CO_2/kWh).

For example, considering a grid emission factor of 0.936 kg CO_2/kWh and a module life-cycle emission factor of 0.049 kg CO_2/kWh, a PV plant with an annual energy output of 1,000,000 kWh would result in approximately 936 tonnes of avoided grid emissions and 49 tonnes of life-cycle emissions. Thus, the net annual CO_2 mitigation would be approximately 887 tonnes.

In addition to carbon-related benefits, floating photovoltaic (FPV) systems present unique interactions with the aquatic environment. Typically deployed on water bodies such as reservoirs, lakes, and irrigation tanks, FPV installations can affect ecological balance by limiting sunlight penetration—a critical factor for photosynthesis in aquatic ecosystems. While controlled shading may suppress

harmful algal blooms and improve water quality in drinking reservoirs, excessive shading might also hinder primary producers such as microalgae, potentially leading to reduced oxygen levels [139]. Therefore, the deployment of FPV systems necessitates careful ecological assessment and management strategies to ensure a balance between renewable energy production and aquatic ecosystem sustainability.

4.5   Description of Case Study Site

This section outlines the geographical and climatic characteristics of the selected case study sites for performance evaluation. A 1.34 kW rooftop solar PV system located at Delhi Technological University and a 2 MW floating solar PV (FSPV) plant in Sector 39, Chandigarh, have been considered. These sites represent distinct configurations are urban rooftop and large-scale floating facilitating a comprehensive comparative analysis under varying environmental conditions.

4.5.1   Site Description for Roof Top Plant

For this study, a grid-connected solar photovoltaic (PV) plant located in Delhi, India's capital city, has been chosen as the case study site. Delhi lies in northern India with a humid subtropical climate marked by hot summers, a moderate monsoon, and mild winters. The PV system is installed at the Rooftop of the Electrical Engineering Department of Delhi Technological University, representing a typical urban rooftop or ground-mounted installation. Geographically, Delhi is at about 28.6° N latitude and 77.2° E longitude, with an elevation of 216 meters. The site receives good solar radiation year-round, with an average daily global horizontal irradiance (GHI) of about 5.2 kWh/m²/day and an average temperature of 25 °C, providing favorable conditions for efficient solar power generation.

4.5.2   Site Description for FSPV Plant

For analysis of FSPV, a 2 MW FSPV sited in Sector 39, Chandigarh, was selected as the focus area for this case study. Located in the western part of Chandigarh, it

is approximately 8 km from the city center as in Fig. 4.6.
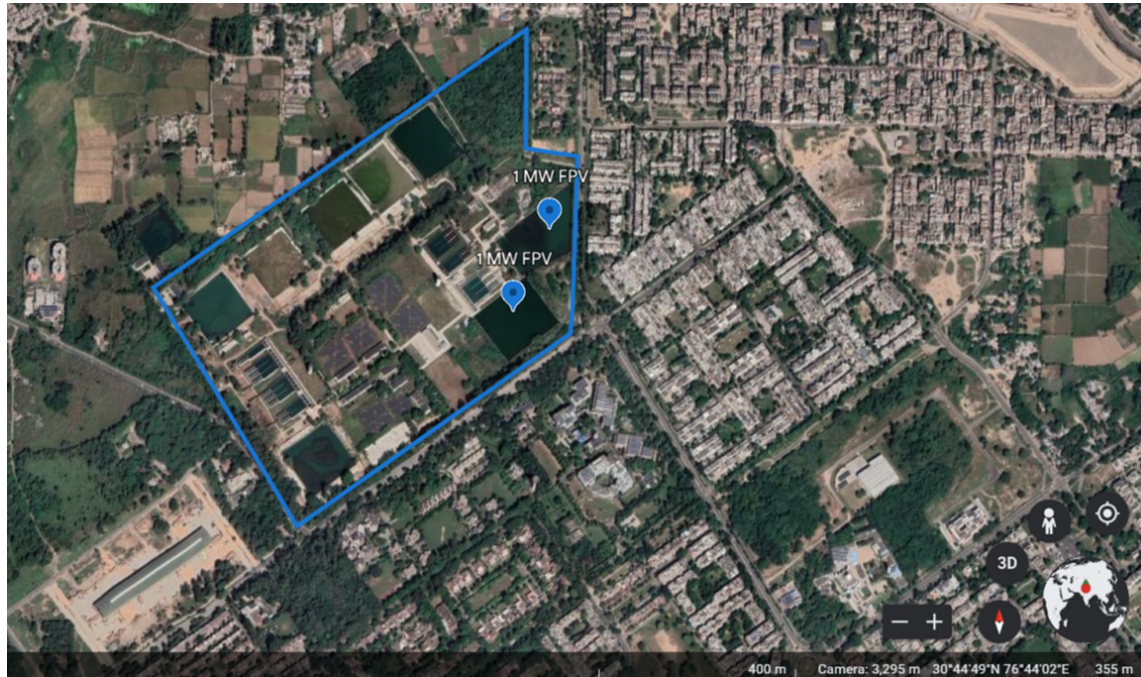
FIGURE 4.6: Geographical map location of study area from google Earth.

The site's geographic coordinates are 35° 75′ 22″ latitude and 76° 72′ 85″ longitude. The waterworks depicted in Fig. 4.6 covers an area of 0.45 km^2. The daily average global horizontal irradiance (GHI) is 4.09 kWh/m^2, the average wind speed is 7.5 m/s, and the ambient temperature is 23.8 °C at the site of installation. The solar radiation, temperature, and velocity of wind data for Chandigarh taken from Metronorm 8.1 software has presented in Appendix **??**.

4.6   Performance Evaluation of Roof Top SPV Plant

This section presents a performance evaluation of a 1.34 kW grid-connected rooftop PV system at Delhi Technological University (DTU), New Delhi, based on monitored data from February–August 2023 and February–August 2024. The study analyzes the system's operational behavior and performance trends under real environmental conditions.

4.6.1   Technical Analysis

Delhi Technological University (DTU), located in north-west Delhi with a humid subtropical climate, provided solar irradiation and ambient temperature data via the plant SCADA system over 211 days across two years. As the rooftop system primarily monitors AC-side data, DC-side parameters such as array yield (Y_A), final yield (Y_F), reference yield (Y_R), PV module efficiency, and inverter efficiency could not be obtained. Consequently, performance evaluation is based on available metrics: monthly energy generation, performance ratio (PR), capacity factor (CF), and overall system efficiency.

4.6.1.1 Irradiations and Temperature

Fig. 4.7 illustrates the comparison of solar irradiation and ambient temperature (in °C) from February to August for the years 2023 and 2024.
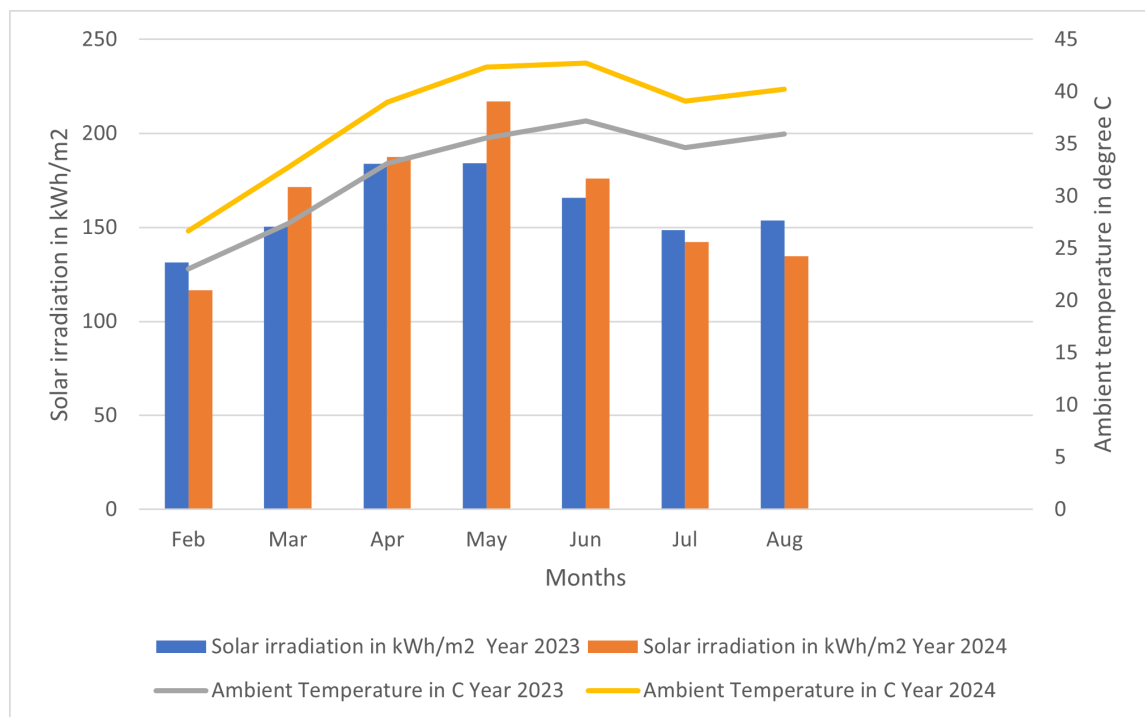

FIGURE 4.7: Solar irradiation and ambient temperature data of experimental location

Solar irradiation in year 2023 is consistently higher across all months compared to year 2024. In year 2023, irradiation values increase from February, peak in May, and gradually decline towards August. This trend reflects the seasonal variation of solar insolation, with May typically receiving the highest irradiation due to longer daylight hours and clearer skies. Similarly, in year 2024, solar irradiation follows the same seasonal pattern but remains lower throughout the observed period.

In year 2023, the higher solar irradiation coincides with relatively lower ambient temperatures, creating favorable conditions for efficient photovoltaic (PV) operation. Conversely, in year 2024, despite slightly reduced irradiation, the higher ambient temperatures likely further diminish PV efficiency, underscoring the importance of temperature management in PV system design.

Ambient temperatures in year 2023 gradually rise from February, peak around May-June, and slightly decline by July-August, reflecting typical seasonal weather patterns. In contrast, year 2024 experiences consistently higher ambient temperatures than year 2023, particularly from April to June, with a more pronounced peak in May-June. This suggests the possibility of increased heatwaves or warmer weather conditions during this period. The elevated temperatures in year 2024 may negatively impact solar PV performance, as high module temperatures are known to reduce efficiency.

4.6.1.2 Energy Generation

Fig. 4.8 compares monthly energy generation (kWh) from a 1.34 kW system between years 2023 and 2024. In 2024, energy production is more consistent, slightly surpassing year 2023 from February to June but dipping in August. Notably, July 2024 shows a significant improvement (150 kWh) over year 2023 (110 kWh), while April and August 2023 exhibit higher peaks (180–200 kWh). The trends suggest seasonal variability, with higher generation during longer daylight months. Overall, the year 2024 performance indicates greater stability, though the year 2023 system outperformed in peak months like April and August.

4.6. Performance Evaluation of Roof Top SPV Plant

91
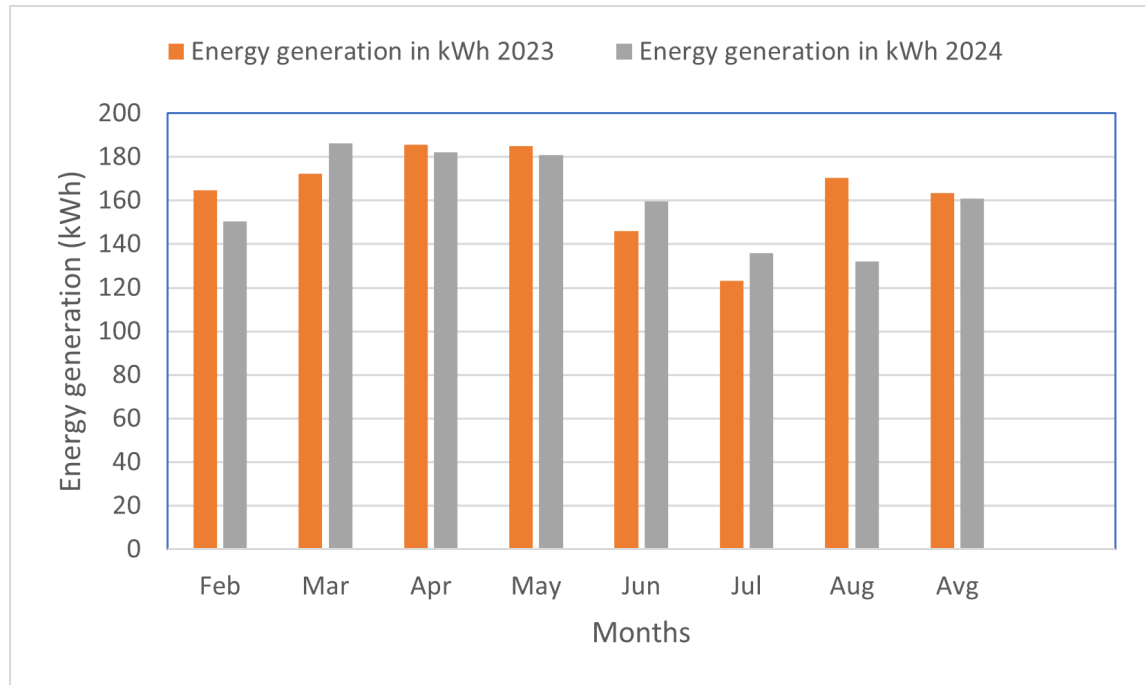
FIGURE 4.8: Monthly energy generation by the 1.34 kW SPV plant

4.6.1.3 Performance Ratio

Fig. 4.9 compares the monthly performance ratios (PR) for a 1.34 kW solar power plant between years 2023 and 2024. Across the months from February to August, the data reveal notable variations in PR, reflecting differences in system efficiency or external conditions impacting energy output.

In February, both years exhibit high PRs, with years 2023 slightly outperforming year 2024. This trend continues in March, where the performance ratio in year 2023 remains superior, though both years show a consistent decrease. April and May highlight a significant drop in year 2024 compared to year 2023, with May showing the largest performance gap. From June to August, the performance ratio in year 2024 improves, closing the gap with year 2023 but still generally remaining lower. However, August presents a slight exception, as both years perform similarly.

When averaging across all months, year 2023 shows a higher overall PR than year 2024, indicating better operational efficiency or favorable conditions for energy production during the earlier period. The fluctuation in PR across both years suggests that seasonal variations, maintenance practices, or external
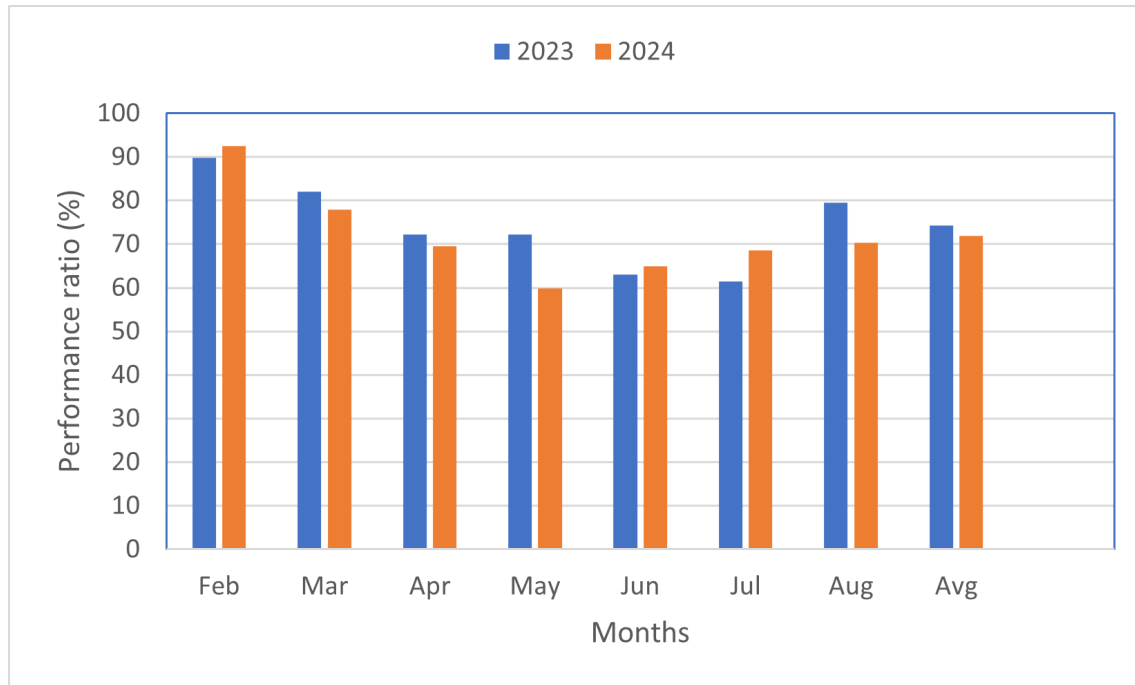
FIGURE 4.9: Monthly performance ratio of 1.34 kW plant

environmental factors might have influenced the solar plant's overall performance.

4.6.1.4 Capacity Factor

Fig. 4.10 illustrates the capacity factor (CF) of a 1.34 kW solar power plant for the period from February to August, comparing data between years 2023 and 2024. The capacity factor is generally higher in year 2023 than in year 2024, reflecting better system utilization or more favorable environmental conditions in the earlier year. February starts with similar CFs for both years, but from March onward, year 2023 consistently outperforms year 2024, with noticeable differences in May and June, where the year 2023 values are particularly higher. In July and August, the trend remains, though the gap narrows in August, where the year 2024 CF approaches that of year 2023. On average, year 2023 exhibits a higher overall capacity factor than year 2024, suggesting reduced efficiency or lower solar insolation in the latter year. These trends may indicate seasonal effects or system-related factors that require further investigation for optimization of performance in year 2024.

The major variation in the performance ratio and capacity factor of the plant mainly depends on the total energy generation of the PV plants. The performance ratio is directly correlative to the solar irradiation fall on the surface of the PV modules. On the other hand, the capacity factor of the plant depends on the running time of the plant.
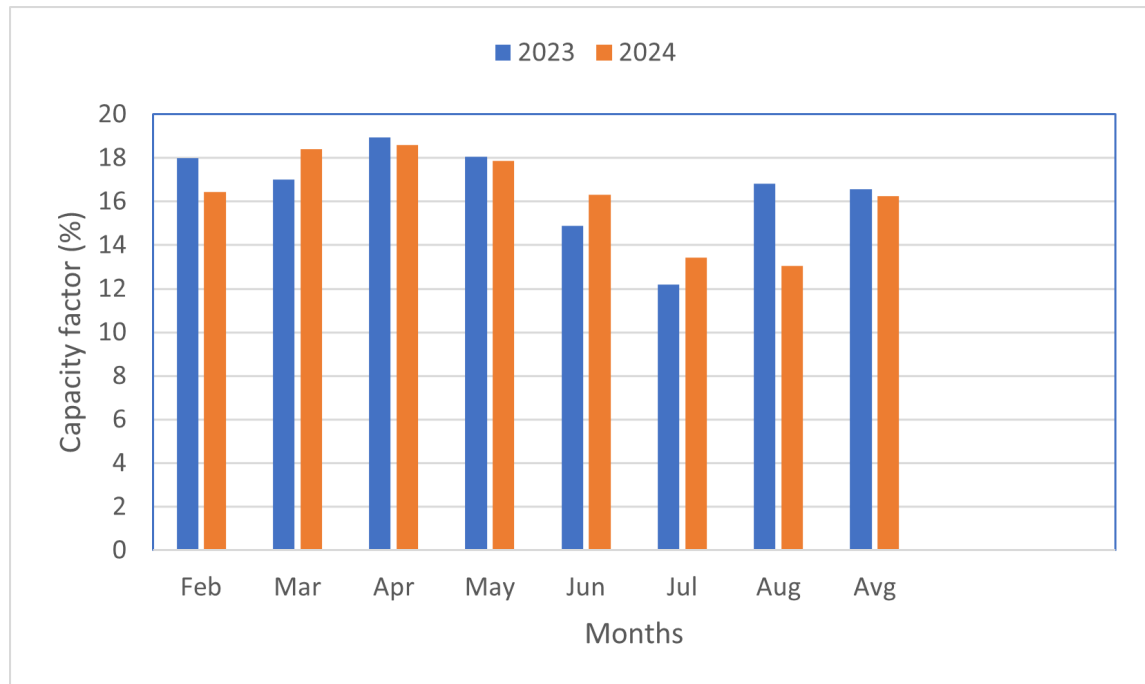
FIGURE 4.10: Monthly capacity factor of 1.34 kW SPV plant

4.6.1.5 System Efficiency

Fig. 4.11 compares system efficiency (%) between year 2023 and year 2024 across the months from February to August and shows a slight overall decline in efficiency in year 2024. While February exhibited similar high efficiency for both years, with values around 16%, there was a noticeable drop in efficiency in year 2024, especially from April to June, where the plant's performance significantly lagged behind year 2023. In contrast, March and July saw relatively smaller differences between the two years. The average plant efficiency across the months was higher in year 2023, indicating an overall reduction in year 2024 performance. This suggests that operational or external factors may have impacted the plant's efficiency more in year 2024.
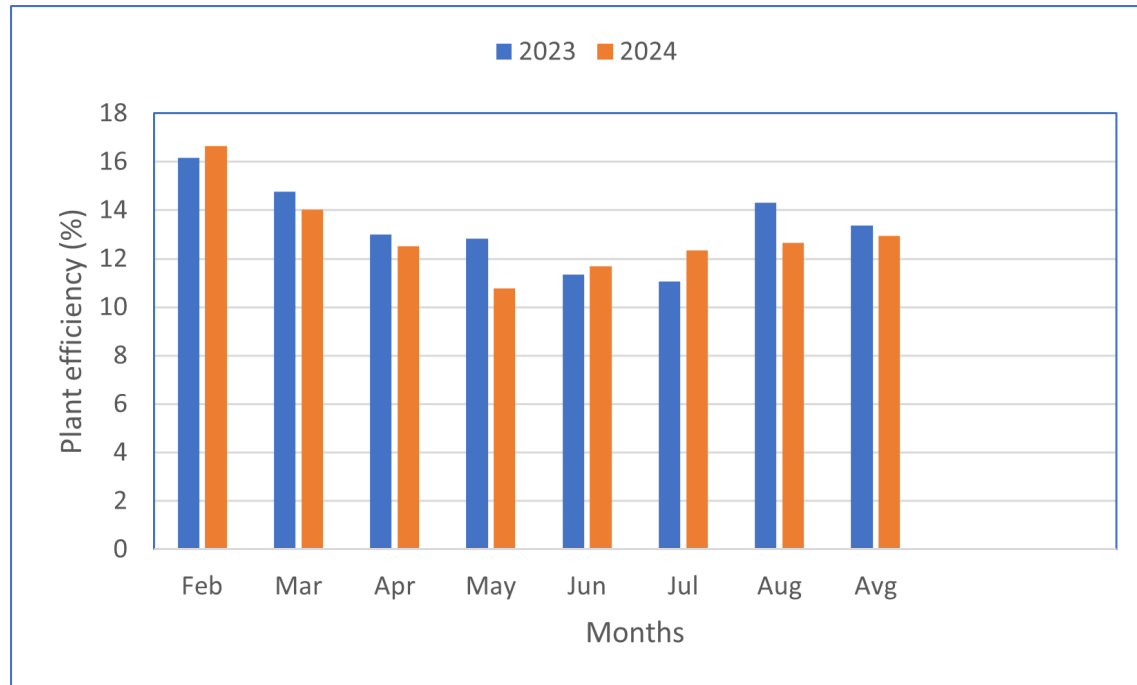
FIGURE 4.11: Monthly system efficiency of the 1.34 kW plant

4.6.2   Economic Analysis

A comprehensive economic analysis has been conducted to evaluate the financial analysis of the 1.34 kW rooftop solar photovoltaic (PV) system installed at the Electrical Engineering Department of Delhi Technological University.   The analysis considers actual capital expenditure, estimated annual cost savings, payback period, and the levelized cost of electricity (LCOE) over the system's operational lifetime.

4.6.2.1 Annual Energy Generation

Based on the monitored performance data, the rooftop PV system generates an average of approximately 163.53 kWh per month, resulting in an estimated total annual energy generation of about 1144.65 kWh.

4.6.2.2 Net Present Value (NPV)

The Net Present Value (NPV) is used to assess the economic viability of the rooftop PV system by comparing the present value of future cash inflows with

the initial investment. Assuming an annual savings of 13,440 INR, for a system lifetime of 25 years, and a discount rate of 8%, the NPV is calculated using standard discounted cash flow analysis. The resulting NPV is approximately 11,841 INR, indicating that the project is financially feasible. A positive NPV confirms that the investment will yield returns above the assumed cost of capital over its operational life, thereby supporting its long-term economic justification.

4.6.2.3 Capital Cost and Payback Period Analysis

The total capital cost for the installation of the 1.34 kW rooftop solar photovoltaic (PV) system is estimated to be 120,000 INR. This investment covers the procurement of PV modules, inverter, mounting structures, electrical wiring, labour charges, and system commissioning.

Based on the monitored performance, the system generates an estimated 1144.65 kWh of electricity per year. Considering an average electricity tariff of 7 INR per kWh in Delhi, the resulting annual savings are calculated as follows:

$$\text{Annual Savings} = 1,920 \text{ kWh/year} \times 7 \text{ INR per kWh} = 13,440 \text{ INR per year}.$$

Accordingly, the simple payback period for the rooftop PV system is determined by dividing the total capital cost by the annual savings:

$$\text{Payback Period} = \frac{120,000}{13,440} = 8.9 \text{ years}.$$

This indicates that the initial investment can be recovered in approximately nine years through savings on electricity bills. The payback duration may be further reduced if government subsidies, incentives, or net metering benefits are availed.

4.6.2.4 Internal Rate of Return and Levelized cost of energy

The IRR for the rooftop plant is 11% , indicating project yields around a 10% return per year over its life. The Levelized Cost of Electricity (LCOE) is an important parameter for assessing the long-term economic competitiveness of

the PV system. It represents the average cost per unit of electricity generated over the system's lifetime. The LCOE for this plant is 3.13 INR per kWh.

4.6.2.5 Reduction in Carbon Emission

The 1.34kW rooftop solar photovoltaic (PV) system significantly contributes to the reduction of carbon emissions by generating clean and renewable electricity, thereby reducing dependency on fossil fuel-based power sources. Based on the average grid emission factor in India, which is approximately 0.82 kg of CO_2 per kilowatt-hour (kWh), the system helps in avoiding around 1,574 kg of CO_2 emissions annually. Over its expected operational lifetime of 25 years, this leads to an estimated total mitigation of approximately 39 metric tonnes of CO_2. Such reductions play a vital role in combating climate change and support national and global efforts toward achieving sustainable and low-carbon energy systems.

4.7   Performance Evaluation of FSPV Plant

The PVsyst software is utilized for modeling and simulating the proposed FSPV plant, incorporating PV modules, inverters, and grid interface circuits. It is specifically designed to assist in system design and accurately estimate energy output while accounting for the influence of geographical and climatic conditions. The software provides detailed monthly insights into parameters such as energy yield, system losses, performance ratio, and overall efficiency.

PVsyst supports customization of system parameters and offers flexibility in selecting component configurations, tilt angles, orientations, and design constraints. It is widely used in both academic research and industrial applications for evaluating PV system performance prior to installation. These steps are depicted in the flowchart as shown in Fig. 4.12. The simulation methodology is structured into three primary steps: project definition, system variant creation, and simulation with results analysis.

1. **Project Definition**: Navigating to the project design menu, inputting location and meteorological data, and creating a new project for a grid-connected PV system.
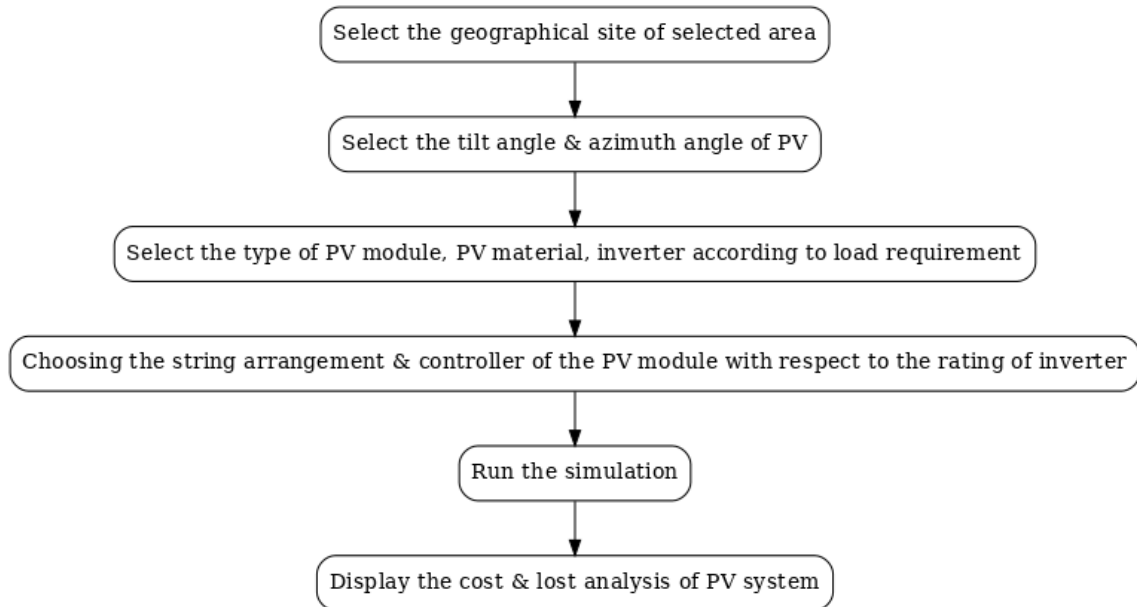
FIGURE 4.12: Flow chart of PVsyst software

2. **Creating a System Variant**: Specifying system design details, including PV module selection, orientation, installation parameters, system sizing, load profile, and inverter characteristics.

3. **Simulation and Analysis**: Executing simulations using the defined system variant, generating performance reports and graphical results. This stage provides a detailed evaluation of energy generation and system behavior, discussed in subsequent sections.

4.7.1   Technical Analysis

The findings from the $FSPV_M$ and $FSPV_B$ installations are based on simulated data, utilizing equipment specifications tailored to each plant. In the absence of an actual $FSPV_B$ system operating under comparable environmental conditions, simulations were employed for both monofacial ($FSPV_M$) and bifacial ($FSPV_B$) configurations. These simulations were carried out using PVsyst software, providing a comprehensive assessment of key performance indicators such as energy generation, performance ratio, system efficiencies, and greenhouse gas

TABLE 4.1: Energy production evaluation for monofacial module
with different tilt angles

Tilt angle in (°)	Global Irradiations on PV Module	Yearly energy produced	IAM factor (%)	L_A	L_S	PR (%)	CUF (%)
5°	1467.7	2103.2	-2.82	1.05	0.08	66.69	12
10°	1503.9	2154.7	-2.60	1.08	0.08	66.83	12.29
15°	1531.4	2193.7	-2.41	1.10	0.09	66.95	12.51
20°	**1550**	**2220.1**	**-2.25**	**1.12**	**0.09**	**67.05**	**12.67**
25°	1559.4	2233.5	-2.12	1.12	0.08	67.14	12.74
30°	1559.6	2234.1	-2.04	1.12	0.09	67.20	12.75
35°	1550.6	2221.7	-2.01	1.11	0.09	67.24	12.68

(GHG) emissions. Additionally, the study includes an economic evaluation of the proposed systems.

4.7.1.1 Monofacial Floating Solar Power (FSPV$_M$) Plant:

Table 4.1 displays the maximum energy output of monofacial modules at various tilt angles. The recommended tilt angle for solar modules is influenced by the site's latitude, generally aligning them with the latitude to optimize direct sunlight absorption. The highest energy output, totaling 2234.1 MWh, is observed at a 30° tilt angle. Deviating from this angle, above or below, results in reduced annual energy production. In FPV plants, the tilt angle may be constrained by floating structure design and wind load impact. Typically, FPV plants opt for tilt angles not exceeding 20° to mitigate wind load effects on solar modules. Consequently, a 20° tilt angle is chosen for this specific monofacial floating solar power plant.

   Fig. 4.13 depicts the energy at PV array (E_A) and energy at grid (E_G) values of the FSPV$_M$ plant, influenced by its specific design, configuration, and installation conditions. In May, the FSPV$_M$ plant reached its maximum E_A of 231.9 MWh, attributed to increased solar irradiance, while January saw the minimum E_A of
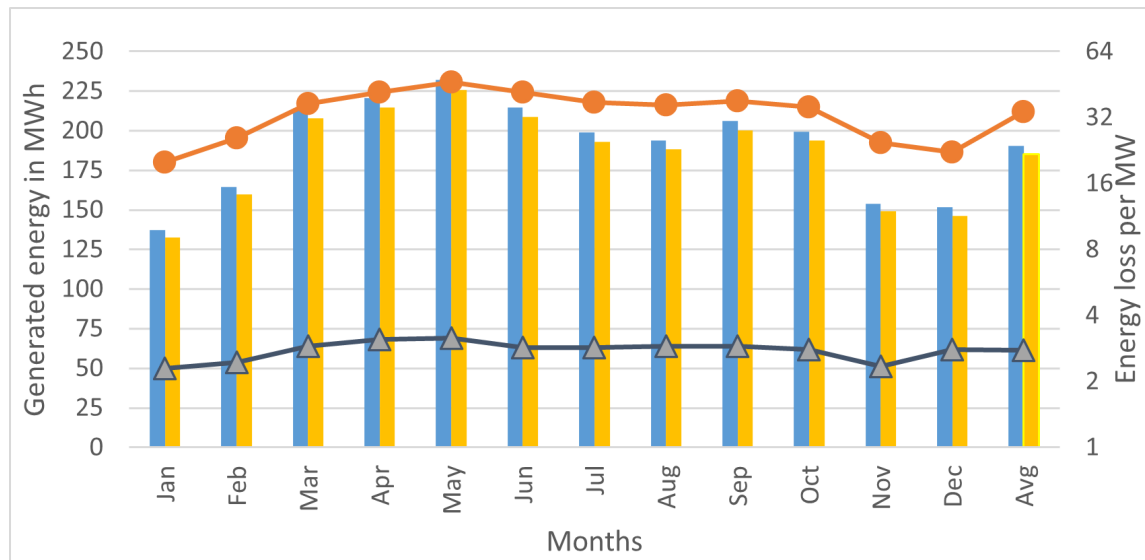
FIGURE 4.13: Energy produced at array (E_A), energy supplied to grid (E_G), array capture loss (L_A) and system loss (L_S) for $FSPV_M$ plant.

137.3 MWh due to lower solar irradiance. The annual averages for energy production at the PV array and energy generated at the grid are 190.49 MWh and 185 MWh, respectively. Array losses (L_A) and system losses (L_S) were analyzed using PVsyst software, revealing reduced losses during low insolation periods from November to February. The higher losses were observed from March to September, correlating with increased monthly insolation during the hot season in Chandigarh, India.

The analysis identified the highest array loss (46.35 MWh/MW) and system loss (3.15 MWh/MW) in May, correlating with more sunlight hours and intense sunlight. The lowest array loss occurred in January, with an average PV array loss of 33.89 MWh/MW and a system loss of 2.77 MWh/MW. Array losses in orange are likely associated with PV module factors influenced by weather conditions, while system losses in grey are linked to equipment efficiency unaffected by seasons.
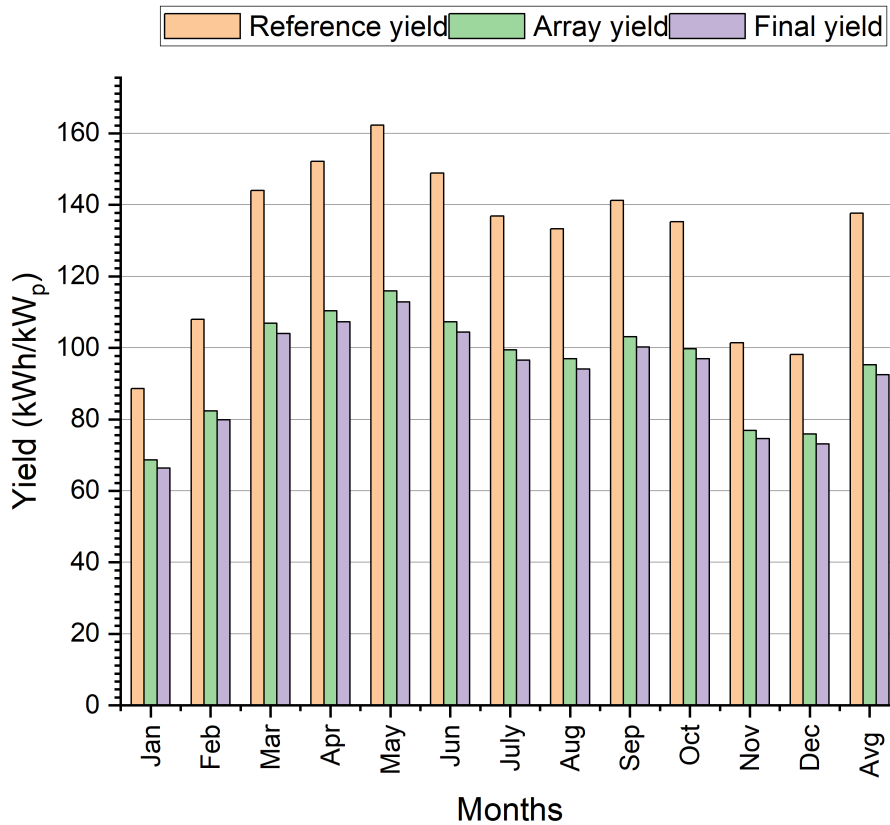
FIGURE 4.14: Monthly values of Y_A, Y_R and Y_F in FSPV$_M$ plant.

Fig. 4.14 illustrates the average array, final, and reference yields for the FSPV$_M$ plant. The array yield (Y_A) peaks in May at 115.95 kWh/kWp and reaches a low of 68.65 kWh/kWp in January. The final yield (Y_F) varies from 66.35 kWh/kWp in January to 112.8 kWh/kWp in May. Similarly, the reference yield (Y_R) ranges from 88.6 kWh/kWp in January to 162.3 kWh/kWp in May. The annual averages for Y_R, Y_A, and Y_F are 137.64 kWh/kWp, 95.27 kWh/kWp, and 92.50 kWh/kWp, respectively.

The yield analysis of the FSPV$_M$ plant reveals a clear seasonal trend, with the highest energy yields observed in May and the lowest in January, corresponding to variations in solar irradiance. The close alignment between the array yield and final yield throughout the year indicates efficient system performance, while the gap between reference and final yields highlights system losses. Overall, the plant demonstrates strong annual performance with an average final yield of

4.7. Performance Evaluation of FSPV Plant   101
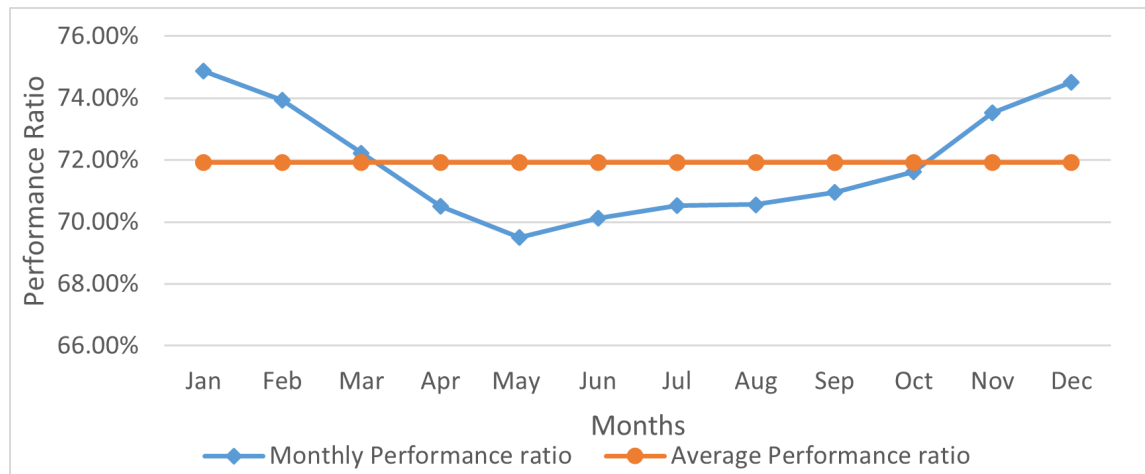
FIGURE 4.15: Monthly performance ratio of FSPV$_M$ plant of 2 MW.

92.50 kWh/kWp, affirming its effectiveness in converting available solar energy into usable output.

In Fig. 4.15, the average performance ratio of FSPV$_M$ plants is shown as 71.90%, with peak performance observed from October to February. January recorded the highest PR at 74.88%, while May had the lowest at 69.51%. Solar module efficiency may decline in the summer due to higher temperatures, as they typically operate more efficiently at around 25°C. Beyond this temperature, their efficiency begins to decrease.

Fig. 4.16 illustrates the monthly efficiency trends of the PV array, inverter, and overall plant. Array efficiency was highest in January (16.19%) due to lower cell temperatures, and lowest in May (14.93%) owing to thermal losses. Inverter efficiency peaked in June at 97.35%, with the lowest in January (96.65%). Plant efficiency followed a similar pattern, ranging from 15.65% in January to 14.53% in May. The annual average efficiencies were 15.41% for the array, 97.13% for the inverter, and 14.97% for the plant.

The overall plant efficiency is closely linked to PV module efficiency, which declines with increasing cell temperature due to the negative temperature coefficient of the modules. During peak summer (May), ambient temperatures can soar up to 60°C, raising cell temperatures and reducing efficiency to 14.93%. Conversely, in cooler months like January and December, reduced thermal stress enhances performance, with peak efficiency reaching 16.19%.
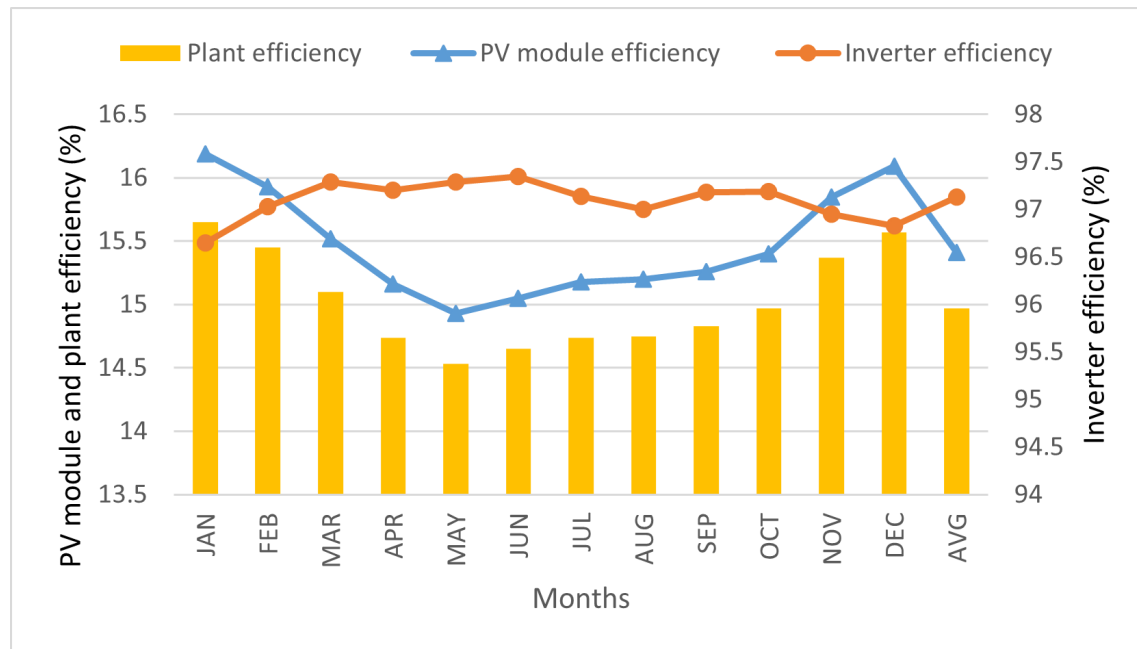
FIGURE 4.16: Monthly PV module, inverter and system efficiencies
of FSPV$_M$ plant.

Additionally, soiling from dust accumulation further impacts efficiency. In May, higher dust levels combined with inadequate cleaning lower system performance, while cleaner module surfaces during winter months contribute to improved efficiency.

4.7.1.2 Bifacial Floating Solar Power (FSPV$_B$) Plant:

Table 4.2 shows the maximum energy output of bifacial modules at various tilt angles, with the optimal angle determined by the site's latitude. Aligning modules with the latitude is recommended for maximum sunlight absorption. The highest energy output, 2890.7 MWh, occurs at a 25° tilt angle. Deviating from this angle reduces annual energy production. However, for FSPV$_B$ plants, the tilt angle may be limited to mitigate wind load and bifacial factors leading to the selection of a 20° tilt angle for this specific PV plant.

The energy production by the array (E$_A$) and the energy supplied to the grid (E$_G$) in the FSPV$_B$ plant. The FSPV$_B$ plant reached its peak E$_A$ value of 297.9 MWh in May, attributed to higher solar irradiance, and the lowest E$_A$ value of 175.8 MWh in January, due to lower solar irradiance as depiced in Fig. 4.17.

TABLE 4.2: Performance and energy metrics at different tilt angles

Tilt Angle (°)	Global Incident in Coll. Plane	Yearly Energy Produced	IAM Factor (%)	L_A	L_S	PR (%)	CUF (%)
5°	1573.2	2768.4	-2.78	78.15	20.25	87.95	15.81
10°	1608.4	2825.4	-2.51	83.65	20.65	87.81	16.12
15°	1634.6	2864.5	-2.29	87.5	20.85	87.59	16.35
20°	**1651.7**	**2887**	**-2.12**	**89.4**	**21.05**	**87.35**	**16.48**
25°	1659.7	2890.7	-2.01	89.7	21.05	87.06	16.49
30°	1658.5	2880.3	-1.95	86.95	21	86.80	16.45
35°	1648.3	2855.6	-1.93	81.6	20.9	86.59	16.30
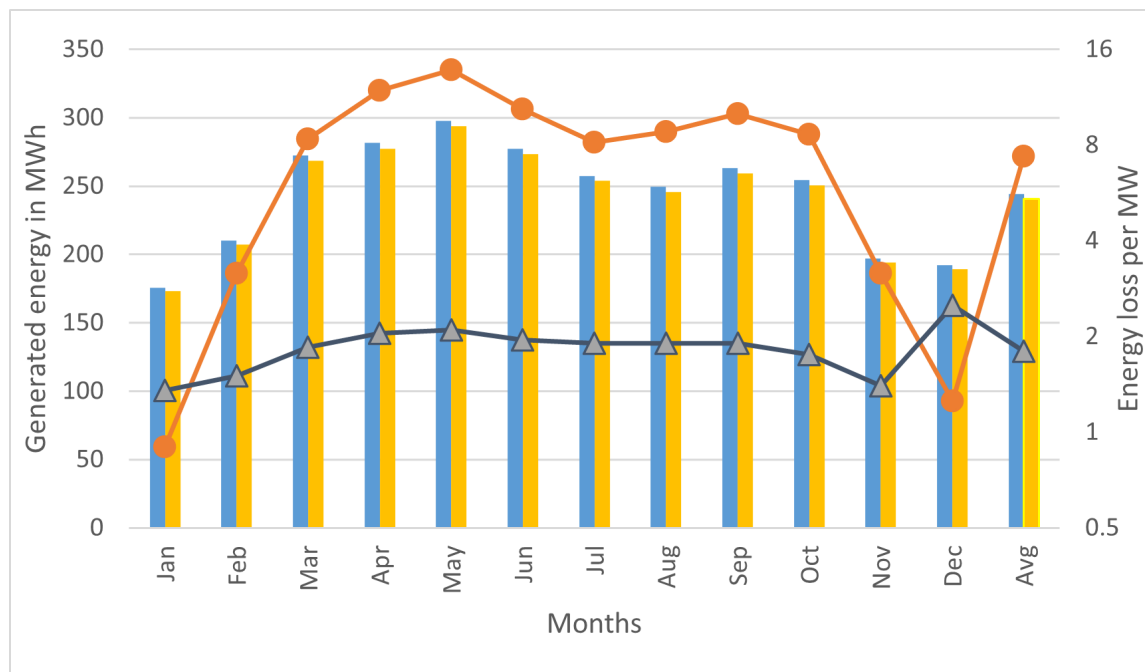
FIGURE 4.17: Analysis of E_A, E_G, L_A and L_S for $FSPV_B$ plant.

Chapter 4. TECHNO-ECONOMIC ANALYSIS OF SOLAR PV PLANT

The average monthly energy generation of the $FSPV_B$ plant was recorded as 244.07 MWh, with an average grid export of 240.56 MWh. As depicted in Fig. 4.17, the plant consistently exhibited higher array capture losses compared to system losses throughout the year. The maximum array loss (L_A) of 13.75 MWh/MW was observed in May, primarily due to extended daylight hours and elevated solar irradiance levels. In contrast, the lowest L_A occurred in January, corresponding to reduced solar insolation. System losses (L_S) peaked at 2.5 MWh/MW in December and reached a minimum of 1.4 MWh/MW in November, with an annual average of approximately 1.80 MWh/MW.
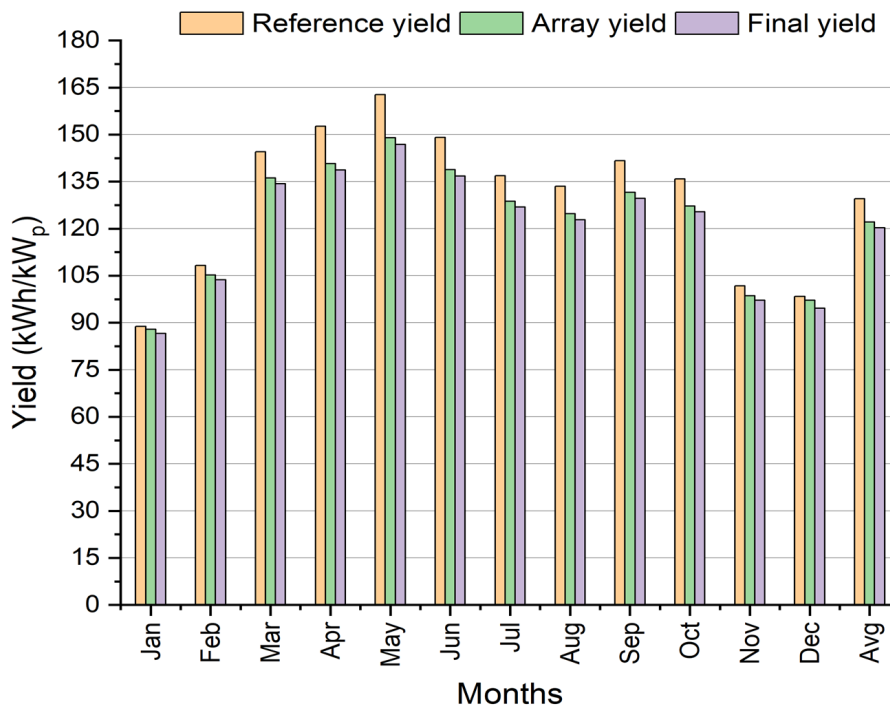
FIGURE 4.18: Monthly Y_R, Y_A and Y_F in $FSPV_B$ plant.

Fig. 4.18 presents the monthly yield characteristics of the $FSPV_B$ system. The reference yield (Y_R) ranged from a maximum of 162.7 kWh/kWp in May to a minimum of 88.8 kWh/kWp in January, reflecting seasonal variation in solar resource availability. The array yield (Y_A) varied between 148.95 kWh/kWp in May and 87.9 kWh/kWp in January, while the final yield (Y_F) ranged from 146.85 kWh/kWp to 86.55 kWh/kWp for the same respective months.   The
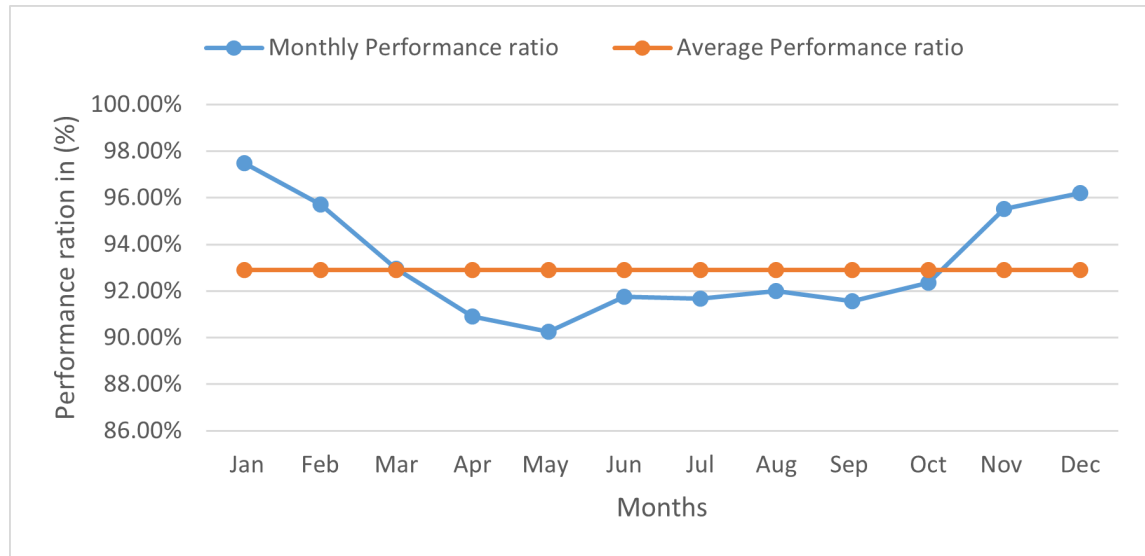
FIGURE 4.19: Monthly performance ratio of FSPV$_B$ plant.

annual average values for Y_R, Y_A, and Y_F were computed as 129.19 kWh/kWp, 122.08 kWh/kWp, and 120.28 kWh/kWp, respectively, indicating the overall energy conversion efficiency of the system.

Fig. 4.19 depicts the FSPV$_B$ plant's average annual PR at approximately 93%, with optimal performance from November to March. January shows the highest PR of 97.47%, while May records the lowest at 90.26%. Bi-facial PV modules contribute to a competitive edge with a back-yield advantage. Solar radiation variations in Chandigarh, influenced by climate and seasons, impact energy production. In Fig. 4.20, the PV module exhibits peak efficiency of 20.73% in January and 19.03% in April. The PV inverter maintains a consistent efficiency of around 98.5%, indicating weather resilience. Plant efficiency peaks at 20.41% in January and reaches a low of 18.90% in May, with average efficiencies for PV modules, PV inverters, and the plant at 19.73%, 98.57%, and 19.45%, respectively.

4.7.1.3 Technical Comparative Analysis of FSPV$_M$ and FSPV$_B$ Plants:

The FSPV$_M$ and FSPV$_B$ plants, both with a 2 MW$_P$ rated capacity, produce 2231 MWh and 2887 MWh of energy, respectively, as shown in Table 4.3.
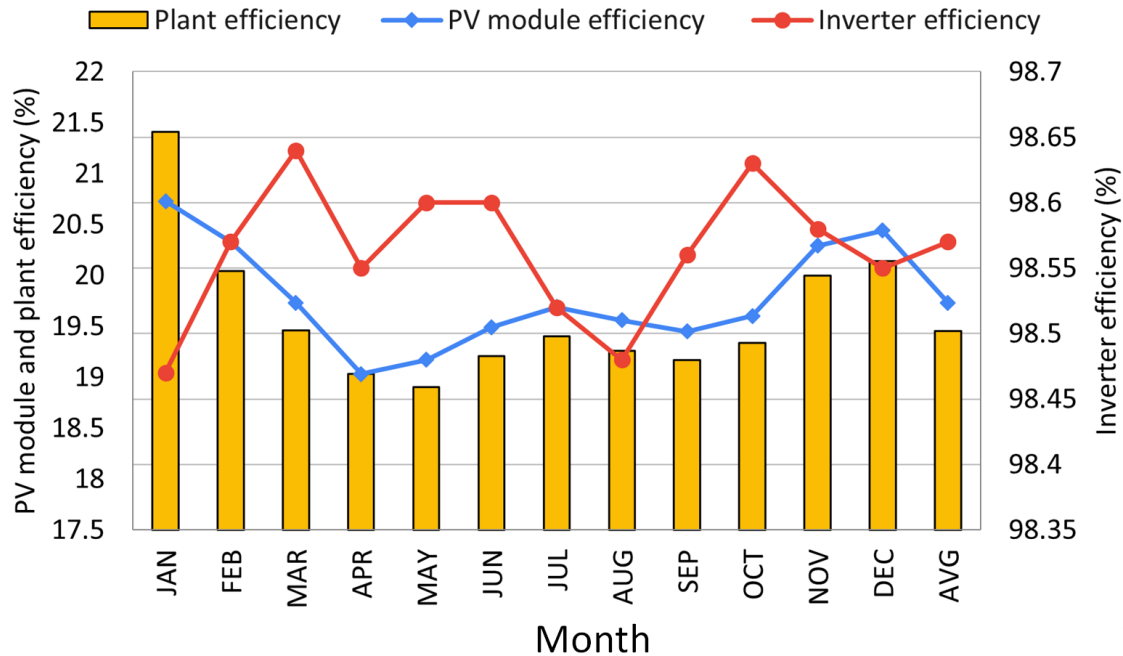
FIGURE 4.20: Monthly PV module, inverter and system efficiencies of $FSPV_B$ plant.

TABLE 4.3: Comparison of $FSPV_M$ and $FSPV_B$ plants

Parameters	$FSPV_M$ Plant	$FSPV_B$ Plant
Rated Capacity (MWp)	2	2
Annual Energy Output (MWh)	2231	2887
No. of modules	3712	3705
Module Tilt Angle (°)	20	20
Each module Rated Capacity (Wp)	540	540
No. of Inverters	16	16
Inverter Capacity (kW)	2000	2000
Performance Ratio (%)	71.90	92.90
Capacity Factor (%)	12.73	16.45
Area Available (km²)	0.45	0.45
Area Covered by Solar PV Modules (m²)	9572	9554
Energy/m² (MWh/m²)	0.23	0.30
Specific Production of Energy (kWh/kWp/year)	1108	1443
Array Losses in MWh	42.37	7.37
System Losses in MWh	2.77	1.80

4.7. Performance Evaluation of FSPV Plant 107

The $FSPV_M$ plant, with 3712 modules at 20° tilt over 9572 m², achieves a 71.9 % average PR, while the $FSPV_B$ plant, with 3705 modules over 9554 m², attains 92.9 % PR. Both have 16 inverters rated 2000 kW with 98.7 % efficiency. $FSPV_B$ delivers higher energy per m², greater daily output, and lower losses. Capacity factors are 12.73% ($FSPV_M$) and 16.47% ($FSPV_B$), with bifacial performance gains attributed to rear-side irradiance and reduced thermal losses, confirming the advantage of bifacial modules in floating PV systems.

Table 4.4 summarizes the loss analysis of monofacial ($FSPV_M$) and bifacial ($FSPV_B$) floating solar PV plants. The $FSPV_M$ plant receives 1590 kWh/m² of effective irradiation, with 20.67% efficiency, and delivers 3107 MWh of nominal energy, but faces higher temperature (-3.98%) and LID losses (-2.00%), resulting in 2231 MWh of grid injection.

TABLE 4.4: Loss analysis comparison between monofacial and bifacial floating solar PV (FSPV) plants

Loss Category	$FSPV_M$ plant	$FSPV_B$ plant
Global Horizontal Irradiation	$1531\,kWh/m^2$	$1531\,kWh/m^2$
Effective Irradiation on Collectors	$1590\,kWh/m^2$	$1660\,kWh/m^2$
Efficiency at STC	20.67%	20.94%
Array Nominal Energy	3107 MWh	3404 MWh
Module Degradation Loss	-0.20%	-0.40%
Irradiance Level Loss	-0.73%	-1.01%
Temperature Loss	-3.98%	-0.30%
Light-Induced Degradation (LID)	-2.00%	-0.74%
Mismatch, Ohmic, Wiring Losses	-2.06% (Mismatch), -0.21% (Ohmic)	-0.30% (each: MV + Transformer)
Inverter Loss (Operation)	-1.44%	-1.46%
Available Energy at Inverter Output	2262 MWh	2929 MWh
Auxiliary Losses	-0.03%	-0.01%
AC Ohmic Loss	-0.00%	-0.00%
Transformer Loss	-1.11%	-0.30%
MV Line Ohmic Loss	0.00%	-0.30%
System Unavailability	-0.27%	-0.21%
Energy Injected into Grid	2231 MWh	2882 MWh

In comparison, the $FSPV_B$ plant benefits from rear-side irradiation, receiving 1660 kWh/m² with 20.94% efficiency. Despite slightly higher degradation losses, it shows reduced thermal and LID losses, achieving 2887 MWh of energy injection and superior overall performance.

4.7.2   Economic Analysis of $FSPV_M$ and $FSPV_B$ Plants

In the development of any project, financial analysis plays a pivotal role in decision-making. Key economic metrics essential for decision-making include the LCOE, annualized cost, and simple payback time.

4.7.2.1 Cost Analysis

The total capital cost of the solar plant includes installation, approvals, and certificates. Scholars analyzed both $FSPV_M$ and $FSPV_B$ plants expenses, ranging from 0.51 USD to 2.05 USD per watt [140]. Monofacial and bifacial solar PV modules cost 0.23 USD and 0.29 USD per watt, while the inverter costs approximately 0.12 USD per watt [141] [142]. The estimated installation costs for $FSPV_M$ and $FSPV_B$ plants are 6.29 million USD and 8.79 million USD per MW, respectively. Annual energy production, rated capacity, and PV array area for both plants were simulated using PVsyst software. These factors, along with the total capital cost, are crucial for evaluating the PV plant financial viability.

4.7.2.2 Internal Rate of Return

The IRR for the $FSPV_M$ plant is 27.69% whereas 45.66% for the $FSPV_B$ plant. The higher IRR of the $FSPV_B$ plant is mainly due to the additional energy gain from the bifacial modules, which improves annual generation and boosts project returns.

4.7.2.3 Payback Period

The $FSPV_B$ and $FSPV_M$ plants exhibit a payback period of 8.3 years and 12.7 years, respectively. Both plants demonstrate economic feasibility, with payback periods shorter than the 25-year system lifetime, ensuring a relatively swift recovery of the initial investment. Notably, the $FSPV_B$ plant's payback period is shorter than the $FSPV_M$ plant.

4.7.2.4 Levelized Cost of Energy (LCOE)

To compute the LCOE for $FSPV_M$ and $FSPV_B$ plants, factors like capital costs, operating expenses, maintenance costs, and expected energy output over the system's lifetime are considered. Despite the $FSPV_B$ plant having higher capital and operating and maintenance costs than the $FSPV_M$ plant, its LCOE is lower. The LCOE is 0.067 USD per kWh and 0.050 USD per kWh for the $FSPV_M$ and $FSPV_B$ plants.

4.7.2.5 Economical Comparison of $FSPV_M$ and $FSPV_B$ Plants

Table 4.5 compares capital costs between $FSPV_M$ and $FSPV_B$ plants, indicating an additional 1.55 million USD per MW for the $FSPV_B$ plant. The cost of $FSPV_M$ and $FSPV_B$ plants is 6.29 million USD and 8.79 million USD, respectively. Annual operating costs are 0.20 million USD and 0.24 million USD per MW for $FSPV_M$ and $FSPV_B$ plants. The specific cost per watt is 0.63 USD for $FSPV_M$ and 0.78 USD for $FSPV_B$ plants.

TABLE 4.5: Cost calculation of $FSPV_M$ and $FSPV_B$ plants

Parameters	$FSPV_M$ plant / MW	$FSPV_B$ plant / MW
Total capital cost (million USD)	6.29	8.79
Operating cost with 9% inflation per year (million USD/year)	0.20	0.24
IRR (%)	27.69	45.66
Rate of Return (ROI) (%)	299.6	1572.2
Payback Period (Year)	8.3	12.7
LCOE (USD/kWh)	0.067	0.050

110   *Chapter 4. TECHNO-ECONOMIC ANALYSIS OF SOLAR PV PLANT*

4.7.2.6 Reduction in Carbon Emission

A $FSPV_B$ plant could result in lower total CO_2 emissions compared to a $FSPV_M$ plant, depending on a variety of factors as per Tables 4.6 , 4.7 and 4.8. Bifacial solar modules have the ability to produce more electricity per unit surface area than monofacial solar panels, which could lead to the requirement of fewer panels to generate the same amount of electricity. The total CO_2 saved by the $FSPV_M$ plant was 3,655,081 kg CO_2 while 3,433,113 kg CO_2 was saved by the $FSPV_B$ plant.

TABLE 4.6: System lifecycle emission details of modules used in $FSPV_M$ and $FSPV_B$ plants

Item	LCe (kgCO$_2$/kWp)	PV Array Nominal Power (kWp)	Total CO$_2$ Emission (kgCO$_2$)
Monofacial	1713	2134	3,655,081
Bifacial	1713	2004	3,433,113

TABLE 4.7: System lifecycle emission details of supports used in $FSPV_M$ and $FSPV_B$ plants

Item	LCe (kgCO$_2$/kg)	Weight (kg)	Total CO$_2$ Emission (kgCO$_2$)
Monofacial	6.24	39,520	246,728
Bifacial	6.24	37,120	231,745

TABLE 4.8: System lifecycle emission details of inverters used in $FSPV_M$ and $FSPV_B$ plants

Item	LCe (kgCO$_2$/unit)	No. of Units	Total CO$_2$ Emission (kgCO$_2$)
Monofacial	619	16	9,896
Bifacial	619	16	9,896

4.8 Concluding Remarks

This chapter presents a comprehensive techno-economic assessment of grid-connected solar photovoltaic (PV) systems and floating solar PV plant, focusing on the comparison between terrestrial rooftop installations and floating solar PV (FSPV) systems utilizing monofacial and bifacial modules. The rooftop PV system at Delhi Technological University exhibited stable performance, with favorable technical metrics, a payback period of around nine years, and a competitive levelized cost of electricity, affirming its viability for urban applications.

The comparative evaluation of monofacial ($FSPV_M$) and bifacial ($FSPV_B$) floating solar PV plants underscores the superior performance of bifacial technology in floating applications. Simulation results indicated that the bifacial FSPV plant yielded approximately 29% higher annual energy output than its monofacial counterpart, primarily due to the additional rear-side irradiation capture. Furthermore, the bifacial system exhibited higher module, inverter, and overall plant efficiencies, along with significantly lower array and system losses.

From an economic perspective, although the bifacial floating PV system requires a higher initial investment, it demonstrated a shorter payback period and a considerably higher internal rate of return, reaffirming its economic viability for large-scale clean energy generation. The lifecycle carbon emission analysis further corroborated the environmental benefits of deploying FSPV systems, contributing meaningfully to carbon footprint reduction goals.

Overall, the findings presented in this chapter highlight the potential of integrating bifacial module technology with floating solar PV systems as an effective strategy to enhance energy yield, optimize land and water resource utilization, and achieve economic and environmental sustainability in solar power generation. These insights provide a robust foundation for further exploration into advanced system configurations, such as the incorporation of tracking mechanisms and hybrid renewable energy integrations, to unlock additional performance gains and drive the global transition towards sustainable energy solutions.

The following chapter presents a detailed loss analysis of floating solar PV (FSPV) systems implemented with different tracking configurations, including

112   *Chapter 4. TECHNO-ECONOMIC ANALYSIS OF SOLAR PV PLANT*

fixed-tilt, single-axis, and dual-axis tracking. By comparing these systems, the study evaluates how sun-tracking mechanisms influence various loss components such as shading, soiling, temperature, mismatch, and inverter losses. The analysis highlights the performance improvements achieved through enhanced solar capture, particularly in dual-axis systems, and assesses their impact on overall energy yield and system efficiency. This chapter also discusses the impact of ambient temperature on various performance parameters of dual axis tracking configurations.

113

Chapter 5

ENHANCEMENT OF ENERGY YIELD IN FLOATING SOLAR PV PLANT USING DIFFERENT TRACKING CONFIGURATIONS

5.1   Introduction

Floating Solar Photovoltaic (FSPV) systems have emerged as a promising advancement in renewable energy, providing an effective solution to address both land scarcity and the increasing global demand for clean electricity. By utilizing the surface of water bodies such as reservoirs, lakes, and canals, FSPV installations not only alleviate pressure on land resources but also benefit from the inherent cooling effect of water, which contributes to improved efficiency and extended lifespan of photovoltaic (PV) modules. Despite these advantages, the majority of current FSPV deployments rely on fixed-tilt configurations, which limit their capability to capture optimal solar irradiance across different times of the day and seasonal variations.

The incorporation of solar tracking technologies within FSPV systems presents a viable pathway to enhance energy capture by dynamically aligning the PV modules with the sun's trajectory. Tracking systems, including single-axis and dual-axis mechanisms, have been shown in several studies to improve energy yields by approximately 10% to 50%, depending on geographic and climatic conditions. However, the deployment of tracking configurations in

floating environments introduces distinct technical and economic challenges. These include increased structural complexity, higher initial capital expenditure, and the requirement for robust anchoring and mooring solutions to ensure mechanical stability and operational reliability under varying water conditions. Til now, most studies on fixed-tilt, seasonal tilt-adjustable, and horizontal single-axis tracking (HSAT) systems have primarily focused on ground-mounted solar PV installations. This chapter addresses a critical gap in the literature by extending the analysis of these configurations specifically fixed-tilt, HSAT, and dual-axis tracking systems to floating solar photovoltaic (FSPV) plants.

The novelty of this chapter lies in its systematic evaluation of tracking technologies integrated into FSPV systems. It presents a detailed analysis of the operational principles, technical performance, and energy generation potential associated with each configuration, offering new insights into the feasibility and effectiveness of solar tracking in floating environments.

5.2   Solar Trackers Configurations

Solar tracking technologies allow PV panels to follow the sun's path, optimizing their angle to maximize solar energy capture. These systems are typically classified into four main configurations.

5.2.1   Fix Tilt Solar Tracker

In FSPV plants, fixed tilt PV modules mounted on floaters platforms at a set tilt angle. Unlike ground-mounted systems, their design must consider not only latitude and seasonal sun angles but also water movement, wind forces, and structural stability. Typically set between 5° and 15°, the tilt angle balances energy capture and stability while minimizing wind loads. Fixed tilt systems offer a cost-effective, stable alternative to tracking systems, with lower complexity and maintenance requirements, as shown in Fig. 5.1.

Additionally, their integration with water bodies helps mitigate overheating of PV modules, enhancing efficiency compared to land-based systems. The implementation of fixed tilt configurations in floating solar plants is particularly

advantageous in regions with high diffuse radiation, where the benefits of tracking systems are less pronounced.
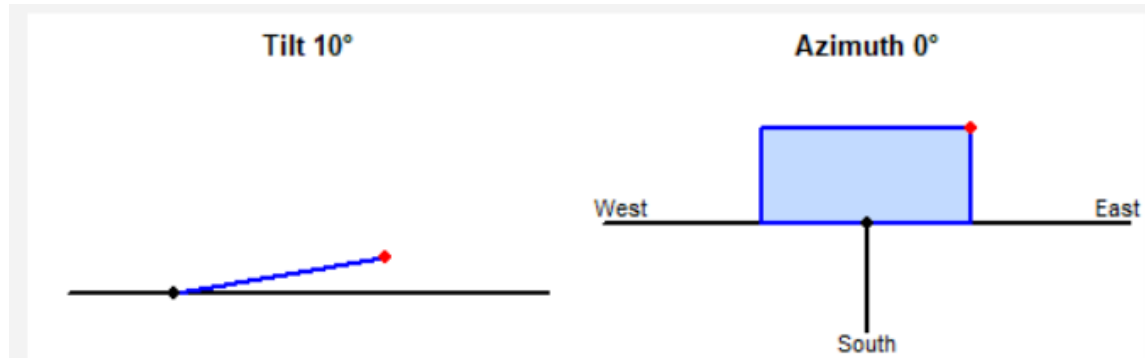
FIGURE 5.1: Fix tilt FSPV plant

5.2.2   Seasonal Adjustable Tilt Tracker

A Seasonal Adjustable-Tilt Floating Solar Photovoltaic (FSPV) plant is designed to optimize solar energy generation by adjusting the tilt angle of PV modules according to seasonal variations in solar irradiance in Fig. 5.2. Unlike fixed-tilt systems, this approach enhances energy yield by aligning the panels more effectively with the sun's position throughout the year. In floating solar applications, adjusting the tilt seasonally can be particularly beneficial due to the reflective properties of water surfaces, which can enhance energy capture.
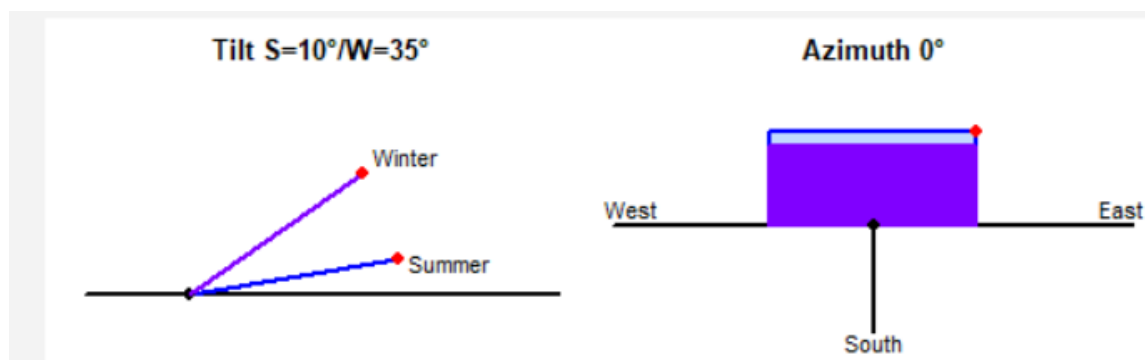
FIGURE 5.2: Seasonal adjustable tilt FSPV plant

Chapter 5. ENHANCEMENT OF ENERGY YIELD IN FLOATING SOLAR PV PLANT USING DIFFERENT TRACKING CONFIGURATIONS

FIGURE 5.3: Horizontal Axis Solar Tracker in FSPV Plant

5.2.3   Horizontal Axis Solar Tracker (HSAT)

A HSAT is a type of single-axis tracking system where photovoltaic (PV) modules are mounted on a structure that rotates around a horizontal axis to optimize solar energy capture as shown in Fig. 5.3. The axis of rotation can be oriented either east-west or north-south, depending on site-specific conditions and energy yield optimization. In an east-west configuration, the panels remain fix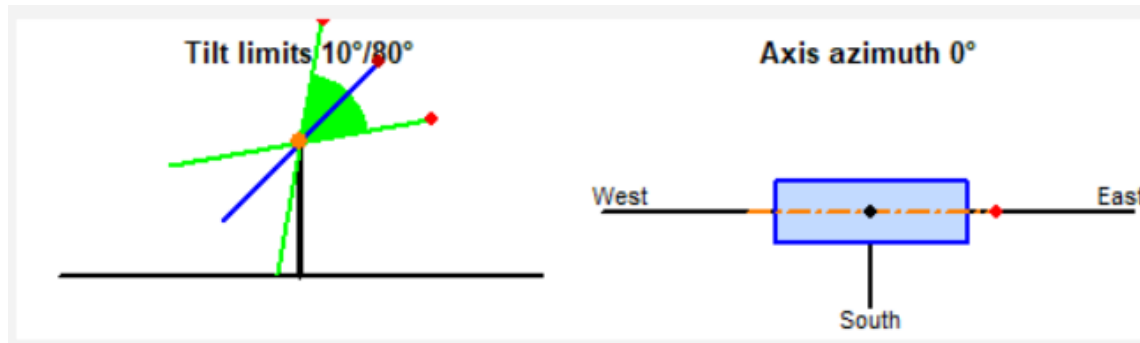ed along this axis while adjusting their tilt throughout the day to maximize sunlight absorption. In contrast, a north-south orientation allows the panels to follow the sun's movement from east to west, improving energy generation, particularly in locations with high direct solar irradiance.

The horizontal axis tracking system enhances energy output by reducing the angle of incidence between incoming sunlight and the PV surface. Compared to fixed tilt systems, it can increase energy generation by 15–25%, depending on location and climatic conditions. This tracking method is particularly beneficial in areas with high solar exposure and minimal cloud cover, where direct irradiance significantly contributes to energy production. Additionally, horizontal axis trackers improve performance during early morning and late afternoon hours, extending the effective energy harvesting period.

5.2.4   Dual Axis Solar Tracker (DAT)

The integration of dual-axis solar tracking in floating solar photovoltaic (FSPV) systems presents a potential advancement in optimizing energy generation by maximizing solar irradiance capture as shown in Fig. 5.4. Unlike fixed-tilt or
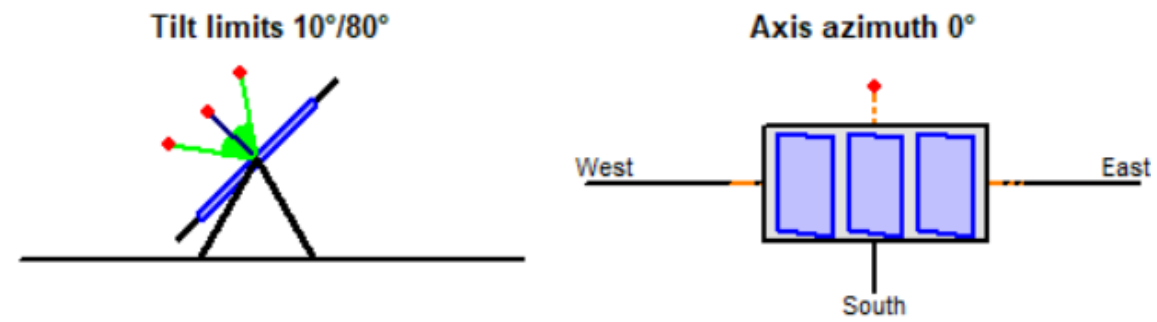
FIGURE 5.4: Dual axis solar tracker in FSPV plant

single-axis tracking systems, dual-axis trackers adjust both azimuth and tilt angles dynamically, ensuring optimal panel orientation throughout the day and across seasons. This capability enhances energy yield by reducing cosine losses and improving the direct normal irradiance (DNI) reception.

In the context of floating solar installations, dual-axis tracking introduces both technical advantages and engineering challenges. The cooling effect of the water surface can mitigate thermal losses, leading to improved module efficiency. However, the additional mechanical complexity associated with continuous movement, increased structural loads due to wind and water currents, and the need for robust anchoring mechanisms necessitate careful design considerations. Furthermore, the energy consumption of the tracking system must be analyzed in relation to the net gain in energy generation to assess overall feasibility.

5.3   Technical Performance Parameters

The technical performance parameters of the FSPV plant, such as yields (Y_A, Y_F, Y_R), performance ratio (PR), capacity factor (CUF), PV module efficiency (η_{PV}), PV inverter efficiency (η_{inv}), system efficiency (η_{sys}), array capture loss (L_A), and system loss (L_S), have been considered for evaluating the system performance. These parameters have been described in detailed in subsection 4.4.1 of Chapter 4, and will later be employed in this Chapter to analyze and compare different solar tracking system configurations.

Chapter 5. ENHANCEMENT OF ENERGY YIELD IN FLOATING SOLAR PV PLANT USING DIFFERENT TRACKING CONFIGURATIONS

5.4 Energy Losses

Energy losses in floating solar photovoltaic (FSPV) plants arise from various factors that affect the overall efficiency of energy conversion. These losses can be categorized into optical, thermal, electrical, and environmental losses. Optical losses, in particular, are influenced by factors such as reflection, refraction, and the incidence angle of sunlight on the PV module surface. Understanding and quantifying these losses is crucial for optimizing system design and operation.

5.4.1 Incidence Angle Modifier (IAM) Factor Loss

The Incidence Angle Modifier (IAM) factor represents the reduction in irradiance absorption due to the angle of sunlight on the PV module surface. In FSPV plant, IAM losses are influenced by tilt variations from wave-induced movements, seasonal sun path changes, and dynamic water reflections. These losses are more pronounced in fixed-tilt systems, especially during morning and evening hours.

Mathematically, IAM is given by:

$$IAM(\theta) = \frac{G_\theta}{G_0} \tag{5.1}$$

where G_θ and G_0 are the irradiance values at incidence angle θ and normal incidence, respectively. Using the ASHRAE model, IAM is approximated as:

$$IAM(\theta) = 1 - b(1 - \cos\theta) \tag{5.2}$$

where b (0.02–0.05) is an empirical loss coefficient. The effective irradiance after IAM correction is:

$$G_{\text{eff}} = G_T \times IAM(\theta) \tag{5.3}$$

and IAM losses are calculated as:

$$L_{\text{IAM}} = G_T \times (1 - IAM(\theta)) \tag{5.4}$$

$$L_{\text{IAM}}(\%) = (1 - IAM(\theta)) \times 100 \tag{5.5}$$

IAM losses can be mitigated by seasonal tilt adjustments, tracking systems, and anti-reflective coatings, which help optimize energy yield in FSPV plants.

5.4.2 Soiling Loss

Soiling loss in floating solar power plants (FSPVs) occurs due to the accumulation of dust, algae, and bird droppings, reducing energy generation. The soiling loss factor (SLF) quantifies this effect and is expressed as:

$$SLF = 1 - \eta_s \tag{5.6}$$

where η_s is the soiling efficiency, defined as the ratio of energy output from a soiled panel (E_s) to a clean panel (E_c):

$$\eta_s = \frac{E_s}{E_c} \tag{5.7}$$

The cumulative soiling loss over n days follows an exponential model:

$$SLF(n) = 1 - e^{-\beta n} \tag{5.8}$$

where β is the soiling accumulation coefficient. Soiling also affects the performance ratio (PR), given by:

$$PR_s = PR_c \cdot (1 - SLF) \tag{5.9}$$

The total energy loss due to soiling over a period T is:

$$E_{\text{loss}} = \sum_{t=1}^{T} E_c(t) \cdot SLF(t) \tag{5.10}$$

Mitigation strategies include hydrophobic coatings, optimized panel tilt for rainwater cleaning, automated cleaning systems, and bird deterrents. Accurate modeling and mitigation of soiling loss are crucial for maximizing the performance of the FSPV plant.

Chapter 5. ENHANCEMENT OF ENERGY YIELD IN FLOATING SOLAR PV PLANT USING DIFFERENT TRACKING CONFIGURATIONS

5.4.3 Module Degradation Loss

Module degradation loss in FSPV plant refers to the gradual decline in photovoltaic (PV) module performance over time due to environmental and operational factors. While FSPVs generally experience lower temperature-induced degradation compared to ground-mounted systems due to water-based cooling effects, they are still susceptible to degradation mechanisms such as UV exposure, moisture ingress, and potential-induced degradation (PID).

The module degradation factor (MDF) quantifies the reduction in module efficiency over time and is expressed as:

$$MDF(t) = 1 - \eta_m(t) \tag{5.11}$$

where $\eta_m(t)$ is the module efficiency at time t, typically modeled as:

$$\eta_m(t) = \eta_{m0} \cdot (1 - DR \cdot t) \tag{5.12}$$

where, η_{m0} is the initial module efficiency, DR is the degradation rate (typically 0.5–1.0% per year for silicon PV modules) and t is the time in years.

The energy loss due to module degradation over a period T can be calculated as:

$$E_{\text{loss}} = \sum_{t=1}^{T} E_c(t) \cdot MDF(t) \tag{5.13}$$

where $E_c(t)$ is the clean energy output without degradation.

To mitigate degradation losses, FSPVs can utilize anti-reflective coatings, improved encapsulation materials, and periodic electrical insulation testing to minimize PID effects. Regular maintenance and real-time performance monitoring are essential to ensure optimal long-term operation of floating PV systems.

5.4.4 Loss Due to Temperature

Temperature-induced losses in floating solar power plants (FSPVs) occur due to the negative temperature coefficient of photovoltaic (PV) modules. Although

FSPVs benefit from water-induced cooling, reducing temperature stress compared to ground-mounted systems, temperature variations still impact module efficiency and overall energy output.

The temperature loss factor (TLF) quantifies the reduction in power output due to module temperature (T_m) and is given by:

$$TLF = 1 - \eta_T \tag{5.14}$$

where η_T is the temperature efficiency correction factor, expressed as:

$$\eta_T = 1 + \gamma(T_m - T_{\text{ref}}) \tag{5.15}$$

where, γ is the temperature coefficient of power (typically -0.3% to -0.5% per °C for silicon PV modules), T_m is the module temperature (°C), T_{ref} is the reference temperature (usually 25°C).

The energy loss due to temperature effects over a period T is:

$$E_{\text{loss}} = \sum_{t=1}^{T} E_c(t) \cdot (1 - \eta_T(t)) \tag{5.16}$$

where $E_c(t)$ is the expected energy output without temperature loss.

To mitigate temperature-related losses, FSPVs can use high-efficiency PV modules with lower temperature coefficients, enhanced module cooling designs, and floating structures that improve convective heat dissipation. Understanding and minimizing temperature losses is crucial for maximizing energy yield in floating solar power plants.

5.4.5 Light Induced Degradation

Light-Induced Degradation (LID) is a performance loss that occurs in photovoltaic (PV) modules when they are exposed to sunlight for the first time. This degradation is mainly caused by the interaction of oxygen and boron in silicon wafers, leading to a temporary reduction in efficiency. Although floating solar power plants (FSPVs) experience lower operating temperatures due to water cooling, LID still affects their initial performance.

The LID factor (LIDF) represents the relative efficiency drop due to light exposure and is given by:

$$LIDF = 1 - \eta_L \tag{5.17}$$

where η_L is the efficiency factor after degradation, modeled as:

$$\eta_L = \eta_{m0} \cdot (1 - D_{\text{LID}}) \tag{5.18}$$

where, η_{m0} is the initial module efficiency before light exposure, D_{LID} is the LID degradation rate (typically 1–3% for monocrystalline silicon modules).

The total energy loss due to LID over the exposure period T is:

$$E_{\text{loss}} = \sum_{t=1}^{T} E_c(t) \cdot LIDF \tag{5.19}$$

where $E_c(t)$ is the clean energy output without degradation.

To mitigate LID, FSPVs can utilize low-boron or gallium-doped silicon wafers, preconditioning treatments like light soaking or electrical biasing, and improved cell passivation techniques. Understanding and minimizing LID is crucial for ensuring stable long-term performance in floating solar power systems.

5.4.6 Mismatch Loss

Mismatch loss occurs in photovoltaic (PV) systems when modules within the same string operate at different electrical conditions, leading to a reduction in overall system efficiency. In floating solar power plants (FSPVs), mismatch losses can arise due to variations in shading, soiling, temperature differences, and manufacturing tolerances. These losses prevent modules from operating at their maximum power point (MPP) simultaneously, reducing the overall energy yield.

The Mismatch Loss Factor (MLF) is defined as:

$$MLF = 1 - \eta_M \tag{5.20}$$

where η_M is the mismatch efficiency factor, given by:

$$\eta_M = \frac{P_{\text{array}}}{\sum_{i=1}^{N} P_i} \tag{5.21}$$

where, P_{array} is the actual power output of the array, P_i is the power output of the ith module in the string and N is the number of modules in the array. The total energy loss due to mismatch over a period T is:

$$E_{\text{loss}} = \sum_{t=1}^{T} E_c(t) \cdot MLF \tag{5.22}$$

where $E_c(t)$ is the clean energy output without mismatch losses.

To minimize mismatch losses, FSPVs can utilize module-level power electronics (MLPE) such as power optimizers and microinverters, careful string design, bypass diodes, and periodic performance monitoring. Optimizing system design and maintenance can significantly improve the energy yield of floating solar power plants.

5.4.7 Ohmic Wiring Losses

Ohmic wiring losses occur due to the resistance in electrical cables connecting photovoltaic (PV) modules, inverters, and other system components. These losses result in power dissipation as heat and can be quantified using Ohm's Law:

$$P_{\text{loss}} = I^2 R \tag{5.23}$$

where, P_{loss} is the power loss in the wiring, I is the current flowing through the cable, R is the resistance of the cable.

The total ohmic loss percentage in a PV system is given by:

$$\eta_{\text{ohmic}} = 1 - \frac{P_{\text{array}} - P_{\text{loss}}}{P_{\text{array}}} \tag{5.24}$$

where P_{array} is the total power generated by the PV array. To minimize wiring losses, FSPVs should use appropriately sized cables, high-conductivity materials, and optimized cable routing.

Chapter 5. ENHANCEMENT OF ENERGY YIELD IN FLOATING SOLAR PV PLANT USING DIFFERENT TRACKING CONFIGURATIONS

5.4.8 Inverter Loss

Inverter loss represents the efficiency reduction when converting DC power generated by PV modules into AC power suitable for grid connection. The inverter efficiency η_{inv} is given by:

$$\eta_{\text{inv}} = \frac{P_{\text{AC}}}{P_{\text{DC}}} \tag{5.25}$$

where, P_{AC} is the AC power output from the inverter, P_{DC} is the DC power input to the inverter.

The total energy loss due to inverter inefficiency over a period T is:

$$E_{\text{loss,inv}} = \sum_{t=1}^{T} P_{\text{DC}}(t) \cdot (1 - \eta_{\text{inv}}) \tag{5.26}$$

Inverter losses can be minimized by selecting high-efficiency inverters, operating within optimal loading conditions, and implementing proper cooling strategies.

5.4.9 Medium Voltage Loss

Medium voltage (MV) loss occurs when transmitting power from inverters to the grid substation via medium voltage cables and transformers. These losses include resistive and inductive losses and can be expressed as:

$$P_{\text{MV}} = I^2 R \tag{5.27}$$

where, I is the current flowing through the MV cable, and R is the resistance of the MV line.

The percentage MV loss is given by:

$$\eta_{\text{MV}} = 1 - \frac{P_{\text{delivered}}}{P_{\text{sent}}} \tag{5.28}$$

where, P_{sent} is the power injected into the MV system and $P_{\text{delivered}}$ is the power received at the substation.

Reducing MV losses requires the use of optimized conductor sizes, improved transformer efficiency, and reactive power compensation techniques.

5.5 Probability Distribution Analysis of Solar Trackers

Probability distribution analysis in the context of a solar power plant involves the use of probability theory and statistical analysis to investigate several facets of solar energy generation and operation such as PV modelling parameters, uncertainty in inverter efficiency, soiling and mismatch, and degradation uncertainty. Probability distributions give a mathematical structure for representing and analyzing uncertain situations. Probability distributions are used in solar power plants to measure and assess the uncertainty and forecast of energy output, which is influenced by variables such as solar radiation and temperature. Probability distribution analysis can be applied in several major areas:

- **Modeling of Solar Irradiance**: The amount of solar energy that a solar panel receives depends on several variables, including the time of day, season, weather, and location. It is possible to use probability distribution analysis to depict the distribution of solar irradiance values over a certain period. It is usual practice to represent sun irradiation using the normal (Gaussian), Weibull, and gamma distributions.

- **Uncertainty Quantification**: The generation of solar energy is influenced by multiple factors that introduce unpredictability, such as variations in weather patterns, cloud cover, atmospheric conditions, and the functioning of equipment. Probability distribution analysis allows for the measurement of the level of uncertainty related to these parameters and offers valuable information regarding the probability of various energy production outcomes. This information is vital for the evaluation of risks, formulation of financial plans, and execution of decision-making procedures.

The $P50$ or $P90$ values are determined by calculating the cumulative distribution function (CDF) of the normal distribution, assuming that the data distribution also follows a normal distribution. The normal distribution, often known as the Gaussian distribution, is a type of continuous probability distribution. The shape is defined by the mean μ and standard deviation σ. The

mean and standard deviations were calculated using the Maximum Likelihood Estimation (MLE). The $P50$ value represents the median value, whereas the $P90$ value can be derived by evaluating the cumulative distribution function (CDF) of the normal distribution, as shown in equation (5.29). The $P90$ value is determined when the function $F(x)$ equals 0.1.

$$f(x) = \frac{1}{\sqrt{2\pi}\sigma} e^{-\frac{(x-\mu)^2}{2\sigma^2}}$$
(5.29)

where, $f(x)$ represents a probability density function. x is the variable. μ is the mean of the distribution. σ is the standard deviation of the distribution. e is the base of the natural logarithm.

5.6 Results and Discussions

This section provides a detailed evaluation of the performance of the proposed solar tracking configurations are Single Axis Tracker (SAT), Horizontal Single Axis Tracker (HSAT), and Dual Axis Tracker for a Floating Solar Photovoltaic (FSPV) system. A detailed discussion of the performance parameters is provided in section 4.4.1. The PVsyst program acquires simulation data by taking into account the system's technical specifications, design factors, and location-specific weather conditions that are provided as input.

Fig.5.5 depicts the monthly variations in the amount of solar radiation received by the solar PV modules. The fixed-tilt power plant receives an average solar irradiation of 123.95 kWh/m², whereas the SAT plant, HSAT plant, and DAT receive average solar irradiation of 130 , 133.95 , and 152.85 kWh/m² respectively. The solar irradiation gain on the DAT plant is 18.90% greater than that of the FT plant.

5.6.1 Estimation of Energy Production

Table 5.1 provides a comparative evaluation of the annual energy yield and capacity factor for solar PV plants configured with different tracking technologies: Fixed Tilt (FT), Seasonal Adjustable Tilt (SAT), Horizontal Single-Axis Tracking (HSAT), and Dual-Axis Tracking (DAT) plants. Among the
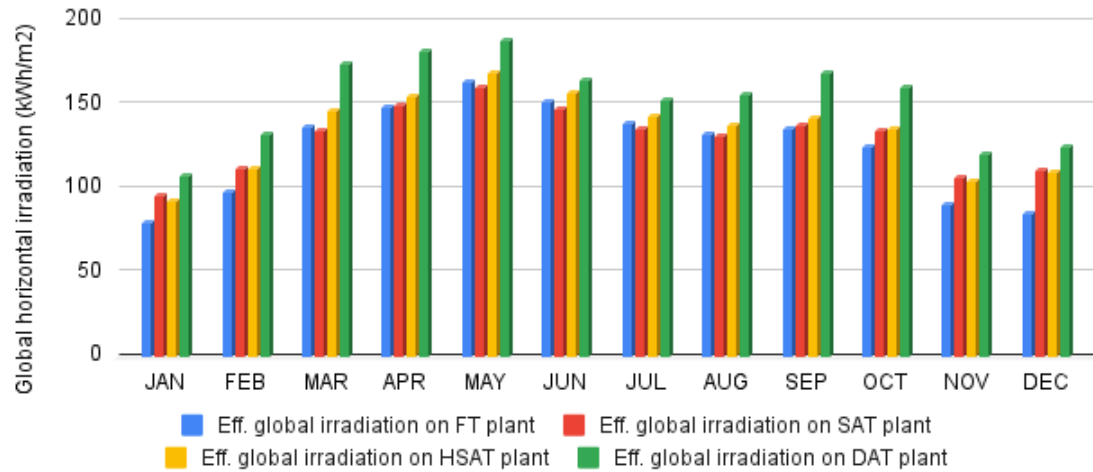
5.6. Results and Discussions

127

FIGURE 5.5: Monthly solar irradiation on FT, SAT, HSAT, and DAT plants

TABLE 5.1: Comparison of Annual Energy Yield and Capacity Factor of FT, SAT, HSAT, and DAT Plants

Comparison of Different Configurations	FT	SAT	HSAT	DAT
Annual energy yield (MWh)	2133.7	2236.5	2302.8	2711.6
Capacity factor (%)	12.17%	12.76%	13.14%	15.47%
Energy production gain over FT plant	–	4.59%	7.34%	21.32%

four configurations, the DAT plant demonstrates the highest annual energy yield of 2711.6 MWh, followed by the HSAT plant (2302.8 MWh), SAT plant (2236.5 MWh), and FT plant (2133.7 MWh). The capacity factor follows a similar trend, with the DAT plant achieving the highest value of 15.47%, while the FT plant records the lowest at 12.17%. Compared to the FT plant, the SAT, HSAT, and DAT plants exhibit energy production gains of 4.59%, 7.34%, and 21.32%, respectively. These results underscore the enhanced performance of PV plants employing tracking mechanisms, especially the dual-axis tracking system, in maximizing energy generation.

Chapter 5. ENHANCEMENT OF ENERGY YIELD IN FLOATING SOLAR PV PLANT USING DIFFERENT TRACKING CONFIGURATIONS
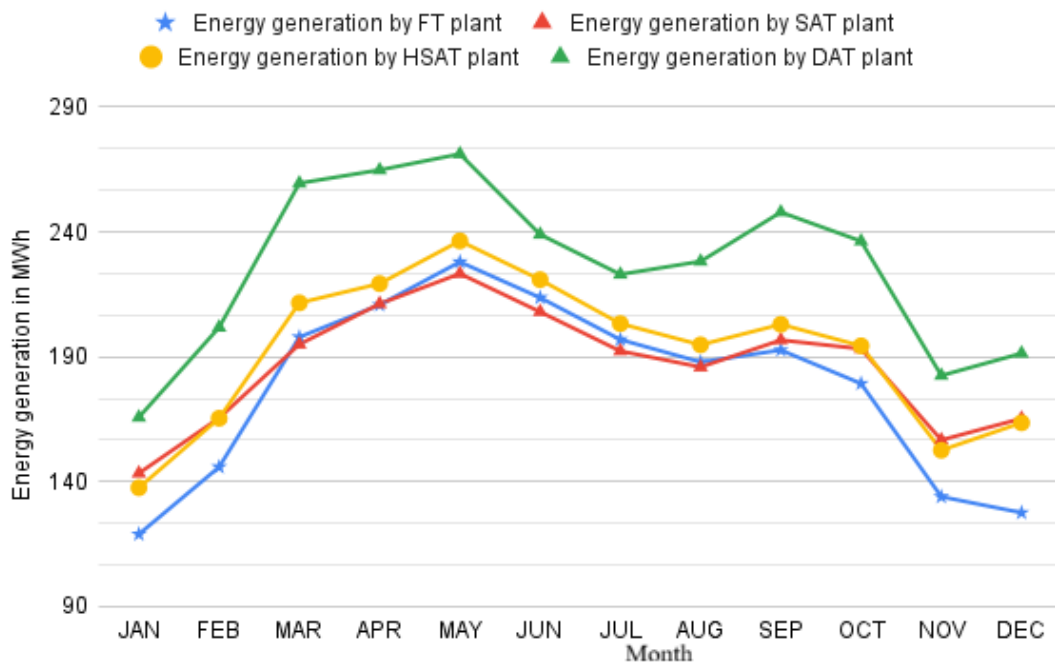
FIGURE 5.6: Monthly energy generation by FT, SAT, HSAT, and DAT plants

Fig.5.6 illustrates the monthly energy production for different plant schemes. The FT plant generates an average of 177.81 MWh, while SAT, HSAT, and DAT plants produce 186.38 MWh, 191.91 MWh, and 225.95 MWh, respectively. Lower sun angles in November reduce generation, but adjustable tilt trackers optimize panel orientation. The DAT plant achieves the highest output by tracking the sun both horizontally and vertically, maximizing solar radiation capture.

5.6.2   Capacity Factor

Fig.5.7 presents the monthly capacity factors for various plant configurations. Among these configurations, the FT (Fixed Tilt) plant exhibits the lowest capacity factor at 12.17%, while the SAT (Single-Axis Tracking), HSAT (Horizontal Single-Axis Tracking), and DAT (Dual-Axis Tracking) plants demonstrate slightly higher capacity factors at 12.76%, 13.14%, and 15.47%, respectively. Multiple factors intricately link the capacity factor of solar power plants,
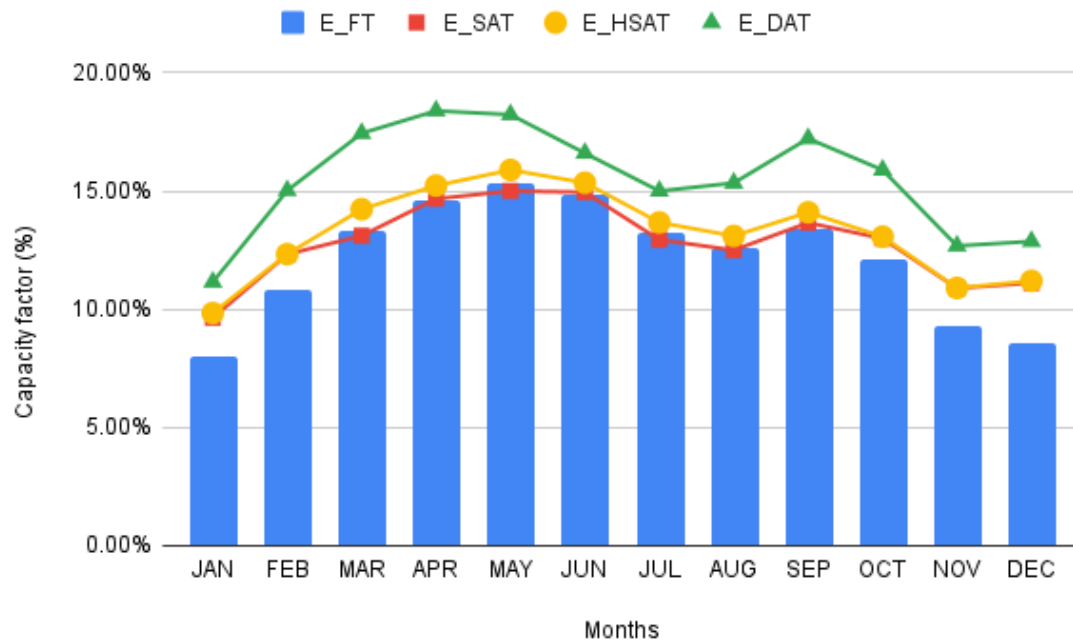
FIGURE 5.7: Monthly capacity factor of FT, SAT, HSAT, and DAT plants

including the availability of solar irradiation, the orientation and location of the site, and the prevailing weather conditions at the installation site.

5.6.3 Performance Ratio

Fig.5.8 illustrates the performance ratios of several plant systems. The recommended DAT plants exhibited superior performance compared to FT, SAT, and HSAT plants, particularly across all seasons of the year. The performance ratios of the FT plant vary seasonally, with the minimum and maximum values observed in May and January, respectively. The SAT, HSAT, and DAT plants have minimal performance ratios of 69.65%, 69.74%, and 71.94%, respectively. On the other hand, their highest performance ratios are 74.61%, 74.46%, and 76.75%, respectively. Average performance ratios for the FT, SAT, HSAT, and DAT plants are 66.74%, 67.20%, 71.88%, and 74.17%, respectively. The performance ratio of DAT plants has been seen to be 11.13% superior than that of alternative tracking systems.

## Chapter 5.   ENHANCEMENT OF ENERGY YIELD IN FLOATING SOLAR PV PLANT USING DIFFERENT TRACKING CONFIGURATIONS
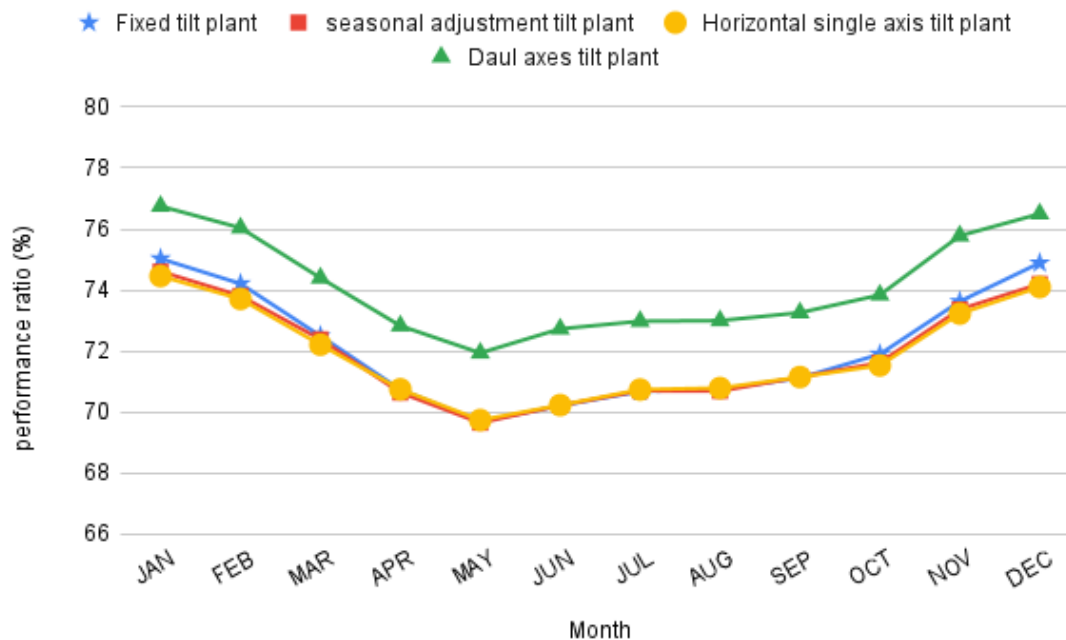
FIGURE 5.8: Monthly performance ratio of FT, SAT, HSAT, and DAT plants

The rated performance ratio of the plants cannot be achieved under actual environmental conditions due to various losses, including array capture losses and system losses. During the summers in Chandigarh, elevated ambient temperatures can markedly increase the temperature of the water surface supporting floating solar panels. This temperature rise can adversely affect the efficiency of the solar panels, as their performance generally declines at higher temperatures.

Additionally, the summer season is associated with increased dust and particulate matter, which can reduce the amount of sunlight reaching the panels and further diminish efficiency through dust accumulation. Although higher solar irradiance might enhance electricity generation, it also raises panel temperatures, potentially negating these benefits. Although floating solar panels benefit from the cooling effect of the water, this advantage is diminished if the water temperature rises significantly.

In the FT, SAT, and HSAT plants, the performance ratio remains the same from April to September because all experience identical changes in energy generation
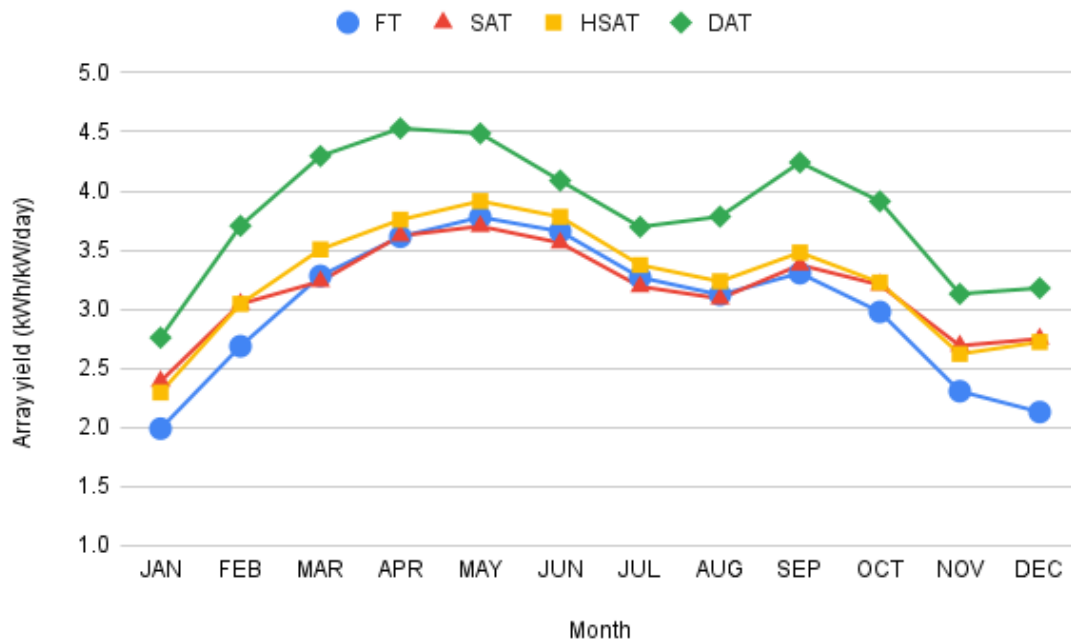
FIGURE 5.9: Monthly array yield of FT, SAT, HSAT, and DAT plants

and irradiance.

5.6.4   Array Yield

Fig.5.9 illustrates variations in monthly array yields among different photovoltaic (PV) tracker technologies.   The array yield denotes the energy output produced by a photovoltaic (PV) module array. Observations revealed distinct array yield values across different months. The FT, SAT, HSAT, and DAT plants recorded minimum array yields of 1.99, 2.39, 2.29, and 2.75 kWh/kW/day in January, respectively. Conversely, the maximum array yields occurred in May, reaching 3.77, 3.70, 3.91, and 4.48 kWh/kW/day for the FT, SAT, HSAT, and DAT plants, respectively. On average, the array yield values for the FT, SAT, HSAT, and DAT plants were 3.01, 3.15, 3.24, and 3.81 kWh/kW/day, respectively.

The optimized exposure to sunlight significantly influences this yield. It is imperative to ensure that solar radiation is consistently perpendicular to the PV module for optimal energy capture. Factors such as the tilt angle, shading,

geographical location, and prevailing weather conditions also play pivotal roles in determining the array yield.

Significantly, the output of the array usually declines significantly throughout the winter months because to the shorter days and lower angle of the sun. In contrast, during the summer season, the amount of energy produced by the array often shows a progressive rise due to the extended duration of daylight, resulting in more direct solar exposure on the PV modules.

5.6.5 Final Yield
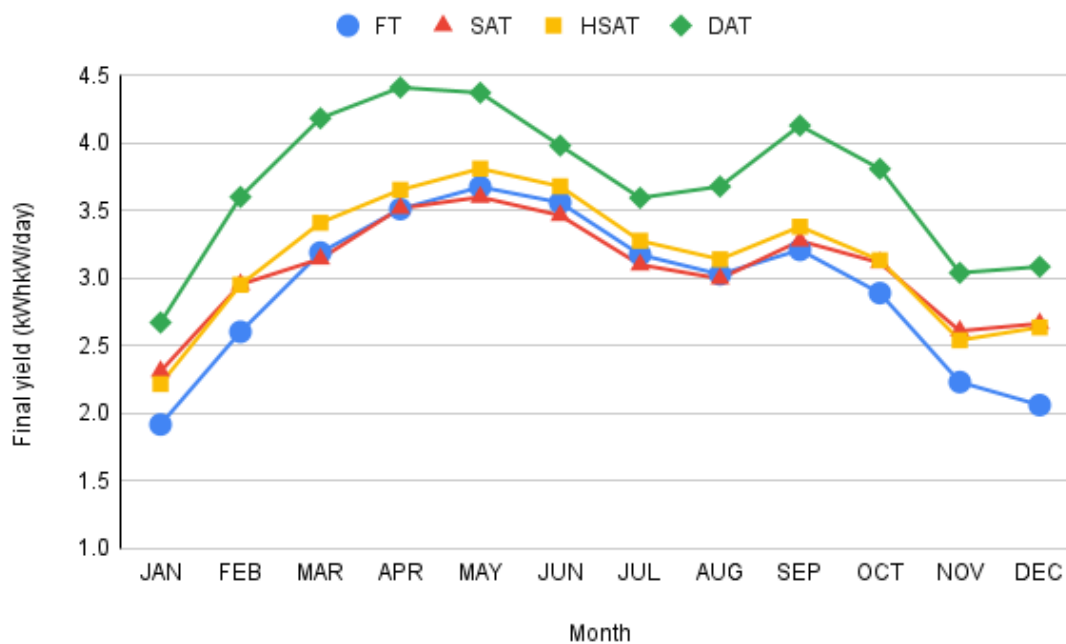
FIGURE 5.10: Monthly final yield of FT, SAT, HSAT, and DAT plants

The monthly variations in the final yields of several photovoltaic (PV) tracker technologies are illustrated in Fig. 5.10. The energy produced by the inverter's output side is referred to as the final yield. Notably, different values surfaced over the months. For the FT, SAT, HSAT, and DAT plants in January, the corresponding minimum final yields were 1.91, 2.31, 2.21, and 2.67 kWh/kW/day. On the other hand, the FT, SAT, HSAT, and DAT plants had top final yields in May of 3.67, 3.60, 3.81, and 4.37 kWh/kW/day, respectively. Averaging across months, the

final yield values for FT, SAT, HSAT, and DAT plants were 2.92, 3.06, 3.15, and 3.71 kWh/kW/day, respectively. The incident solar radiation on the PV array typically increases from January to May, resulting in a corresponding boost in output energy. However, beyond the midpoint of the year, the PV arrays receive reduced incident solar energy, leading to a decrease in production yield.

5.6.6   Reference Yield

Fig.5.11 illustrates variations in monthly reference yields among different photovoltaic (PV) tracker technologies. Observations revealed distinct reference yield values across different months.
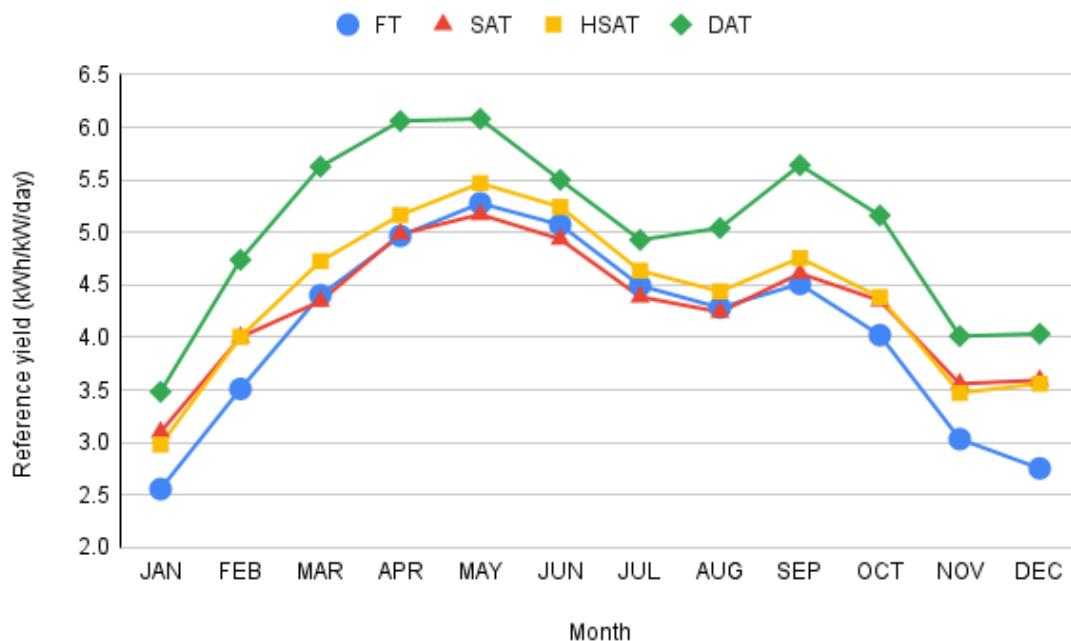
FIGURE 5.11: Monthly reference yield of FT, SAT, HSAT, and DAT plants

In January, the FT, SAT, HSAT, and DAT plants recorded minimum reference yields of 2.55, 3.1, 2.98, and 3.81 kWh/kW/day, respectively. Conversely, the maximum reference yields occurred in May, reaching 5.27, 5.17, 5.46, and 6.08 kWh/kW/day for the FT, SAT, HSAT, and DAT plants, respectively. On average, the reference yield values for the FT, SAT, HSAT, and DAT plants were 4.07, 4.27,

134 *Chapter 5. ENHANCEMENT OF ENERGY YIELD IN FLOATING SOLAR PV PLANT USING DIFFERENT TRACKING CONFIGURATIONS*

4.40, and 5.02 kWh/kW/day, respectively. The PV module calculates the reference yield based on incident solar radiation. From January to May, solar radiation rises due to longer days, whereas it decreases in the monsoon and winter seasons because of shorter days.

5.6.7   Array Capture Loss

Fig.5.12 illustrates the monthly array losses for four distinct solar photovoltaic (PV) tracking technologies.
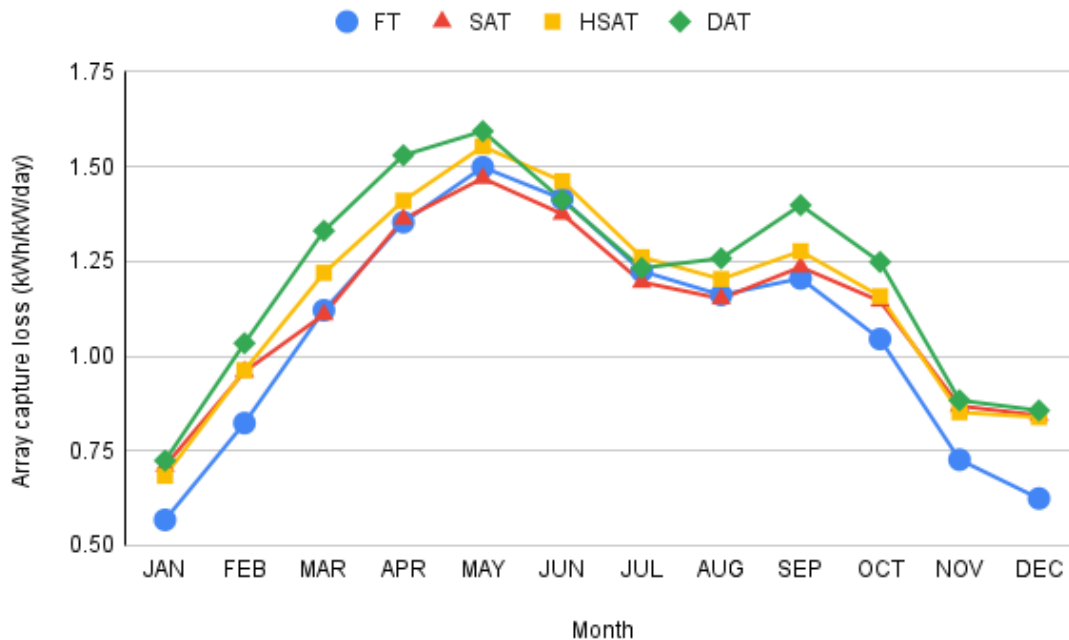
FIGURE 5.12: Monthly array side loss of FT, SAT, HSAT, and DAT plants

The SAT plant shows array losses ranging from 1.46 kWh/kW/day in May to 0.70 kWh/kW/day in January. For the HSAT plant, losses peak at 1.55 kWh/kW/day in May and drop to 0.68 kWh/kW/day in January. The DAT plant records the highest array loss of 1.59 kWh/kW/day in May and 0.72 kWh/kW/day in January. Annual average panel-side losses are 0.08, 0.09, 0.10, and 0.12 kWh/kW/day for FT, SAT, HSAT, and DAT plants, respectively. Array

capture loss, largely driven by shading and dirt accumulation, notably intensifies during Chandigarh's dry May season, further reducing performance.

5.6.8   Inverter Loss

Fig.5.13 shows monthly system losses for four PV tracking technologies. FT losses range 0.01–0.06 kWh/kW/day, SAT 0.07–0.10, HSAT 0.07–0.10, and DAT 0.08–0.11, with annual averages of 0.08, 0.09, 0.09, and 0.10 kWh/kW/day, respectively. Losses arise from PV module and inverter degradation, mismatch, cable/transmission losses, and temperature effects.
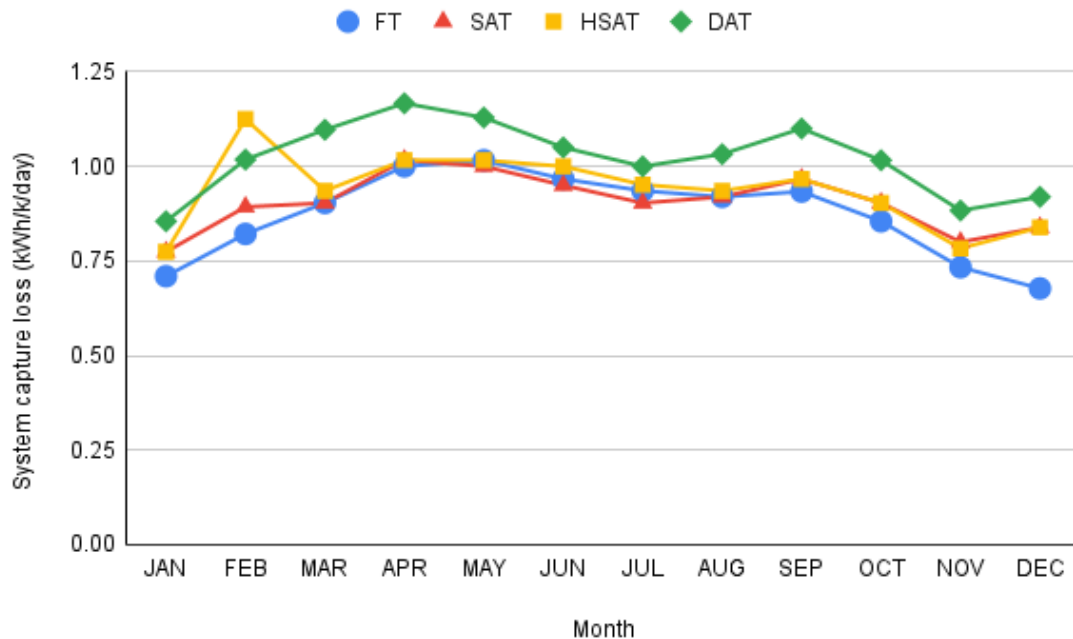
FIGURE 5.13: Monthly inverter losses of FT, SAT, HSAT, and DAT plants

5.6.9   Solar PV Module Efficiency

Fig.5.14 graphically illustrates the monthly average efficiencies for four distinct solar photovoltaic (PV) tracking technologies. Specifically, the FT plant's panel efficiency (η_{PV}) varies from 14.79% in May to 16.06% in January. Similarly, the SAT plant displays an efficiency range of 14.79% in May to 15.92% in January.

Chapter 5. ENHANCEMENT OF ENERGY YIELD IN FLOATING SOLAR PV PLANT USING DIFFERENT TRACKING CONFIGURATIONS

Notably, the HSAT plant registered the lowest efficiency of 14.80% in May and the highest efficiency of 15.85% in January. Meanwhile, the DAT plant demonstrates an efficiency range from 14.76% in May to 15.83% in January. Additionally, the annual average panel efficiencies for the FT, SAT, HSAT, and DAT plants are 15.28%, 15.15%, 15.25%, and 15.20%, respectively.

The improvement in PV module efficiency indicates a higher conversion rate for incident sunlight into electricity. However, in Chandigarh, as May approaches, the onset of hot weather leads to a decrease in PV module efficiency. The negative temperature coefficient of solar PV modules, which reduces the efficiency of PV cells as temperatures rise, is the cause of this decline.
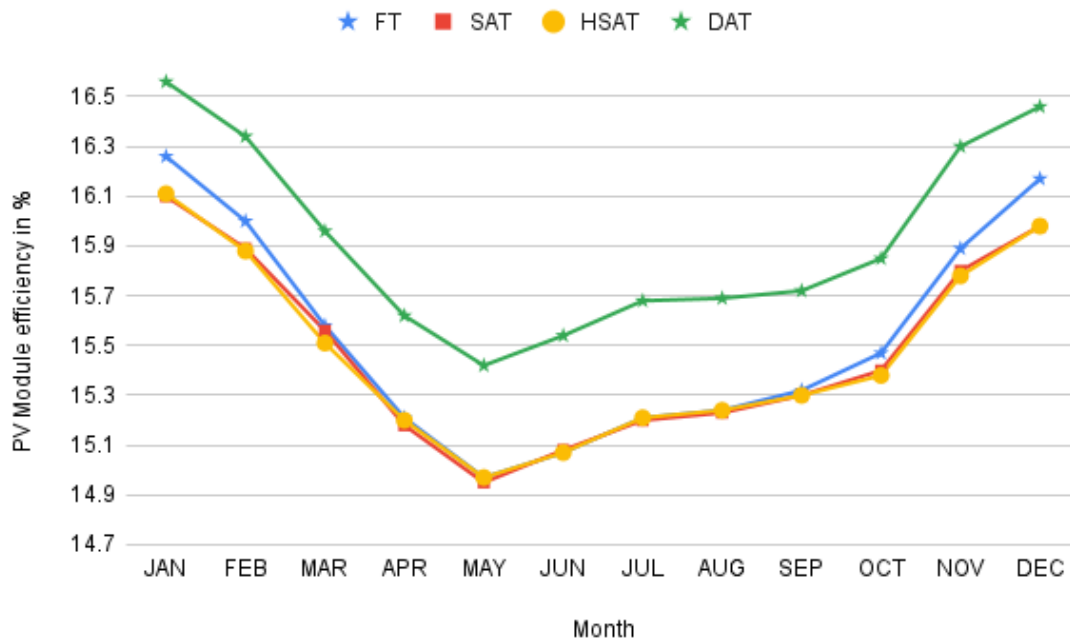
FIGURE 5.14: Monthly PV module efficiency of FT, SAT, HSAT, and DAT plants

5.6.10   Plant Efficiency

Fig.5.15 depicts the monthly average plant efficiencies of four distinct solar photovoltaic (PV) tracking technologies. The FT plant's system efficiency η_{sys} fluctuates from 14.56% in May to 15.68% in January. Similarly, the SAT plant

5.6. Results and Discussions   137

exhibits an efficiency range of 14.56% in May to 15.60% in January. Notably, the HSAT plant recorded the lowest efficiency of 14.58% in May and the highest efficiency of 15.56% in January. Meanwhile, the DAT plant demonstrates an efficiency range from 15.04% in May to 16.03% in January, as illustrated in Fig.5.15. Additionally, the annual average panel efficiencies for the FT, SAT, HSAT, and DAT plants are 15.01%, 15.04%, 15.02%, and 15.50%, respectively. System efficiency denotes the overall efficiency of the plant, which is primarily reliant on the efficiency of PV modules. An increase in PV module efficiency corresponds to a rise in system efficiency; conversely, a decrease in PV module efficiency leads to a decline in system efficiency.
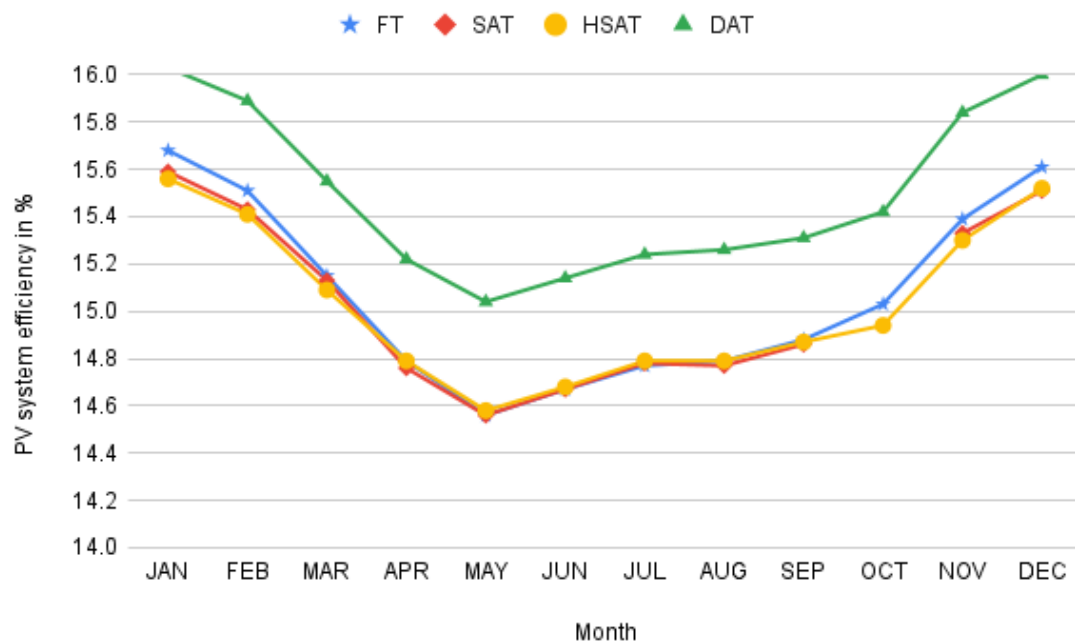
FIGURE 5.15: Monthly system efficiency of FT, SAT, HSAT, and DAT plants

5.6.11   Analysis of Energy losses

Predicting energy losses with high accuracy in a photovoltaic (PV) system is challenging, but it is crucial for designing and installing an appropriately sized PV system that accounts for all factors contributing to energy loss. The

Chapter 5. ENHANCEMENT OF ENERGY YIELD IN FLOATING SOLAR PV PLANT USING DIFFERENT TRACKING CONFIGURATIONS

anticipated energy losses at the proposed site over a year, as determined by the PVsyst simulation methodology are presented in Table 5.2.

TABLE 5.2: Energy Losses in FT, SAT, HSAT, and DAT Plants

| Description	FT Plant	SAT Plant	HSAT Plant	DAT Plant
Global incident on array	+4.2%	+8.6%	+11.6%	+26.2%
IAM factor on global	-2.85%	-2.14%	-1.92%	-1.07%
Soiling loss factor	-4.00%	-4.00%	-4.00%	-4.00%
Module degradation loss	-9.80%	-9.80%	-9.80%	-9.80%
PV loss due to irradiance level	**-0.87**%	**-0.78**%	**-0.72**%	**-0.48**%
PV loss due to temperature	-5.96%	-6.07%	-6.24%	-6.60%
Module quality loss	-3.00%	-3.00%	-3.00%	-3.00%
Light-induced degradation	-2.50%	-2.50%	-2.50%	-2.50%
Mismatch losses	-6.42%	-6.42%	-6.42%	-7.42%
Ohmic wiring loss	-0.96%	-1.01%	-1.03%	-1.12%
Inverter loss	-1.54%	-1.52%	-1.50%	-1.42%
Auxiliaries' losses	-0.20%	-0.20%	-0.19%	-0.16%
Medium voltage loss	-1.18%	-1.17%	-1.19%	-1.16%

Energy losses ranged from -0.16% (auxiliaries) to -9.80%, with AC ohmic losses on the inverter side at 1.07%. Module orientation significantly affects incident solar radiation, with increases of +4.2%, +8.5%, +11.6%, and +26.2% for FT, SAT, HSAT, and DAT plants, respectively. FT plants receive less radiation due to fixed arrays, while DAT plants maximize capture via vertical and horizontal tracking. PV losses from irradiance deviations are 0.87%, 0.78%, 0.72%, and 0.48% for FT, SAT, HSAT, and DAT plants, respectively, with DAT plants achieving the highest radiation and lowest irradiance loss.

5.6.12   Effect of Ambient Temperature on Various Performance Parameters of DAT Plant

Ambient temperature strongly impacts solar PV performance.   Due to the negative temperature coefficient of modules, higher temperatures reduce efficiency, lowering power output and energy generation. Elevated temperatures also affect key metrics Performance Ratio (PR), Capacity Factor (CF), and Plant Load Factor (PLF) used to assess the DAT plant's overall effectiveness and reliability.

5.6.12.1 Impact of Ambient Temperature on Capacity Factor

Fig.5.16 shows a moderate positive correlation (R^2 = 0.54) between ambient temperature and the DAT plant's CUF, with higher summer temperatures and longer daylight increasing CUF. The linear regression model is given in equation (5.30).

$$y = 0.2374x + 9.9245 \tag{5.30}$$
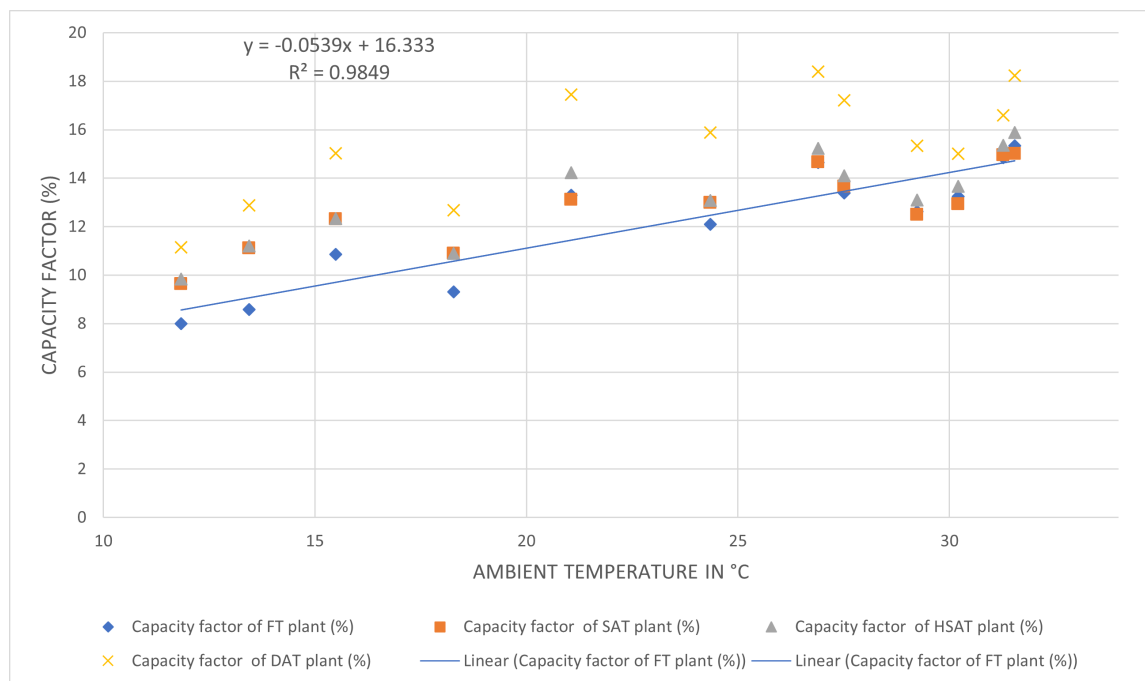
FIGURE 5.16:   Variation of capacity factor due to ambient temperature in DAT plants

Chapter 5.   ENHANCEMENT OF ENERGY YIELD IN FLOATING SOLAR PV PLANT USING DIFFERENT TRACKING CONFIGURATIONS
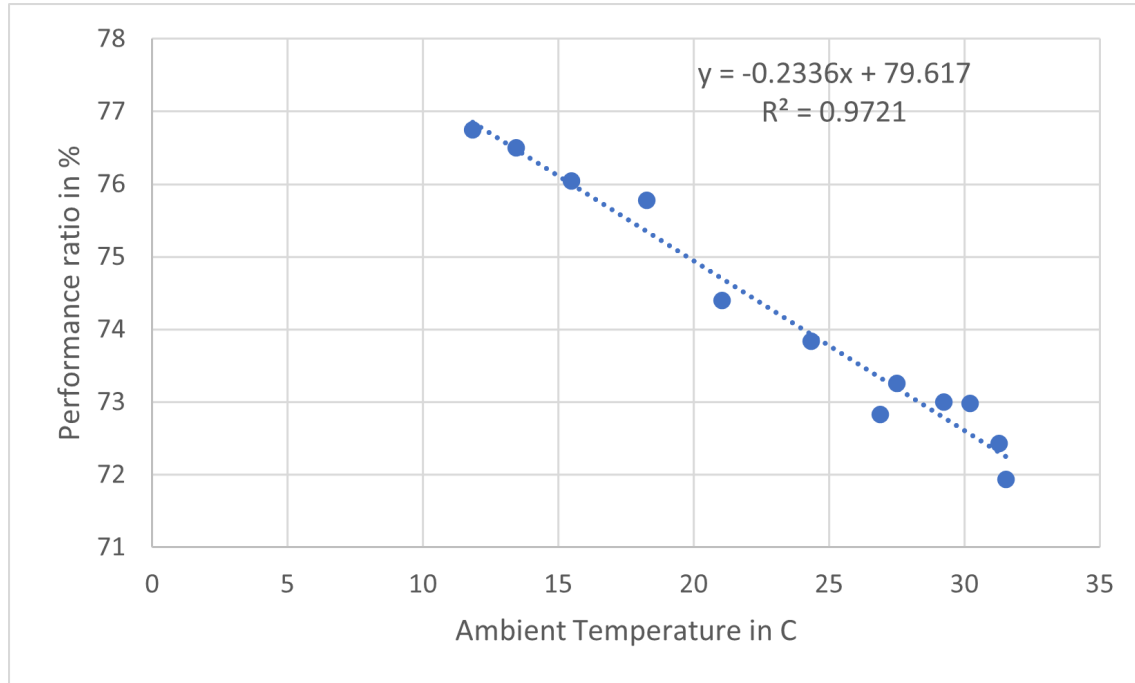
FIGURE 5.17:   Deviation of performance ratio due to ambient temperature in DAT plants

Ambient temperature affects the capacity factor of FSPV plants, which generally rises with increasing temperature. Optimal capacity factors are observed when ambient temperatures are between 25–30°C.

5.6.12.2 Impact of Ambient Temperature on Performance Ratio of Plant

Fig.5.17 shows the inverse relationship between ambient temperature and the performance ratio (PR) of a solar plant. The DAT plant outperforms FT by capturing more solar radiation, reducing angle-of-incidence losses. Rising temperatures lower module and inverter efficiency, decreasing energy output and the overall PR.

The expression for the correlation between the performance ratio and the ambient temperature is shown in equation (5.31).

$$y = -0.2336x + 79.617 \tag{5.31}$$
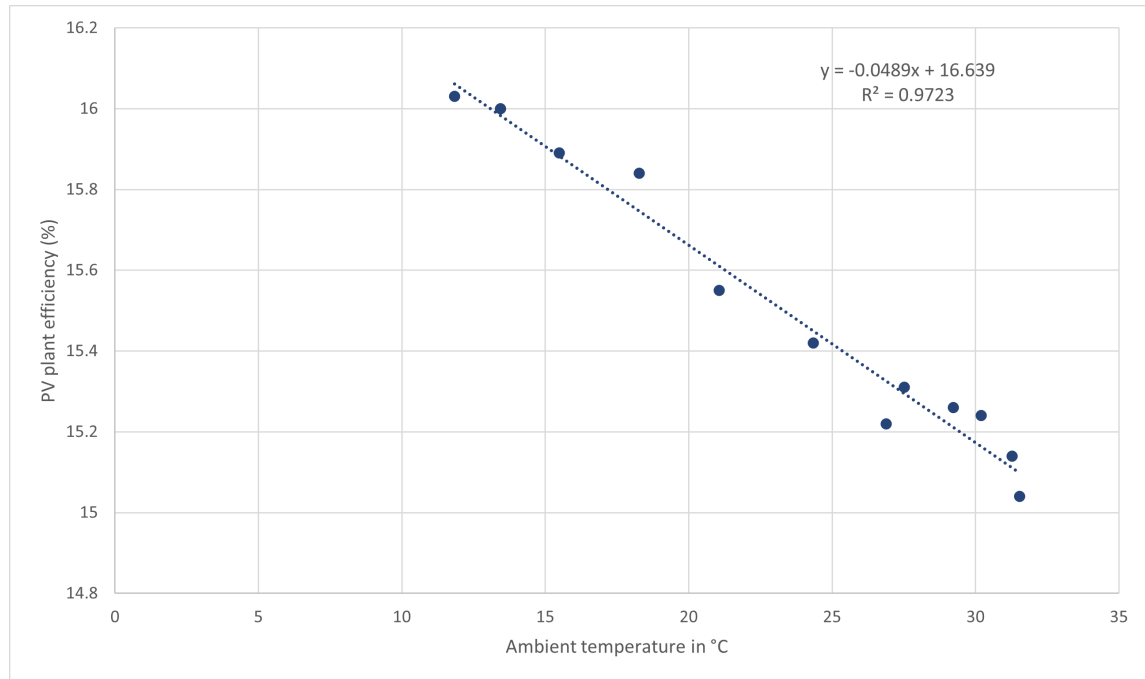
FIGURE 5.18: Impact of ambient temperature on the PV module efficiency of DAT plants

5.6.12.3 Impact of Ambient Temperature on Solar PV Module and Plant Efficiency

Fig.5.18 plots the monthly average efficiency of the PV module against the ambient temperature at the location. The graph shows a clear trend, indicating a strong correlation between module efficiency and ambient temperature. Statistical analysis confirms this, with a correlation coefficient (R^2) of 0.9723, highlighting a strong negative relationship. This suggests that as ambient temperature rises, the PV module efficiency declines. The regression equation describing this relationship is presented in (5.32), providing a quantitative basis for predicting efficiency variations with temperature.

$$y = -0.0489x + 16.34 \qquad (5.32)$$

where y is the PV module's efficiency and x represents the independent variable, ambient temperature. Almost every point on the regression line indicates that there is a direct proportionality between the two variables.
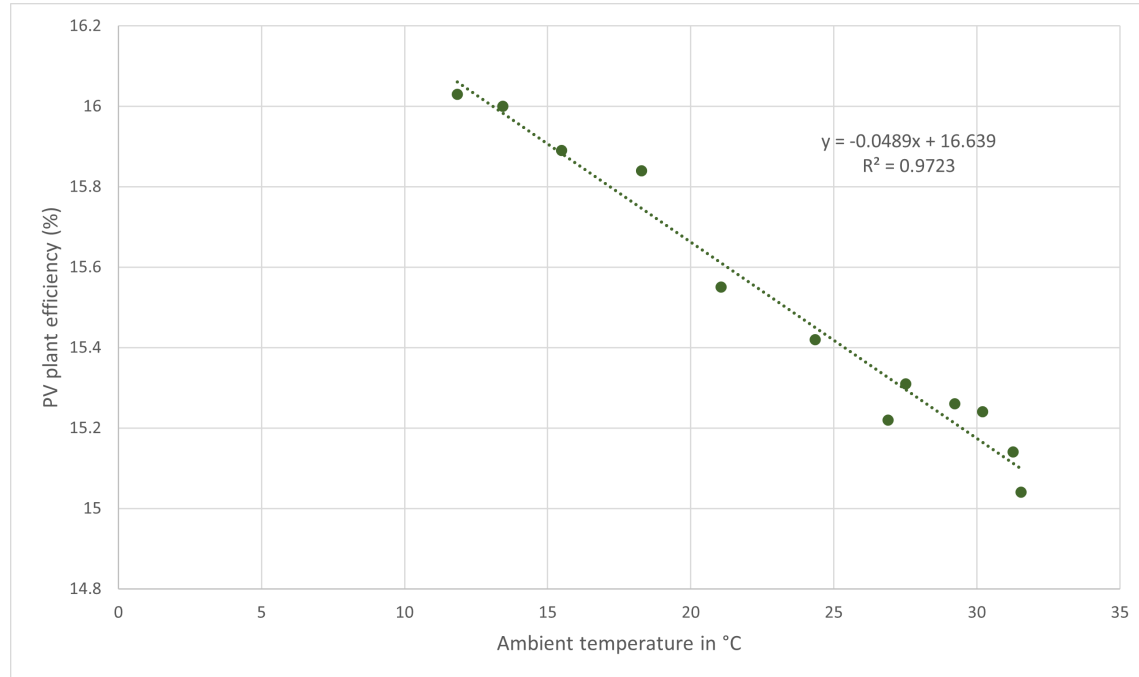
FIGURE 5.19: Impact of ambient temperature on the performance of
plant efficiency of DAT plants

Fig.5.19 shows the plant's monthly average efficiency values plotted against
the ambient temperature at the location. This graph illustrates the negative
relation between plant efficiency and ambient temperature. The correlation
coefficient between ambient temperature and plant efficiency is 0.97, which
indicates that the relationship between plant efficiency and ambient temperature
is somewhat positive. The regression equation in (5.33).

$$y = -0.0489x + 16.339 \qquad (5.33)$$

x signifies independent variable ambient temperature, and y signifies dependent
variable plant efficiencies.

5.6.13   Probability Distribution Analysis of Solar Trackers

Additionally, PVsyst performs a probability distribution analysis to evaluate the
system's total annual energy output, potentially affecting its integration into the
grid network. Multiple factors influence the variability in the probability

5.6. Results and Discussions   143

distribution of the production forecast for the plant.The uncertainties of PV modules, inverters, soiling, mismatch uncertainties, and degradation are 1.0%, 0.5%, 1.0%, 0.5% 1.0%, and 1.0% respectively. The probability law posits that over the numerous years of operation of the PV system, the distribution of annual yield will adhere to a statistical law, with the assumption that this law follows a normal or Gaussian distribution.

The P50-P90 metric delineates varying levels of yield, signifying the probabilities that the production for a given year exceeds these values by 50%, 90%, and 95% respectively. The probability distribution analysis for all the considered cases PV plant's energy generation forecast is shown in Fig.5.20.

FIGURE 5.20: Probability distribution analysis for FT, SAT, HSAT, and DAT plant

Based on simulation results, the anticipated annual production probabilities for the FT plant are as follows: P50 = 2134 MWh, P90 = 1986 MWh, and P95 = 1944 MWh, with a variance of 115 MWh. Similarly, for the SAT plant, the figures are

144

*Chapter 5.   ENHANCEMENT OF ENERGY YIELD IN FLOATING SOLAR PV
PLANT USING DIFFERENT TRACKING CONFIGURATIONS*

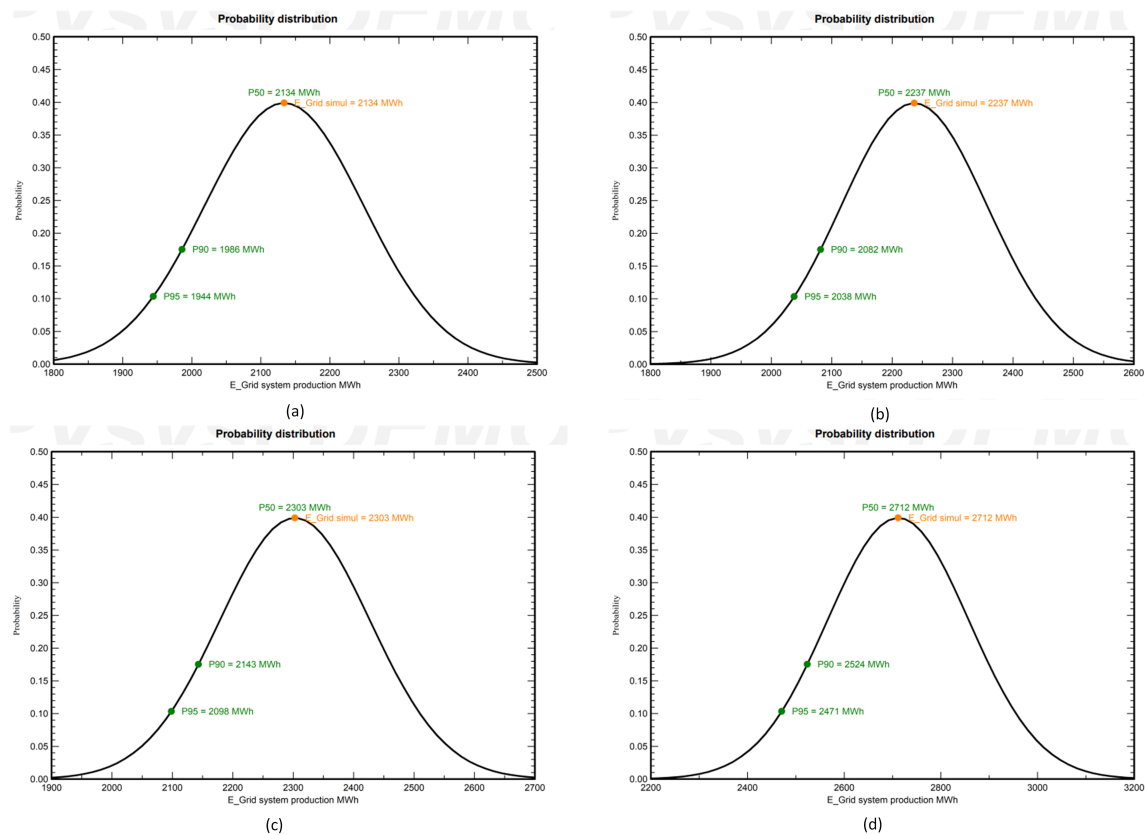2237 MWh, 2082 MWh, and 2038 MWh with variability of 121 MWh, whereas for the HSAT plant, they are 2303 MWh, 2143 MWh, and 2098 MWh with variability of 124 MWh. Regarding the DAT plant, the yearly production probabilities for P50, P90, and P95 are 2712 MWh, 2524 MWh, and 2471 MWh, respectively, with variability of 147 MWh.

P50 serves as a reference point or center for analysis. The statistic offers a measure of the most typical value in a dataset and is commonly seen as a reliable indicator, particularly in cases when the data may be skewed. The average energy generation by the FT, SAT, HSAT and DAT plant is 2134 MWh, 2237 MWh, 2303 MWh and 2712 MWh respectively.

5.7   Concluding Remarks

In this chapter, the performance of a a 2 MW_P floating solar photovoltaic (PV) system has been discussed using different types of tracking technologies. The investigation encompassed PV module efficiency (η_{PV}), plant efficiency (η_{Plant}), array capture losses (L_A), and system losses (L_S). We obtained the outcomes through simulations using PVsyst software, which incorporated technical specifications, design parameters, and site-specific weather conditions.

The performance analysis revealed variation in monthly and annual efficiencies for different tracking technologies. Panel efficiency (η_{PV}) and system efficiency (η_{Plant}) fluctuated across months, with annual averages ranging from 14.97% to 16.56% and 14.56% to 16.03%, respectively. Additionally, array capture losses (L_A) and system losses (L_S) were illustrated, showcasing the impact of inefficiencies within the PV array and the DC-to-AC conversion process on overall system performance.

The subsequent results and discussions delved into the comparative performance of seasonal adjustable tracking (SAT), horizontal single-axis tracking (HSAT), and dual-axis tracking (DAT) configurations. A comprehensive analysis included monthly solar irradiation, capacity factors, and energy generation. DAT configuration demonstrated superior performance, yielding energy production gains of 4.59%, 7.34%, and 21.32% compared to FT, SAT, and HSAT, respectively.

5.7. Concluding Remarks   145

The study finds that dual-axes solar tracking (DAT) plants offer better performance compared to FT, SAT, and HSAT plants.

Chapter 6

IMPROVING ENERGY OUTPUT IN FLOATING SOLAR PV PLANTS VIA INVERTER LOADING RATIOS

6.1 Introduction

The growing demand for clean and renewable energy has made solar power one of the most promising solutions for sustainable electricity generation. Among various solar technologies, floating solar power plants have gained attention for their ability to maximize space utilization while reducing water evaporation and improving panel efficiency.

The inverter loading ratio (ILR) is a key factor in optimizing solar power systems' performance. It determines how efficiently the system converts solar energy into usable electricity. While a higher ILR can increase energy production, excessive values may lead to power losses due to inverter limitations. Therefore, finding the right balance is essential to maximizing efficiency and minimizing energy wastage.

So far, all studies related to inverter loading ratio (ILR) have been conducted on ground-mounted solar power plants. There has been no significant work on ILR in the context of floating solar PV plants. In this study, various inverter loading ratios have been analyzed specifically for floating solar installations, including both technical performance assessment and economic analysis.

This study explores the impact of different ILRs on floating solar PV systems by analyzing energy production, efficiency, and economic feasibility. The findings

148

Chapter 6. IMPROVING ENERGY OUTPUT IN FLOATING SOLAR PV PLANTS VIA INVERTER LOADING RATIOS
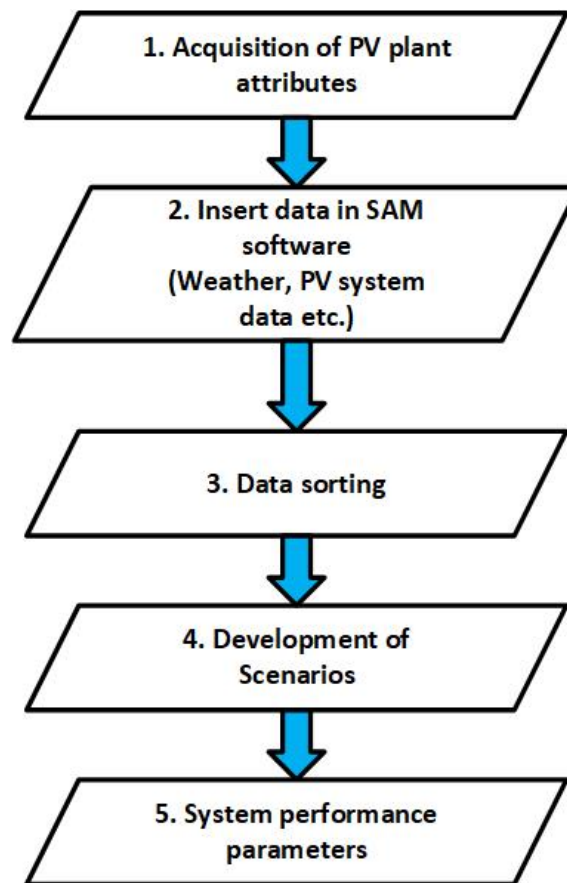
FIGURE 6.1: Flow diagram of System Advisor Model (SAM)

aim to provide useful insights for engineers and policymakers to improve the design and performance of floating solar PV plants.

6.2 Methodology

This study investigates the influence of varying DC to AC ratios on the performance of a commercial-scale floating solar photovoltaic (FSPV) plant located in Chandigarh, India. The simulation-based analysis was carried out using the System Advisor Model (SAM), version 2020.2.29, developed by the National Renewable Energy Laboratory (NREL), USA. The overall modeling framework adopted in this study is illustrated in Fig. 6.1.

A key parameter explored in this analysis is the DC to AC ratio, also referred to as the Inverter Loading Ratio (ILR). This ratio is defined as the quotient of the

total installed DC capacity of the PV array to the rated AC capacity of the inverter, and is mathematically expressed as:

$$\text{DC to AC ratio (ILR)} = \frac{P_{\text{DC, STC}}}{P_{\text{AC, rated}}} \tag{6.1}$$

where $P_{\text{DC, STC}}$ is the total DC power output of the photovoltaic modules under standard test conditions (STC), and $P_{\text{AC, rated}}$ is the nominal AC power rating of the inverter. The ILR is a critical design parameter that influences the energy yield, inverter utilization, clipping losses, and overall techno-economic performance of the system. A higher ILR may improve energy capture under low irradiance but can result in energy clipping during periods of peak insolation due to inverter capacity limitations.

The simulation was conducted for multiple ILR configurations by adjusting the PV array sizing relative to inverter capacities. Site-specific meteorological data comprising global horizontal irradiance (GHI), ambient temperature, wind speed, and albedo were employed, alongside detailed system parameters such as module characteristics, inverter efficiency, and losses due to soiling, mismatch, and wiring. These datasets were preprocessed to ensure completeness, consistency, and compatibility with the SAM simulation environment.

To assess the robustness of the simulation outputs, a comprehensive sensitivity analysis was performed. Key input variables were systematically perturbed within realistic operational bounds to evaluate their impact on essential performance indicators, including annual energy generation, performance ratio (PR), capacity factor (CF), clipping loss, and levelized cost of energy (LCOE). This analysis facilitated the quantification of input uncertainty propagation and enabled the derivation of confidence intervals for the simulation results.

Finally, the simulation outcomes were cross-verified against theoretical expectations and validated through comparison with published literature benchmarks. The following subsections describe the system configuration, data acquisition and preprocessing methodologies, modeling approach, scenario definitions, and the evaluation of system performance metrics.

Chapter 6. IMPROVING ENERGY OUTPUT IN FLOATING SOLAR PV PLANTS VIA INVERTER LOADING RATIOS

6.2.1   Characteristics of FPV system Components

The floating photovoltaic (PV) system is situated in a town in Chandigarh, India, and was commissioned in 2023. The system has a capacity of 2 MWp and is composed of 3,704 solar PV modules, each with a rating of 350 Wp, installed on a floating platform with an azimuth angle of 0° and a tilt angle of 10°. The outline of the characteristics of the rated PV module (monofacial module; model JKM-540M-72HL4-TV). The module rated power is 540 W and the open circuit voltage, short circuit current, Maximum Power Voltage, Maximum Power Current and efficiency of the module is 37.38 V, 18.18 A , 31.46 V, 17.17 A and 20.7 % respectively are presented in Table 2 in Appendix.

The specifications of the solar inverter installed, which has a 125 kW capacity are presented in Table 4 in Appedix. This inverter is designed for use in self-consumption systems and is equipped with two MPPTs that have a broad operational range, as well as a 5-year product warranty. It includes a metering system to monitor solar PV parameters at both the array level and the inverter output.

6.2.2   Simulation Input for SAM Software

The 2 MW FPV plant located in Sector 39, Chandigarh, situated approximately 8 km west of the city center. The site is positioned at geographic coordinates 35° 75′ 22″ N latitude and 76° 72′ 85″ E longitude and covers an area of 0.45 km². The average daily global horizontal irradiance (GHI) at the site is 4.09 kWh/m², with an average wind speed of 7.5 m/s and an ambient temperature of 23.8 °C. Table 5 provides solar radiation, temperature, and wind velocity data for Chandigarh, sourced from Metronorm 8.1 software. Meteonorm 8.1 was chosen as the GHI data source due to its long-term historical data (since 1981) and hybrid approach, combining ground-based and satellite data for improved accuracy.

Several key parameters related to the PV system configuration, inverter characteristics, system design, and loss assumptions were considered. These parameters ensure a realistic assessment of system performance under varying operational conditions. A summary of the input parameters used in the SAM simulation is provided in Table 6.1.

TABLE 6.1: Input parameters used in SAM simulation

Parameter Type	Description
Meteorological Data	Solar irradiation, ambient temperature, wind speed
PV Module Specifications	Model type, rated power, efficiency, temperature coefficient, degradation rate
Inverter Characteristics	Rated AC power, MPPT voltage range, maximum efficiency
System Design Factors	DC to AC ratio (ILR), tilt angle, azimuth angle, ground coverage ratio
Loss Assumptions	Soiling losses, wiring losses, degradation losses, shading factors

The SAM simulations were conducted at an hourly temporal resolution, which matches the resolution of the real energy output data recorded by the plant's data logger. While sub-hourly simulations may better capture momentary clipping events, the use of hourly data ensures consistency between simulated and measured datasets, providing a valid basis for performance comparison.

The data for this study was collected through a combination of onsite visits and an installed data logger. The data logger continuously recorded key performance parameters, including energy generation, solar irradiance, and ambient temperature. The data for this study was collected through a combination of onsite visits and an installed data logger. The data logger continuously recorded key performance parameters, including energy generation, solar irradiance, and ambient temperature. To verify and direct inspection site, the authors conducted field visits to the site in Year 2023 and 2024.

6.2.3 Data Preprocessing Methods

The energy consumed by the load, E_{L}, is calculated through an energy balance, as outlined in equation (6.2).

$$E_L = E_{\text{PV}} - E_{\text{G}} \tag{6.2}$$

The grid energy E_{G}, is positive when energy is fed into the grid and negative when energy is drawn from it. It is important to note that E_{L} remains positive when the PV system is not generating power, and E_{G} becomes negative when there is an energy demand. The self-consumed energy from the PV system, E_{PV}, is derived using equation (6.3).

$$E_{\mathrm{PV\,load}} = \begin{cases} E_{\mathrm{PV}} - E_{\mathrm{G}} & \text{if } E_{\mathrm{G}} > 0 \\ E_{\mathrm{PV}} & \text{if } E_{\mathrm{G}} \leq 0 \end{cases} \tag{6.3}$$

Here, E_{PV} indicates the energy produced by the PV system, while E_{G} refers to the grid energy. According to equation (6.3), when there is excess energy, the PV system produces more energy than needed to satisfy the demand, leading to surplus energy being fed into the grid ($E_{\mathrm{G}} > 0$). Conversely, when the system fails to meet the demand, the grid provides the additional energy required, as reflected by $E_{\mathrm{G}} < 0$.

6.2.4   Case Study Considering Different ILRs

To assess the effects of varying DC to AC ratios, simulations of seven different DC to AC ratio scenarios for 2 MW floating solar PV plant were performed as in Table 6.2. The current DC to AC ratio of the PV system is 1. To increase the DC to AC ratio, the rated DC capacity of the solar array was maintained constant, while the rated AC output capacity of the inverter was reduced.

The physical layout, module spacing, and overall footprint of the floating structure do not change across scenarios. Therefore, environmental impacts typically associated with oversizing—such as increased self shading due to tighter module spacing or elevated thermal loading on the platform are not applicable in this case.

The decision to vary the inverter loading ratio (ILR) by reducing the inverter AC output rather than oversizing the DC capacity was primarily methodological, aimed at isolating the impact of inverter sizing on performance metrics while maintaining a fixed PV generation profile. This approach ensured that the same PV system characteristics (orientation, irradiance exposure, and module type) were retained across scenarios, allowing a clearer comparison of

TABLE 6.2: DC to AC power ratios for different DC to AC ratios

Energy generation in MW(P_{AC})	DC to AC Ratio($R_{\text{DC-AC}}$)
1.81	1.11
1.56	1.28
1.38	1.45
1.20	1.67
1.09	1.85
0.99	2.04
0.90	2.22

clipping losses, energy yield, and LCOE solely as functions of ILR. In this study, the inverter DC to AC power ratio (ILR) is defined by equation (6.4).

$$ILR = \frac{P_{\text{DC}}}{P_{\text{AC}}} \tag{6.4}$$

where P_{DC} represents the input power from the PV arrays to the solar inverter, and P_{AC} denotes the output power of the solar inverter, which is the energy supplied by the entire PV system.

The ILR values considered in this study are 1.11, 1.28, 1.45, 1.67, 1.85, 2.04, and 2.22. This set was chosen to systematically assess the performance and economic impact of increasing DC-to-AC ratios.

To accurately assess the impacts of inverter clipping, several assumptions were implemented. The system was configured with a double subarray, excluding both self-shading and external shading effects. DC losses were estimated at 4.4%, with 2% attributed to module mismatch and 2% to DC wiring losses. Furthermore, AC losses of 1%, resulting from wiring, were incorporated into the analysis. A soiling loss of 5% was considered for the floating solar PV plant. Although FPV systems generally exhibit lower soiling rates compared to ground-mounted systems due to the cooling and dust-suppressing effect of the water body, the selected value accounts for potential bird droppings, pollen accumulation, and limited cleaning frequency observed in the specific project location.

6.2.5   System Performance

To comprehensively evaluate the influence of varying the DC to AC ratio, simulation results were analyzed across annual, monthly, and daily timescales, capturing both long-term and short-term performance dynamics of the photovoltaic system. This study focused on two optimization criteria: enhancing the performance ratio as an energy-related measure and reducing the levelized cost of energy (LCOE) as an economic measure. The total system generation was determined by summing the inverter's AC output throughout the year, considering AC losses.

To evaluate the results, several energy metrics were utilized. The capacity factor (CF, %) is calculated as the ratio of the system's anticipated electrical output during its first year of operation to its nameplate capacity. This metric indicates the amount of energy the system would generate if it operated at its nameplate capacity continuously throughout the year.   Therefore, for photovoltaic (PV) systems, the capacity factor represents the AC-to-DC ratio, as demonstrated in equation (6.5):

$$CF = \frac{E_{\text{AC total}}}{P_{\text{DC}} * 24 * 365} \tag{6.5}$$

Here, $E_{\text{AC,total}}$ represents the net annual energy output in kWh/year, P_{DC} denotes the DC nameplate capacity of system in kW, and 24 * 365 corresponds to the total number of hours in a year.

Power lost due to clipping (P_{clip} in MW) refers to the power limit loss that occurs when the AC power output of inverter surpasses the nameplate AC capacity of inverter during specific time steps. During these periods, SAM adjusts the inverter output to match the inverter-rated capacity without altering the inverter's input voltage. The total generation loss due to clipping is the cumulative sum of P_{clip} over time, as described by equation (6.6):

$$P_{\text{clip}} = \begin{cases} P_{\text{AC}} - P_{\text{AC,rated}}, & \text{if } P_{\text{AC}} > P_{\text{AC,rated}} \\ 0, & \text{if } P_{\text{AC}} \leq P_{\text{AC,rated}} \end{cases} \tag{6.6}$$

where P_{AC} represents the AC power generation, and $P_{AC,rated}$ denotes the rated capacity of inverter.

The inverter model equation employed by SAM to calculate the AC power (P_{AC}) is given by equation (6.7). Additionally, SAM assumes the inverter operates in night mode when the DC input power is less than the operating power losses ($P_{DC} < P_{SO}$). Under these conditions, equation (6.8) is applied.

$$P_{AC} = \frac{P_{AC,rated}}{P_{DC,rated} - P_{S,0}} \cdot (P_{DC} - P_{SO,0})^2 \tag{6.7}$$

where $P_{AC,rated}$ represents the maximum AC power, $P_{DC,rated}$ denotes the rated maximum DC power of inverter, $P_{S,0}$ is the power consumption during operation, and $P_{SO,0}$ is the inverter's power consumption loss.

$$P_{AC} = -P_{nt,0} \tag{6.8}$$

where $P_{nt,0}$ represents the power consumption (in night).

Additionally, the system performance has been assessed using the concept of effective energy. This is defined as the energy obtained from the difference between the overproduction relative to the base case and the clipping losses (E_{clip}), as illustrated in equation (6.9). This equation represents the net gain in usable energy output compared to the base case, after subtracting clipping losses. This metric is proposed by the authors as a practical means to evaluate the real benefit of increasing ILR, considering both increased DC generation and associated energy losses.

$$E_{effective} = (E_{PV} - E_{PV, base case}) - E_{clip} \tag{6.9}$$

where $E_{PV, base case}$ represents the energy generated and supplied by the PV system in the base case, which refers to the current installation configuration with slope of 10°, and a DC to AC ratio of 1.11.

Finally, the discounted payback period (DPB) serves as an economic criterion. It is used to determine the number of years (n) required to reach the break-even point from the initial expenditure, by discounting future cash flows and

Chapter 6. IMPROVING ENERGY OUTPUT IN FLOATING SOLAR PV
PLANTS VIA INVERTER LOADING RATIOS

accounting for the time value of money, as specified in equation (6.10).

$$\sum_y \frac{\Delta I_y}{(1+d)^y} \leq \sum_y \frac{\Delta S_y}{(1+d)^y} \tag{6.10}$$

where y represents the number of years, DPB is the minimum number of years required for the discounted sum of annual net savings to equal the discounted incremental investment costs. Here, ΔI denotes the incremental investment costs, and ΔS represents the annual savings net of future annual costs (e.g., ΔS includes incremental energy costs, incremental non-fuel operation, maintenance, and repair costs, incremental repair and replacement costs, minus incremental salvage costs). The variable d is the annual nominal discount rate, which was considered to be 8.35%.

The LCOE is calculated by dividing the total cost of constructing and operating a power plant over its lifetime by the total electricity generated during the same period. It accounts for all expenses, including initial capital investment, ongoing maintenance, operational costs, and fuel or resource expenditures, as shown in equation (6.11).

$$LCOE = \frac{\sum_{t=1}^{N} \frac{C_t + O_t + F_t}{(1+r)^t}}{\sum_{t=1}^{N} \frac{E_t}{(1+r)^t}} \tag{6.11}$$

where C_t is Capital investment (CAPEX) in year t; O_t is Operational and maintenance costs (OPEX) in year t; F_t is fuel costs in year t (Negligible or zero in case of FSPV plant); E_{AC} is AC energy generated in year t; r is the Discount rate and N is the lifespan of the PV plant (25 Years).

6.3 Results

This section presents the detailed analysis of key performance parameters including energy generation, clipping losses, performance ratio, and capacity factor across different inverter loading ratios (ILRs). All simulations and evaluations were conducted using the System Advisor Model (SAM) software.

The SAM result data files were carefully checked to make sure they were complete and then validated. After validation, calculations were done on the data, and the final dataset was carefully filtered to ensure it was accurate and relevant.

6.3.1 Energy Generation

Fig. 6.2 presents a comparison between the actual AC generation and the simulated output from the SAM model. The largest discrepancy between the real AC generation and the SAM model's estimated energy output occurs in November, with a difference of 197.75 MWh, attributed to unpredictable weather fluctuations.
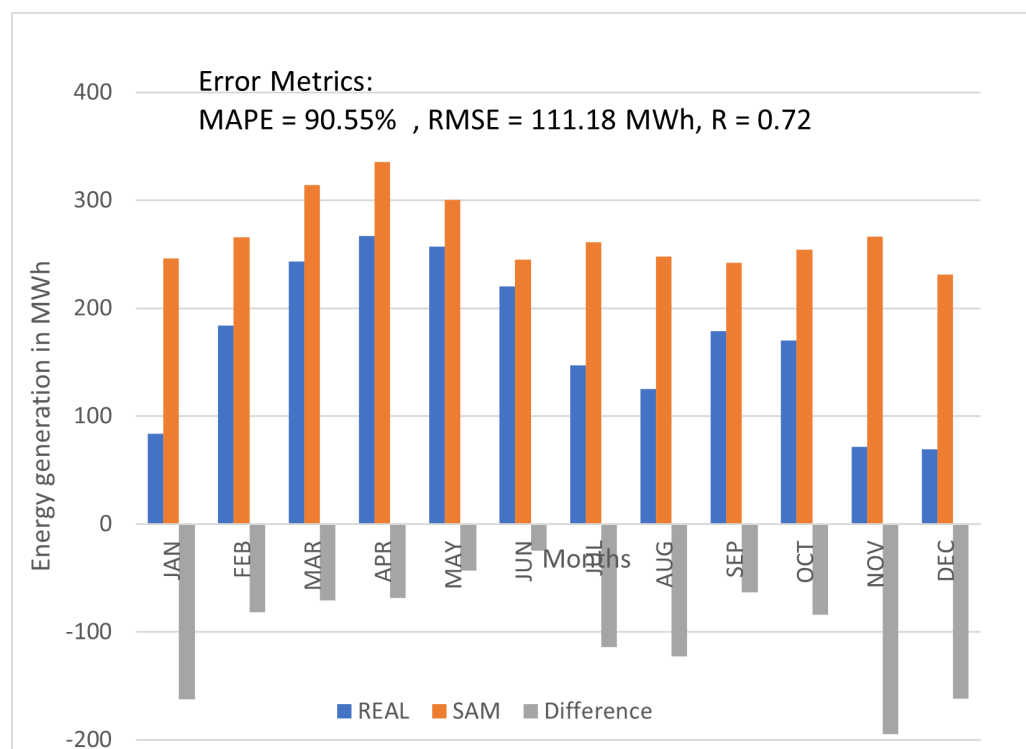

FIGURE 6.2: Real energy generation and energy generation by SAM model

In addition to the visual comparison presented in Fig. 6.2, three statistical error metrics were calculated to quantify the accuracy of the SAM simulation relative to real energy generation data: the Mean Absolute Percentage Error (MAPE), Root

Mean Square Error (RMSE), and the Pearson correlation coefficient (R). MAPE is calculated as the average of the absolute percentage differences between the simulated and actual values, expressed as:

$$\text{MAPE} = \frac{1}{n}\sum_{i=1}^{n}\left|\frac{A_i - P_i}{A_i}\right| \times 100 \qquad (6.12)$$

where A_i and P_i represent the actual and predicted values, respectively. A higher MAPE indicates greater relative error in prediction. RMSE is used to measure the average magnitude of the error and is given by:

$$\text{RMSE} = \sqrt{\frac{1}{n}\sum_{i=1}^{n}(A_i - P_i)^2} \qquad (6.13)$$

It provides an absolute measure of fit in the same units as the original data (MWh). The Pearson correlation coefficient (R) quantifies the linear relationship between actual and predicted values and is computed as:

$$R = \frac{\sum_{i=1}^{n}(A_i - \bar{A})(P_i - \bar{P})}{\sqrt{\sum_{i=1}^{n}(A_i - \bar{A})^2} \cdot \sqrt{\sum_{i=1}^{n}(P_i - \bar{P})^2}} \qquad (6.14)$$

where $\bar{A}$ and $\bar{P}$ are the means of the actual and predicted datasets. R values close to 1 indicate a strong positive correlation.For the current dataset, MAPE, RMSE, and R were found to be 90.55%, 111.18 MWh, and 0.72, respectively. The high MAPE highlights significant overestimation by SAM, especially during low-generation months. RMSE confirms considerable deviations in absolute terms, while the R value indicates a moderately strong positive correlation, suggesting SAM captures the seasonal pattern of energy generation but overestimates its magnitude.

6.3.2   Clipping loss

Fig. 6.3 illustrates the comparison between the actual AC energy generation and the ideal AC energy generation, assuming no clipping losses at the inverter. The term "difference" denotes the clipping loss caused by the inverter.

It is observed that increasing the DC to AC ratio significantly boosts energy generation, although clipping losses begin to occur from a ratio of 1.11 onward.

6.3. Results 159
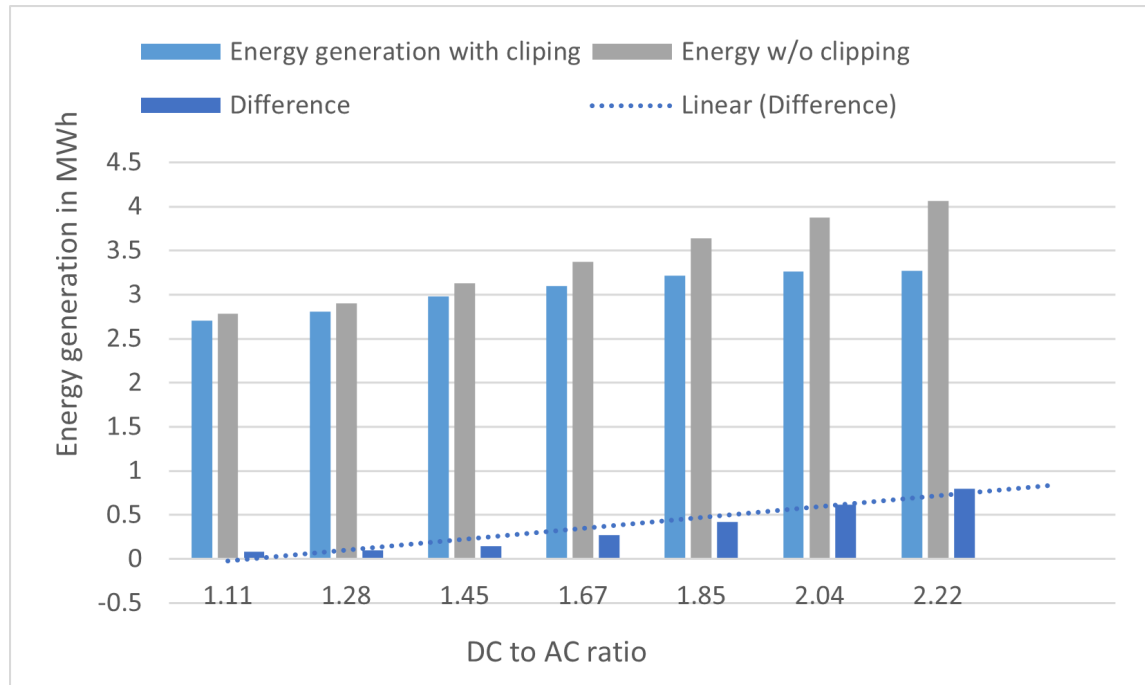
FIGURE 6.3: Comparison of energy generation with and without clipping losses across all ILRs

As the ratio increases, energy production continues to rise, reaching about 4 MWh at a ratio of 2.22. Although clipping reduces some of the potential output, the overall energy yield remains higher at larger DC to AC ratios, indicating that systems with higher ratios can still produce considerably more energy. The linear growth in the gap between clipped and unclipped energy suggests that, up to a certain point, the increased energy production outweighs the clipping losses, making higher DC to AC ratios advantageous for maximizing energy generation in solar PV systems.

At lower DC to AC ratios (e.g., 1.11, 1.28, 1.45, 1.67), the difference in energy generation is minimal, indicating that the system operates efficiently with little or no energy being clipped. However, as the ratio exceeds 1.85, a more noticeable divergence between the clipped and non-clipped values is observed. The linear trendline for the difference emphasizes that clipping losses become progressively significant with higher DC-to-AC ratios.

Therefore, optimizing the DC to AC ratio is critical to balancing energy yield and minimizing losses in systems with high inverter loading ratios.

Chapter 6. IMPROVING ENERGY OUTPUT IN FLOATING SOLAR PV PLANTS VIA INVERTER LOADING RATIOS

6.3.3   Performance Measures

Fig. 6.4 illustrates the relationship between the DC to AC ratio and three key performance measures in a solar photovoltaic (PV) system: clipping loss, performance ratio, and capacity factor. As the DC to AC ratio increases, clipping loss rises significantly, particularly beyond a ratio of 1.85, indicating greater energy loss due to inverter capacity limits. Concurrently, the performance ratio and capacity factor gradually decline, suggesting reduced system efficiency and underutilization of inverter capacity as the system becomes increasingly oversized on the DC side. This decline is likely due to the increased frequency of inverter clipping and other system inefficiencies. These trends underscore the importance of optimizing the DC to AC ratio to balance the trade-offs between maximizing energy capture and minimizing efficiency losses. The data suggests that a ratio near 1.85 may offer an effective compromise, as it maximizes energy output while keeping clipping losses and efficiency reductions manageable.
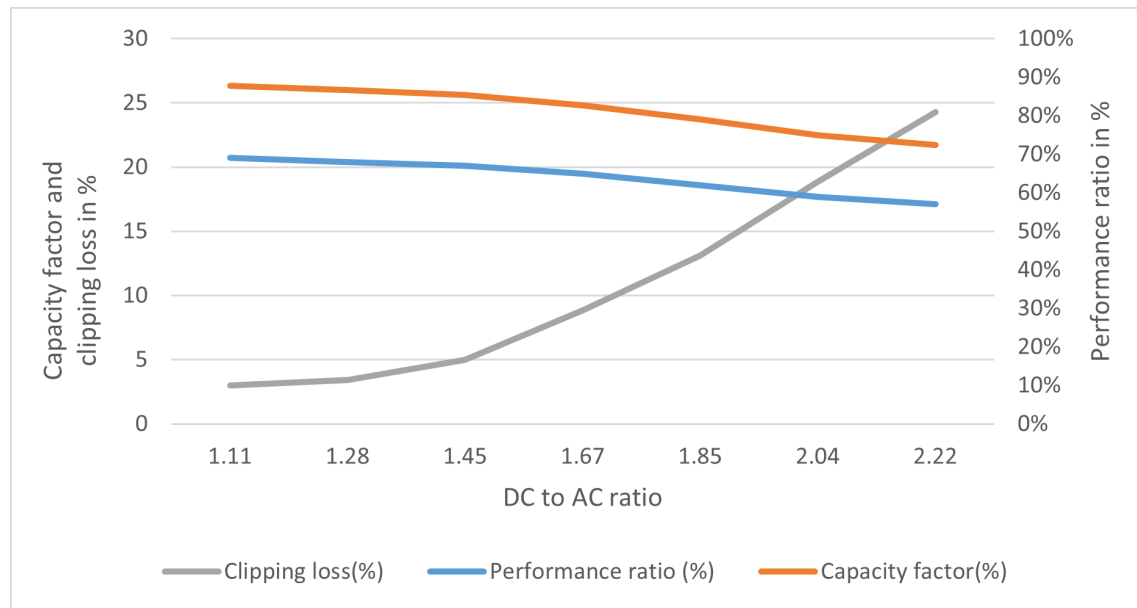

FIGURE 6.4: Variation of capacity factor (CF) and clipping loss percentage across all inverter loading ratios (ILRs).

6.3.4   Monthly Fluctuations in Energy Generation and Clipping Losses

Fig. 6.5 illustrates the monthly energy generation in megawatt-hours (MWh) for a solar photovoltaic (PV) system, plotted across various DC to AC ratios ranging from 1.11 to 2.22. The analysis reveals significant seasonal variability in energy
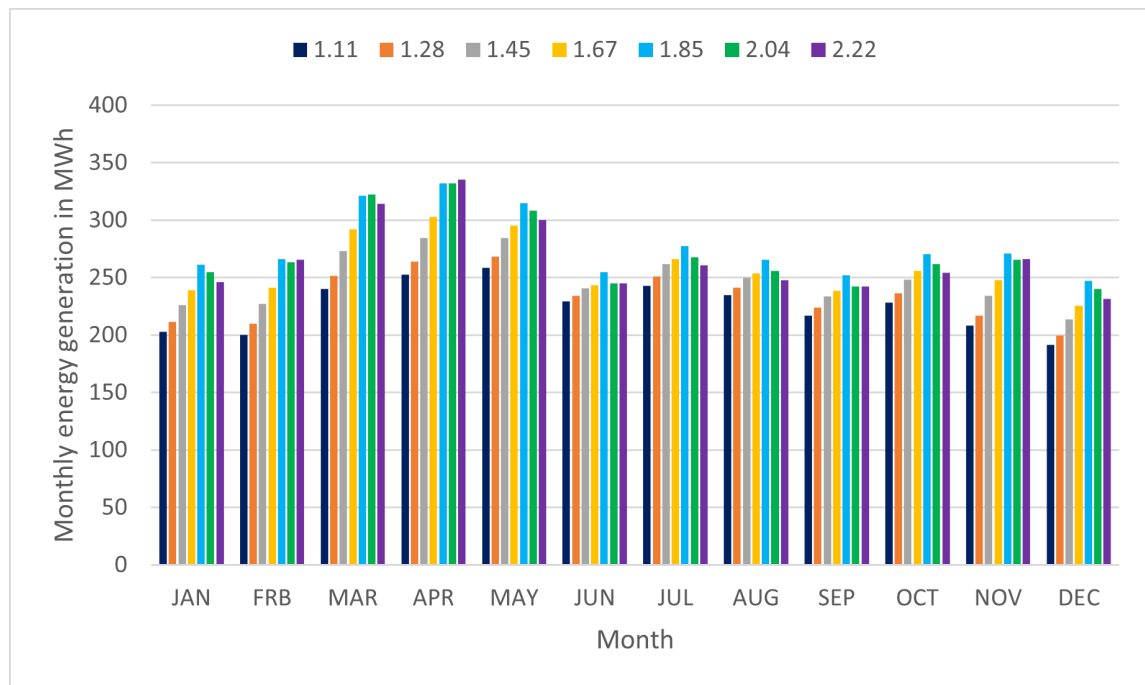
FIGURE 6.5: Monthly energy generation at multiple ILRs

production, with peaks occurring between March and July, and troughs from December to January. Notably, higher DC to AC ratios, particularly 2.22, generally result in increased energy output during months with higher solar irradiance, underscoring the system's enhanced capacity to capture available solar energy. However, the diminishing returns observed at the highest ratios in certain months suggest the presence of clipping losses, where the inverter's capacity limits prevent full utilization of the generated DC power. This pattern underscores the need for an optimal DC to AC ratio that maximizes energy yield while minimizing inefficiencies due to inverter clipping. The figure highlights the critical balance required in system design to optimize performance across

Chapter 6. IMPROVING ENERGY OUTPUT IN FLOATING SOLAR PV
PLANTS VIA INVERTER LOADING RATIOS
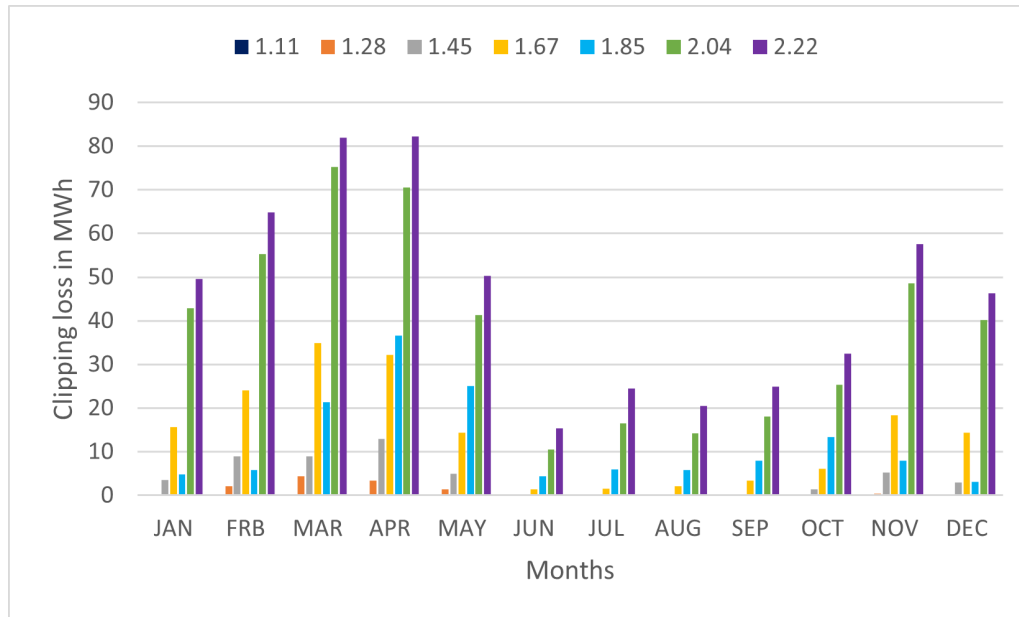
FIGURE 6.6: Monthly clipping losses at multiple values of DC to AC
ratios

varying seasonal solar conditions, emphasizing the nuanced interplay between system capacity and energy production efficiency.

The analysis suggests that ILR 1.85 is an efficient and balanced choice for maximizing energy generation across all months, providing stable output without significant clipping losses. While higher ILRs such as 2.04 and 2.22 may generate more energy during peak months, they may not be as consistent throughout the year, making ILR 1.85 a solid middle ground for reliable performance.

The Fig. 6.6 illustrates monthly clipping losses across various DC to AC ratios, with higher ratios like 2.22 experiencing significant losses, particularly in spring months (March to May), where losses exceed 80 MWh. Lower ratios, such as 1.11 and 1.28, show minimal clipping but generate less energy. Clipping decreases during summer (June to August) and rises slightly in the late fall months. Mid-range ratios (1.85 and 2.04) provide a better balance, offering higher energy generation with moderate clipping losses, making them more suitable for optimizing energy yield and overall system efficiency throughout the year.

6.3. Results 163

6.3.5   Daily and Seasonal Clipping Losses

Fig.6.6 offers valuable insights into seasonal trends but does not depict the variations in clipping losses occurring on a day-to-day basis. Fig. 6.7 illustrates the hourly distribution of clipping losses for each month. As anticipated, the highest clipping losses occurred mid-month, coinciding with peak radiation levels. Seasonally, the greatest clipping losses were observed in the spring months (March, April, and June), while the lowest were in the winter months (November, December, and January). This pattern aligns with the expected performance of a system with a fixed slope angle matching the site's latitude. Additionally, the data indicates that higher DC to AC ratios result in increased hourly clipping losses.

(a) DC to AC ratio= 1.11

(b) DC to AC ratio= 1.28

(c) DC to AC ratio= 1.45

(d) DC to AC ratio= 1.67

(e) DC to AC ratio= 1.85

(f) DC to AC ratio= 2.04

(g) DC to AC ratio= 2.22

FIGURE 6.7:   Hourly generation lost (MW) due to clipping for inverter DC to AC ratio variations

Chapter 6.   IMPROVING ENERGY OUTPUT IN FLOATING SOLAR PV
PLANTS VIA INVERTER LOADING RATIOS

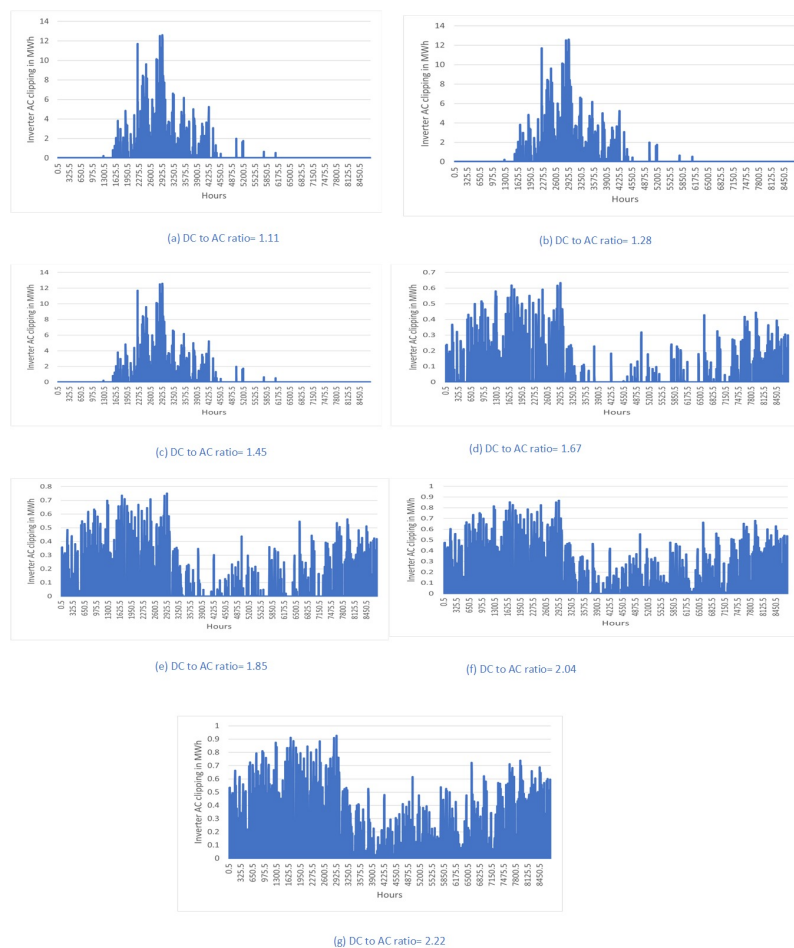### 6.3.6   Levelized Cost of Energy (LCOE)

It is crucial to consider the economic perspective. The DC to AC ratio varies between 1.11 and 2.22 to illustrate the results obtained from applying equation (6.11). As previously mentioned, a lower DC to AC ratio results in a shorter LCOE, as fewer PV inverters are needed as in Fig. 6.8. The lowest LCOE occurs at 1.85 ILR due to a lesser number of inverters and lowest clipping loss. Table 6.3 presents the cost estimation of a 1 MW floating solar PV (FSPV) plant, covering capital and operating costs along with key financial metrics. The plant shows strong economic viability, with an IRR of 27.69%, ROI of 299.6%, a payback period of 8.3 years, and a levelized cost of electricity (LCOE) of 0.067 USD/kWh.
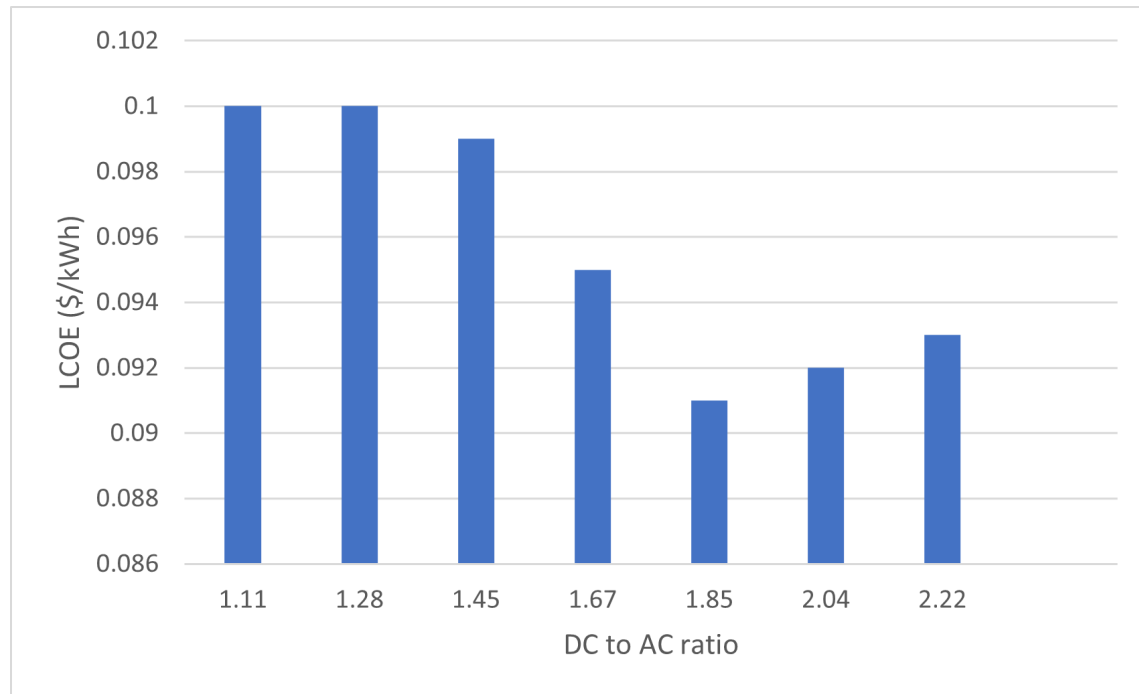
FIGURE 6.8: LCOE at the multiple values of DC to AC ratios

Table 6.4 reveals that an inverter loading ratio (ILR) of 1.85 offers the best performance, delivering the highest annual energy generation (1054.8 MWh) and the lowest levelized cost of energy (0.091 USD/kWh). ILRs lower than 1.85, such as 1.11 and 1.28, result in reduced energy output and higher LCOE, indicating underutilization of inverter capacity. Conversely, ILRs above 1.85, specifically 2.04 and 2.22, show a sharp decline in energy generation and a slight increase in

TABLE 6.3: Cost calculation of FSPV plants

Parameters	FSPV plant / MW
Total capital cost (million USD)	6.29
Operating cost with 9% inflation per year (million USD/year)	0.20
IRR (%)	27.69
Rate of Return (ROI) (%)	299.6

LCOE due to increased clipping losses. The inclusion of uncertainty bounds (±5% for energy and ±3% for LCOE) reinforces these trends, confirming ILR 1.85 as the most efficient and cost-effective configuration.

TABLE 6.4: LCOE and Annual Energy Generation with Uncertainty Bounds

ILR	LCOE (USD/kWh)	LCOE ±3% (USD/kWh)	Annual Energy (MWh)	Energy ±5% (MWh)
1.11	0.100	0.097–0.103	688.19	653.78–722.60
1.28	0.100	0.097–0.103	779.32	740.35–818.29
1.45	0.099	0.096–0.102	910.35	864.83–955.87
1.67	0.095	0.092–0.098	915.05	869.30–960.80
1.85	0.091	0.088–0.094	1054.80	1002.06–1107.54
2.04	0.092	0.089–0.095	783.35	744.18–822.52
2.22	0.093	0.090–0.096	640.82	608.78–672.86

6.3.7   Sensitivity Analysis

Sensitivity analysis offers a structured approach to evaluating how variations in critical parameters, such as inverter loading ratio (ILR), influence solar PV plant performance metrics, including energy yield, capacity factor, clipping losses, and inverter efficiency. By quantifying the effects of different ILR values, alongside

Chapter 6. IMPROVING ENERGY OUTPUT IN FLOATING SOLAR PV PLANTS VIA INVERTER LOADING RATIOS

economic and operational considerations, sensitivity analysis enables the identification of configurations that optimize output while balancing efficiency and cost. This approach is particularly applicable in contexts where solar resources, ambient conditions, and economic factors fluctuate, highlighting the limitations of a standardized design approach.

This study conducts a sensitivity analysis to assess the performance of a solar PV system across varying ILRs, aiming to determine an optimal range that maximizes energy production while balancing efficiency and cost-effectiveness. This study investigate the impact of different ILR values on key performance indicators and assess their influence on the LCOE. The outcomes of this analysis provide valuable insights into system configurations that improve both technical and economic performance for solar PV plants.
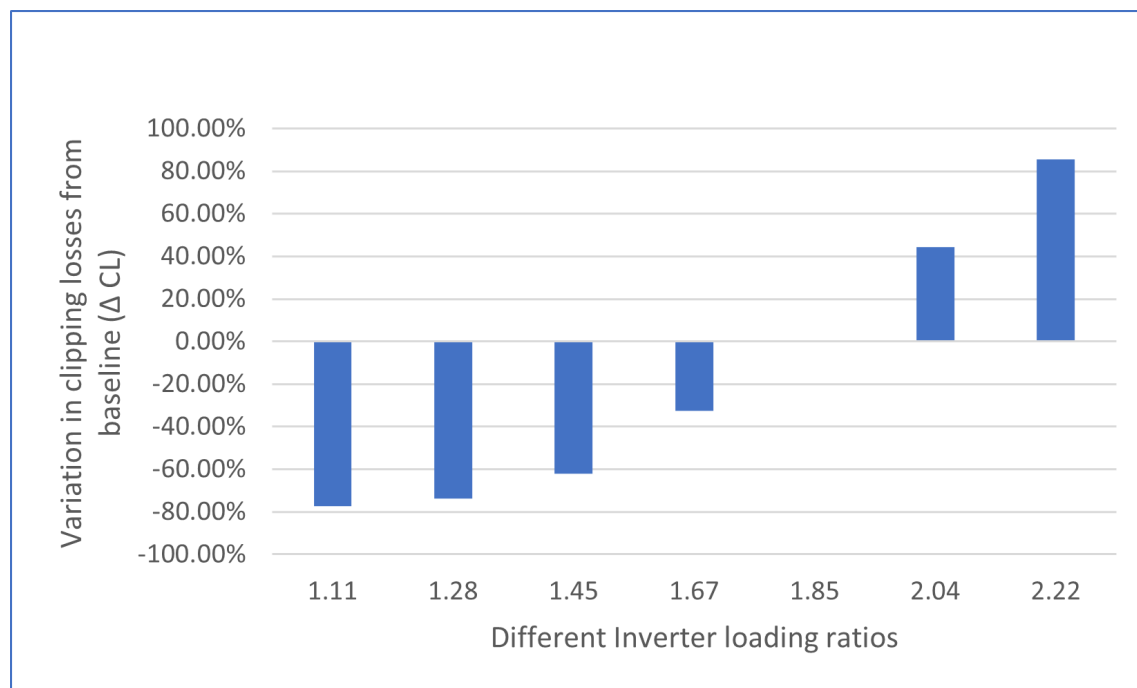

FIGURE 6.9: Effect of variation of inverter loading ratio on clipping loss

This study examines clipping losses in PV systems for various inverter loading ratios (ILRs). Clipping occurs when PV generation exceeds inverter capacity, causing energy loss and affecting overall system efficiency. Fig. 6.9 shows that at lower ILRs (1.11 to 1.67), clipping losses are significantly reduced,

with negative variations observed from a baseline, indicating that the inverter capacity is well-matched to the PV array's output, thus minimizing energy losses. However, as the ILR increases beyond 1.85, clipping losses rise markedly, reaching up to 80% above the baseline at an ILR of 2.22, demonstrating that an oversized PV array leads to frequent and severe energy clipping. These results suggest a critical threshold around an ILR of 1.85, where clipping losses shift from negative to positive, signifying an optimal balance point. For system design, this implies that maintaining an ILR within 1.11 to 1.67 may optimize energy yield while keeping clipping losses low, enhancing overall system efficiency and cost-effectiveness.

Fig. 6.10 demonstrates the relationship between the changes in energy generation with respect to different inverter loading ratios. Fig. 6.10 reveals that at lower ILRs (1.11 to 1.45), energy generation improves, with percentage change in energy generation compared to reference case i.e. ILR 1.85 (ΔE_{gen}) showing positive deviations from the baseline.
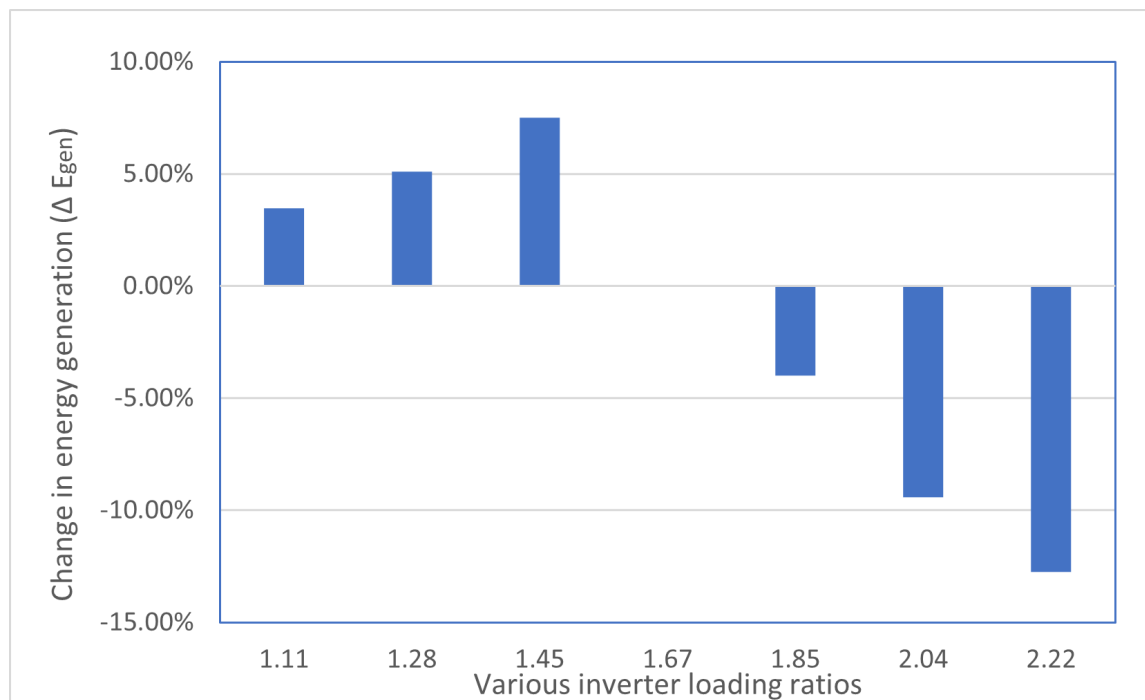

FIGURE 6.10: Percentage change in annual energy generation ΔE_{gen} relative to the baseline ILR of 1.85.

This trend reaches its peak at an ILR of 1.45, indicating that, in this range, the

Chapter 6. IMPROVING ENERGY OUTPUT IN FLOATING SOLAR PV
PLANTS VIA INVERTER LOADING RATIOS

inverter capacity is well-matched to the PV array output, resulting in optimal energy harvesting with minimal losses. However, as the ILR increases to 1.67 and higher, a negative trend emerges, with ΔE_{gen} showing a marked decline, particularly at ILRs of 2.04 and 2.22. This drop suggests that at higher ILRs, energy clipping, and system inefficiencies become more prevalent, as the inverter is frequently unable to process the excess power generated by the oversized PV array. These findings suggest that while a moderate increase in ILR can boost energy generation, excessive oversizing beyond an ILR of approximately 1.45 leads to diminishing returns and reduced efficiency. This analysis underscores the importance of carefully selecting an ILR that maximizes energy output without incurring significant clipping losses, contributing valuable insights for optimizing PV system design to enhance overall performance and cost-effectiveness.

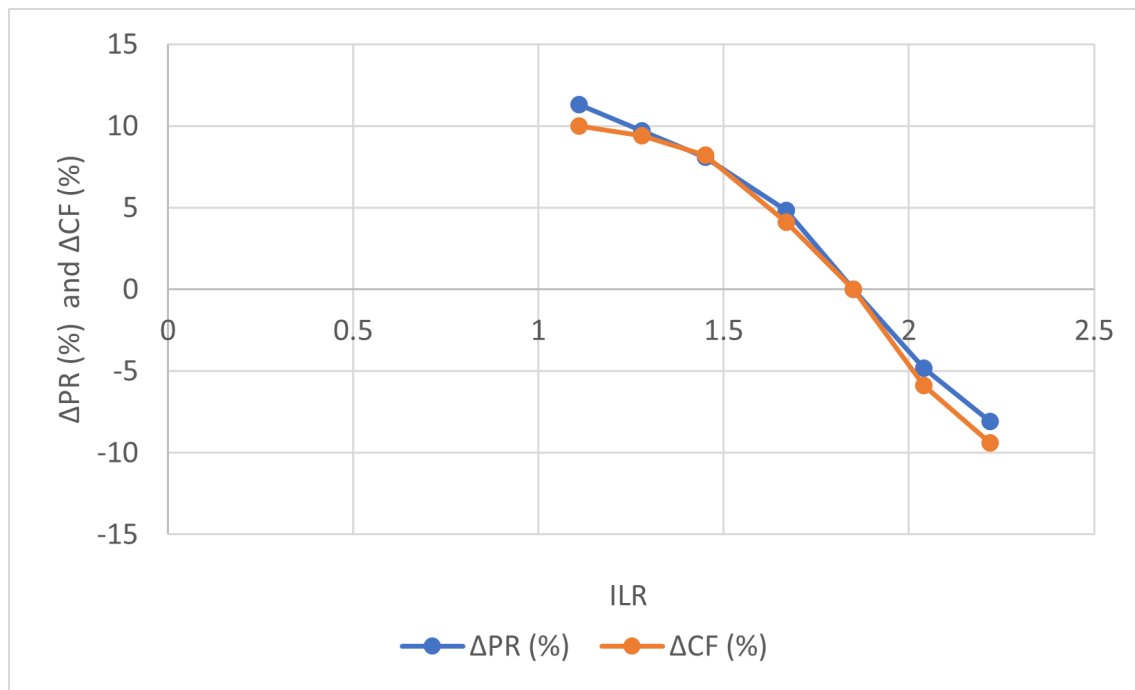FIGURE 6.11: Percentage change in performance ratio (ΔPR) and
capacity factor (ΔPR) compared to the base case ILR = 1.85.

Fig. 6.11 shows solar plant performance at different inverter loading ratios (ILRs) via changes in performance ratio (ΔPR) and capacity factor (ΔCF) relative to a baseline ILR of 1.85. Both metrics peak at ILRs of 1.0–1.2 (10% ΔPR, 8% ΔCF),

reflecting optimal inverter utilization with minimal clipping. Beyond this range, performance drops sharply—at ILR 1.85, ΔPR nearly equal to –8% and ΔCF nearly equal to –10%, and at ILR 2.5, –15% and –16%, respectively—highlighting the negative impact of excessive ILR and the optimal range of 1.0–1.5 for maximal efficiency.
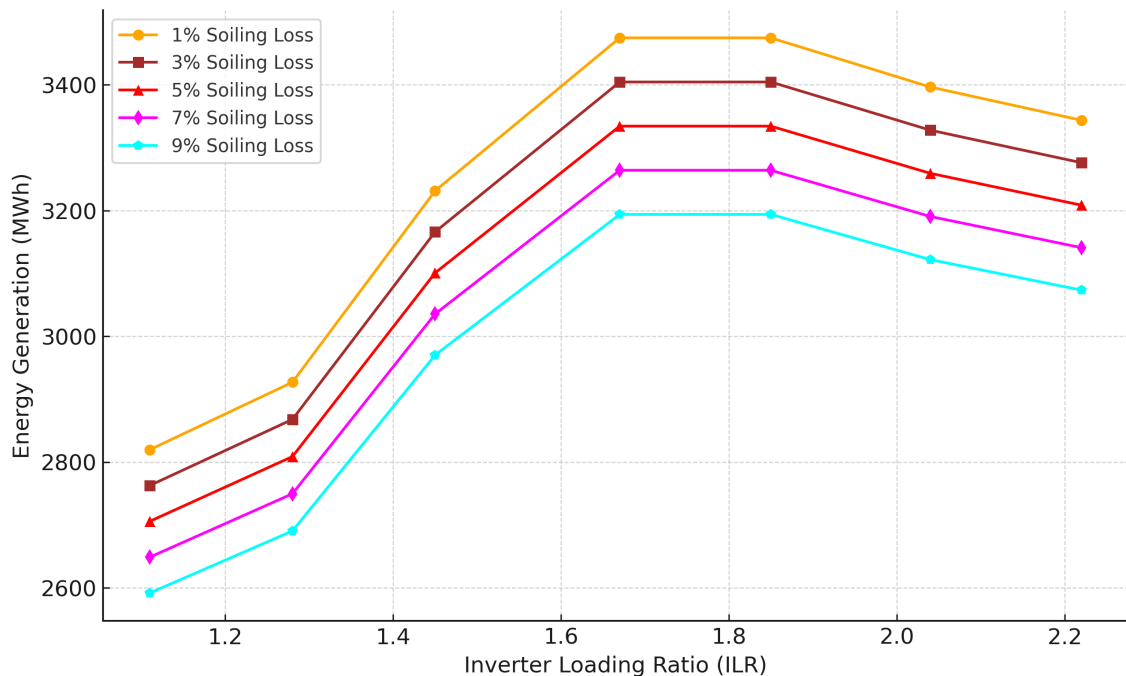
FIGURE 6.12: Impact of soiling loss on the energy generation

Analysis of inverter loading ratios (ILRs) shows that while ILRs of 1.45–1.67 provide marginal gains in performance ratio (ΔPR) and capacity factor (ΔCF), an ILR of 1.85 is optimal overall. It maximizes total energy generation (Δ*E*) by balancing energy capture and clipping losses, offering higher financial returns and alignment with grid demand. Over a 25-year FSPV lifespan with 1.18% annual degradation, ILR = 1.85 consistently delivers superior annual yield and stable performance, making it the best choice for long-term efficiency and reliability.

Fig. 6.12 illustrates the variation in energy generation with respect to different inverter loading ratios (ILRs), showing an increasing trend up to the ILR range of 1.67–1.85. Within this range, energy yield reaches its maximum before declining due to increased inverter clipping losses. Additionally, higher soiling losses are

Chapter 6. IMPROVING ENERGY OUTPUT IN FLOATING SOLAR PV PLANTS VIA INVERTER LOADING RATIOS

observed to consistently reduce energy generation across all ILRs. For instance, a soiling loss of 9% can lead to an energy reduction of up to 8%. Among the evaluated ILRs, the range of 1.67–1.85 yields the highest energy output, with ILR = 1.85 emerging as the most optimal choice in terms of balancing system efficiency and associated losses. Furthermore, maintaining soiling losses below 3% is critical to preserve more than 97% of the potential energy generation. This highlights the importance of regular module cleaning, particularly in regions susceptible to dust accumulation, to ensure sustained performance and efficiency of the PV system.

Fig. 6.13 shows the effect of mismatch losses on energy generation across different ILRs. As mismatch losses rise from 0.5% to 3%, energy output declines for all ILRs. Higher ILRs generally produce more energy, with ILR 1.85 achieving the maximum, highlighting its optimal performance. The results emphasize minimizing mismatch losses, especially at higher ILRs, to maximize system energy yield.
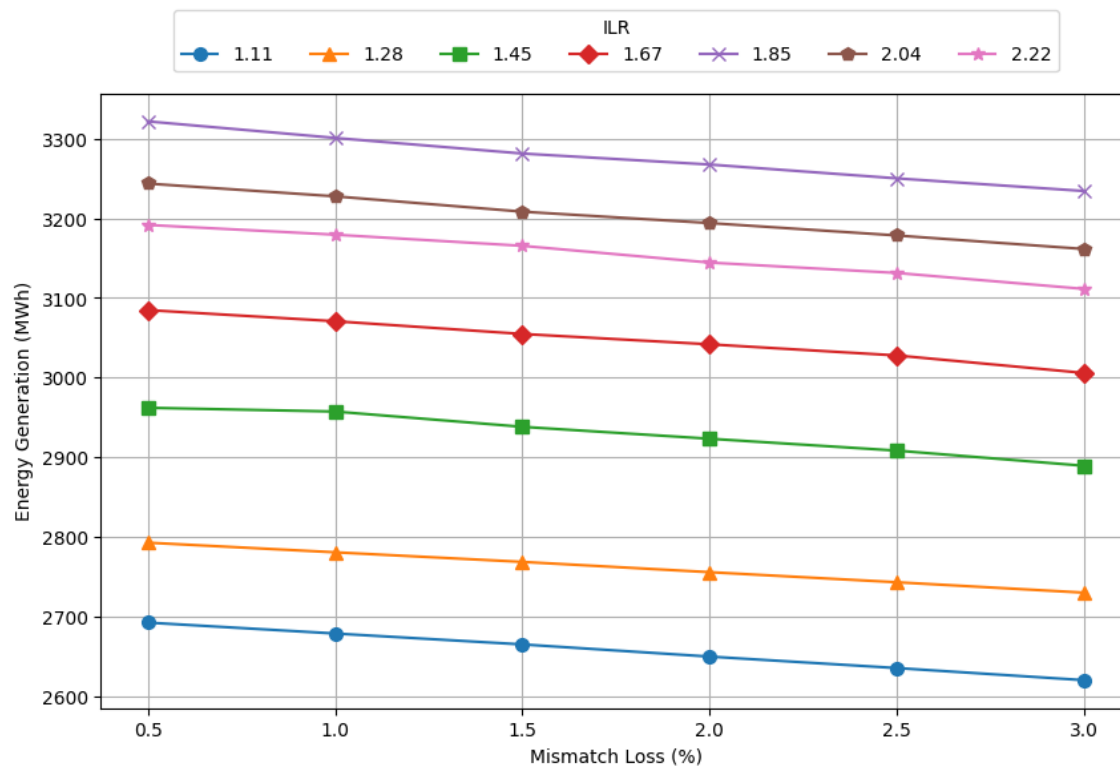

FIGURE 6.13: Impact of mismatch loss on energy generation across different ILRs

6.3. Results   171

The heatmap analysis in Fig. 6.14 reveals a clear trend in clipping loss across different inverter loading ratios (ILRs). At an ILR of 1.11, there is no visible clipping loss, indicating that the inverter capacity is sufficient to handle the generated power. As the ILR increases to 1.28, minor clipping losses appear, primarily during peak irradiance months (April and May), but remain minimal. At 1.45, clipping loss becomes more noticeable, especially from March to June, as the inverter starts reaching its capacity limits more frequently.   The trend continues with ILR 1.67, where clipping losses extend from March to August, particularly around midday hours, signifying that a larger portion of generated energy is curtailed. At an ILR of 1.85, the clipping loss peaks during summer months, covering a significant part of the day. This ILR appears to be the threshold where the trade-off between increased energy generation and inverter clipping loss becomes critical. As the ILR rises further to 2.02 and 2.22, clipping losses become widespread throughout the year, particularly from April to August, leading to significant energy curtailment. The analysis indicates that while higher ILRs increase energy capture, excessive clipping losses beyond 1.85 ILR diminish the benefits. Seasonal variations also play a crucial role, with clipping losses being more pronounced in high-irradiance months and minimal in winter. Therefore, an ILR around 1.85 offers an optimal balance between energy generation and system efficiency, minimizing unnecessary energy losses.

Chapter 6. IMPROVING ENERGY OUTPUT IN FLOATING SOLAR PV PLANTS VIA INVERTER LOADING RATIOS
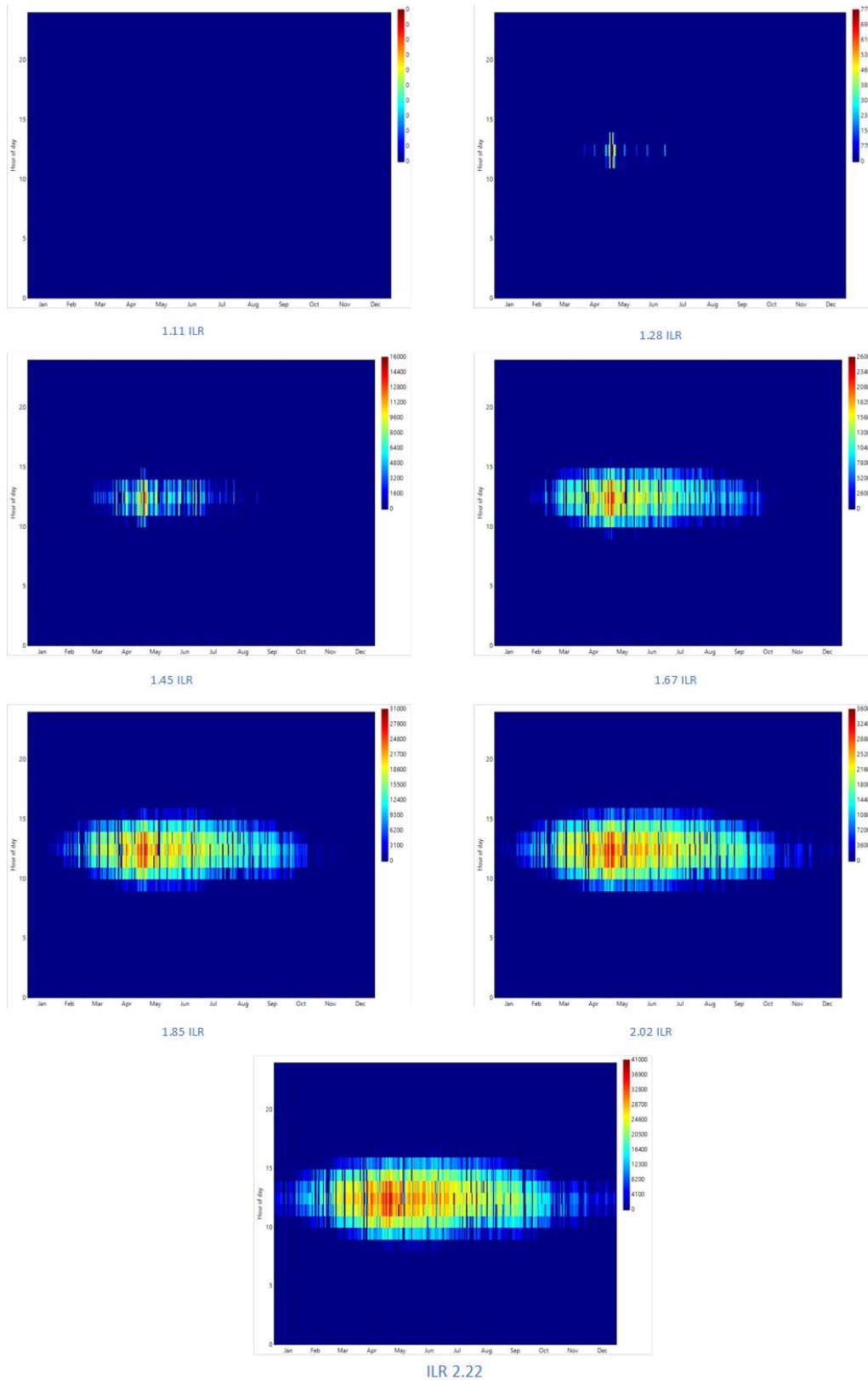
FIGURE 6.14: Heatmap graph for the clipping loss at different ILR

To further substantiate the selection of ILR = 1.85 as the optimal configuration, a multi-objective optimization plot is presented in Fig. 6.15. This chart compares the variation of performance ratio (PR), annual energy generation, and levelized cost of energy (LCOE) for each ILR scenario. The plot reveals that at ILR = 1.85, the system achieves a high energy yield, low LCOE, and a moderate PR, representing an optimal trade-off among these competing objectives. Beyond ILR = 1.85, although energy generation continues to rise slightly, the increase in clipping losses leads to diminishing gains in effective energy and a rise in LCOE. This reinforces ILR = 1.85 as the technically and economically optimal point under the given site and design constraints.

FIGURE 6.15: Multi-objective optimization plot comparing PR, CF, energy yield, and LCOE across ILRs.

6.4   Concluding Remarks

This chapter investigated the influence of varying DC-to-AC ratios on the performance and efficiency of 2 MW floating solar PV plant. The study employs

Chapter 6. IMPROVING ENERGY OUTPUT IN FLOATING SOLAR PV PLANTS VIA INVERTER LOADING RATIOS

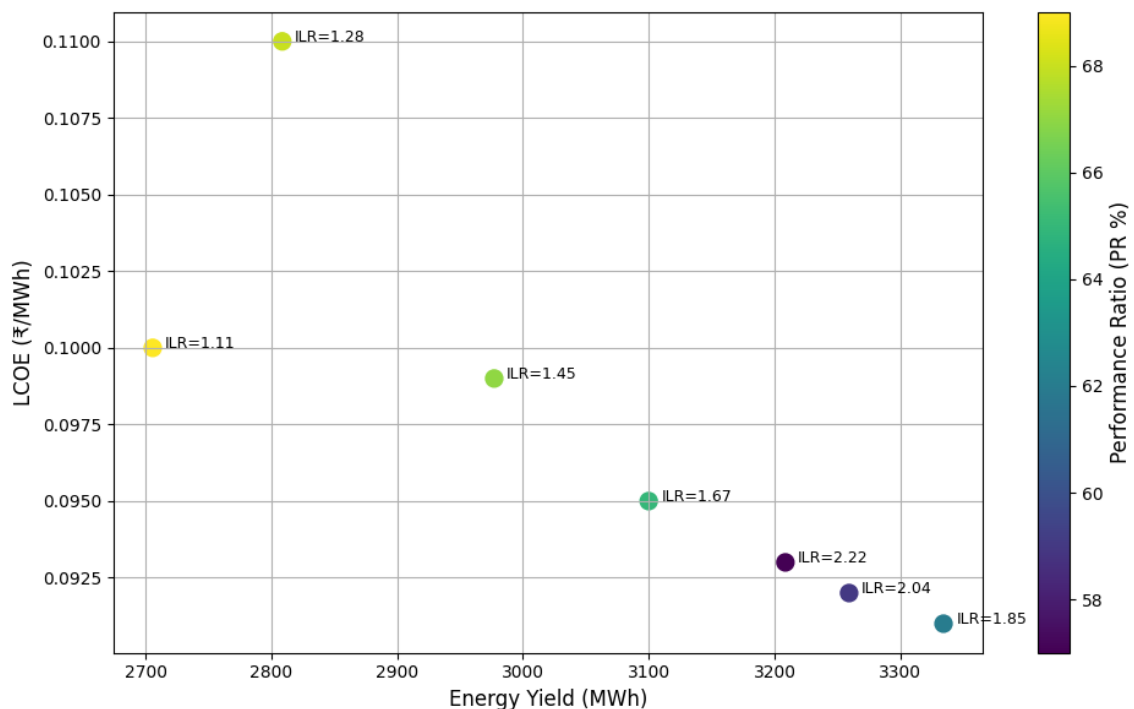simulations to analyze different DC-to-AC ratios, focusing on energy production, clipping losses, and system performance metrics. The findings revel that as the ILR increases from 1.11 to 1.85, energy generation improves by 23.2% due to the higher DC capacity, which allows the system to capture and convert more solar energy. However, the performance ratio decreases by 8.7% and the capacity factor declines by 8.0%, primarily due to increased inverter clipping losses that limit the effective utilization of the generated energy. Despite these efficiency reductions, the LCOE decreases by 9%, as the significant rise in total energy generation offsets the cost per unit of electricity. Seasonal analysis shows that higher DC to AC ratios perform better during periods of high solar irradiance, such as spring and early summer, where they capture more energy. However, in months with lower solar irradiance, the advantage of higher ratios diminishes, highlighting the need for a balanced approach to system design. The study also demonstrates that higher DC to AC ratios result in greater clipping losses during peak irradiance periods, suggesting a trade-off between maximizing energy capture and minimizing efficiency losses. Economic evaluation through the discounted payback period (DPB) indicates that while higher DC to AC ratios can increase initial energy production, they may also extend the payback period due to increased inverter costs and clipping losses. Thus, a ratio of around 1.85 represents an effective balance between enhanced energy capture and acceptable clipping losses, offering an optimal compromise between performance and economic viability. In summary, this study underscores the need for strategic ILR optimization to balance performance and economic viability.

175

Chapter 7

CONCLUSION AND FUTURE SCOPE OF WORK

7.1   Inroduction

This thesis presents an in-depth study on the performance analysis and control of grid-connected and floating solar photovoltaic (PV) systems. The research integrates theoretical modeling, simulation, algorithm development, and techno-economic analysis to enhance the efficiency, reliability, and cost-effectiveness of PV systems under varying environmental conditions. The work begins by establishing the increasing significance of solar energy in the context of global and national energy demands, particularly highlighting India's rapidly expanding solar infrastructure. A detailed design and simulation of both stand-alone and grid-connected PV systems are carried out using conventional and advanced control techniques. In particular, bio-inspired algorithms such as Flying Squirrel Search Optimization (FSSO) for maximum power point tracking (MPPT) demonstrate superior performance over traditional tracking methods, offering improved tracking speed, reduced power losses, and better dynamic response.

The study also implements and evaluates two inverter control strategies: Synchronous Reference Frame Theory (SRFT) and Instantaneous Reactive Power Theory (IRPT). SRFT control method is delivers enhanced power quality and harmonic suppression than IRPT control method. These insights contribute to developing more robust control strategies for grid integration. Furthermore, a techno-economic analysis is conducted comparing monofacial and bifacial

floating solar PV systems. Bifacial systems, benefiting from water surface albedo, yield significantly higher energy output and demonstrate lower levelized cost of energy (LCOE), thereby proving their economic and operational superiority for floating applications.

The thesis further explores the impact of solar tracking technologies—fixed tilt, seasonal adjustable tilt, single-axis, and dual-axis—on the energy yield of floating solar PV systems. The results indicate that dual-axis trackers offer the highest gain in performance but require careful evaluation due to increased structural complexity and cost. Additionally, the influence of inverter loading ratios (ILR) on system performance and economics is studied using simulation-based approaches. An optimal ILR range is identified that maximizes energy generation while minimizing clipping losses and cost inefficiencies. Seasonal variability is also taken into account, offering practical insights into inverter sizing for floating solar PV deployments.

This work contributes a comprehensive framework for improving the technical and economic performance of solar PV systems. It addresses critical gaps in existing research related to real-time MPPT under dynamic conditions, inverter control optimization for grid-tied systems, bifacial PV applications in floating platforms, and the application of tracking and inverter sizing strategies tailored for water-based PV installations. The outcomes of this thesis support the deployment of efficient, land-saving, and sustainable solar energy solutions, aligning with India's and the world's renewable energy goals.

7.2   Main Conclusions

The following outlines convey the key notable conclusions extracted from the research examination, which is structured in a chapter-wise manner:

1. The significance of solar photovoltaic (PV) technology in addressing energy security, sustainability, and climate change challenges. It highlighted the global and Indian renewable energy scenarios, follwed by different types of PV systems than the different configuation of solar Pv plants..

2. The modeling and simulation of both stand-alone and grid-connected PV systems. FSSO-based MPPT control showed superior performance over

conventional P&O and fuzzy logic in extracting maximum power under dynamic irradiance conditions. For inverter control in grid-connected systems, SRFT and IRPT algorithms were implemented. SRFT demonstrated better harmonic suppression and steady-state performance than IRPT control method.

3. A case study compared rooftop and floating solar PV systems using monofacial and bifacial modules. Bifacial FSPV systems showed higher energy yield and better performance ratios due to albedo gains from water surfaces. Economically, bifacial modules resulted in a lower levelized cost of energy (LCOE), improving the return on investment. The study concluded that bifacial floating PV systems are more efficient and economically viable than monofacial and rooftop systems in water-rich, land-constrained areas.

4. Various solar tracking technologies i.e. fixed tilt, seasonal adjustable tilt, horizontal single-axis, and dual-axis—were analyzed for their impact on energy generation in floating solar PV systems. Dual-axis tracking achieved the highest performance improvements but required higher investment and structural complexity. The analysis of energy losses (e.g., soiling, mismatch, and thermal) showed that tracking can mitigate some of these losses. This study confirmed that smart tracking significantly enhances energy yield and efficiency in FSPV plants.

5. The effect of varying DC-to-AC ratios (ILR) on the performance of FSPV systems using simulation. Results showed that increasing ILR enhances energy generation up to a certain point but also increases clipping losses. An optimal ILR was identified (e.g., around 1.85), balancing energy output, clipping loss, and system cost. Seasonal variations and sensitivity analysis confirmed the robustness of these results. This study highlighted that careful ILR selection can significantly impact technical and economic performance.

Chapter 7.   CONCLUSION AND FUTURE SCOPE OF WORK
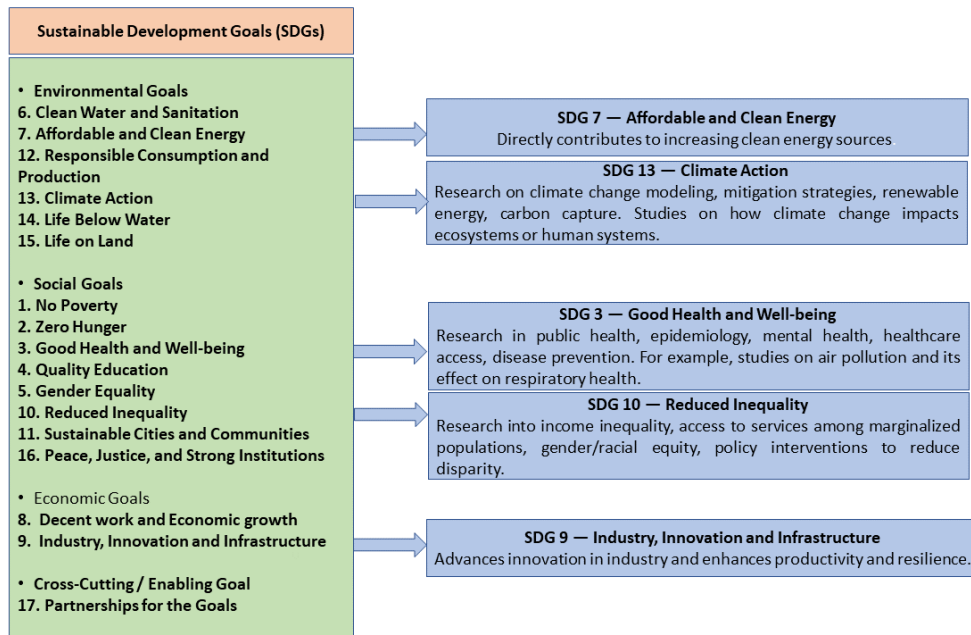
FIGURE 7.1: SDGs targeted by the research work

7.3   Social Impact of Research Work

The outcomes of this research have significant social implications, particularly in the context of sustainable development, energy accessibility, and climate resilience as in Fig. 7.1. By focusing on the performance enhancement and economic optimization of solar photovoltaic (PV) systems including advanced control strategies, bifacial floating PV technologies, and inverter sizing techniques. This study contributes to making solar energy more efficient, affordable, and deployable across diverse geographic and socio-economic settings.

One of the key social benefits of this research is its potential to promote decentralized and clean energy generation, especially in rural and remote areas where grid infrastructure is either weak or absent. The optimized stand-alone PV system designs and improved MPPT control strategies presented in this work can ensure reliable power supply for lighting, communication, education, and healthcare services in underserved regions, thus directly improving quality of life and enabling socio-economic development.

Furthermore, the investigation into floating solar PV systems supports the

sustainable use of natural water bodies while addressing the challenges of land scarcity a critical concern in densely populated and agriculturally intensive countries like India. This land-efficient approach to solar deployment reduces competition for land, preserves agricultural productivity, and mitigates potential conflicts related to land acquisition for energy infrastructure.

The research also contributes to environmental and public health improvements by accelerating the transition from fossil fuels to renewable energy. Reduced dependence on conventional energy sources lowers greenhouse gas emissions, air pollution, and associated health hazards, especially in urban areas. Additionally, the improved efficiency and cost-effectiveness of bifacial PV modules and inverter configurations may encourage faster adoption of solar technologies, further amplifying their environmental and social benefits.

Finally, this work supports national and international clean energy goals, including India's targets under the National Solar Mission and global commitments like the United Nations Sustainable Development Goals (SDGs), particularly SDG 7 (Affordable and Clean Energy), SDG 13 (Climate Action), and SDG 11 (Sustainable Cities and Communities). By advancing PV system design and deployment strategies, this research helps create a more equitable, resilient, and sustainable energy future for all.

7.4 Future Work

For future advancements in this thesis work, the following recommendations are proposed:

1. Focus on real-time FSSO implementation, hybrid optimization, adaptability to environmental changes, comparison with emerging MPPT techniques, and integration with grid-connected PV systems.

2. The study on comparative analysis of bifacial and monofacial floating solar power plants presents several avenues for future research and development.Future research can explore hybrid floating solar-wind systems, assess long-term performance and maintenance strategies, analyze economic incentives for large-scale adoption, and evaluate environmental impacts on aquatic ecosystems for sustainable energy development.

3. Future research can explore AI-driven tracking algorithms for better energy capture and advanced materials for enhanced durability and stability of floating solar platforms.

4. Future research can refine economic models for large-scale deployment, assess floating PV's environmental impact, and enhance inverter technology for better efficiency and reliability.

181

Bibliography

[1] S. Manju and N. Sagar, "Progressing towards the development of sustainable energy: A critical review on the current status, applications, developmental barriers and prospects of solar photovoltaic systems in india," *Renewable and Sustainable Energy Reviews*, vol. 70, pp. 298–313, 2017.

[2] A. Masoom, P. Kosmopoulos, A. Bansal, and S. Kazadzis, "Solar energy estimations in india using remote sensing technologies and validation with sun photometers in urban areas," *Remote Sensing*, vol. 12, no. 2, p. 254, 2020.

[3] Ministry of Information & Broadcasting, "India's Power Sector Transformation: A Journey Towards Sustainable Energy and Universal Access," Posted on: 08 June 2023, 12:41 PM, 2023, accessed on: [15 Jan 2025]. [Online]. Available: https://mib.gov.in/

[4] Ministry of Power, "Power Sector at a Glance All India," Online, May 2023, accessed: 31 March 2024. [Online]. Available: https://powermin.gov.in/en/content/power-sector-glance-all-india

[5] Central Electricity Authority, "Installed Capacity Report," Online, June 2024, accessed: 28 July 2024. [Online]. Available: https://cea.nic.in/installed-capacity-report/?lang=en

[6] J. Baba, A.-D. Vidal, Y. Komazawa, N. Ledanois, and H. Yaqoob, "Renewables 2023 global status report," 2023.

[7] IRENA, "Renewable capacity statistics 2023," 2023.

[8] Central Electricity Authority (CEA), "Annual Report 2019-2020," 2020, [Accessed: 08-Jan-2025]. [Online]. Available: https://cea.nic.in/wpcontent/uploads/annual_reports/2020/Annual_Report_2019_20.pdf

[9] M. of New and R. Energy, "Physical achievements: Programme/scheme wise cumulative physical progress as on december 2024," 2024, accessed: 2025-01-13. [Online]. Available: https://mnre.gov.in

[10] D. Parlevliet and S. R. Moheimani, "Advances in photovoltaic technology," *Solar Energy Journal*, 2014.

[11] S. Madougou and Others, "History of photovoltaic effect," *Energy and Environment*, 2010.

[12] A. L. Fahrenbruch and R. H. Bube, *Fundamentals of Solar Cells*. Elsevier, 2012.

[13] L. M. Fraas and L. D. Partain, *Solar Cells and Their Applications*. John Wiley & Sons, 2010.

[14] B. Hodge, *Alternative Energy Systems and Applications*. Wiley, 2017.

[15] R. Müller, *Semiconductor Devices: Physics and Technology*. Springer, 2017.

[16] A. Singh *et al.*, "Advancements in photovoltaic technologies," *Journal of Solar Energy*, vol. 45, no. 3, pp. 215–229, 2021.

[17] B. Maehlum, "Mono-silicon solar panels: A comprehensive review," *Solar Energy Reviews*, vol. 12, no. 1, pp. 120–130, 2015.

[18] V. Fthenakis and H. Kim, "Sustainability of photovoltaics: The case for thin-film solar cells," *Renewable and Sustainable Energy Reviews*, vol. 15, no. 8, pp. 4426–4438, 2011.

[19] M. A. Green *et al.*, "The impact of poly-silicon on solar cell efficiency," *Journal of Photovoltaic Research*, vol. 15, no. 4, pp. 225–236, 2018.

[20] D. Akinyele *et al.*, "Gallium arsenide solar cells: Efficiency, cost, and application in solar power systems," *Renewable Energy Journal*, vol. 76, no. 3, pp. 45–60, 2015.

[21] N. R. E. Laboratory, "Gaas solar cells: High efficiency and cost-effectiveness," https://www.nrel.gov, 2019, accessed: 2024-01-08.

[22] Perovskite Info, "Perovskite solar," https://www.perovskite-info.com/perovskite-solar, 2025, [Online; accessed 8-Jan-2025].

[23] Ministry of New and Renewable Energy, "Programme/Scheme wise Cumulative Physical Progress as on December, 2023," Jun. 2023, [Online]. Available:

urlhttps://mnre.gov.in/physical-progress/. [Accessed: 28-Jun-2024].

[24] R. I. Jabbar, K. K. Mohammed, S. Mekhilef, M. Mubin, M. Seyedmahmoudian, A. Stojcevski, B. Horan, and M. Becherif, "A modified p&o-mppt technique using fuzzy logic controller for pv systems," in *2023 IEEE IAS Global Conference on Emerging Technologies (GlobConET)*. IEEE, 2023, pp. 1–7.

[25] K. Vora, S. Liu, and H. Dhulipati, "A comparative analysis of perturb and observe and fuzzy logic control methods for maximum power point tracking in photovoltaic systems," in *2024 IEEE Canadian Conference on Electrical and Computer Engineering (CCECE)*. IEEE, 2024, pp. 944–948.

[26] A. Youssfi, A. Alioui, and Y. Kadi, "Study, simulation and realization of a fuzzy logic-based mppt controller in an isolated dc microgrid," *Indones. J. Electr. Eng. Comput. Sci*, vol. 34, pp. 1420–1433, 2024.

[27] M. A. Jafar, M. I. Zakaria, N. Y. Dahlan, M. N. Kamarudin, and N. El Fezazi, "Enhancing photovoltaic system maximum power point tracking with fuzzy logic-based perturb and observe method," *Int. J. Electr. Comput. Eng*, vol. 14, no. 3, pp. 2386–2399, 2024.

[28] F. Çakmak, Z. Aydoğmuş, and M. R. Tür, "Analyses of po-based fuzzy logic-controlled mppt and incremental conductance mppt algorithms in pv systems," *Energies*, vol. 18, no. 2, p. 233, 2025.

[29] F. A. Eshete, D. P. Samajdar, and A. Kumar, "Implementation of modified p&o and an adaptive fuzzy logic controller based mppt tracking system under partial shading and variable environmental conditions," *Physica Scripta*, vol. 99, no. 6, p. 065212, 2024.

[30] X. Li, Z. B. H. Zakaria, and M. N. B. Hidayat, "Optimizing photovoltaic power generation: A fuzzy control-perturbation observation approach for maximum power point tracking," in *2024 International Conference on Energy and Electrical Engineering (EEE).* IEEE, 2024, pp. 1–6.

[31] F. Tahiri, A. Harrouz, V. Dumbrava, P. Wira, and M. A. Hartani, "Maximum power point tracking for pv systems: A comparison of perturb & observe and fuzzy logic control," in *2023 11th International Conference on ENERGY and ENVIRONMENT (CIEM).* IEEE, 2023, pp. 1–6.

[32] M. M. Rana, M. R. Ali, A. K. Ajad, and M. Moznuzzaman, "Analysis of p&o and inc mppt techniques for pv array using matlab," *IOSR journal of electrical and electronics engineering*, vol. 11, no. 04, pp. 80–86, 2016.

[33] S. S. Mohammed, "Enhanced the maximum power point tracking (mppt) of photovoltaic systems using the flying squirrel search optimization (fsso) algorithm and feed forward neural network," *University of Thi-Qar Journal for Engineering Sciences*, vol. 14, no. 1, pp. 120–136, 2024.

[34] A. Avasthi, R. Garg, and P. Mahajan, "Flying squirrel search optimization based mppt controller for stand-alone pv system," in *2023 International Conference for Advancement in Technology (ICONAT).* IEEE, 2023, pp. 1–7.

[35] D. Kumar, R. Dutta, and D. K. Tanti, "Performance analysis of flying squirrel search optimization technique for mppt in photovoltaic system," in *2022 2nd Odisha International Conference on Electrical Power Engineering, Communication and Computing Technology (ODICON).* IEEE, 2022, pp. 1–6.

[36] N. Singh, K. K. Gupta, S. K. Jain, N. K. Dewangan, and P. Bhatnagar, "A flying squirrel search optimization for mppt under partial shaded photovoltaic system," *IEEE Journal of Emerging and Selected Topics in Power Electronics*, vol. 9, no. 4, pp. 4963–4978, 2020.

[37] I. Setyawan, R. N. Hasanah, and H. Suyono, "Optimization of maximum power point tracking using hybrid differential evolution flying squirrel search algorithm under partial shading conditions," in *2024 IEEE Third International Conference on Power Electronics, Intelligent Control and Energy Systems (ICPEICES).* IEEE, 2024, pp. 335–340.

[38] D. Kumar, Y. K. Chauhan, A. S. Pandey, A. K. Srivastava, V. Kumar, F. Alsaif, R. M. Elavarasan, M. R. Islam, R. Kannadasan, and M. H. Alsharif, "A novel hybrid mppt approach for solar pv systems using particle-swarm-optimization-trained machine learning and flying squirrel search optimization," *Sustainability*, vol. 15, no. 6, p. 5575, 2023.

[39] M. Muthuramalingam and P. Manoharan, "Comparative analysis of distributed mppt controllers for partially shaded stand alone photovoltaic systems," *Energy Conversion and Management*, vol. 86, pp. 286–299, 2014.

[40] K.-H. Chao and M. N. Rizal, "A hybrid mppt controller based on the genetic algorithm and ant colony optimization for photovoltaic systems under partially shaded conditions," *Energies*, vol. 14, no. 10, p. 2902, 2021.

[41] R. K. Phanden, L. Sharma, J. Chhabra, and H. İ. Demir, "A novel modified ant colony optimization based maximum power point tracking controller for photovoltaic systems," *Materials Today: Proceedings*, vol. 38, pp. 89–93, 2021.

[42] R. Patel, A. Mehta, and P. Joshi, "Enhanced synchronous reference frame control for grid-connected pv inverter under dynamic conditions," *IEEE Transactions on Sustainable Energy*, vol. 13, no. 4, pp. 2156–2164, 2022.

[43] A. Verma, P. Chauhan, and N. Gupta, "Performance assessment of dual-loop synchronous reference frame control for grid-connected solar pv under grid faults," *IEEE Access*, vol. 13, pp. 45 567–45 576, 2025.

[44] L. Zhang and H. Li, "Adaptive phase-locked loop design for srf-based pv inverter control in weak grids," *IEEE Journal of Emerging and Selected Topics in Power Electronics*, vol. 11, no. 1, pp. 189–198, 2023.

[45] R. Sharma and S. Kumar, "Performance analysis of irpt-based control strategy for grid-connected pv systems," *IEEE Transactions on Sustainable Energy*, vol. 12, no. 4, pp. 2050–2058, 2021.

[46] R. Singh, M. Yadav, and S. Mishra, "Robust current regulation of grid-tied pv inverters using sliding mode control with synchronous reference frame extraction," *Renewable Energy*, vol. 218, pp. 158–168, 2024.

[47] V. Sharma and S. Kumar, "Model predictive current control integrated with synchronous reference frame theory for distributed pv systems," *IET Renewable Power Generation*, vol. 17, no. 2, pp. 250–260, 2023.

[48] G. Kaur and B. Singh, "Adaptive instantaneous reactive power theory for power quality improvement in pv-integrated systems," *IET Renewable Power Generation*, vol. 14, no. 9, pp. 1612–1620, 2020.

[49] M. Ahmed and M. M. Rahman, "Irpt-based predictive current control for grid-connected pv systems under weak grid conditions," *IEEE Access*, vol. 11, pp. 17 812–17 822, 2023.

[50] S. Bagchi, D. Chatterjee, R. Bhaduri, and P. K. Biswas, "An improved low-voltage ride-through (lvrt) strategy for pv-based grid connected inverter using instantaneous power theory," *IET Generation, Transmission & Distribution*, vol. 15, no. 5, pp. 883–893, 2021.

[51] P. Mandal and S. Das, "Hybrid irpt-hysteresis control for harmonic compensation in grid-connected pv inverters," *IEEE Transactions on Power Electronics*, vol. 37, no. 8, pp. 9461–9472, 2022.

[52] A. Meena and P. Shivam, "Volt-var control of grid-connected pv inverter based on instantaneous reactive power theory," *IET Renewable Power Generation*, vol. 17, no. 2, pp. 342–350, 2023.

[53] S. Valedsaravi, A. E. Aroudi, and J. A. Barrado-Rodrigo, "Multi-resonant irpt control of pv-fed multifunctional inverter under unbalanced conditions," *Journal of Control, Automation and Electrical Systems*, vol. 34, no. 4, pp. 766–781, 2023.

[54] Q. Wei, L. Xing, D. Xu, B. Wu, and N. R. Zargari, "Reactive power control of pv inverter based on irpt and virtual synchronous generator concept," *IET Renewable Power Generation*, vol. 16, pp. 107–118, 2022.

[55] S. I. Irshad, F. P. Marafão, and M. G. Simoes, "Improved pq theory based control of dvr for compensation of grid sag/swell," *Energy Reports*, vol. 7, pp. 6786–6805, 2021.

[56] C. Ramanan, K. H. Lim, J. C. Kurnia, S. Roy, B. J. Bora, and B. J. Medhi, "Towards sustainable power generation: Recent advancements in floating photovoltaic technologies," *Renewable and Sustainable Energy Reviews*, vol. 194, p. 114322, 2024.

[57] W. Shi, C. Yan, Z. Ren, Z. Yuan, Y. Liu, S. Zheng, X. Li, and X. Han, "Review on the development of marine floating photovoltaic systems," *Ocean Engineering*, vol. 286, p. 115560, 2023.

[58] M. S. Erlangga, F. D. Wijaya, and Y. S. Wijoyo, "State-of-the-art optimization approaches for battery energy storage in utility-scale floating pv systems," in *2024 16th International Conference on Information Technology and Electrical Engineering (ICITEE)*. IEEE, 2024, pp. 398–403.

[59] A. Ahmed, M. Elsakka, N. Elminshawy, A. Mohamed, and S. Sundaram, "Recent advances in floating photovoltaic systems," *The Chemical Record*, vol. 23, no. 12, p. e202300229, 2023.

[60] A. Djalab, Z. Djalab, A. El Hammoumi, G. M. Tina, S. Motahhir, and A. A. Laouid, "A comprehensive review of floating photovoltaic systems: Tech advances, marine environmental influences on offshore pv systems, and economic feasibility analysis," *Solar Energy*, vol. 277, p. 112711, 2024.

[61] A. Garrod, S. N. Hussain, A. Ghosh, S. Nahata, C. Wynne, and S. Paver, "An assessment of floating photovoltaic systems and energy storage methods: A comprehensive review," *Results in Engineering*, p. 101940, 2024.

[62] G. Cipriani, V. Di Dio, A. Dioguardi, and S. Guarino, "Comparative analysis of the performance of floating and ground-mounted photovoltaic panels: An experimental approach," in *2024 IEEE International Conference on Environment and Electrical Engineering and 2024 IEEE Industrial and Commercial Power Systems Europe (EEEIC/I&CPS Europe)*. IEEE, 2024, pp. 1–6.

[63] V. S. Nysted, D. Lindholm, J. Selj, and T. Kjeldstad, "Floating photovoltaics: modelled and experimental operating temperatures and the impact of wind speed and direction," *EPJ Photovoltaics*, vol. 15, p. 23, 2024.

[64] J. Zhang, Z. Li, J. Tao, Y. Ge, Y. Zhong, Y. Wang, and B. Yan, "Observed impacts of ground-mounted photovoltaic systems on the microclimate and soil in an arid area of gansu, china," *Atmosphere*, vol. 15, no. 8, p. 936, 2024.

[65] G. M. Tina, F. B. Scavo, L. Micheli, and M. Rosa-Clot, "Economic comparison of floating photovoltaic systems with tracking systems and active cooling in a mediterranean water basin," *Energy for Sustainable Development*, vol. 76, p. 101283, 2023.

[66] B. Sutanto, H. Iacovides, A. Nasser, A. Cioncolini, I. Afgan, Y. S. Indartono, T. Prasetyo, and A. T. Wijayanta, "Design and analysis of passively cooled floating photovoltaic systems," *Applied Thermal Engineering*, vol. 236, p. 121801, 2024.

[67] E. Alonso, C. Pérez-Rábago, J. González-Aguilar, and M. Romero, "A novel lab-scale solar reactor for kinetic analysis of non-volatile metal oxides thermal reductions," *Energy Procedia*, vol. 57, pp. 561–569, 2014.

[68] G. M. Tina, A. Osama, G. Mannino, A. Gagliano, A. V. Cucuzza, and F. Bizzarri, "Thermal comparison of floating bifacial and monofacial photovoltaic modules considering two laying configurations," *Applied Energy*, vol. 389, p. 125732, 2025.

[69] R. O. Yakubu, D. A. Quansah, L. D. Mensah, W. Ahiataku-Togobo, P. Acheampong, and M. S. Adaramola, "Comparison of ground-based and floating solar photovoltaic systems performance based on monofacial and bifacial modules in ghana," *Energy Nexus*, vol. 12, p. 100245, 2023.

[70] G. R. Pandian, G. B. Balachandran, P. W. David, and S. K, "Performance analysis of floating bifacial stand-alone photovoltaic module in tropical freshwater systems of southern asia: an experimental study," *Scientific Reports*, vol. 14, no. 1, p. 20352, 2024.

[71] N. Saeed, J. Gong, Y. Wan, K. Long, A. Saeed, L. Mei, C. Xiong, W. Long, H. Zhou, and L. Li, "A novel design of multifunctional offshore floating platform structure based on topology optimization," *Engineering Structures*, vol. 306, p. 117782, 2024.

[72] C. Veliathur Chinnasamy Srinivasan, P. K. Soori, and F. A. Ghaith, "Techno-economic feasibility of the use of floating solar pv systems in oil platforms," *Sustainability*, vol. 16, no. 3, p. 1039, 2024.

[73] C. Ramanan, S. Roy, K. S. Yam, K. H. Lim, B. J. Bora, and B. J. Medhi, "Floating solar pv systems—global research reported in the year 2022," in *Conference on Fluid Mechanics and Fluid Power*. Springer, 2022, pp. 61–78.

[74] S. K. A. Dzamesi, W. Ahiataku-Togobo, S. Yakubu, P. Acheampong, M. Kwarteng, R. Samikannu, and E. Azeave, "Comparative performance evaluation of ground-mounted and floating solar pv systems," *Energy for Sustainable Development*, vol. 80, p. 101421, 2024.

[75] N. Ravichandran, N. Ravichandran, and B. Panneerselvam, "Comparative assessment of offshore floating photovoltaic systems using thin film modules for maldives islands," *Sustainable Energy Technologies and Assessments*, vol. 53, p. 102490, 2022.

[76] N. K. Singh, A. Goswami, and P. K. Sadhu, "Energy economics and environmental assessment of hybrid hydel-floating solar photovoltaic systems for cost-effective low-carbon clean energy generation," *Clean technologies and environmental policy*, vol. 25, no. 4, pp. 1339–1360, 2023.

[77] L. W. Farrar, A. S. Bahaj, P. James, A. Anwar, and N. Amdar, "Floating solar pv to reduce water evaporation in water stressed regions and powering water pumping: Case study jordan," *Energy Conversion and Management*, vol. 260, p. 115598, 2022.

[78] N. Zhang, T. Jiang, C. Guo, L. Qiao, Q. Ji, L. Yin, L. Yu, P. Murto, and X. Xu, "High-performance semitransparent polymer solar cells floating on water: Rational analysis of power generation, water evaporation and algal growth," *Nano Energy*, vol. 77, p. 105111, 2020.

[79] A. Martinez and G. Iglesias, "Mapping of the levelised cost of energy from floating solar pv in coastal waters of the european atlantic, north sea and baltic sea," *Solar Energy*, vol. 279, p. 112809, 2024.

[80] S. Oliveira-Pinto and J. Stokkermans, "Assessment of the potential of different floating solar technologies–overview and analysis of different case studies," *Energy conversion and Management*, vol. 211, p. 112747, 2020.

[81] A. Kowsar, M. Hassan, M. T. Rana, N. Haque, M. H. Faruque, S. Ahsan, and F. Alam, "Optimization and techno-economic assessment of 50 mw floating solar power plant on hakaluki marsh land in bangladesh," *Renewable Energy*, vol. 216, p. 119077, 2023.

[82] E. M. Deschamps and R. Rüther, "Optimization of inverter loading ratio for grid connected photovoltaic systems," *Solar Energy*, vol. 179, pp. 106–118, 2019.

[83] R. O. Yakubu, L. D. Mensah, D. A. Quansah, and M. S. Adaramola, "A systematic literature review of the bifacial photovoltaic module and its applications," *The Journal of Engineering*, vol. 2024, no. 8, p. e12421, 2024.

[84] M. H. Shahverdian, H. Sayyaadi, and A. Sohani, "An optical-based comparative study to detect best configurations for installation of monofacial and bifacial pv technologies," *Solar Energy*, vol. 266, p. 112184, 2023.

[85] S. M. Moreno-Buesa, E. Muñoz-Cerón, G. Nofuentes Garrido, S. Gulkowski, J. de la Casa Higueras, and J. Aguilera Tejero, "Characterization of bifacial technology pv systems," *Proceedings of the Institution of Mechanical Engineers, Part A: Journal of Power and Energy*, vol. 238, no. 6, pp. 1084–1098, 2024.

[86] J. Johnson and S. Manikandan, "Experimental study and model development of bifacial photovoltaic power plants for indian climatic zones," *Energy*, vol. 284, p. 128693, 2023.

[87] D. Pokhrel, X. Mathew, K. Khanal Subedi, A. Patel, A. B. Phillips, E. Bastola, A. Abudulimu, M. K. Jamarkattel, S. Rijal, A. Quader *et al.*, "Bifacial cdte solar cells with copper chromium oxide back-buffer layer," *Solar Rrl*, vol. 6, no. 11, p. 2200501, 2022.

[88] A. E. Cosgun and H. Demir, "Investigating the effect of albedo in simulation-based floating photovoltaic system: 1 mw bifacial floating photovoltaic system design," *Energies*, vol. 17, no. 4, p. 959, 2024.

[89] S. Tsuchida, Y. Tsuno, D. Sato, T. Oozeki, and N. Yamada, "Albedo-dependent bifacial gain losses in photovoltaic modules with rear-side support structures," *IEEE Journal of Photovoltaics*, vol. 13, no. 6, pp. 938–944, 2023.

[90] H. Imran, I. Durrani, M. Kamran, T. M. Abdolkader, M. Faryad, and N. Z. Butt, "High-performance bifacial perovskite/silicon double-tandem solar cell," *IEEE journal of photovoltaics*, vol. 8, no. 5, pp. 1222–1229, 2018.

[91] C. Ma, R. Wu, Z. Liu, and X. Li, "Performance assessment of different photovoltaic module technologies in floating photovoltaic power plants under waters environment," *Renewable Energy*, vol. 222, p. 119890, 2024.

[92] A. Goswami and P. K. Sadhu, "Adoption of floating solar photovoltaics on waste water management system: a unique nexus of water-energy utilization, low-cost clean energy generation and water conservation," *Clean Technologies and Environmental Policy*, pp. 1–26, 2021.

[93] N. A. Elminshawy, A. Ahmed, A. Osama, A. Kabeel, and O. Elbaksawi, "The potential of optimized floating photovoltaic system for energy production in the northern lakes of egypt," *Engineering Analysis with Boundary Elements*, vol. 161, pp. 226–246, 2024.

[94] A. Sharma, P. Mahajan, and R. Garg, "Performance and cost benefit analysis of solar photovoltaic power plant for delhi secretariat building," *Water and Energy International*, vol. 60, no. 9, pp. 16–25, 2017.

[95] R. Cazzaniga, M. Cicu, M. Rosa-Clot, P. Rosa-Clot, G. Tina, and C. Ventura, "Floating photovoltaic plants: Performance analysis and design solutions," *Renewable and Sustainable Energy Reviews*, vol. 81, pp. 1730–1741, 2018.

[96] P. Tillmann, K. Jäger, and C. Becker, "Minimising the levelised cost of electricity for bifacial solar panel arrays using bayesian optimisation," *Sustainable Energy & Fuels*, vol. 4, no. 1, pp. 254–264, 2020.

[97] T. M. Mahim, A. Rahim, and M. M. Rahman, "Review of mono-and bifacial photovoltaic technologies: A comparative study," *IEEE Journal of Photovoltaics*, 2024.

[98] C. Ramanan, K. H. Lim, J. C. Kurnia, S. Roy, B. J. Bora, and B. J. Medhi, "Design study on the parameters influencing the performance of floating solar pv," *Renewable Energy*, vol. 223, p. 120064, 2024.

[99] A. Alshaabani, "Developing the design of single-axis sun sensor solar tracking system," *Energies*, vol. 17, no. 14, p. 3442, 2024.

[100] N. Ravichandran, N. Ravichandran, and B. Panneerselvam, "Performance analysis of a floating photovoltaic covering system in an indian reservoir," *Clean Energy*, vol. 5, no. 2, pp. 208–228, 2021.

[101] M. H. de Sá Campos and C. Tiba, "nptrack: a n-position single axis solar tracker model for optimized energy collection," *Energies*, vol. 14, no. 4, p. 925, 2021.

[102] B. Huang, J. Huang, K. Xing, L. Liao, P. Xie, M. Xiao, and W. Zhao, "Development of a solar-tracking system for horizontal single-axis pv arrays using spatial projection analysis," *Energies*, vol. 16, no. 10, p. 4008, 2023.

[103] N. Ravichandran, N. Ravichandran, and B. Panneerselvam, "Floating photovoltaic system for indian artificial reservoirs—an effective approach to reduce evaporation and carbon emission," *International Journal of Environmental Science and Technology*, pp. 1–18, 2022.

[104] M. Hammas, H. Fituri, A. Shour, A. A. Khan, U. A. Khan, and S. Ahmed, "A hybrid dual-axis solar tracking system: Combining light-sensing and time-based gps for optimal energy efficiency," *Energies*, vol. 18, no. 1, p. 217, 2025.

[105] H. Shang and W. Shen, "Design and implementation of a dual-axis solar tracking system," *Energies*, vol. 16, no. 17, p. 6330, 2023.

[106] M. Saeedi and R. Effatnejad, "A new design of dual-axis solar tracking system with ldr sensors by using the wheatstone bridge circuit," *IEEE sensors journal*, vol. 21, no. 13, pp. 14 915–14 922, 2021.

[107] U. Mamodiya and N. Tiwari, "Dual-axis solar tracking system with different control strategies for improved energy efficiency," *Computers and Electrical Engineering*, vol. 111, p. 108920, 2023.

[108] J.-M. Wang and C.-L. Lu, "Design and implementation of a sun tracker with a dual-axis single motor for an optical sensor-based photovoltaic system," *Sensors*, vol. 13, no. 3, pp. 3157–3168, 2013.

[109] J. Wu, X. Chen, and L. Wang, "Design and dynamics of a novel solar tracker with parallel mechanism," *IEEE/ASME Transactions on Mechatronics*, vol. 21, no. 1, pp. 88–97, 2015.

[110] S. L. Jurj and R. Rotar, "Increasing the solar reliability factor of a dual-axis solar tracker using an improved online built-in self-test architecture," *IEEE Access*, 2024.

[111] D. A. Flores-Hernández, A. Luviano-Juárez, N. Lozada-Castillo, O. Gutiérrez-Frías, C. Domínguez, and I. Antón, "Optimal strategy for the improvement of the overall performance of dual-axis solar tracking systems," *Energies*, vol. 14, no. 22, p. 7795, 2021.

[112] L. Huang, Y. Yang, D. Khojasteh, B. Ou, and Z. Luo, "Floating solar power loss due to motions induced by ocean waves: An experimental study," *Ocean Engineering*, vol. 312, p. 118988, 2024.

[113] L. Huang, "Energy fluctuation of floating photovoltaic solar panel due to wave-induced motions," in *International Conference on Offshore Mechanics and Arctic Engineering*, vol. 87851.   American Society of Mechanical Engineers, 2024, p. V007T09A092.

[114] E. L. Alberti, R. Paludo, K. F. Portella, M. D. G. P. Bragança, G. P. U. Rocha, M. M. Mazur, and A. C. F. Portella, "New concept on 100.74 kwp floating solar photovoltaic plant and a real mechanical failures assessment: Case of study at santa clara hydroelectric power plant reservoir in southern brazil," *Sustainable Energy Technologies and Assessments*, vol. 60, p. 103455, 2023.

[115] E. Cuce, P. M. Cuce, S. Saboor, A. Ghosh, and Y. Sheikhnejad, "Floating pvs in terms of power generation, environmental aspects, market potential, and challenges," *Sustainability*, vol. 14, no. 5, p. 2626, 2022.

[116] A. Sahu, N. Yadav, and K. Sudhakar, "Floating photovoltaic power plant: A review," *Renewable and sustainable energy reviews*, vol. 66, pp. 815–824, 2016.

[117] D. Mittal, B. K. Saxena, and K. Rao, "Floating solar photovoltaic systems: An overview and their feasibility at kota in rajasthan," in *2017 international conference on circuit, power and computing technologies (ICCPCT).* IEEE, 2017, pp. 1–7.

[118] R. Chowdhury, M. A. Aowal, S. M. G. Mostafa, and M. A. Rahman, "Floating solar photovoltaic system: An overview and their feasibility at kaptai in rangamati," in *2020 IEEE International Power and Renewable Energy Conference.* IEEE, 2020, pp. 1–5.

[119] F. Saeed and A. Zohaib, "Quantification of losses in a photovoltaic system: A review," *Engineering Proceedings*, vol. 11, no. 1, p. 35, 2022.

[120] T. C. V. Santos, A. T. G. Cavalcante, and C. R. Da Silva, "Perdas na produção de energia solar fotovoltaica devido aos efeitos elétricos e térmicos," *Brazilian Applied Science Review*, vol. 4, no. 6, pp. 3448–3457, 2020.

[121] K. S. Anderson, W. B. Hobbs, W. F. Holmgren, K. R. Perry, M. A. Mikofski, and R. A. Kharait, "The effect of inverter loading ratio on energy estimate bias," in *2022 IEEE 49th Photovoltaics Specialists Conference (PVSC).* IEEE, 2022, pp. 0714–0720.

[122] R. Nasiri, M. Khayamy, M. Rashidi, A. Nasiri, and V. Bhavaraju, "Optimal solar pv sizing for inverters based on specific local climate," in *2018 IEEE Energy Conversion Congress and Exposition (ECCE).* IEEE, 2018, pp. 6214–6219.

[123] A. Demirci, Z. Ozturk, S. M. Tercan, and İ. Nakir, "Determination of photovoltaic inverter ratio minimizing energy clipping for electric vehicle charging station under different solar radiations," in *2022 International Congress on Human-Computer Interaction, Optimization and Robotic Applications (HORA).* IEEE, 2022, pp. 1–6.

[124] T. S. Ustun, Y. Aoto, J. Hashimoto, and K. Otani, "Optimal pv-inv capacity ratio for residential smart inverters operating under different control modes," *IEEE access*, vol. 8, pp. 116 078–116 089, 2020.

[125] E. Mohammadi and G. Moschopoulos, "Optimization of pv array-to-inverter power ratio in grid-connected systems to maximize system profit," in

2021 IEEE Applied Power Electronics Conference and Exposition (APEC). IEEE, 2021, pp. 2084–2089.

[126] M. of New and R. E. (MNRE), "Annual report 2022–2023," 2023, available: https://mnre.gov.in.

[127] I. R. E. A. (IRENA), "Renewable capacity statistics 2022," 2022, available: https://www.irena.org.

[128] MNRE, "Jawaharlal nehru national solar mission (jnnsm): Mission document," 2023, available: https://mnre.gov.in.

[129] I. Farhat, A. N. Tabish, M. Raashid, M. I. Rashid, M. Asif Hussain, M. Irshad, A. Ghafoor, M. U. Farid, N. H. Ansari, and A. Naseer, "Performance analysis of monofacial and bifacial over-canal solar photovoltaic (pv) system and assessment of water and land conservation potential," *Energy Sources, Part A: Recovery, Utilization, and Environmental Effects*, vol. 45, no. 3, pp. 6981–6993, 2023.

[130] V. K. Domakonda, S. Farooq, S. Chinthamreddy, R. Puviarasi, M. Sudhakar, and S. Boopathi, "Sustainable developments of hybrid floating solar power plants: Photovoltaic system," in *Human Agro-Energy Optimization for Business and Industry.* IGI Global, 2023, pp. 148–167.

[131] H. Madhi, S. Aljabair, and A. A. Imran, "A review of photovoltaic/thermal system cooled using mono and hybrid nanofluids," *International Journal of Thermofluids*, p. 100679, 2024.

[132] K. Osmani, A. Haddad, H. Jaber, T. Lemenand, B. Castanier, and M. Ramadan, "Mitigating the effects of partial shading on pv system's performance through pv array reconfiguration: A review," *Thermal Science and Engineering Progress*, vol. 31, p. 101280, 2022.

[133] K. Narasimman, V. Gopalan, A. Bakthavatsalam, P. Elumalai, M. I. Shajahan, and J. J. Michael, "Modelling and real time performance evaluation of a 5 mw grid-connected solar photovoltaic plant using different artificial neural networks," *Energy Conversion and Management*, vol. 279, p. 116767, 2023.

[134] M. Mehdi, N. Ammari, A. A. Merrouni, A. Benazzouz, and M. Dahmani, "Experimental investigation on the effect of wind as a natural cooling agent for photovoltaic power plants in desert locations," *Case Studies in Thermal Engineering*, vol. 47, p. 103038, 2023.

[135] R. Akpahou, F. Odoi-Yorke, and L. K. Osei, "Techno-economic analysis of a utility-scale grid-tied solar photovoltaic system in benin republic," *Cleaner Engineering and Technology*, vol. 13, p. 100633, 2023.

[136] M. Bhavani, K. V. Reddy, K. Mahesh, and S. Saravanan, "Impact of variation of solar irradiance and temperature on the inverter output for grid connected photo voltaic (pv) system at different climate conditions," *Materials Today: Proceedings*, vol. 80, pp. 2101–2108, 2023.

[137] A. Sharma, P. Mahajan, and R. Garg, "End-of-life solar photovoltaic panel waste management in india: forecasting and environmental impact assessment," *International Journal of Environmental Science and Technology*, vol. 21, no. 2, pp. 1961–1980, 2024.

[138] M. I. Islam, M. S. Jadin, A. A. Mansur, N. A. M. Kamari, T. Jamal, M. S. Hossain Lipu, M. N. M. Azlan, M. R. Sarker, and A. Shihavuddin, "Techno-economic and carbon emission assessment of a large-scale floating solar pv system for sustainable energy generation in support of malaysia's renewable energy roadmap," *Energies*, vol. 16, no. 10, p. 4034, 2023.

[139] W. Li, Y. Guo, and K. Fu, "Enclosure experiment for influence on algae growth by shading light," *Procedia Environmental Sciences*, vol. 10, pp. 1823–1828, 2011.

[140] N. K. Singh and P. K. Sadhu, "The investigation of energy and economy for floating solar pv system on saline water," *Microsystem Technologies*, vol. 30, no. 9, pp. 1079–1086, 2024.

[141] M. Acharya and S. Devraj, "Floating solar photovoltaic (fspv): a third pillar to solar pv sector," *New Delhi, India: The Energy and Resources Institute*, 2019.

[142] C. D. Rodríguez-Gallegos, M. Bieri, O. Gandhi, J. P. Singh, T. Reindl, and S. Panda, "Monofacial vs bifacial si-based pv modules: Which one is more cost-effective?" *Solar Energy*, vol. 176, pp. 412–438, 2018.

199

Appendix A

Specification of Roof Top and Floating PV Plant

TABLE 1: PV module specifications for rooftop PV plant

Specification (ENVIRO PVM6-335)	
Module Type	Monocrystalline
Module Efficiency	17.28%
Maximum Power (P_{max})	335 W
Voltage at P_{max} (V_{mp})	37.9 V
Current at P_{max} (I_{mp})	8.85 A
Open Circuit Voltage (V_{oc})	46.27 V
Short Circuit Current (I_{sc})	9.41 A
Operating Temperature Range	$-40°C$ to $+85°C$

200

TABLE 2: Comparison of monofacial and bifacial PV modules for FSPV plant

Models	JKM-540M-72HL4-TV (Monofacial PV module)	JKM-540M-72HL4-BDVP (Bifacial PV module)
Peak power (P_{peak})	540 Wp	540 Wp
Open circuit voltage (V_{oc})	37.78 V	49.73 V
Short circuit current (I_{sc})	18.18 A	13.89 A
Max. Power Point voltage (V_{mpp})	31.46 V	41.13 V
Max. Power Point current (I_{mpp})	17.17 A	13.13 A
Efficiency at STC	20.7%	20.94%
Coeff. of P_{max}, in °C	−0.34%/C	−0.35%/C
Coeff. of V_{oc}, in °C	−0.25%/C	−0.28%/C
Coeff. of I_{sc}, in °C	0.04%/°C	0.048%/°C
Bifacial factor	–	70 ± 5%

TABLE 3: PV inverter specifications at roof-top of DTU, Delhi

Specification (Hoymiles MI 1200)	
Input	
DC power Maximum	1520 W
DC voltage Maximum	60 V
PV voltage at MPP	48 V
Output	
Nominal output voltage	230 V AC
AC power Maximum	1200 W
Max. Output current	6 A
Maximum efficiency	96.5%

TABLE 4: Technical specifications of MAX125KTL3-XLV inverter at FSPV plant in Chandigarh

Parameter	Value
Model	MAX125KTL3-XLV
Max. Input Voltage	1100 V
Nominal DC Voltage	600 V
Max. Input Current per MPPT	32 A
Total Input Current	640 A
Rated Output Power	125 kW
Max. Output Power	137.5 kW
Max. Output Current	198.5 A
Nominal AC Voltage	340–440 V
Max. Efficiency	98.7%

TABLE 5: Monthly global horizontal irradiation (GHI), wind velocity, and ambient temperature data for Chandigarh

Month	GHI (kWh/m^2/day)	Wind Speed (m/s)	Temperature (°C)
January	2.46	4.56	11.84
February	3.42	5.10	15.49
March	4.47	5.27	21.06
April	5.19	5.28	26.99
May	5.65	5.25	31.54
June	5.49	4.64	31.27
July	4.85	3.84	30.21
August	4.55	3.57	29.33
September	4.63	3.75	27.51
October	3.99	3.93	24.35
November	2.96	4.29	18.28
December	2.57	4.38	13.44
Annual Average	4.09	4.48	23.48

List of Publications

Papers in Refereed Journals

[1] Atul Avasthi, Rachana Garg, and Priya Mahajan. Comparative analysis of bifacial and monofacial floating solar power plants: performance evaluation and economic analysis. *Iranian Journal of Science and Technology, Transactions of Mechanical Engineering*, 48(4):2167–2185, 2024.

[2] Atul Avasthi, Rachana Garg, and Priya Mahajan. Optimizing energy harvesting: a comprehensive analysis of tracking technologies in a 2 mwp floating solar photovoltaic system. *Electrical Engineering*, 107(4):4663–4681, 2025.

[3] Atul Avasthi, Rachana Garg, and Priya Mahajan. Enhanced energy yield in floating solar power plants through optimal inverter loading ratios. *Electrical Engineering*, 2025. Accept on 16.08.2025.

[4] Atul Avasthi, Rachana Garg, and Priya Mahajan. Long-term degradation assessment of a 2 mw floating solar pv system in a humid subtropical climate using time-series analysis. *Computers and Electrical Engineering*, 2025. Revision submitted.

International Conference Proceedings

[1] Atul Avasthi, Rachana Garg, and Priya Mahajan. Bio-inspired mppt and inverter control for grid-connected spv system. In *Lecture Notes in Electrical Engineering*. Springer. (Presented).

[2] Atul Avasthi, Rachana Garg, and Priya Mahajan. Flying squirrel search optimization based mppt controller for stand-alone pv system. In *2023*

204

International Conference for Advancement in Technology (ICONAT), pages 1–7. IEEE, 2023.

[3] Atul Avasthi, Rachana Garg, and Priya Mahajan. Field performance assessment of a 1.34 kw rooftop pv plant in delhi: Insight from two comparative periods. In *2025 International Conference on Sustainable Energy Technologies and Computational Intelligence (SETCOM)*, pages 1–6. IEEE, 2025.